Montanuniversität Leoben

New findings on the mechanisms during mechanical alloying of a Fe-Y_2O_3 model alloy and an oxide dispersion strengthened high-alloyed steel

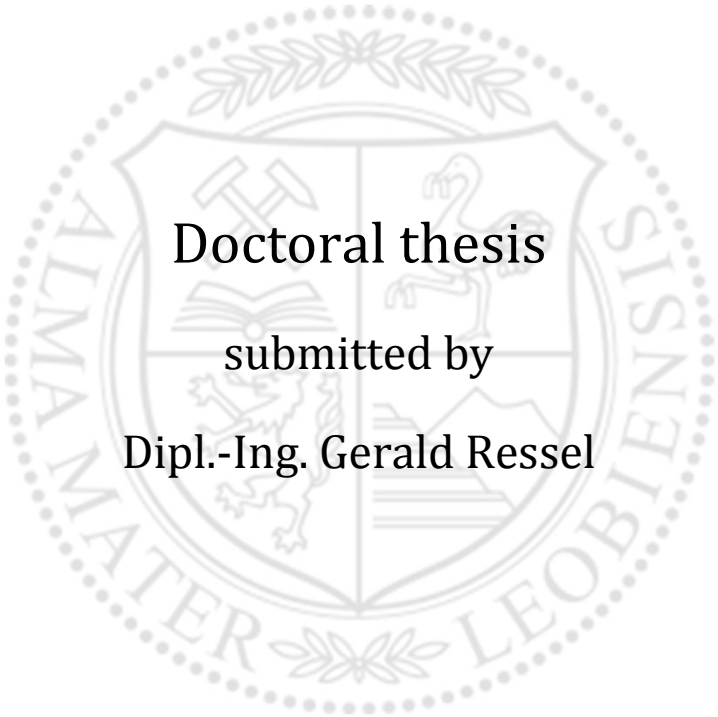

Doctoral thesis

submitted by

Dipl.-Ing. Gerald Ressel

Department of Physical Metallurgy and Materials Testing

Montanuniversität Leoben

Leoben, December 2013

Affidavit

I declare in lieu of oath that I wrote this thesis and performed the associated research myself, using only literature cited in this volume.

Leoben, December 2013 Gerald Ressel

Acknowledgements

Ich möchte in den folgenden Zeilen Personen danken, die in unterschiedlichster Art und Weise einen nicht unerheblichen Anteil an meiner Arbeit haben:

Zu aller erst möchte ich meinem Betreuer, Dr. Harald Leitner, danken, da er mir diese Dissertation ermöglicht hat. Ohne Harald wäre dieses sehr interessante Thema wahrscheinlich gar nicht zu Stande gekommen. Ich bin Harald sehr dankbar, dass ich mich mit diesem Thema beschäftigen durfte.

Einen weiteren großen Dank meinerseits verdienen mein Erstbegutachter Prof. Helmut Clemens und Dr. Sophie Primig, die mich nach Haralds Wechsel zu Böhler wahnsinnig gut betreuten und unterstützten.

Auch bei meinen Bürokollegen Christopher, David und Stephi, sowie meinen Kollegen Chrisi, Turki und Francisca möchte ich mich für die schöne Zeit bedanken. Die vielen lustigen Stunden im Büro oder bei der Kaffeepause werde ich nie vergessen.

Speziell möchte ich meiner Familie und im Besonderen meinen Eltern danken, die jederzeit für mich da sind und mich immer unterstützen. Ich habe ihnen sowieso alles zu verdanken, da sie mir das Studium und somit die Dissertation ermöglichten. Mein Bruder, Robert, ist bei meiner Arbeit immer mit Rat beiseite gestanden.

Zu guter Letzt möchte ich Katharina für ihre Liebe und Freundschaft während dieser Arbeit danken und sagen, dass ich sie liebe und dass ich froh bin, dass es uns beiden so gut geht.

Table of contents

Abbreviations

APT	atom probe tomography
bcc	body-centered-cubic
BET	Brunauer-Emmett-Teller
BPR	ball-to-powder-ratio
DP	Doppler broadening
DSC	differential scanning calorimetry
EBSD	electron-back-scatter-diffraction
fcc	face-centered-cubic
FIB	focused ion beam
HIP	hot isostatic pressing
IPF	inverse pole figure
LEAP	local electrode atom probe
MD	molecular dynamics
NFA	nano featured alloy
ODS	oxide dispersion strengthening
PAS	positron annihilation spectroscopy
PCA	process control agents
PSD	particle size distribution
RDF	radial distribution function
ROI	region of interest
R_g	radius of gyration
SANS	small angle neutron scattering
SEM	scanning electron microscopy
TEM	transmisson electron microscopy
XPS	x-ray photoelelectron spectroscopy
XRD	x-ray diffraction
XRF	X-ray fluorescence spectroscopy
YSZ	yttrium stabilized zirconia

1 Introduction

Mechanical alloying is used to synthesize various materials with stable or metastable phases. The different types of materials include amorphous, quasi-crystalline, nanocrystalline and crystalline alloys. According to Suryanarayana [1], in the mid-1980s it was realized that with mechanical alloying it is possible to produce alloys from elements that are not easily formed by conventional methods. Moreover, even materials which are impossible to prepare by conventional methods, e.g. elements that are immiscible under equilibrium conditions, have been successfully produced by mechanical alloying. The main reason for the invention and development of mechanical alloying has been the production of so-called oxide dispersion strengthened (ODS) alloys in which extremely fine particles (2-50 nm in diameter) of Y_2O_3 or ThO_2 are homogenously dispersed in the material which is intended to be strengthened [1]. In the present time it is state of the art to add about 0.3 m.% to 1 m.% oxide to for example Ni- or Fe-based superalloys. Y_2O_3 and ThO_2 are extremely stable oxides, which do not dissolve in Fe or Ni until extremely high temperatures. Mechanically alloyed ODS materials exhibit a high strength at room temperature and also at elevated temperatures. According to [1], this fact is based on more than one mechanism. First of all, the uniform dispersion of these very fine introduced oxide particles inhibits dislocation motion [2–5]. Because of the high stability of these oxides, this particle strengthening mechanism exists also at elevated temperatures. Therefore, ODS materials also exhibit a high resistance against creep deformation [6,7]. Furthermore, it is known that mechanical alloying produces extremely fine grain sizes, which is the only mechanism which improves the strength as well as the toughness of the material. As the introduced oxides reduce grain growth at elevated temperatures and inhibit recovery and recrystallization the strength of the ODS material is further increased at elevated temperatures. Moreover, a further contribution to the strength is achieved by solid solution-strengthening [1].

However, the mechanisms taking place during the last stage of milling Fe with Y_2O_3 are not clear until now. Therefore, this thesis is divided in two main parts. In the first part experiments have been employed to elucidate the active mechanisms during mechanical alloying. These experiments have been performed on a Fe – Y_2O_3 model alloy to reduce

the influence of other alloying elements. The author of this thesis has published 4 papers in international journals and 2 proceedings on this topic (see attachment).

The second part describes the attempt to combine the process route of a high-alloyed and an ODS steel to clarify the question if it is possible to introduce oxide particles also in high-alloyed steels by means of mechanical alloying. A typical tempering curve of a high speed steel is presented in Figure 1. The maximum of hardness for the type of a HS 18-0-1 steel can be found at a tempering temperature of about 600 °C. At annealing temperatures above 600 °C, a dramatical drop in hardness occurs. This can be related to a coarsening of the secondary hardening carbides precipitated during the tempering heat treatment. The aim of this part of the thesis is to impede this dramatical drop of hardness at tempering temperatures between 600 °C and 800 °C. The idea is to introduce particles into the high-alloyed steel, which are thermodynamically much more stable and, therefore, coarsen much slower at elevated temperatures than common secondary hardening carbides. Also in this part Y_2O_3 has been chosen as dispersions introduced in the high-alloyed steel by means of mechanical milling. In the present time the introduction of such stable oxide particles is a popular topic for steels for fuel claddings of rectors in nuclear power plants. Previous papers [6,8–10] already compared mechanical properties at elevated temperatures of Cr alloyed ODS ferritic steels with common commercial alloys and showed its immense potential to improve their properties. In this work it is the first time that these small Y-O disperoids in a range between 1 and about 50 nm are introduced into high-alloyed steel powders to enhance their mechanical properties at elevated temperatures. These findings have not been published so far, therefore, they are described in detail in the second part.

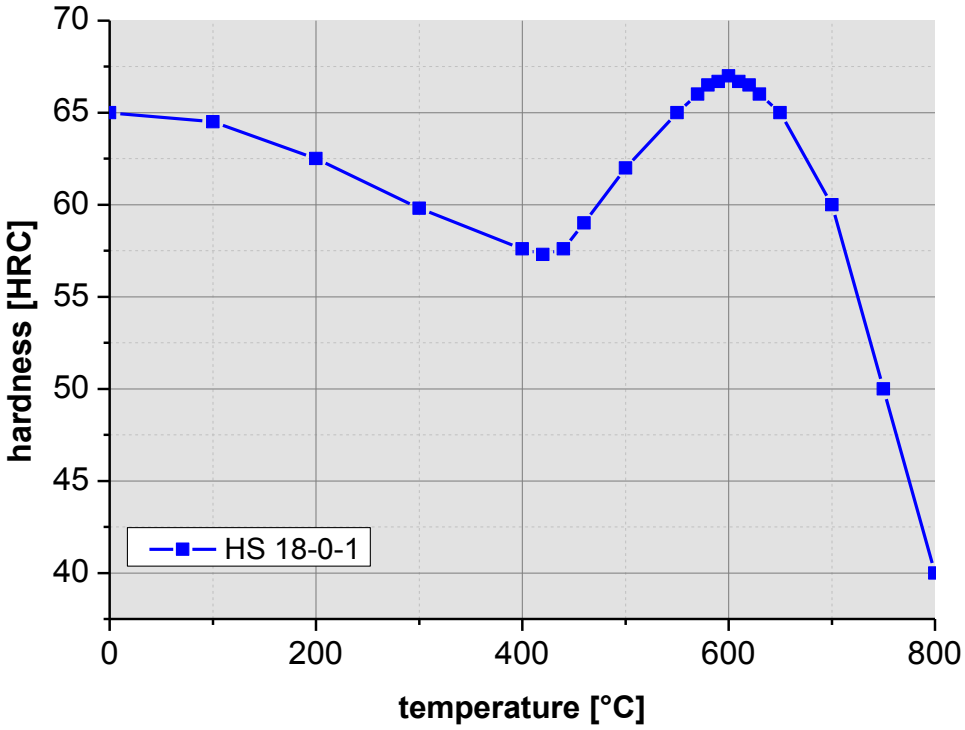

Figure 1: Tempering curve of a HS 18-0-1, which means a content of 18 m.% W and 1 m.% V. This alloy clearly exhibits a typical secondary hardness maximum at about 600 °C tempering temperature [11].

2 Mechanical alloying and its mechanisms

2.1 The history of oxide dispersion strengthened (ODS) alloys

The development of ODS alloys was mentioned for the first time in 1910. The product was called “ductile tungsten”. This material was produced by the common powder metallurgical process and the necessary disperoid size as well as the distance of the particles was achieved by an extremely high deformation as forging or wire drawing. The problem of this process was to produce components with large dimensions [12].

The next, very important milestone in the history of ODS alloys was the development of thoriated nickel by DuPont in the year 1958. To improve the material strength in this process finest oxide powder was mixed with nickel powder. The disadvantage of this product was that it was very expensive [12].

Concerning ODS alloys, another very important developement was the production of powders by mechanical alloying. Benjamin [13,14] invented the mechanical alloying process in the 1960s and 1970s and initiated further developments of different thermodynamically stable and metastable alloys. Solid solution, intermetallics, quasicrystals, amorphous alloys, and bulk metallic glasses are examples of such materials. Additionally, nanostructured materials, hydrogen storage materials and other exotic materials are being synthesized by this process [1].

In the last few years a lot of research was done on ODS - Fe base alloys for application as fuel cladding material in fast breeding reactors in nuclear power plants. Cr alloyed ODS Fe base alloys are a promising candidate to meet the high demands of reactor applications, because good mechanical properties at elevated temperatures and high radiation resistance are necessary.

Figure 2 gives detailed information about the historical evolution of the development of ODS alloys.

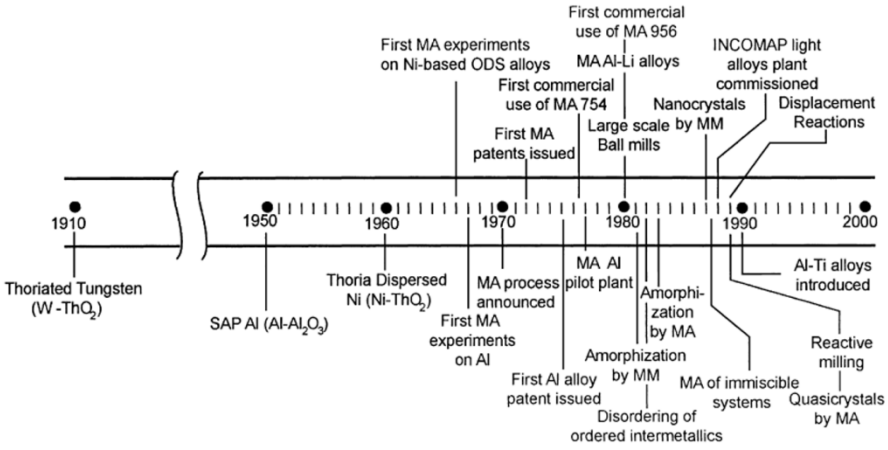

Figure 2: Historical evolution of the development of ODS alloys [1].

2.2 Particle hardening

Particle hardening is besides solution hardening and work hardening one important factor for adjusting hardness and strength of a material. This hardening mechanism can raise the hardness of a material for more than two orders of magnitude. All three mechanisms are based on obstructing the movement of dislocations. Arzt et al. [2–5,15] published several papers on models of the strengthening mechanism of dispersions. They showed a size dependence of particle hardening, which is illustrated in Figure 3. As the material is heated up, the particles coarsen and their contribution to the hardness decreases. This is the main drawback of steels regarding the mechanical properties at elevated temperatures. At coherent precipitates dislocations either cut through the particles, which is energetically favorable at small particle radii, or they circumvent at larger particle sizes according to the Orowan mechanism.

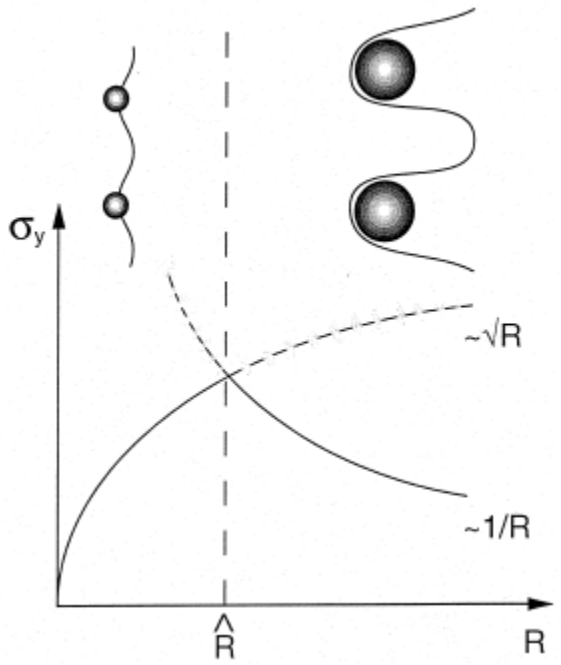

Figure 3: The contribution of particle size to strength as a function of their radius [2].

As already mentioned especially at temperatures above 600 °C carbide precipitates coarsen in several types of steels and, consequently, at a certain size their contribution to the hardness of the steel decreases.

To avoid this drop in mechanical properties at elevated temperatures, particles can be introduced into the matrix, which are thermodynamically more stable than the common carbides. This would, consequently, enable steels for an application at higher temperatures. The materials strengthened with these stable particles (also called dispersions) are called oxide dispersion strengthened (ODS) materials. In the last few years these steels have also been called nano featured alloys (NFAs). It is not clear until now, if these dispersions are all incoherent particles or if there are also coherent nano-particles present. The following section describes the model of Arzt et al. [2] based on incoherent dispersoids with sizes between about 20 and 50 nm.

Dislocations cannot cut through incoherent dispersoids. Hence, they have to circumvent these particles, which is known as the Orowan mechanism [2]. Dislocations are forced to deflect at hard, incoherent obstacles, which are distributed in a fine manner. Hence, particle hardening with dispersoids is mainly based on this deflecting effect. To pass-by incoherent particles, the following condition must be fulfilled [2]:

$$d(\tau) \leq L \qquad (1)$$

d(τ) is the diameter of the deflected dislocation line and L the distance of the particles, which is shown in Figure 4.

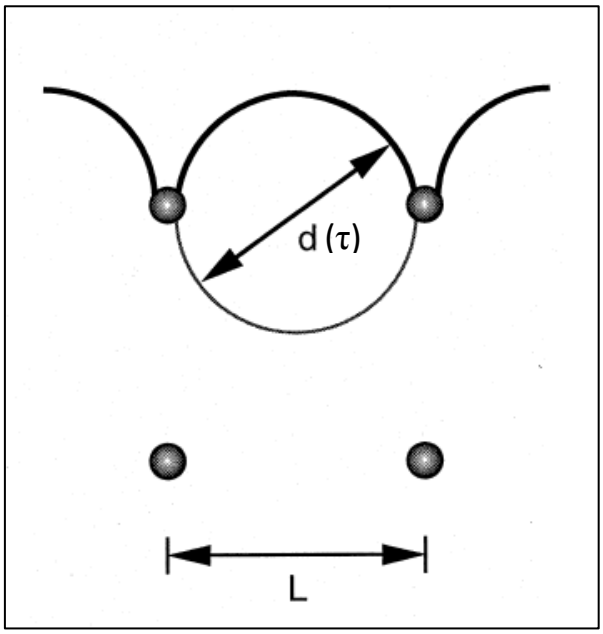

Figure 4: Deflection of a dislocation line caused by dispersoids distributed in the matrix [2].

This implies that a plastic deformation, or a dislocation motion, of the dispersion strengthened material requires the formation of deflected dislocation lines. From this fundamental consideration the following formula is derived, which describes the maximum increase of the yield stress of disperoid strengthened metallic materials [2]:

$$\tau_{Or} = \frac{2T_d}{bL} \approx \frac{Gb}{L} \propto \frac{Gb}{R}$$

With τ_{Or}, which is called the Orowan stress, i.e. the shear stress needed for a dislocation to circumvent the particles. T_d is the line stress, b the Burger's vector, G the shear modulus of the matrix and L the average distance of the particles, which is proportional to the average particle radius R.

The smaller the radius of the particles, the higher is the Orowan stress and the higher is the strength contribution of the particles to the material [2].

Another possibility for dislocations to pass incoherent particles at elevated temperatures is to cross-slip from one glide plane to another. Additionally, at higher temperatures dislocations can climb, assisted by vacancies, to overcome these particles. Materials applied at high temperatures contain obstacles at which a climbing of dislocation or cross slipping is impeded [2].

At elevated temperatures either large precipitates reduce the mobility of dislocations, such as the γ‘ phase in Al containing Ni-base alloys for example, or fine dispersoids, which cause an attractive force to dislocations. The latter mechanism is based on an attractive force of a dislocation and the interface of the incoherent particle. Investigations and theories, especially by Arzt and Roesler [5–7], suggest that the surfaces of incoherent particles are favorable positions for dislocations because at these interfaces their stress fields can be relaxed. Thus, repelling forces act on dislocations trapped on the surface of the dispersions. This is due to a stress relaxation of the dislocation stress field at the interface [16]. In Figure 5 a transmission electron microscope (TEM) image of an adherence of a dislocation on a surface of an incoherent particle is depicted.

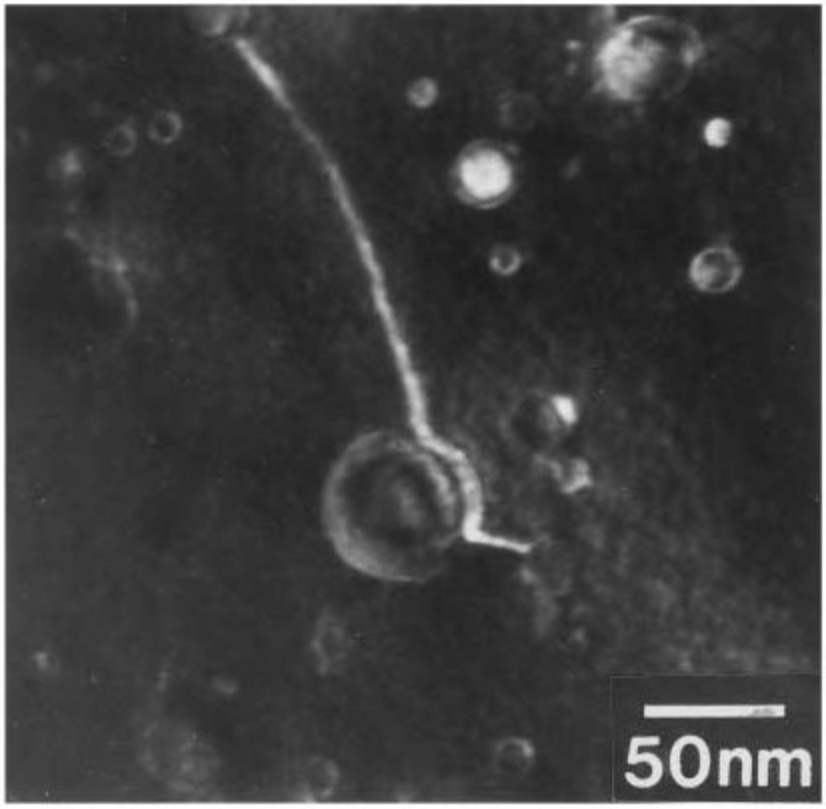

Figure 5: Repelling force of a Y_2O_3 disperoid on a dislocation in a ODS Ni-base alloy. This is caused by a relaxation of the stress field of both partners [17].

The attractive force between the dispersion-interface and the dislocation can be calculated with the assumption that the line energy of the dislocation segment at the interface is lower than at the segment of the dislocation in the matrix. It is also known that a very small relaxation at the interface is enough to cause an adherence of the

dislocation at the interface. Rösler and Arzt [15] developed the following formula, which takes the adherence of a dislocation at the interface into account:

$$\frac{\tau}{\tau_d} = 1 - \frac{1}{1-\kappa}\left[\frac{kTln\dot{\varepsilon}_0/\dot{\varepsilon}}{Gb^2R}\right]^{2/3}$$

With τ_d, which can be calculated according to the formula $\tau_d = \tau_{Or}\sqrt{1-\kappa^2}$. τ_d is the athermal adherence stress. T is the absolute temperature, k is the Boltzmann constant, $\dot{\varepsilon}$ the strain rate, and $\dot{\varepsilon}_0$ is a factor, which includes the diffusivity and the density of mobile dislocations [2].

2.3 Characteristics of the introduced dispersions

In *Publications A-F* as well as in the second part of this thesis Y_2O_3 has been chosen as dispersions introduced in the material, because it is thermodynamically much more stable than carbides, which are the more common particles in steels. The chemical composition of the powder analyzed in *Publications A-F* before and after milling is listed in Table 1.

Table 1: Chemical composition of the of the analyzed powders before and after milling (in at.%).

	Fe	Al	Mn	Cr	Ni	Mo	W	Cu	Y_2O_3
before milling	bal.	-	0.12	0.05	0.03	-	-	-	0.13
12 h mechanically alloyed state	bal.	0.34	0.14	0.09	0.05	0.01	0.8	-	0.12
24 h mechanically alloyed state	bal.	-	0.18	0.08	0.1	0.08	-	0.23	0.13
48 h mechanically alloyed state	bal.	0.1	0.16	0.24	0.1	0.01	0.05	-	0.13

There are numerous studies dealing with yttria containing ODS steels. For example, Miller et al. [18–20], Hirata et al. [21] or Klimiankou et al. [22–24] worked on ODS ferritic steels. However, their chemical composition differs from the ingredients of this

work especially in the Cr and Ti content, which is reported to be ~14 m.% as well as ~0.5 m.%, respectively.

Figure 6 compares the standard formation enthalpies ($\Delta_f G^0$) of Y_2O_3, TiC, $Cr_{23}C_6$, and VC, which is a scale for the stability of different phases.

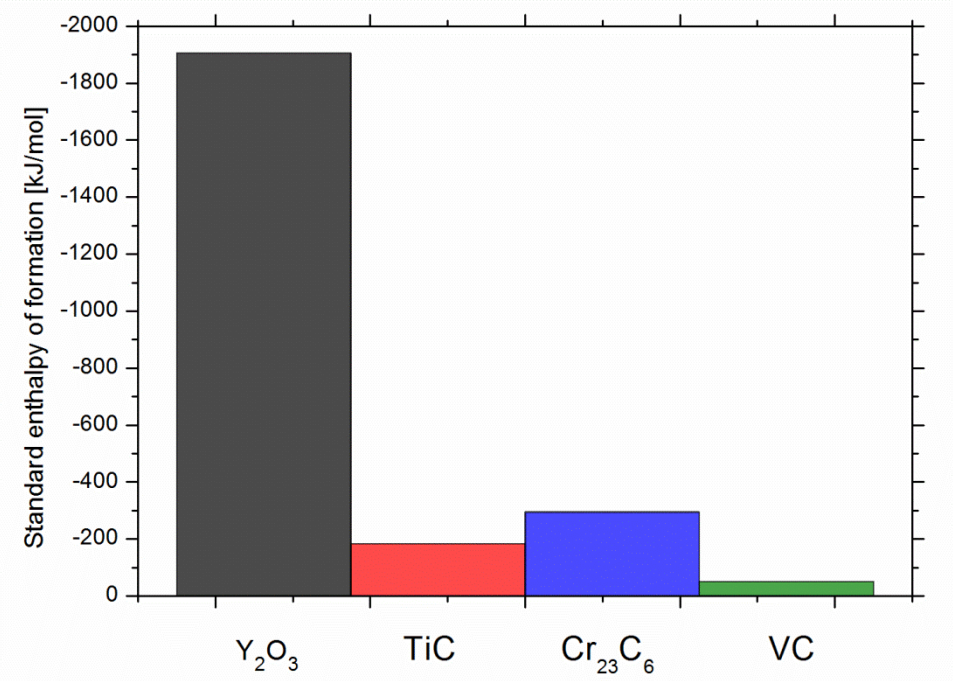

Figure 6: Comparison of the standard enthalpy of formation ($\Delta_f G^0$) of Y_2O_3, carbides such as TiC, $Cr_{23}C_6$ and VC [25,26].

The more negative the standard enthalpy of formation of a certain phase, the higher is its thermodynamical stability. Y_2O_3 shows an enthalpy of formation of about -1900 kJ mol^{-1} and the carbides an enthalpy between -200 to -100 kJ mol^{-1}. This is about one order of magnitude lower and indicates the immense thermodynamical stability of Y_2O_3. Due to this fact, yttria has an extremely low solubility in Fe and, therefore, a positive heat of mixing. Thermodynamic calculations were conducted by Domagala et al. [27] and Gschneider [28] in 1961. More present studies were published by Kubaschewski [29] and Zhang et al. [30]. Their calculations revealed a maximum solubility of Y in Fe of lower than 0.6 at.% at a temperature of approximately 1345 °C. At lower temperatures the solubility of Y in Fe is even smaller. Figure 7 shows the calculated phase diagram of Fe and Y. This can be related to the quasibinary phasediagram of Fe-Y_2O_3.

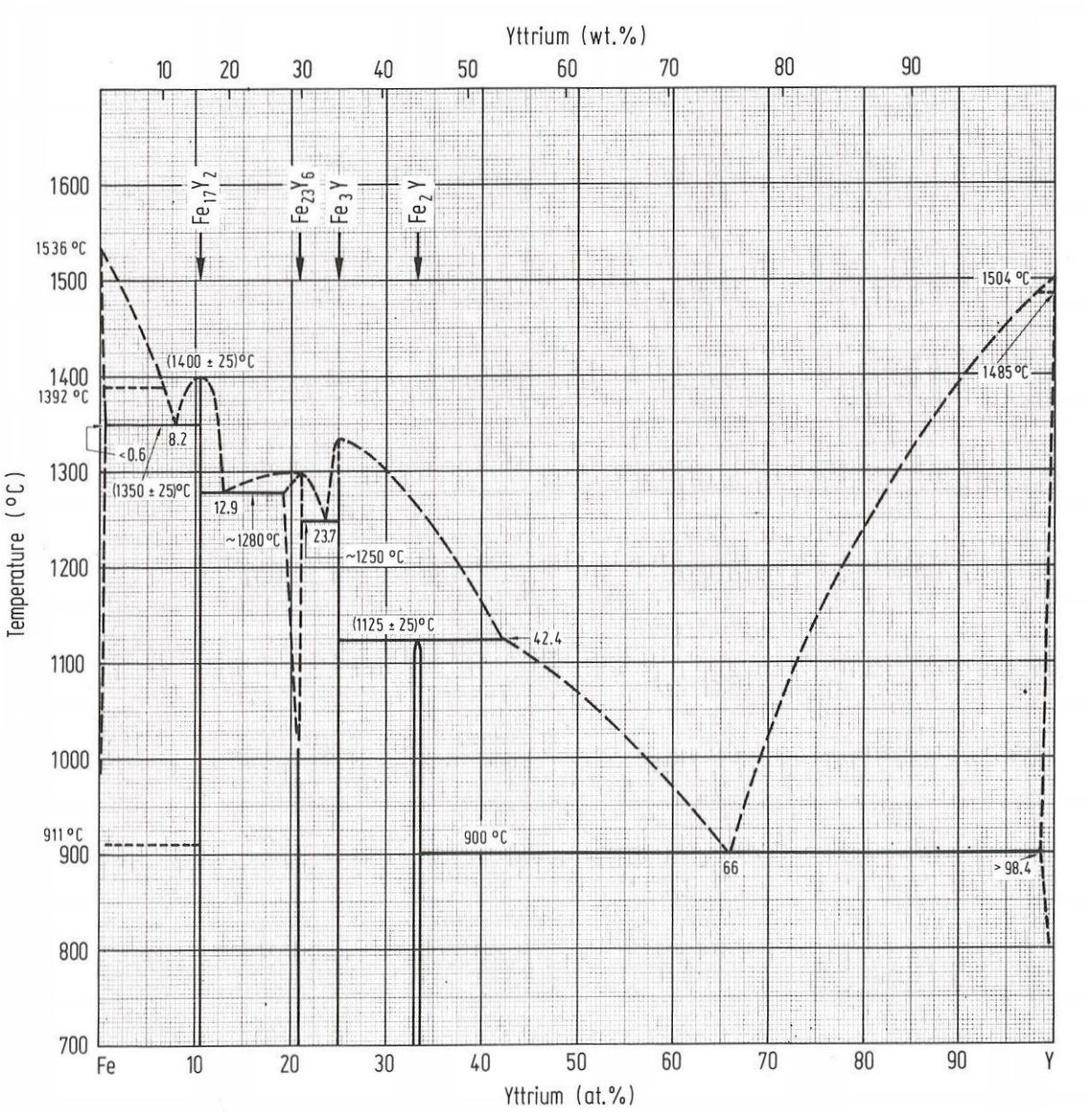

Figure 7: Fe-Y system, showing a very narrow phase field at the Fe rich side, meaning an extremely low solubility of Y in Fe, especially at low temperatures [29].

Because of this exceptionally low solubility other production routes than conventional metallurgy must be applied to distribute fine oxide particles in Fe. Mechanical milling is a method to produce metastable phases and a material where these oxides are finely distributed in the Fe matrix. In earlier years it was assumed that during mechanical alloying no dissolution occurs, but a very fine distribution of Y_2O_3 in Fe [7,12–14,31–33]. In more recent publications [20,34–36] it is assumed that in the Fe-Y_2O_3 system (typically Fe alloyed with ~14 m.% Cr, ~0.5 m.% Ti, ~0.5 m.% Y_2O_3 and a very low C content) Y_2O_3 dissolves in the Fe matrix and fine Y-O particles precipitate after hot

isostatic pressing (HIPing). However, this assumption has not been clearly evidenced until now.

2.4 Mechanical alloying

For the last four decades mechanical alloying has been a demanding field of research which continuously growing with more than 500 publications each year [1]. There are different processes to produce metastable alloys. The most prominent method is to quench a melt or a high temperature phase. Additional possibilities are the production with the help of a plasma as well as vapor deposition and mechanical alloying. The main topic of all of these techniques is that, first of all, energy is introduced in the system and subsequent quenching is applied to achieve a metastable phase as initial state. In the case of this thesis the initial state is a Fe or a steel matrix with extended solubility of Y or O. Figure 8 shows the basic concept schematically [37].

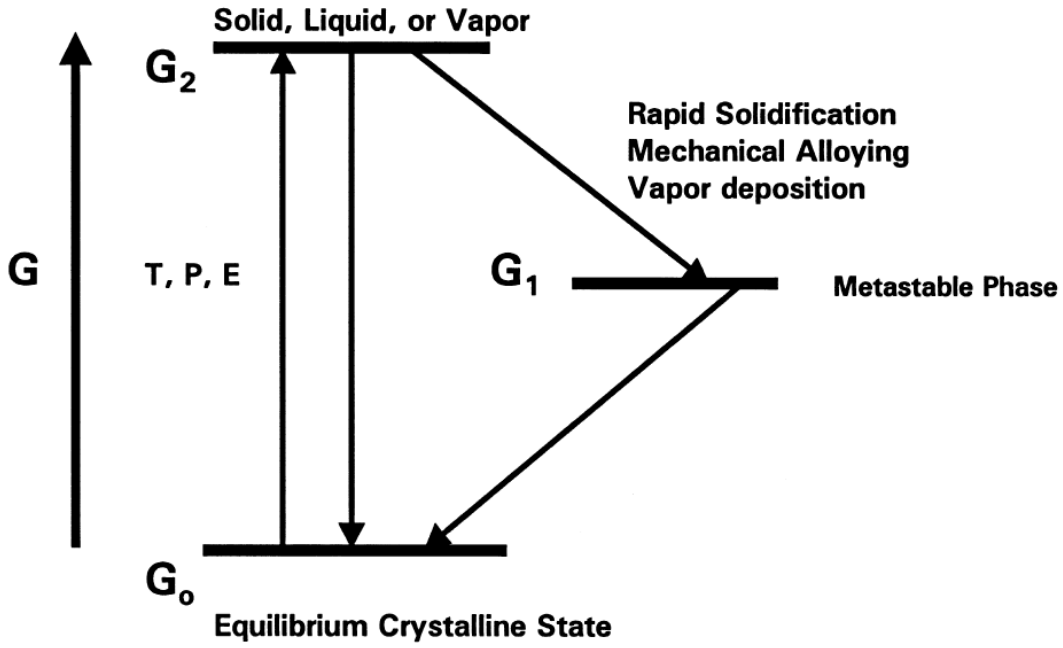

Figure 8: The basic concept, energy input and quenching to achieve metastable alloys [37].

During the mechanical alloying process the metastable state is achieved by particle compression causing plastic deformation. Several previous publications [38,39] estimated that the local temperature occurring at a powder particle during the collision with the balls is far above room temperature. Subsequently, the powder particle cools down quickly. This process is permanently repeated during milling. The temperature is

increasing in the vial with progressing time and consequently also in the trapped particle.

Table 2 shows the various processes and their possibility to deviate from thermodynamic equilibrium in kJ/mol.

Table 2: Deviation of the thermodynamic equilibrium due to the different processes [22,23].

Technique	Effective quench rate [K/s]	Maximal deviation from equilibrium [kJ/mol]
Solid state quench	10^3	16
Rapid solidification processing	$10^5 – 10^8$	24
Mechanical alloying	-	30
Mechanical cold work	-	1
Irradiation/ion implantation	10^{12}	30
Condensation from vapor	10^{12}	160

The mechanical milling process generates about 30 kJ/mol. Thus, this is, besides irradiation, the second highest energetic deviation from the thermodynamic equilibrium [41].

Before the start of the mechanical alloying process the various constituents are blended in a tumbling mixer with the preferred ratio. Also in the *publications A-F* the Fe powder is mixed with the Y_2O_3 powder prior to milling. Subsequently, the vial is loaded with the powder blend and milling balls in a specific ratio, which is called the ball to powder ratio (BPR). Optionally, Process Control Agents (PCA) can be added to the batch. Subsequently, the milling process is started for a certain duration. Depending on the type of alloy and the constituents, saturation is reached after a certain time, where further milling has no effect on the structure and composition of the powder particles. In some alloys this is a metastable phase, where the dissolved concentration exceeds the thermodynamic equilibrium.

2.4.1.1 Types of mills

There are various types of mills for mechanical alloying. The most frequently used ones are SPEX shaker mills, planetary ball mills and so-called attritors, which were used in this study.

A conventional ball mill consists of a rotating horizontal drum, half-filled with balls. The powder is milled by the rotating drum and by colliding balls. The rate of milling increases with the speed of rotation. At high rotational velocities the centrifugal force exceeds the gravity of the balls which has the effect that the balls stick to the container wall and a milling effect of the balls is missing [1,37].

Attritors consist of a vertical drum also half-filled with balls. In this system a shaft with rotating arms is inserted. An engine powers the shafts to rotate, which agitate the balls. The powder particles are subjected to different forces, which are impacts of balls, shearing as well as rotation. Milling with attritors is much more efficient because most of the energy is used for the movement of the grinding media. Moreover, because the drum is not rotating, the sticking of the balls at the vial wall at high rotation speed is impeded [1,37].

Normally, attritors work batchwise, but for mechanical alloying of a high quantity of powder also continuous processes can be applied. The attritor can be batched on the upper side and the processed powder unloaded on the lower side. In the continuous method the height of the attritor as well as the flow rate of the powder, which is influenced by the particle size and size of the balls, are the main parameters which determine the milling intensity of the powders [1,37]. Figure 9 shows the set-up of an attritor mill schematically.

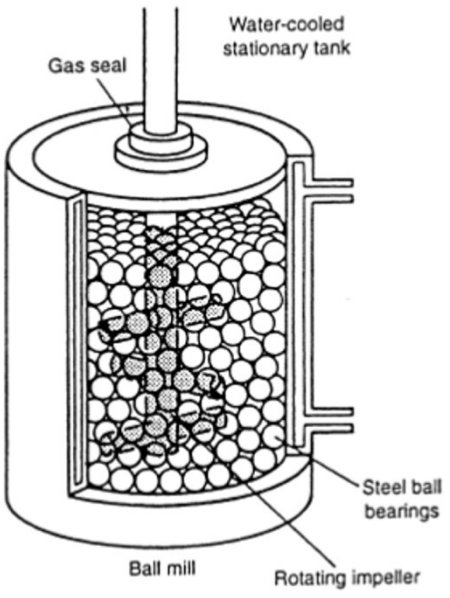

Figure 9: Set-up of an attritor mill with rotating arms and balls as grinding media [1,37].

2.5 Mechanism of mechanical alloying

A large number of different alloys in various constitutions have been produced by mechanical alloying. For example, solid solutions which are in the thermodynamic equilibrium, metastable or amorphous materials. Although the number of different sorts of phases formed during mechanical alloying is very large and many applications for these materials have been investigated [37], the number of works dealing with the mechanism of mechanical alloying is very limited. This following chapter gives an overview of the literature of the last few years concerning the mechanism of milling and compares them with the findings of this work.

2.5.1 Ball-powder-ball collisions

Whenever two balls collide or balls collide with the vial, a small amount of powder is trapped in between them. Therefore, mechanical alloying means a random impact of blended powder or pre-alloyed powder with balls, causing a heavy deformation of the powder particles. It is assumed that, normally, about 1000 particles with an aggregate weight of about 0.2 mg are trapped during each ball collision. During this process the particles are repeatedly fractured and again cold-welded. The fracture and cold welding process as well as the milling kinetics depend mainly on the condition of the powder and on their deformation behavior. If the starting powders are soft and ductile, they are deformed, work hardened and, consequently, they are flattened to flakes. Figure 10 shows a scanning electron microscope (SEM) image of a Fe particle before and after milling for 48 h in an attritor with 0.5 m.% Y_2O_3. Because of fracturing and cold-welding also flattened layers of the different powder constituents are formed inside each particle. Brittle powder particles, for example, intermetallic powders or oxides, get fractured and repeatedly fragmented into smaller particles. If a soft and ductile constituent is milled with a hard and brittle powder fraction, the harder and more brittle constituent tends to be incorporated and trapped in the softer material. After a large number of impacts particles obtain a homogenized and refined microstructure if both constituents are mutually soluble. If they are not mutually soluble some authors, for example Suryanarayana [1], assumed that the dispersions get homogenously dispersed in the matrix. For example, dispersoid oxide particles, which are insoluble in the metal matrix, get distributed in a very fine manner in the matrix with progressing milling duration. Figure 11 presents the different deformation characteristics of the various

types of powder constituents during milling. Furthermore, it must be mentioned that the severe deformation as well as the fracturing causes a dramatic increase of the surface to volume ratio and rupture of the surface films of the adsorbed contaminants can take place. Additionally, because of cold welding some powders may coat the grinding media resulting in a thin layer at the surface. This thin layer reduces contamination of the milled powder and can improve the wear resistance of the grinding media [1].

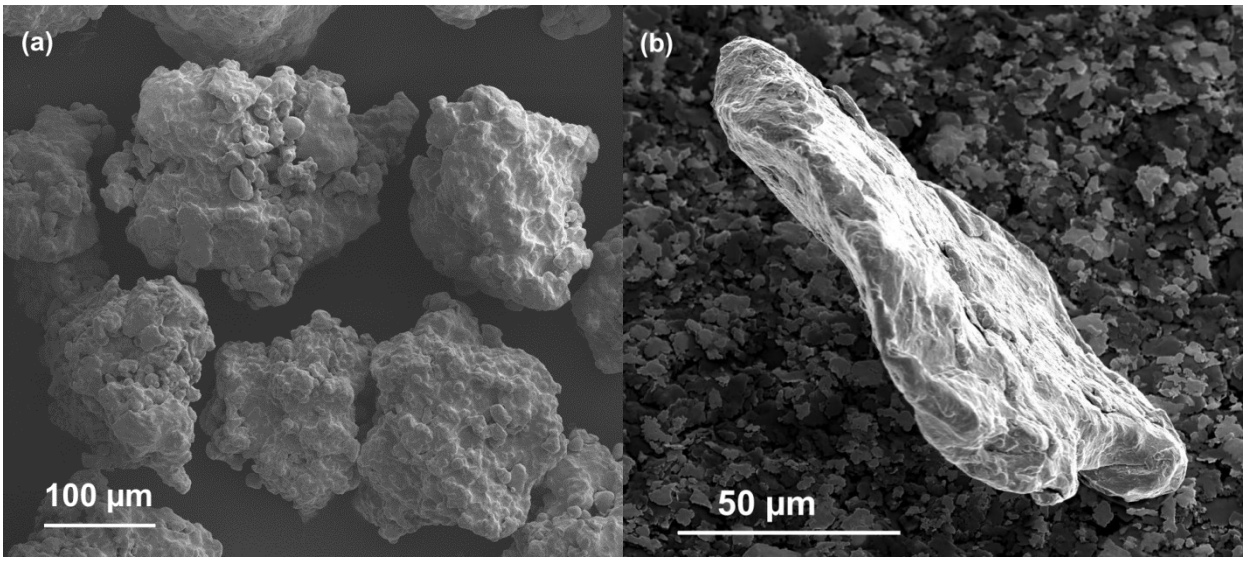

Figure 10: SEM images of Fe particles before (a) and after (b) milling with 0.5 m.% Y_2O_3 for 48 h in an attritor. The ductile Fe particles have been deformed into flakes.

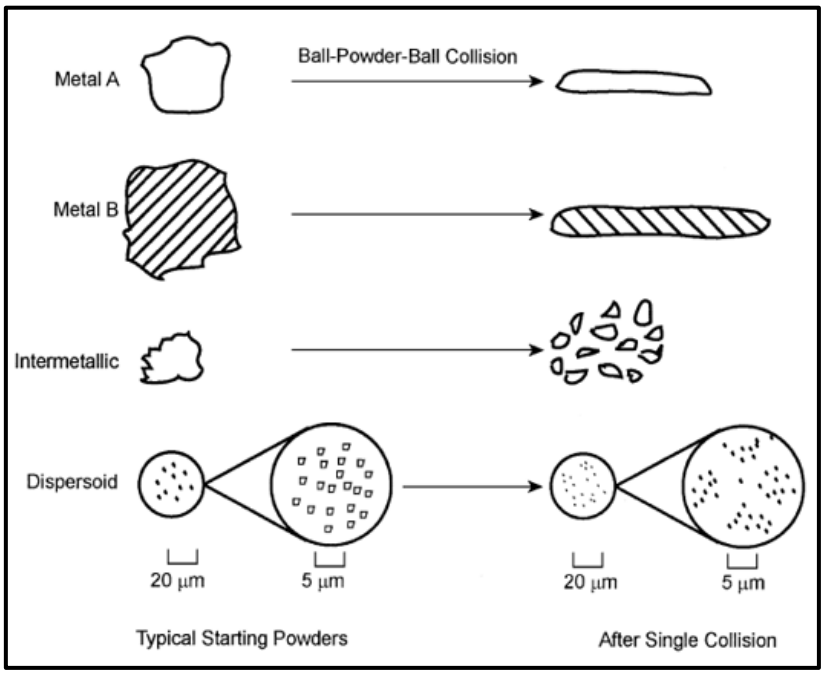

Figure 11: Different deformation characteristics of powders. Ductile metal powders usually get deformed to flakes, whereas brittle intermetallic powders or dispersoids are fragmented into smaller particles [1].

2.5.2 Stages of mechanical alloying

According to Suryanarayana [1,37] different stages of mechanical alloying are described. As already mentioned, in the early stages of milling, soft metal powders undergo a heavy deformation as they are flattened into flakes. Because they also get fractured and again cold-welded also with the second constituent powder, a composite powder exhibiting a lamellar structure is formed. If the second constituent is a dispersoid, the constituents are closely spaced along the lamellar boundaries. At the beginning of the process also original particles may exist, which have not been deformed yet. Therefore, the composition of all particles is not similar in this stage. The size of these particles is in the range of a few micrometers to a few hundred micrometers. Figure 12 presents a schematic illustration of different powder constituents during the early stages [1,37]. This work deals with a ductile phase as metal A and oxides, which are presented as disperoids in Figure 12. Also intermetallic phases can be mechanically alloyed, but are not investigated in this thesis.

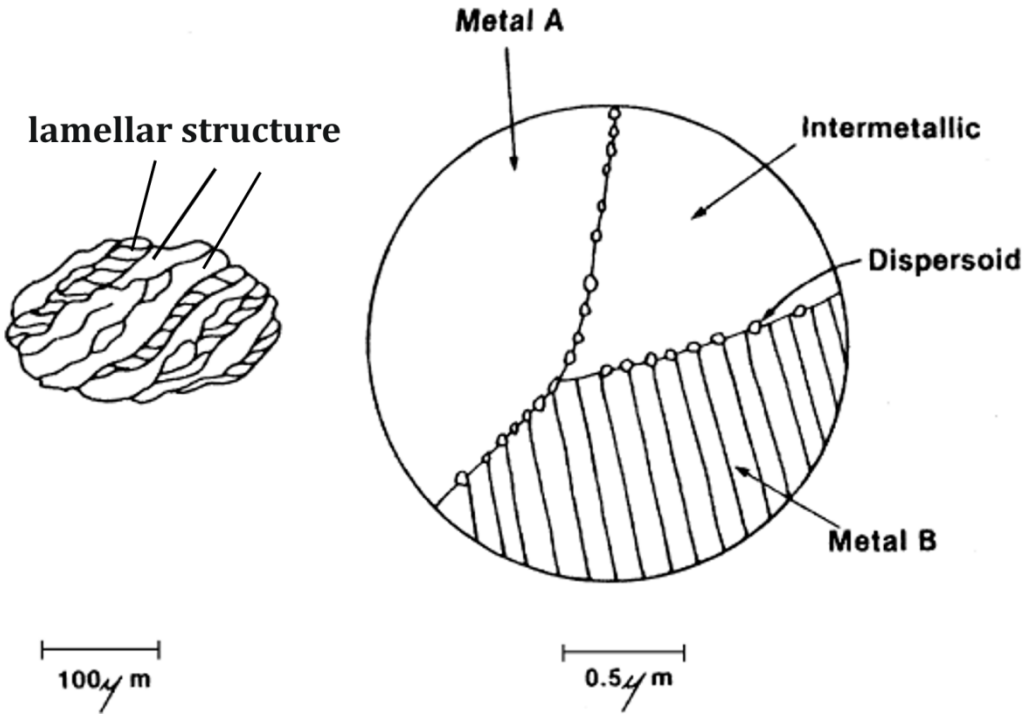

Figure 12: Microstructure of a particle in the early stages of milling [1,37].

Suryanarayana [1,37] called the next stage intermediate stage. As the milling process with cold welding and fracturing continues, the lamellar structure refines and the disperoids are distributed more homogenously and become finer. Figure 13

schematically shows a microstructure of a particle in this stage. At this stage the layers are convoluted, owing to an enhanced amount of cold working and an increased defect density, such as vacancies, dislocations and grain boundaries. Due to ball impacts the temperature increases in the particles which further improves diffusion. Several publications [38,39] estimated the temperature for more than 150 °C to be reached in the particles that become trapped between two colliding balls [1,37].

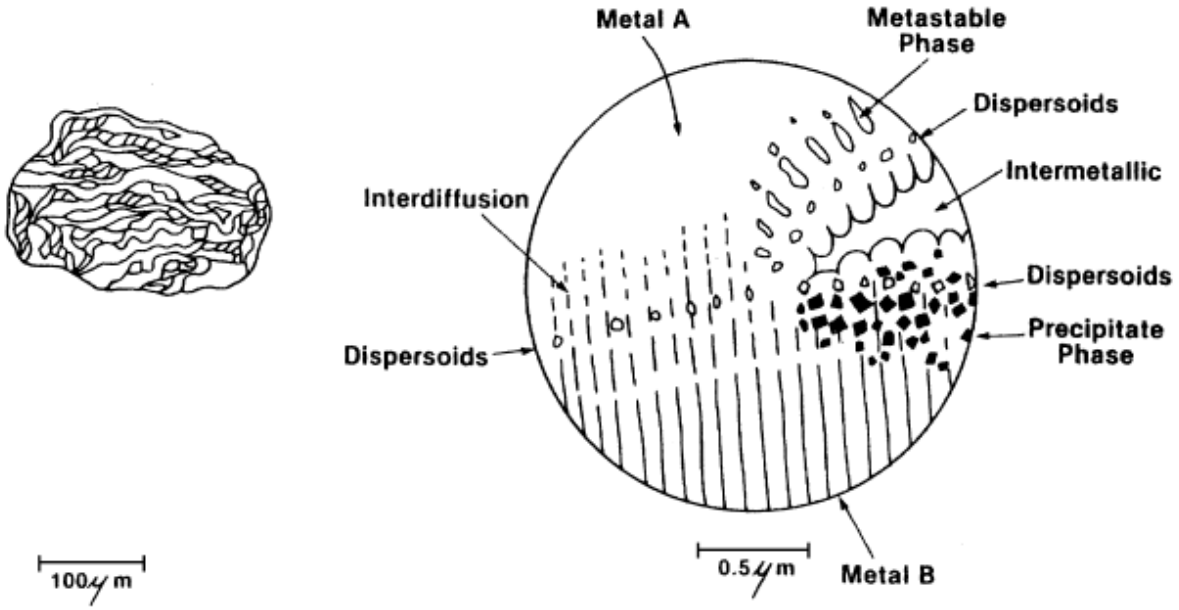

Figure 13: Microstructure of a particle in the intermediate stage of milling [1,37].

In the final stage, as depicted in Figure 14, the layers become finer and also more convoluted. The composition of each milled particle becomes similar to that of the initial blend of powders. The lamellar spacing gets smaller than 1 µm and the microhardness of the particles reaches a saturation level. Finally, the fine lamellae are no longer resolvable under the optical microscope. Early publications assumed that these dispersoids get refined during milling to a size of about 5 – 20 nm. Additionally, they are finely distributed but do not dissolve because of their positive heat of mixing [12–14,31,42]. It was also supposed that further milling would not improve the distribution of these dispersoids.

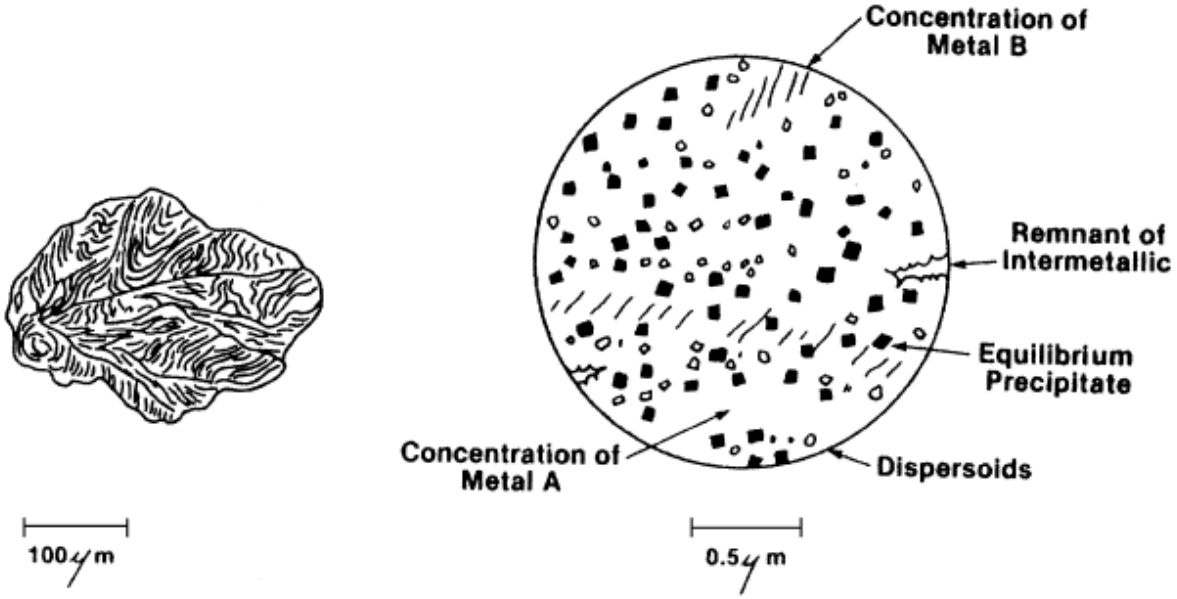

Figure 14: Final stage of mechanical alloying according to Suryanarayana [1,37].

As already mentioned some results have been published recently, which suggest that there is a mixing of Fe and Y_2O_3. For example, Miller et al. [19,20,43] analyzed mechanically alloyed Fe-Cr-Ti-Y_2O_3 alloys after HIPing by means of atom probe tomography (APT). Additional information on the principle of APT can be found in [44]. Small particles in the size of a few nanometers mainly enriched in Y, O and Ti were detected. By analyzing the composition of these particles and by comparing the Y/O ratio to the original Y_2O_3 powder these authors assumed that these nanoparticles are not just remnants of the original yttria powder particles. At this small size of about 1 nm it should be mentioned that the Fe concentration in the particles is overestimated due to uncertainties during atom probe measurements. Field ion microscopy investigations revealed that these Y-O nanoparticles show a preferential evaporation compared to the Fe matrix [45]. Therefore, tip irregularities occur during APT measurements resulting in lower local magnification and an increased amount of Fe matrix atoms detected inside the nanoparticles. Moreover, the re-calculated shape of the particles can differ from the real appearance [44,46]. Finially, the O concentration in the particles can be underestimated due to trajectory aberrations.

Furthermore, several transmission electron microscopy (TEM) investigations of HIPed materials were performed [21–24,47,48]. For example, Klimiankou et al. [22] found an orientation correlation between a Y-Ti-Cr-O nanoparticle and the Fe-Cr matrix. This suggests the dissolution of Y_2O_3 in Fe after milling and the precipitation of such

nanoparticles during HIPing. Hirata et al. [21] reported a high lattice coherency with the bcc matrix and described the structure of a nanoparticle as a defective NaCl structure. However, Bernard et al. [49] employed ab initio calculations with the result that Y-O nanoclusters are most stable in the common Y_2O_3 structure and do not adapt to the Fe lattice. Therefore, it can be assumed that after HIPing or after heat treatments even the smallest particles would form as incoherent phases. According to Arzt, Roesler and Wilkinson [2–5] incoherent particles, which force dislocations to circumvent at any size, have the highest effect on the strength and hardness when their size is as small as possible.

However, in case of solely HIPed materials a detailed verification of the processes active during milling is difficult. Therefore, several investigations have been employed on a Fe-Y_2O_3 model alloy in order to elucidate the functionality of milling, especially in the last stages.

In *publication A* as well as *publications B* a comprehensive set of experiments were carried out, which evidence that in the system Fe and Y_2O_3 intermixing occurs also during milling, where Y and also O are distributed in an extremely fine manner. Atom probe measurements on mechanically alloyed powder particles showed that Y and also O exhibit an extended solubility in the bcc Fe matrix compared to calculations at the thermodynamic equilibrium [27,29,30]. Figure 15 presents the APT measurements conducted on a powder particle, milled for 48 h, which agree with results of Cr and Ti alloyed ferritc steels investigated by Williams at al. [50].

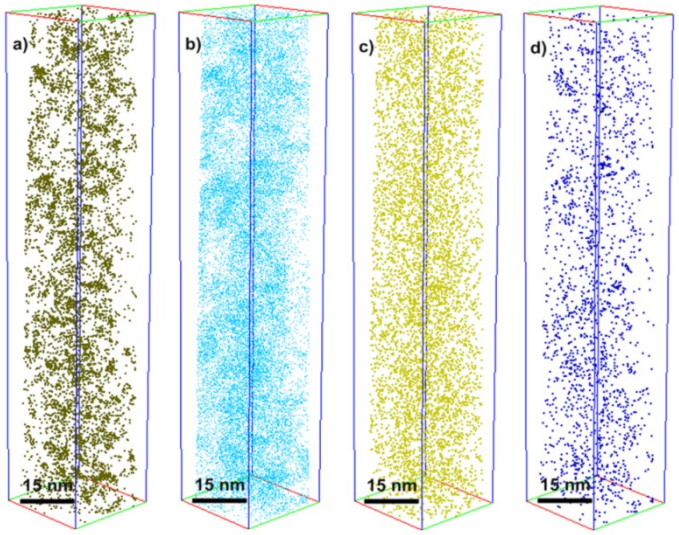

Figure 15: APT measurement of an as-milled powder particle of the Fe-Y_2O_3 model alloy presenting the distribution of the elements Y (a), O (b), Mn (c), and Al (d).

Despite the extended solubility, Y and O also enrich to clusters. APT measurements also revealed that during milling incorporated elements, such as Mn or Al, enrich at the clusters (Figure 15c and d). These enrichments clearly evidence that these particles are not original Y_2O_3 powder particles. APT investigations and the evaluation of radial distribution functions (RDFs), which indicate whether an element is distributed homogenously and evaluates the degree of clustering of an element, showed that HIPing and subsequent annealing cause a formation of distinct particles and a depletion of Y, O, Mn and Al in the matrix. These findings were summarized in *publication A*. As an example the development of the distribution of Y during processing is shown in Figure 16. Also Williams et al. [51] found Mn, but also Ti enrichments in the particles in a HIPed Cr and Ti alloyed steel.

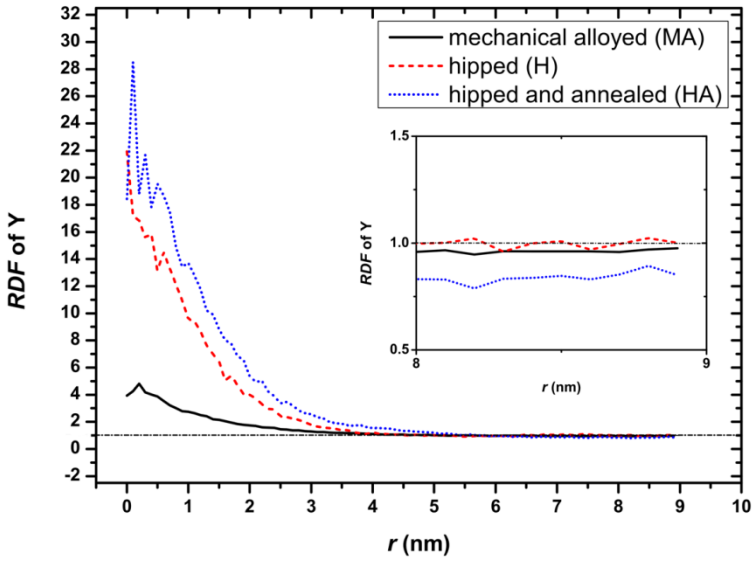

Figure 16: Development of the radial distribution function (RDF) of Y during the process route of the Fe-Y_2O_3 model alloy [*Publication A*].

Furthermore, *Publication B* compared the Y and O as well as the Mn and Al distribution after 12 h and 48 h milling. The results revealed that more Y and O is dissolved in the matrix after 48 h of milling than after 12 h. However, the average Y content of the clusters is roughly the same in both milling states. Also the cluster sizes of both conditions are approximately equal and within the standard deviation. The fact that there is a saturation in the cluster size during milling evidences that these particles are not crushed remnants of original brittle Y_2O_3 powder particles. Moreover, X-ray photoelectron spectroscopy (XPS) measurements, which can give information of the chemical bonding of various elements, showed that after milling the vicinity of Y atoms is more electropositive than before, indicating that besides the original bonding partner O also other more electropositive elements, such as Fe, Mn or Al, are present in the surroundings of Y atoms. After HIPing a further shift of the binding energy towards a more electropositive surrounding is detected, which agrees with APT measurements in *publication A*, showing larger enrichments of Mn and Al at the particles. Figure 17 shows the results of the XPS measurements.

Further investigations on the mechanism, especially during the last stage of milling, were performed. These experiments should elucidate why it is possible to produce a metastable material, where Y exhibits an extended solubility in the Fe matrix.

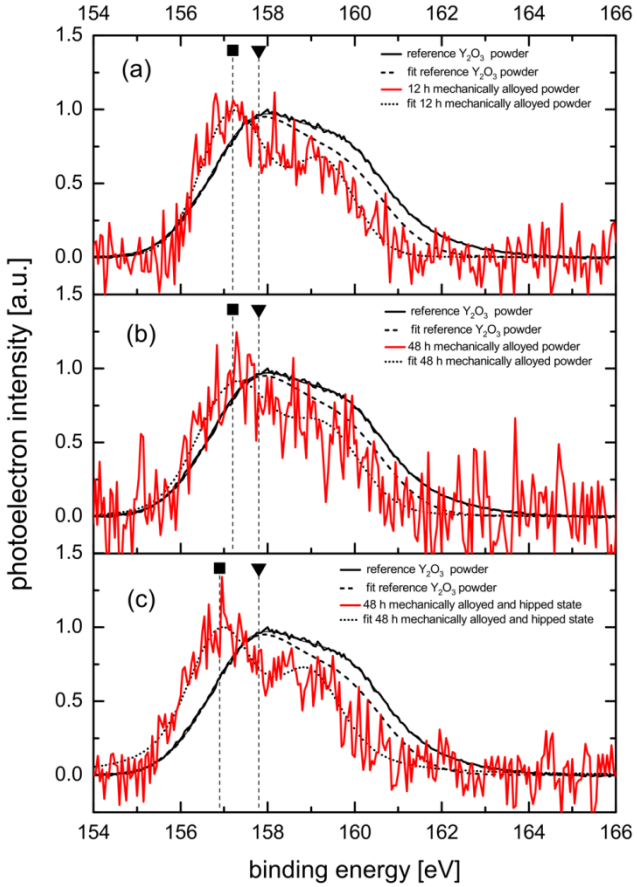

Figure 17: Y3d signals of the 12 h (a) and 48 h (b) milled state as well as the HIPed condition determined by means of XPS [*publication B*], indicating a weaker bonding of core electrons after milling and HIPing, caused by a more electropositive vicinity of the Y atoms.

2.5.3 Theories of mechanisms occurring in the final stages of mechanical alloying

Two different theories were proposed dealing with the mechanism during milling with two immiscible elements. In both theories defects, such as dislocations, play an important role. However, it is also unlikely that the effects are equal in all systems. In the first theory shearing causes a mixing of two different phases. In the second theory enhanced diffusion provides the metastable solid solution.

Shear induced chemical mixing by mechanical alloying

This theory is based on shear stresses, which force dislocations to cut different phases with the consequence that atoms of these phases relocate during high deformation, such as ball milling. Ashkenazy et al. [52] employed molecular dynamics (MD) calculations in order to reveal the behavior of different phase combinations during high deformation. These authors studied the evolution of initially spherical particles in a Cu matrix during strain application. As a second phase either Ag or Ni as fcc metal and either Fe or Nb or V

as bcc metals were used. These different systems include wide ranges of heat of mixing, which strongly influences shear mixing. This has been shown by Odunga et al. [53] and Vo et al.[54]. Moreover, they differ in elastic properties, atomic size and crystalline structure. Figure 18 presents the results of the calculations after a strain of 6. The Cu-Cu system, which is the reference sample, shows the most heavily mixed behavior. The other systems do not show dramatic differences. In Figure 19 the relocation of the particle atoms can be seen at an applied strain of 60. The mixing of different phases proceeds. For example, in the Cu-Ag system, which is a fcc-fcc system, dislocations can transfer from one phase to the other. Consequently, a shear-induced mixing can take place [55]. Conversely, in the Cu-Nb system or Cu-V system, for example, which are fcc-bcc systems, the latter process does not occur [52]. In these systems dislocations cannot cut particles, but cause an amorphous shell [52].

To characterize the mixing behavior of a $Cu_{90}Ag_{10}$ alloy Arshad et al. [55] performed experimental investigations. X-ray diffraction (XRD), Z-contrast TEM and APT were conducted in order to determine the critical strain for intermixing Ag in Cu against the initial particle size. These authors found that the strain scales linearly with the particle size.

Moreover, Klassen et al. [56] investigated an $Ag_{50}Cu_{50}$ alloy in order to discuss the competing mixing and de-mixing reaction rate at temperatures up to 423 K. Calculations using an Arrhenius plot were performed considering differential scanning calorimetry (DSC) and XRD results. For the decomposition upon heat milling a weak temperature dependence has been observed. Calculations revealed an activation enthalpy of 0.11 eV for the decomposition, which is a very low value.

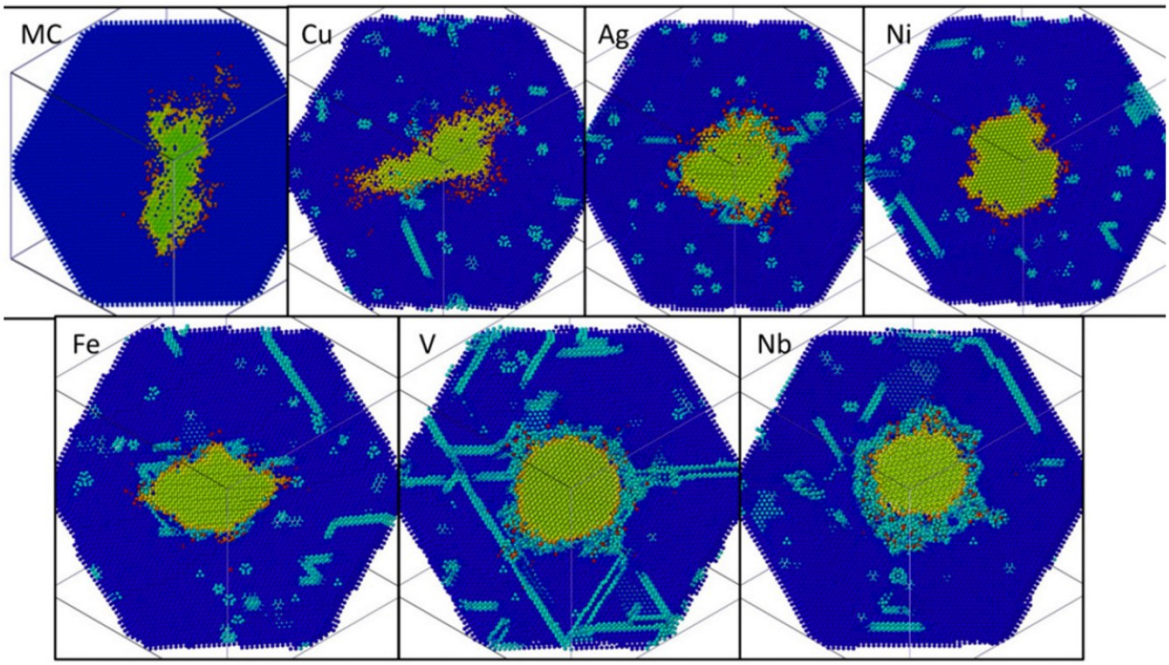

Figure 18: Monte Carlo (MC) and MD calculations showing the morphology of initially spherical particles after a strain of 6. The reference specimen is the Cu-Cu system [52].

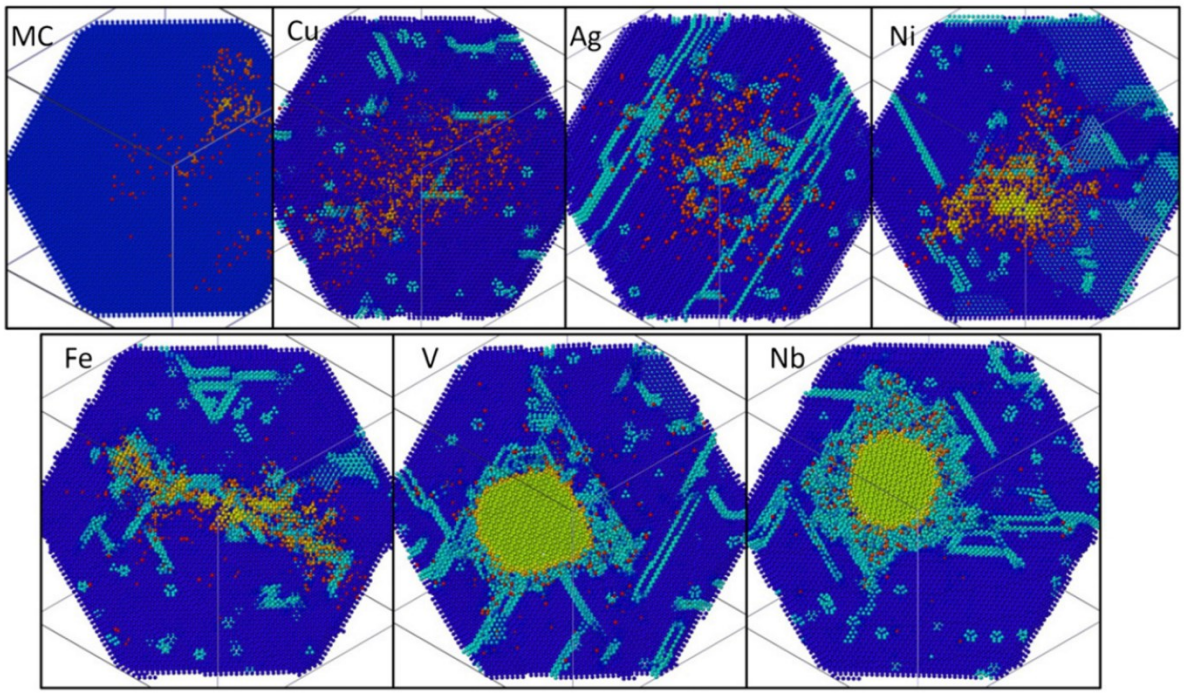

Figure 19: Monte Carlo (MC) and MD calculations are employed to show the morphology of initially spherical particles after a strain of 60. The reference specimen is the Cu-Cu system [52].

However, according to Odunuga et al. [53] shear induced intermixing is suppressed in a system consisting of hard particles in a soft matrix. This is because of localized plastic strain in the soft constituent, for instance due to a difference in shear moduli. This fact

can also be related to the Fe-Y_2O_3 system. Consequently, it can be concluded that this theory solely cannot be the key to understand mixing the system Fe - Y_2O_3.

Chemical mixing by pipe diffusion along dislocations during mechanical alloying

A second microscopic model for mechanical alloying has been published in 1998 by Schwarz [57]. In this theory especially the role of dislocations is considered. If ductile materials, such as Fe or Cu particles are considered, mechanical alloying causes a heavy plastic deformation of these particles and, therefore, a generation and motion of a large number of dislocations and other crystal defects such as vacancies. As already mentioned, the ball collisions induce fracturing and cold-welding of the different particle phases (termed A and B), forming lamellae with A/B interfaces. This situation is schematically shown in Figure 20.

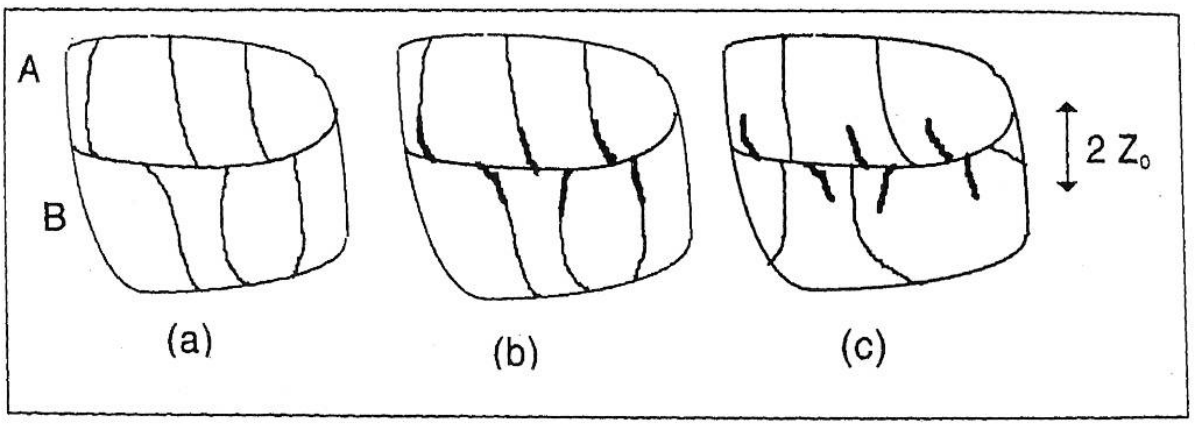

Figure 20: Concept of accelerated intermixing of two phases (A and B) by means of pipe diffusion along dislocations [57].

The theory of Schwarz [57] is based on kinetics of dislocations and the interaction of dislocation-solute in crystals. In the present work the solute B is Y_2O_3 and the solvent A is the iron matrix. It is well known that dislocations interact with solutes through different mechanisms: chemical, elastic, electrostatic, and stress-induced order locking [58]. These various mechanisms operate parallel and concurrently. At edge dislocations the main contribution arises from elastic locking. This means that for example larger substitutional atoms, such as Y in Fe, can relax their stress fields at the expanded space underneath a dislocation. It must be mentioned that in the case of diffusion activities it is assumed that Y_2O_3 decomposes to Y and O atoms, because of the mechanical and thermal energy from ball impacts. Furthermore, a diffusion of large molecules seems rather impossible. In this thesis an 3D energy field of a Y atom as an

Eshelby inclusion in a bcc Fe with an edge dislocation where the Burgers vector b is [111] is calculated and shown in Figure 21 [59].

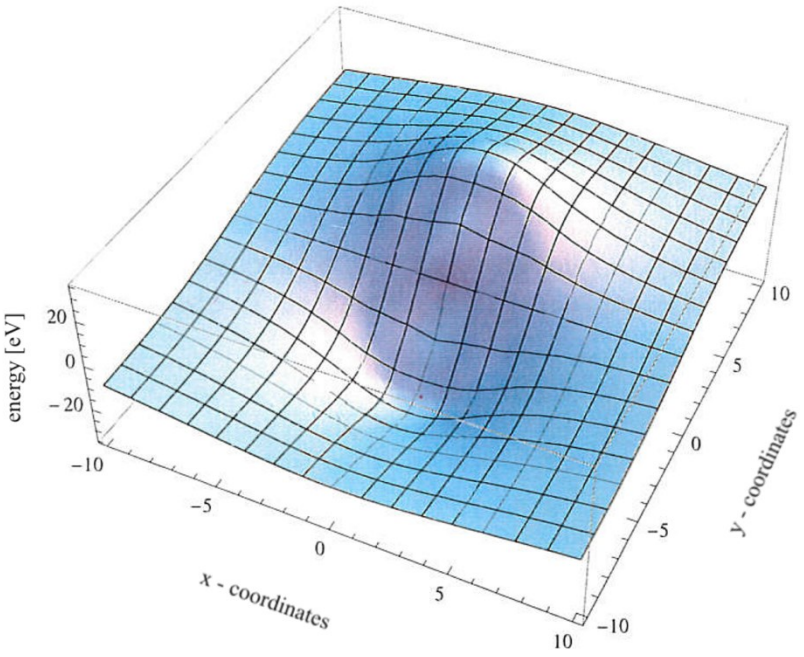

Figure 21: 3D energy field of a Y atom as an eshelby inclusion in a bcc Fe matrix with an edge dislocation , where b is in the [111] direction [59].

Especially smaller interstitial atoms accumulate at these positions underneath dislocations, which are known as Cottrell clouds. The interaction energy for this locking is proportional to a misfit value, which describes the difference of the lattice parameter of a solvent with a concentration of solutes. Thus, the interaction is strongest when the atomic radii of solvent and solute are largely different. For example, according to the work of Teatum et al. [60], Y has an atomic radius of 180.1 pm and Fe a radius of 127.4 pm. For substitutional atoms, the dislocation/solute interaction is typically in the range of 15 kJ/mole. For interstitial atoms the interaction is in the range of 70-150 kJ/mole. Because of this interaction, solutes larger than the matrix atoms are attracted to the expanded regions near the cores of edge dislocations. Thus, according to Schwarz [57] solutes A should easier penetrate a distance Z_0 in crystal B through the core of dislocations, which is schematically shown in Figure 20. These dislocations act as diffusion pipes and this should even occur if crystals A and B have a positive heat of mixing. However, the author suggested that the dislocation-solute interaction energy should be larger than the heat of mixing. He also assumed that these dislocations have a

positive effect on the solute diffusivity. It is known that the activation energy for diffusivity along dislocation cores is about the half value of bulk diffusion [61].

According to Schwarz [57] powder particles are moving freely inside the vial during the milling process. During this time the dislocations are not forced to move by deformation and the solute atoms B are able to diffuse through cores of the dislocations into the bulk solvent A. In Figure 20 the drawn lines mark dislocations and the bold lines represent the solute B decoration of these dislocations, which diffused through their cores. Because the solutes have an attractive interaction with the dislocation, their concentrations are much higher than the equilibrium solubilities.

When the particles are subsequently trapped between colliding balls, shear stress is applied on the dislocations. The stress forces the decorated dislocations to glide in a speed where the solute atoms are not able to follow. Thus, the dislocations break away from the solute atoms and can now act as diffusion pipes for other solute atoms again. Consequently, these dislocations act as agents for mixing of two phases with a positive heat of mixing. As already mentioned in a previous chapter the temperature occurring in a trapped powder particle is assumed to be about 150 °C and is increasing with progressing milling time [38,39]. Therefore, diffusion is further enhanced due to higher temperatures.

These models on the intermixing of two different phases, which have normally a positive heat of mixing, are only theories and assumptions which are not based on proper experimental findings. Especially for the system Fe-Y_2O_3 the mechanisms are not clear until now. Therefore, this doctoral thesis started with investigations trying to elucidate the active mechanisms during the last stage of milling, which are described in the following paragraphs.

In order to reveal the role of defects during milling Fe with Y_2O_3, positron annihilation spectroscopy (*publication C*) as well as *ab initio* calculations (*publication B*) were employed on the powder particles. Detailed information about a*b inito* calculations, which are also called first principle calculations, can be found in [62]. Results of the calculations in publications *B* showed clearly that defects, such as single or double vacancies, have a positive effect on forming a Y substitutional atom in a Fe bcc matrix (shown in Figure 22). It is well known in literature, i.e. Kelly and Nicholson [63], that

solute-vacancy pairs also have a much higher diffusivity in the bulk, increasing the possibility that the solutes diffuse and dissolve in the solvent.

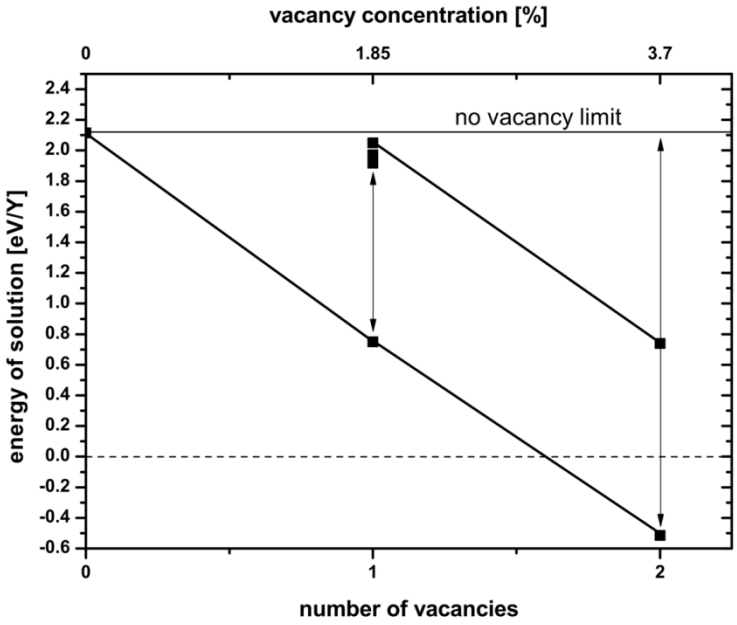

Figure 22: The energy of solution of a substitutional Y atom in a Fe matrix against the number of vacancies and their configuration. At a certain configuration the energy of solution becomes negative, meaning that it is stable [*publication B*].

Indeed, positron annihilation spectroscopy (PAS), Doppler broadening (DB) as well as lifetime measurements, revealed that Y enriches at the free volume of the milled Fe particles. The Doppler broadening results are presented in Figure 23, showing that the milled states show an affinity to Y_2O_3 at higher momenta. This suggests that Y is enriched at the annihilation sites already in the milled particles. Alinger et al. [64,65] performed positron annihilation as well as small angle neutron scattering (SANS) investigations on as-HIPed Cr, W and Ti alloyed Fe-base specimens. They analyzed the cavities and bubbles after HIPing. The authors revealed that after HIPing the nano features (NFs) range from non-equilibrium solute enriched clusters (zones) and transition phases to complex oxides including $Y_2Ti_2O_7$ and Y_2TiO_5. They proposed that up to 50 % of the positrons annihilate at Y-Ti-O NFs, which approximately meets the results of particles directly after milling before HIPing derived in this thesis.

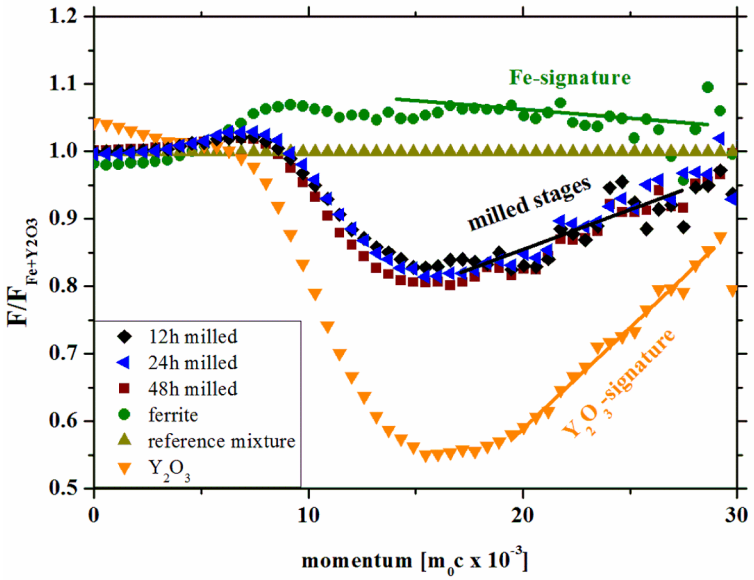

Figure 23: PAS-DB signal which shows that the milled particles of the Fe-Y_2O_3 model alloy have an affinity to Y_2O_3 at higher momenta [*publication C*].

However, because of limited resolution of PAS, yttrium enrichments at grain boundaries of grains smaller than 100 nm in size or at dislocations cannot be excluded. Therefore, electron backscattering diffraction (EBSD) measurements were employed to determine the mean grain size of a milled particle. They revealed a mean grain size of 138 ± 92 nm in diameter after 12 h of milling, leading to the conclusion that grain boundary enrichments can be excluded. Figure 24 shows an overlay of an inverse pole figure (IPF) map and an image quality map of the milled powder grain.

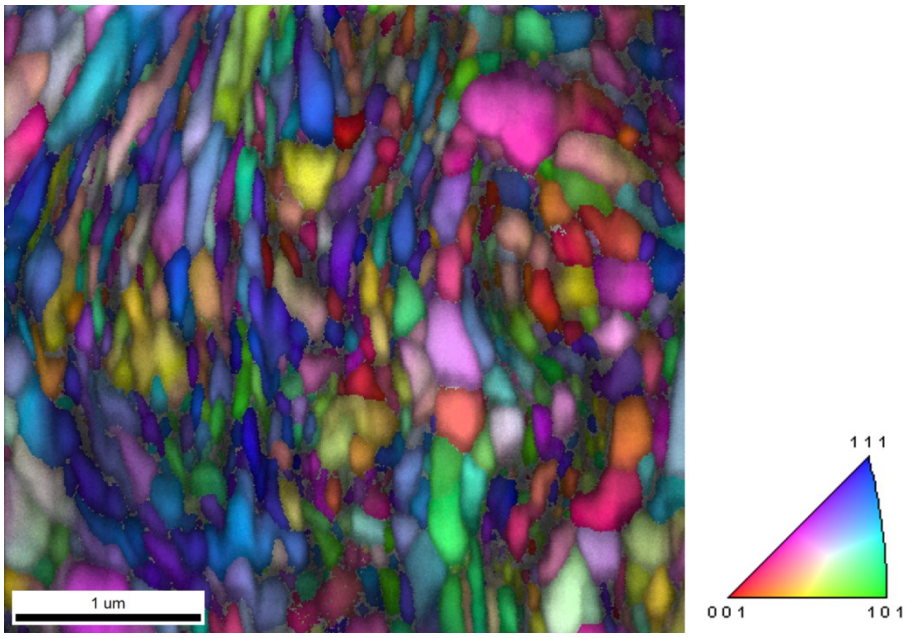

Figure 24: Overlay of an pole figure (IPF) map and an image quality map of the 12 h milled Fe-Y_2O_3 model alloy powder grain [*publication C*].

Furthermore, APT measurements performed in *publication C* revealed an enrichment of Y and O atoms at clusters. Furthermore, the interfaces detected by APT have a distance larger than 100 nm and are enriched in Cr or Mn but not in Y, which supports the results of PAS and EBSD that grain boundaries are not enriched in Y. Moreover, the shape and arrangement of the enrichments suggests that especially vacancies are enriched, which agrees with the *ab initio* calculations in *publication B*. For instance Pereloma et al. [66] detected C enriched dislocations by means of APT. This is not the case in this work. Consequently, also dislocation enrichments of Y can be excluded, because typical one dimensional line enrichments, so called Cottrell clouds, were not detected by APT.

All in all, during the first stages of milling open volumes, such as grain boundaries, dislocations and vacancies are assumed to assist the intermixing of both constituents. However, because of the results of the applied investigations it can be concluded that the most important mechanism occurring during the last stage of milling is vacancy assisted diffusion. In this stage Y and O can diffuse with the support of vacancies into the Fe matrix to form metastable clusters and a supersaturated Fe matrix, exhibiting an extended solubility of Y and O.

Finally, it is assumed that a combination of the following effects can cause the intermixing of Y in Fe, resulting in a metastable matrix. First of all, as already mentioned the diffusion accelerated by the presence of vacancies and the extremely large surface due to the small sizes of powder particles has a beneficial effect on the Fe - Y_2O_3/Y intermixing. Additionally, instead of heat energy, mechanical energy introduced into the particles by ball impacts helps to overcome the diffusion barriers of large Y atoms in a Fe matrix and promotes these diffusion effects. Finally, when Y is already distributed in a very fine manner, also shearing due to dislocation gliding can support the distribution and further intermixing in the ferrite matrix.

2.6 Effect of minor alloying elements on the formation of Y-O nanoparticles

Additional doping elements play an important role during the particle formation of nanostructured ferritc alloys. It follows that they also have an effect on the mechanical properties of the materials, especially at elevated temperatures.

2.6.1 Titanium as minor alloying element and its effect on the microstructure and mechanical properties

Titanium and its effect on the formation of nanoclusters is the most frequently studied minor alloying element in ODS ferritc Fe-based alloys. Ukai et al. [6,67] revealed that a minor alloying addition of Ti to a Cr alloyed steel has an additional positive effect on the mechanical properties at elevated temperatures. For example, the creep strength increases about 100 MPa to approximately 250 MPa at a run time of 1000 h and a temperature of 650 °C. Figure 25 indicates the increase of the strength as a function of Ti content. Ukai et al. [6,67] claimed that this is due to the raise of the particle density as well as the decrease of the particle size.

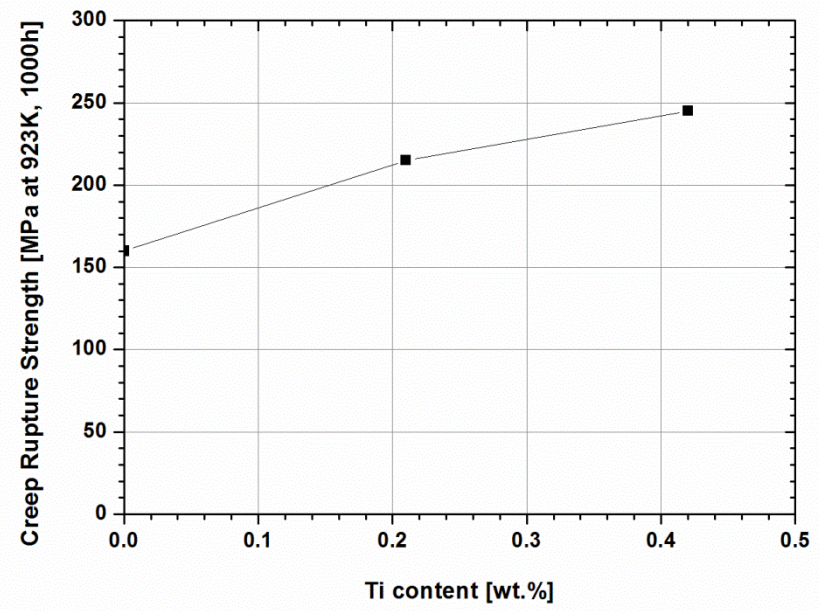

Figure 25: Creep rupture strength of a Cr alloyed steel as a function of the Ti content [6].

Nomura et al. [68] employed TEM investigations. These authors published particle size distributions and also proposed a refinement of these oxide particles. The highest amount of particles without Ti was detected in a range between 10 – 14 nm. A simple alloying addition of 0.3 m.% Ti causes a shift of the particle size maximum to smaller sizes of about 3 nm. They revealed that these particles are complexes such as Y_2TiO_5, $Y_2Ti_2O_7$ or the common Y_2O_3 type. These authors assumed that the Y_2TiO_5 oxide type results from a cold welding process of Y_2O_3 and TiO_2 during milling.

Moreover, Williams et al. [69] analyzed the influence of Ti on the coarsening behavior of the oxide particles at a temperature of 1200 °C and compared a 14Cr-2W-0.3Ti steel

with a 14Cr-2W-0.1Ti Fe-base steel. The authors proposed that Ti has no influence on the kinetics of oxide particle coarsening and, therefore, no influence on the diffusion. Consequently, it is concluded that Ti must have an influence on the nucleation rate of these particles.

Murali et al. [70,71] employed first principle calculations and calculated the binding energies of $Y_2O_4V_2$ particles (note that V stands for vacancy). An addition of four Ti atoms to the particle caused an increase of the binding energy and, therefore, of the stability of the particle. These authors assumed that the higher binding energy reduces the interfacial energy and, as a consequence, the particle density in the matrix is increasing. The reduced interfacial energy can be the reason for the higher nucleation rate with Ti than without. In the common Lifshitz, Slyozov [72] and Wagner [73] (LSW) coarsening theory, the diffusivity of Y is the rate controlling mechanism in this case. Therefore, it can be assumed that coarsening is similar with and without Ti, which was also suggested by Williams et al. [69] and the particles are finer distributed due to an increased nucleation rate.

Because of their finer microstructure and, therefore, improved mechanical properties investigations have been mainly applied on Ti doped ferritic ODS steels. Especially, Miller et al. [18–20,43], Kilmankou et al. [24], Hirata et al. [21] or Larson et al. [74] analyzed these steels by means of APT and TEM. The effect of Zr on the formation and stability of Y-Zr-O particles has been studied less frequently than Ti enriched Y-Ti-O particles. The following chapter describes the effects of Zr on the microstructure and mechanical properties reported in literature and the results derived from experiments in this work.

2.6.2 The effect of the minor-alloying element zirconium on microstructure and properties of the Fe-Y_2O_3 model alloy

Nomura et al. [68] and Uchida et al. [75] studied besides other minor alloying elements also the effect of Zr by means of TEM on high Cr alloyed ferritic steels. Nomura et al. [68] concluded that due to an simple alloying addition of Zr the mean particle size decreases from 13 nm to 3 nm and Uchida et al. [75] found a particle size decrease from a mean radius of 18 nm to 10 nm. Figure 26 compares the particle size distributions of HIPed steel specimens with various minor alloying elements. Moreover,

steel specimens milled with Y_2O_3 and Zr showed improved creep strength compared to the common mechanically alloyed steels without Zr.

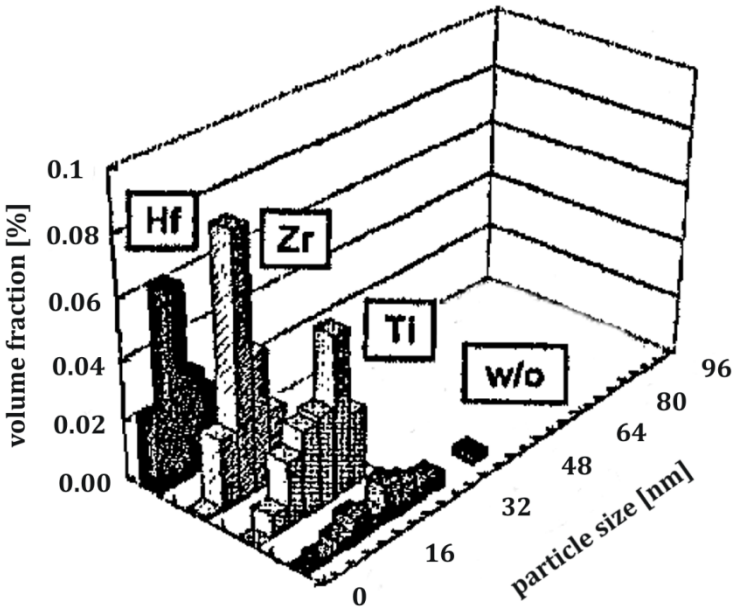

Figure 26: Particle size distribution of Fe-12Cr-Y_2O_3 steels in dependence of the minor alloying element [75].

Furthermore, Murali et al. [70] carried out *ab initio* calculations in order to reveal the role of minor alloying elements on the stability of these particles. As already mentioned before, Ti enhances the binding energy of the atoms inside the particles. Moreover, by replacing Ti with Zr in these particles, Murali et al. [70] found out that the binding energy further increases and, therefore, also the stability improves and the interface energy is reduced. According to Murali et al. [70] this fact suggests that with Zr even smaller particles can be formed for improved mechanical properties at elevated temperatures than with Ti.

In this doctoral thesis the less established Fe-Zr-Y_2O_3 alloy was studied more in detail. Additionally, a new process for the production of this sort of materials was developed. *Publication D* describes a new and cheaper way of producing such alloys by economizing Zr alloying addition with the use of yttrium stabilized zirconia (YSZ) balls as grinding media. In this paper the incorporation of Zr and Y by YSZ ball abrasion as well as the distribution of these elements in as-HIPed materials has been analyzed by means of X-ray fluorescence spectroscopy (XRF) as well as APT. Moreover, the effect of this new method on the particle formation was analyzed by additional TEM investigations and compared to ODS steels produced with common steel balls.

First of all, presented in Figure 27, XRF measurements revealed a constant incorporation rate of Zr and Y during milling due to ball abrasion, which makes the incorporation process predictable.

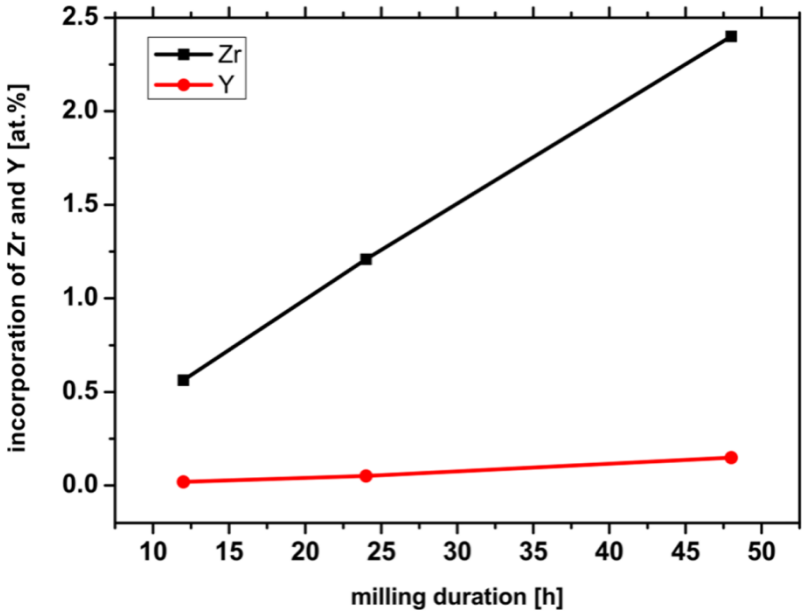

Figure 27: Incorporation of Zr and Y versus the milling duration due to YSZ ball abrasion [*publication D*].

It is also suggested to choose a mixture of steel and YSZ balls as grinding media if a higher milling impact on the particles and a lower Zr and Y incorporation rate are required. APT as well as TEM investigations revealed a higher density of small Y, O and Zr enriched particles in the rage of 1-2 nm in diameter in case of the YSZ ball specimen compared to the sample without Zr incorporation. Figure 28 shows APT reconstructions of the YSZ ball specimen, also enriched in ZrO, and Figure 29 shows larger particles in case of the steel ball sample.

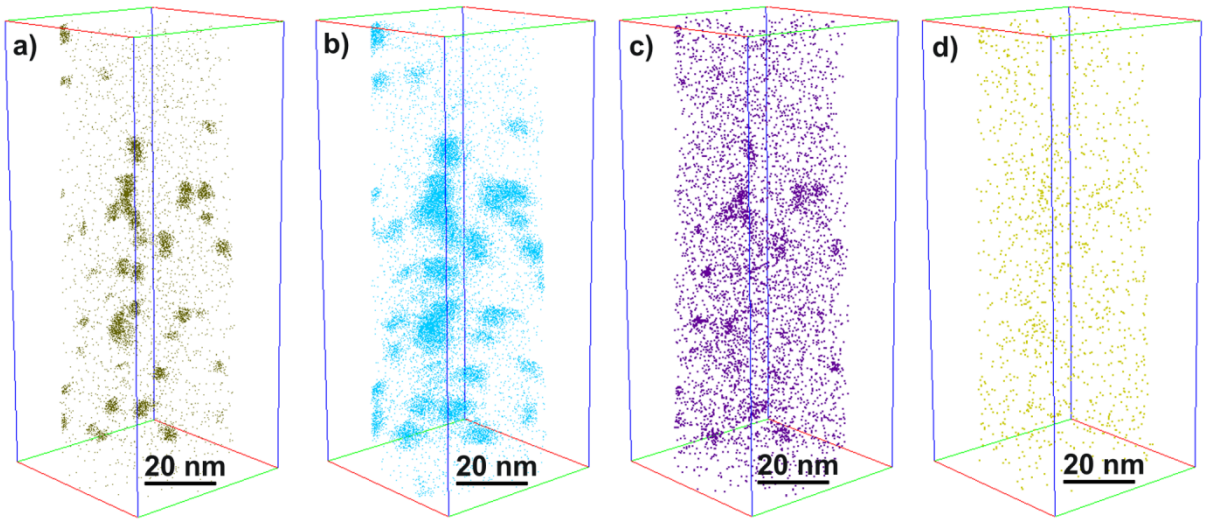

Figure 28: 3D atom maps of the YSZ ball specimen showing small particles enriched in Y (a), O (b), ZrO (c) and Mn (d) [*publication D*].

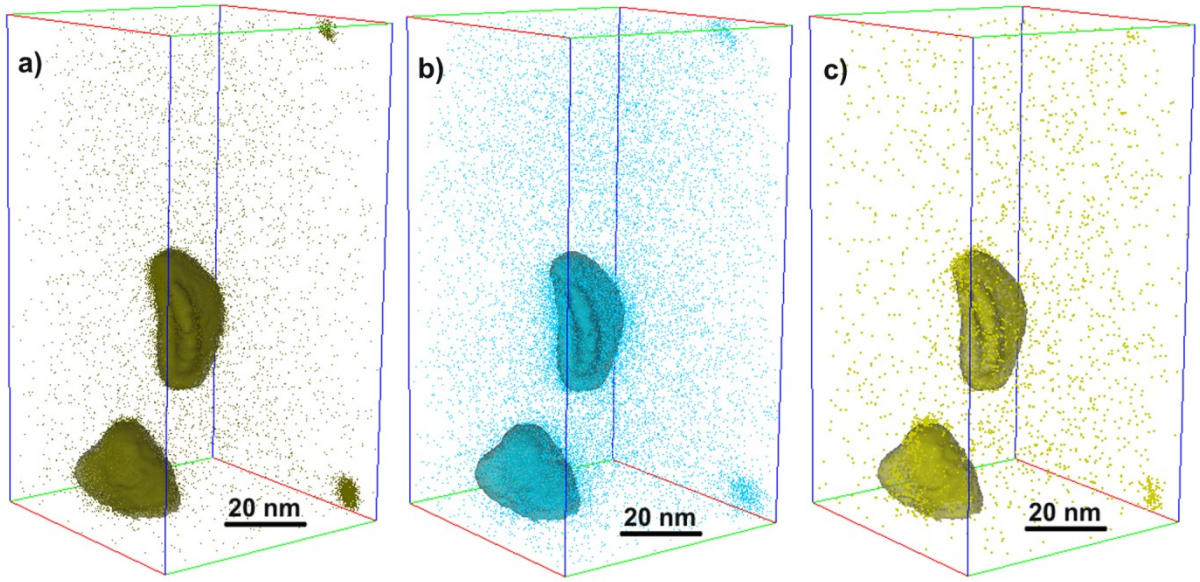

Figure 29: 3D atom maps of the steel ball specimen showing larger particles enriched in Y (a), O (b), ZrO (c) and Mn (d) [*publication D*].

Several TEM investigations has been conducted to gain information on the particle size distribution of both specimens. They revealed that YSZ ball milled specimen exhibit much smaller Y-Zr-O particles, which agrees with the APT results. Hence, also by using this new process the mean particle size decreases to 10.5 nm, which agrees with the results of simple alloying addition from the work of Uchida et al. [75]. Figure 30 compares TEM investigations of the YSZ ball specimen and the steel ball sample.

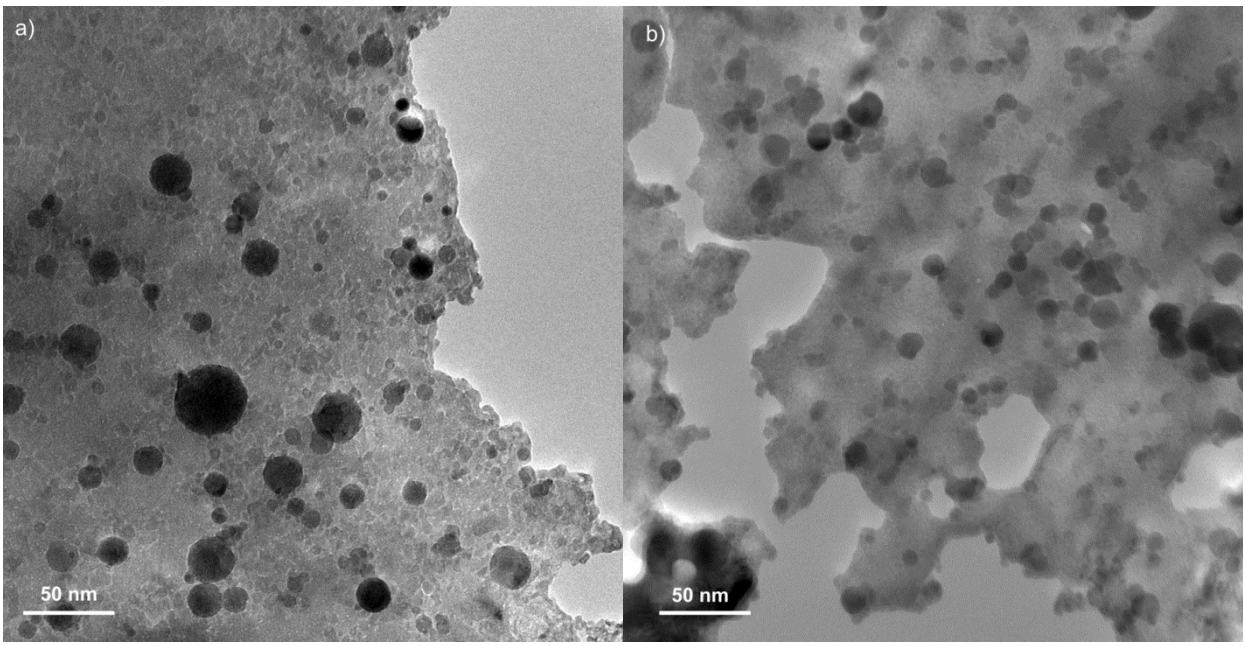

Figure 30: Examples of TEM investigations of the YSZ ball specimen (a) and the steel ball specimen (b) [*publication D*].

Furthermore, hardness measurements have been performed in order to check if there is an influence on the mechanical properties. The measured hardness is 190 ± 4.5 HV 5 in case of the YSZ ball specimen and 169 ± 2.6 HV 5 in case of the steel ball specimen. Therefore, it can be concluded that even at room temperature the use of YSZ balls causes a hardness increase of approximately 20 HV , which is due to Zr and Y incorporation.

All in all, the investigations revealed that Y-Zr-O particles are arranged in a finer manner than Y-Mn-O particles in the common ODS sample. A particle size distribution is shown in Figure 31. Hence, it can be concluded that this new way of producing advanced Zr doped ODS steels is effective. Its advantage is, that it is much easier and cheaper because no alloying addition of Zr is necessary.

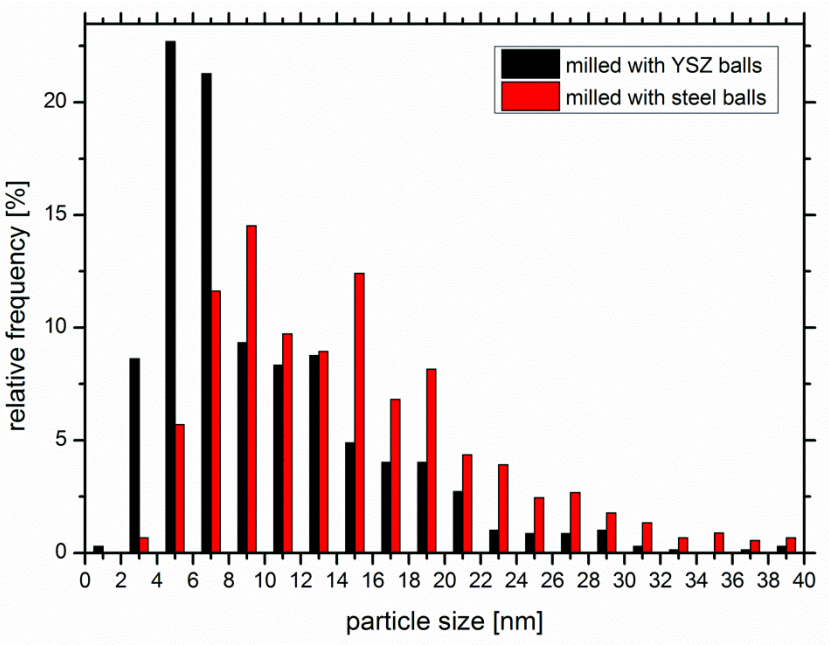

Figure 31: Particle size distribution of the YSZ ball specimen and the steel ball sample showing a higher amount of smaller particles in the Zr incorporated sample due to ball abrasion [*publication D*].

3 Oxide dispersion strengthened high-alloyed steels

3.1 Common powder metallurgical production route of tool steels

Tools, moulds and dies are made of tool-steel-alloys which form, shape or cut other materials, such as steels, nonferrous metals or plastics [76]. Tool steels exhibit a relatively high C content up to more than 1 m% compared to other types of steels. They can be produced in two different ways. Firstly, these steels can be manufactured by the common conventional metallurgical production route. Furthermore, higher quality steels with more homogenous microstructures can be obtained by the powder-metallurgical production route. Figure 32 presents the consecutive steps of the powder-metallurgical process schematically.

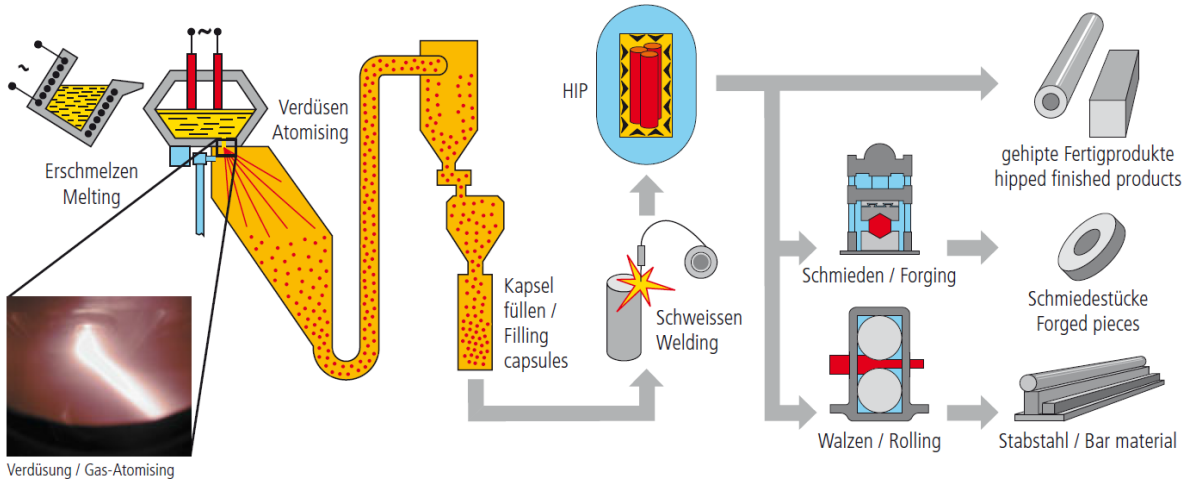

Figure 32: Powder metallurgical production route of a common tool steel [77].

After the powder production by means of gas-atomizing, the powder is filled in a mild steel can. Then the can is welded and subsequently hot isostatically pressed (HIPed). Afterwards, the HIPed material can be deformed by rolling or forging. After HIPing and deformation a certain heat treatment follows. Figure 33 shows schematically the temperature versus the duration of the different heat treatment stages. A stress relieving treatment with subsequent furnace cooling is followed by a hardening process, where the steel is austenitized up to ~1200°C and quenched in oil or water to establish an almost martensitic matrix. Thereafter, the steel is tempered two or three times between 500 °C and 600 °C in order to obtain a higher content of martensite and to form small carbides, which are also called secondary hardening carbides. These commonly

plate-shaped carbides contribute to the hardness of the steel and, consequently, the hardness increases during tempering of the steels.

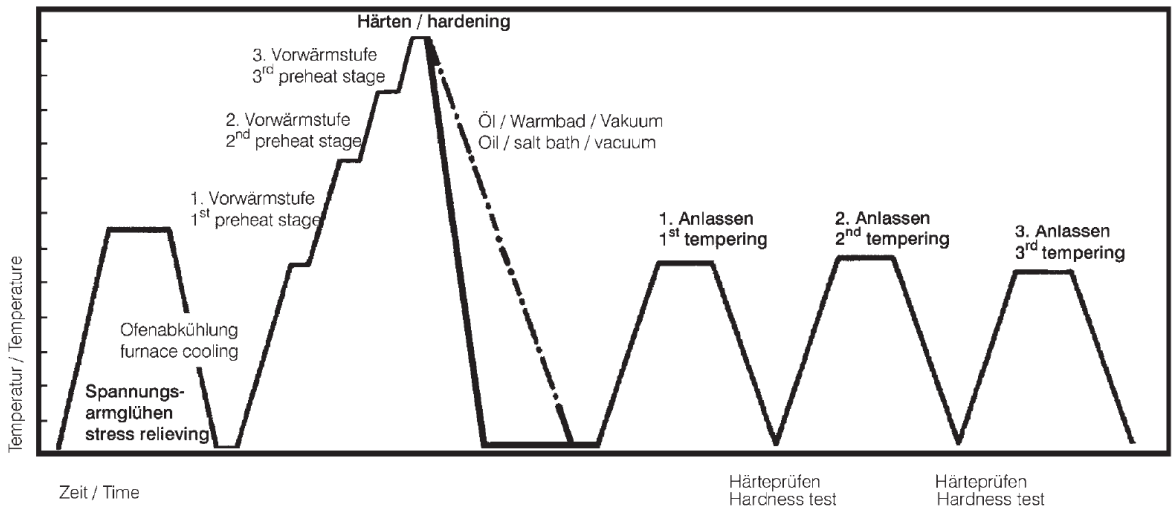

Figure 33: Typical heat treatment process of a tool steel [78].

3.2 Modified production route of an oxide dispersion strengthened high-alloyed steel

To produce a high-alloyed steel strengthened by oxide nano-partilces the common powder metallurgical process route, as mentioned in the introduction, has to be modified. This means that in the production process two new steps must be inserted. In the modified process either a soft-annealing as well as mechanical alloying step or only a milling process is introduced prior to HIPing. In Figure 34 the process route used in this thesis is depicted schematically. After the production of the pre-alloyed steel powder by gas-atomization, some powder batches are soft annealed. Figure 35 present a SEM image of the as-received gas-atomized powder particles which normally have a martensitic microstructure with retained austenite. The subsequent annealing step should provide an almost ferritic matrix. Specimens mechanically alloyed without soft-annealing should verify if the soft-annealing process has a positive effect on milling or not. After milling the powder batches are inserted into a capsule. This capsule, consisting of mild steel, is welded and subsequently HIPed. After HIPing a certain heat treatment is applied.

Danninger et al. [79] proposed an akin process where different hard phases, such as WC, VC, NbC, SiC, TiC or Al_2O_3, have been distributed only by mixing and without severe deformation of original powder particles in order to reinforce a new high speed steel.

Also in this part yttria is chosen as hard phase and milling is applied on the original powder particles obtaining a distribution of oxides in a much finer manner in the steel matrix.

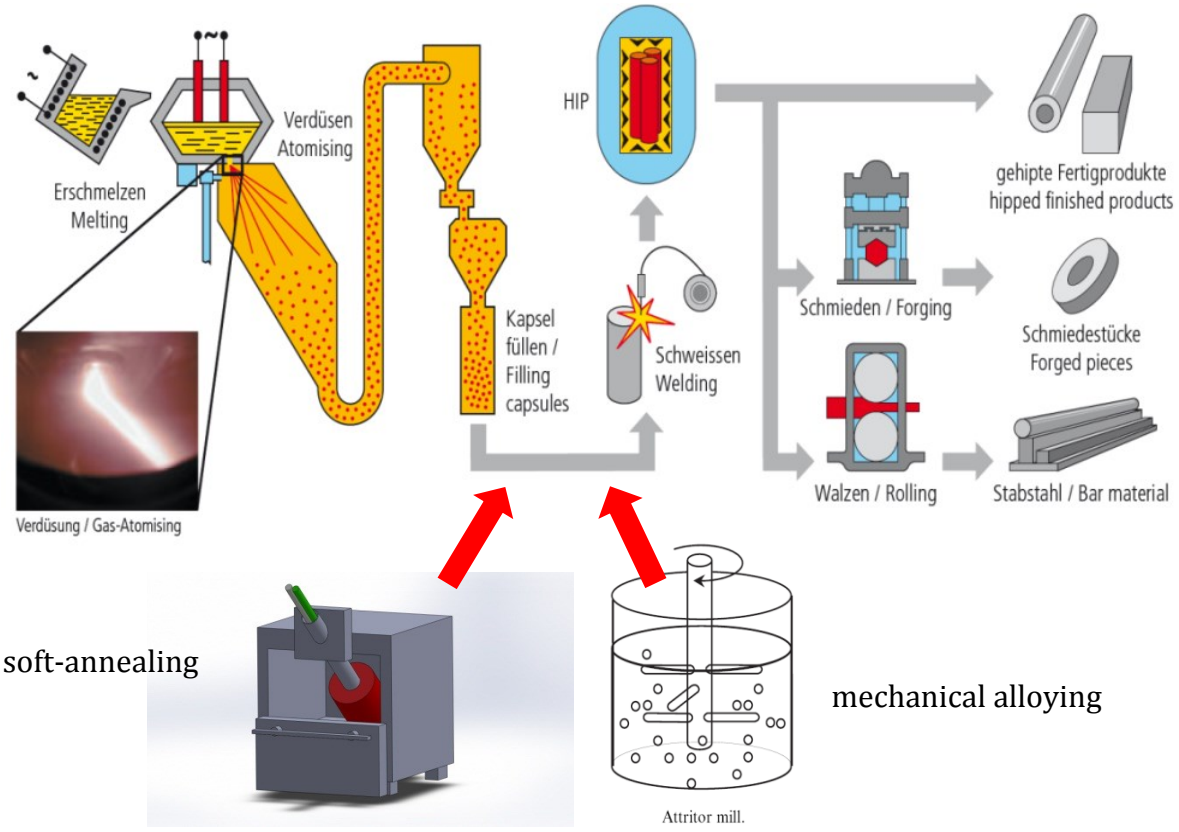

Figure 34: Modified process route of a nanofeatured high-alloyed steel as developed in the framework of this thesis. A soft-annealing step as well as a mechanical alloying step is introduced in the process route [77].

3.3 Powder characteristics

3.3.1 Pre-alloyed and gas-atomized high-alloyed steel powder

For the experiments a pre-alloyed high-alloyed steel powder was used, which was produced by a gas-atomization process at Böhler Edelstahl & Co KG. Its chemical composition is listed in Table 3. To get an impression of the size and shape of these particles, Figure 35 presents some powder particles of the as-received powder. The powder grain size has been determined to be in the range of 10 µm to 500 µm in diameter. The mean diameter is calculated to a value of 120 µm.

Table 3: The chemical composition of the high-alloyed steel powder.

	Fe	Co	Cr	Mo	W	V	Si	Mn
Powder composition [m.%]	Bal.	4.50	4.35	2.80	2.55	2.1	0.55	0.4

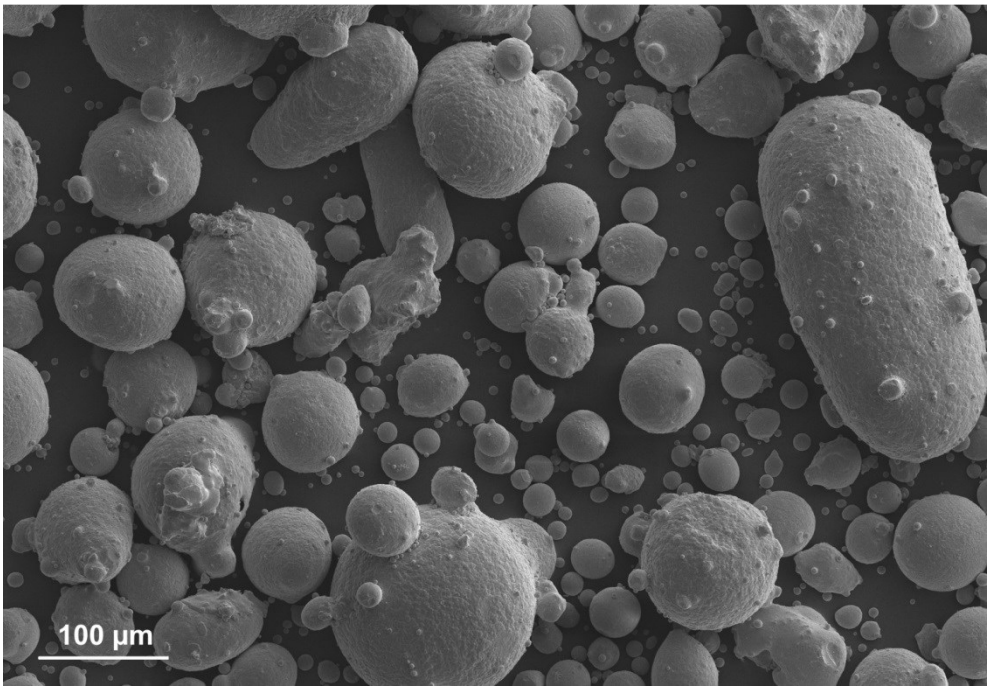

Figure 35: SEM image of the as-received gas-atomized high-alloyed steel powder.

3.3.2 Yttria powder

The submicrometer-sized yttria powders used in this study were provided by Treibacher Industrie AG company, Austria. For the particle size distribution (PSD) a Microtrac™ laser diffraction method was employed. In Table 4 the PSD of the yttira powder is listed.

Table 4: Particle size distribution of the yttria powder obtained by laser diffraction.

d_{10}	0.3 µm
d_{50}	0.59 µm
d_{90}	1.16 µm

A d_{10} of 0.3 µm means that 10 % of the powder particles are smaller than 300 nm. 90 % of the yttria powder particles are smaller than 1.16 µm. Additionally, the powder

exhibits a specific surface, also abbreviated as BET (Brunauer-Emmett-Teller), of 16.51 m^2/g.

The yttria powder has a 99.9 % purity and its composition is listed in Table 5.

Table 5: Composition of the yttria powder.

	Y_2O_3	Zr	Si	Na	K	Ca	Al	Fe	Mg
Powder composition [ppm]	Bal.	135	185	65	55	42	45	19	2

3.4 Soft-annealing of high-alloyed steel powders

Pre-alloyed steel powders are produced by N_2-gas atomizing. In this process powder particles are quenched rapidly, which causes an almost martensitic microstructure with retained austenite. It is known that martensite is a very hard and brittle microstructural condition, because of its extremely high internal stress and high defect density, such as dislocation density.

According to previous works, for example by Suryanarayana [1,37], mechanical alloying is based on continuous fracturing and cold welding of the powder particles due to the great impact of crashing balls during milling. For cold welding a ductile component is necessary. However, also Y_2O_3 can be classified as a ceramic which exhibits brittle characteristics. The author also mentioned that brittle-brittle systems are much harder to mechanically alloy than for example ductile-brittle systems.

Hence, in order to investigate the necessity of a ductile component, a soft-annealing process was carried out on powders to achieve a high ductility component and to reduce the hardness of the very hard and brittle gas atomized powder particles. Thus, the almost martensitc powder should transform into a phase similar to the ferritic system, which is in literature more well-established concerning mechanical alloying. In the following chapters this powder is compared to the original high-alloyed steel powder without soft-annealing, both directly after mechanical alloying. In the previous chapter, experiments (*publication A-D*) revealed that mechanical alloying of pure Fe with Y_2O_3 dissolution and a very fine distribution of the oxide particles is possible during milling. However, these investigations also showed that defects accelerate the intermixing

process. This fact suggests that martensite, with a high defect density, would be beneficial for mechanical alloying compared to ferritic powders.

To enable the soft-annealing process and to impede sintering of the powder particles a special furnace has been constructed, which is described in the following chapter.

3.4.1 Construction of a furnace for the soft-annealing of powders

Soft-annealing has been carried out at elevated temperatures, which normally causes the sintering of particles. However, for mechanical alloying powder particles are necessary, therefore, sintering must be impeded. Hence, particles should be kept in permanent motion. This is achieved with a special furnace, which is schematically depicted in Figure 36.

A crucible has been installed in a furnace, fixed on a bearing on one side and connected to a tube by a screw joint on the other side. The tube passes through a hole outwards of the furnace. During these experiments the crucible is batched before heating. The tube and the crucible are able to rotate on their own axis, which has been achieved by an engine outside of the furnace powered by AC electricity. Moreover, to measure a correct temperature, a thermocouple has been inserted into the crucible through the tube. Additionally, through the same tube an Ar-gas lance has been introduced into the crucible to impede decarburization as well as oxidation of the powder. In the crucible steel plates have been fixed which cause a stronger motion of the powder. The measurement of the isothermal annealing time started when the right temperature was reached. The time of heating has been about 1 h and 20 minutes. During the soft-annealing process, the tube and the crucible rotated permanently. All batches were subsequently furnace-cooled.

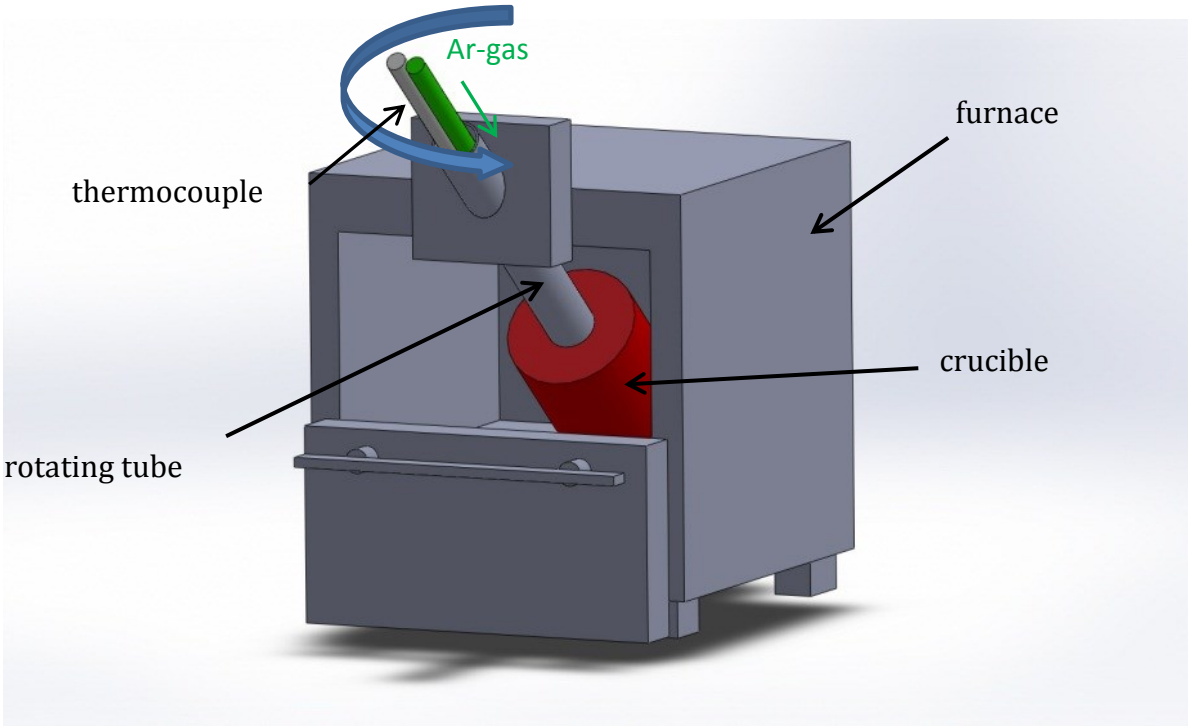

Figure 36: Schematic illustration of the constructed furnace.

3.4.2 Determination of the soft-annealing parameters

In order to achieve proper soft-annealing parameters for the N_2-gas atomized powders, several annealing experiments with different temperatures and durations were carried out. To get the theoretical α/γ-transition temperature, thermodynamical calculations were employed using the software ThermoCalc™ and the database TCFE2. The ideal temperature for soft-annealing is a narrow range below the transition temperature. Figure 37 shows the calculated phase diagram of the high-alloyed steel powder. The phase diagram is shown in the figure up to a C content of 1 m.%. The tool steel contains 0.85 m.% C, which is indicated by a vertical line in Figure 37. Hence, the α/γ-transition temperature can be determined, shown as a horizontal line. Another illustration of the α/γ-transition temperature can be seen in Figure 38, where the phase fraction against the temperature is depicted. In this diagram it can be seen that at a temperature of about 825 °C approximately 90 % austenite (in the diagrams FCC_A1#1) transforms into about 85 % ferrite, which is indicated in the diagrams as BCC_A2. Due to these results it was decided that 800 °C should not be exceeded during soft-annealing.

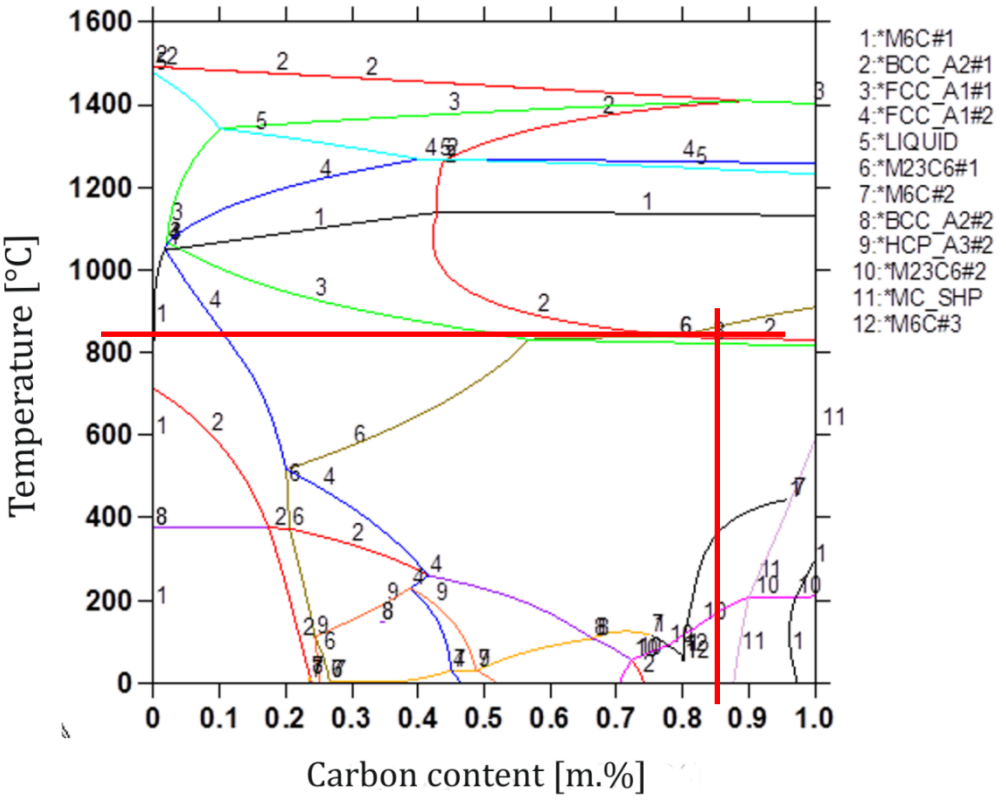

Figure 37: Calculated phase diagram of the high-alloyed steel powder, with a composition listed in Table 3.

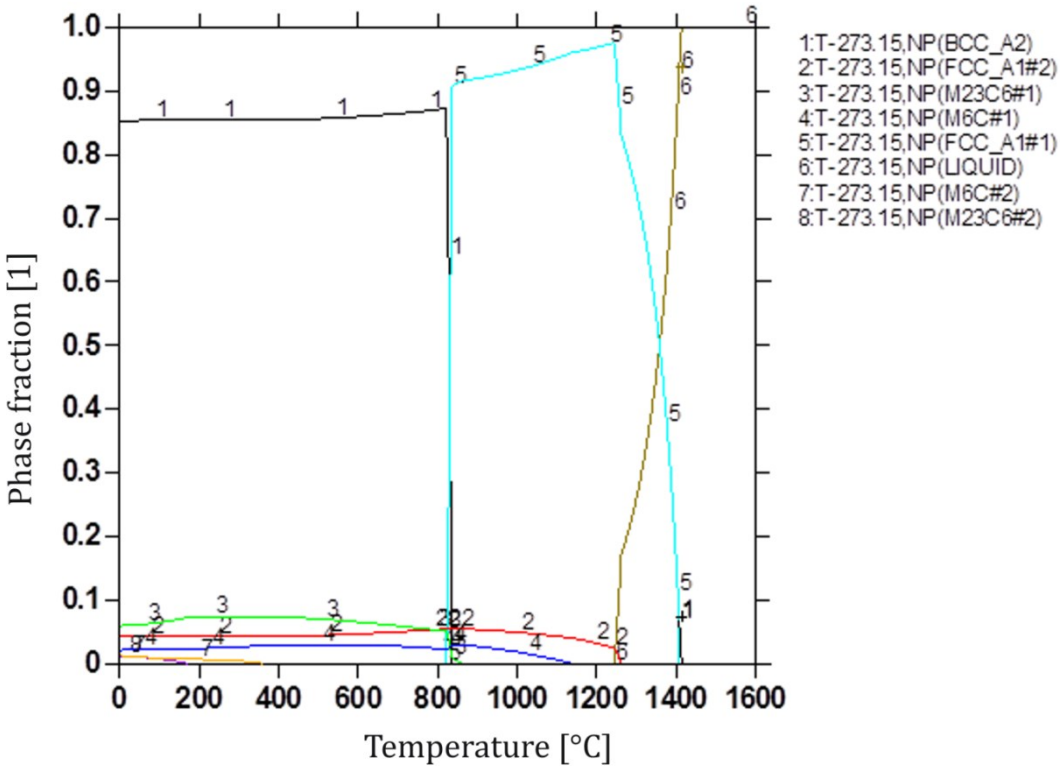

Figure 38: Phase fraction against the temperature of the high-alloyed steel.

Various powder batches were subsequently annealed at different temperatures and durations. In order to reveal the microstructure of the powder particles after the different annealing treatments, SEM images were taken and micro-hardness measurements employed.

In Figure 39 SEM images of the various soft-annealing conditions can be seen. The specimens were mounted, grinded, polished as well as etched with a 3 % HNO_3 acid. In Figure 39a the microstructure of the as-received powder particles is shown. Several martensitic needles in the former austenitic grains with a grain size of about 4 µm can be determined by means of SEM. These martensitic needles are surrounded by retained austenite. After an annealing of 30 min at 600 °C (Figure 39b) the needle-shaped microstructure with some smaller carbides at the grain boundaries still can be seen. Therefore, the annealing temperature was raised to 800 °C, which is close to the α-γ transformation temperature of this steel, as calculated with ThermoCalc™. Considering the SEM image of the specimen annealed at 800 °C for half an hour (Figure 39c) a change in the microstructure from needle-shaped to plate-shaped in comparison to the 600 °C specimen can be determined. However, an extension of the annealing time causes no dramatic change in the microstructure. Both conditions after annealing at 800 °C for 1 h and 3 h featured martensitic plates in the investigated particles. After 8 h annealing at a temperature of 800 °C fewer plates can be found in the microstructure. The same trend can be seen in the 20 h annealing condition. Consequently, these investigations revealed that an annealing temperature of 800 °C is necessary for the high-alloyed steel powder. For determination of the optimum annealing duration further investigations have to be applied.

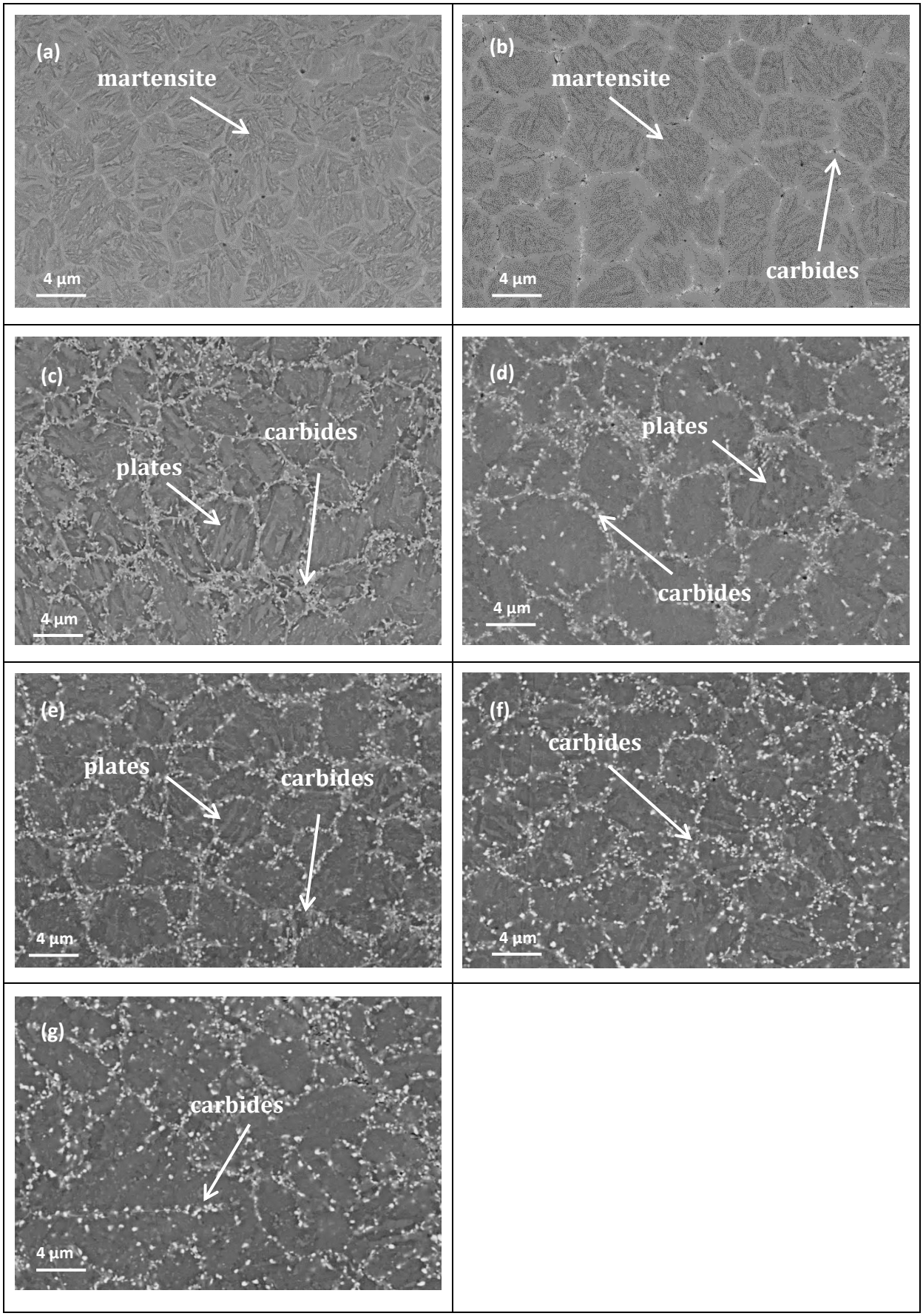

Figure 39: As-received steel powder (a); powder annealed at (b) 600°C for 30 min; (c) 800°C for 30 min; (d) 800°C for 1 h; (e) 800°C for 3 h; (f) 800°C for 8 h and (g) 800 °C for 20h.

In addition to the SEM microstructure investigations also micro-hardness measurements were performed, because hardness can give a further hint which phase is present in the soft annealed steel. In Figure 40 the hardness evolution of the matrix of steel particles during annealing at different temperatures is illustrated. The minimum hardness can be detected at 800 °C and a duration of 8 h. It can be concluded that the higher the annealing temperature and the longer the duration has been the softer the material. Figure 41 shows the micro-hardness evolution versus the annealing duration at a temperature of 800 °C. Considering the hardness of the different states it can be concluded that between 8 h and 20 h annealing only a small difference in hardness can be determined. Consequently, from these results it follows that annealing for longer than 8 h has only a minor effect on the hardness. Therefore, the annealing parameters has been set to a duration of 8 h and a temperature of 800 °C

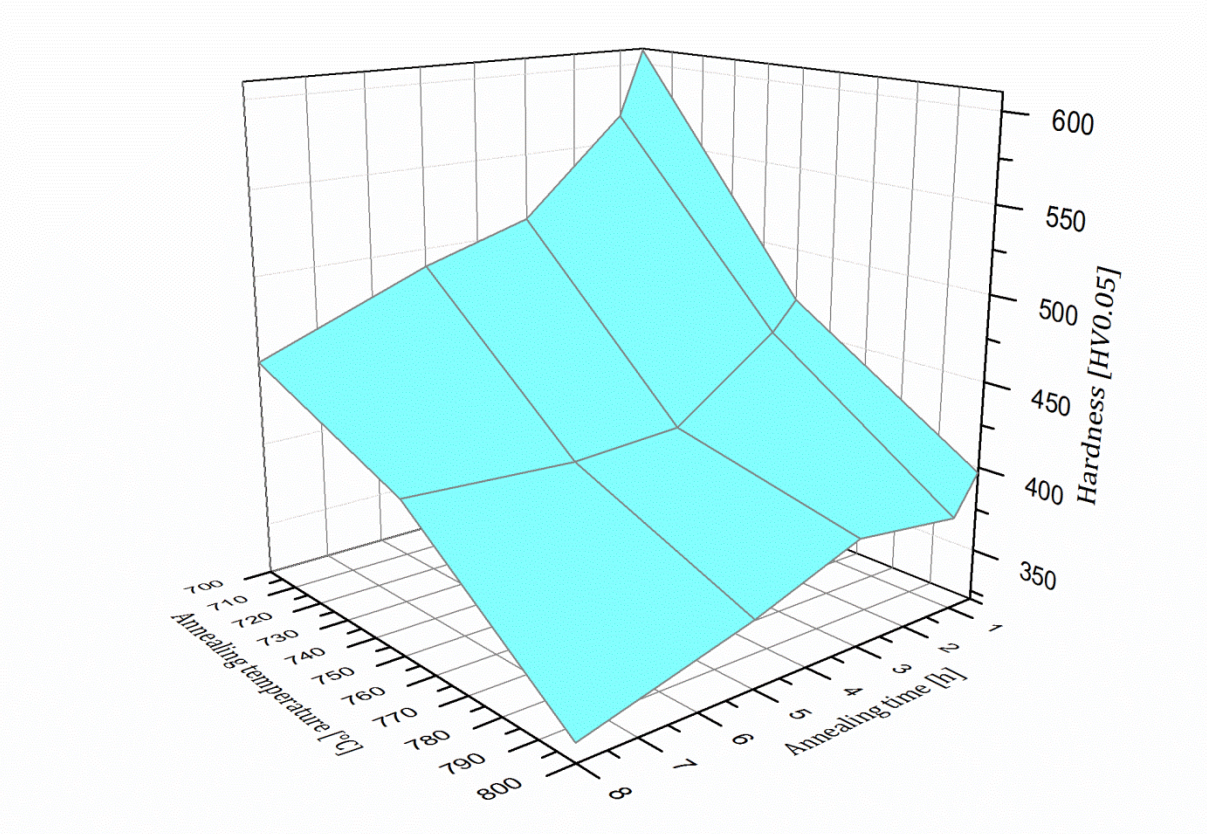

Figure 40: 3D plot showing the hardness decrease depending on the annealing temperature and duration.

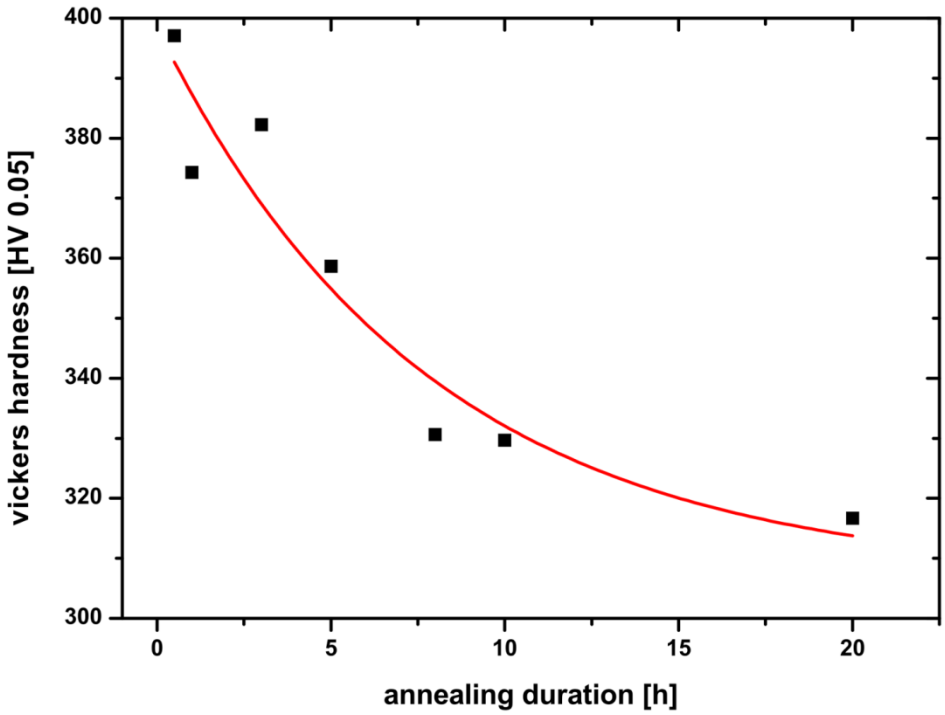

Figure 41: Micro-hardness versus annealing duration at a temperature of 800 °C.

3.5 Microstructure of as-milled high-alloyed steel particles

In order to investigate the microstructure of the high-alloyed steel powder particles directly after 48 h of milling, APT measurements were employed. All APT investigations were performed using a Cameca™ Local Electrode Atom Probe (LEAP™) 3000X HR. Several measurements were carried out in voltage or laser mode, applying a pulse fraction of 20 % and a laser energy of 0.5 nJ at a base temperature of 60 K. The data reconstruction procedure was carried out with the Cameca™ software IVAS 3.4.3.

Tip preparation was done using a FEI™ Versa3D™ Dual Beam focused ion beam (FIB). At a convenient position a wedge was lifted out of a particle. The lift-out process can be seen in Figure 42. After a Pt coating on the surface of a particle, a wedge was cut out of the material. Subsequently, the wedge was lifted out of the powder particle by a micro manipulator. A slice of the wedge was put on a pre-tip and then the tip was formed by annular milling by means of FIB.

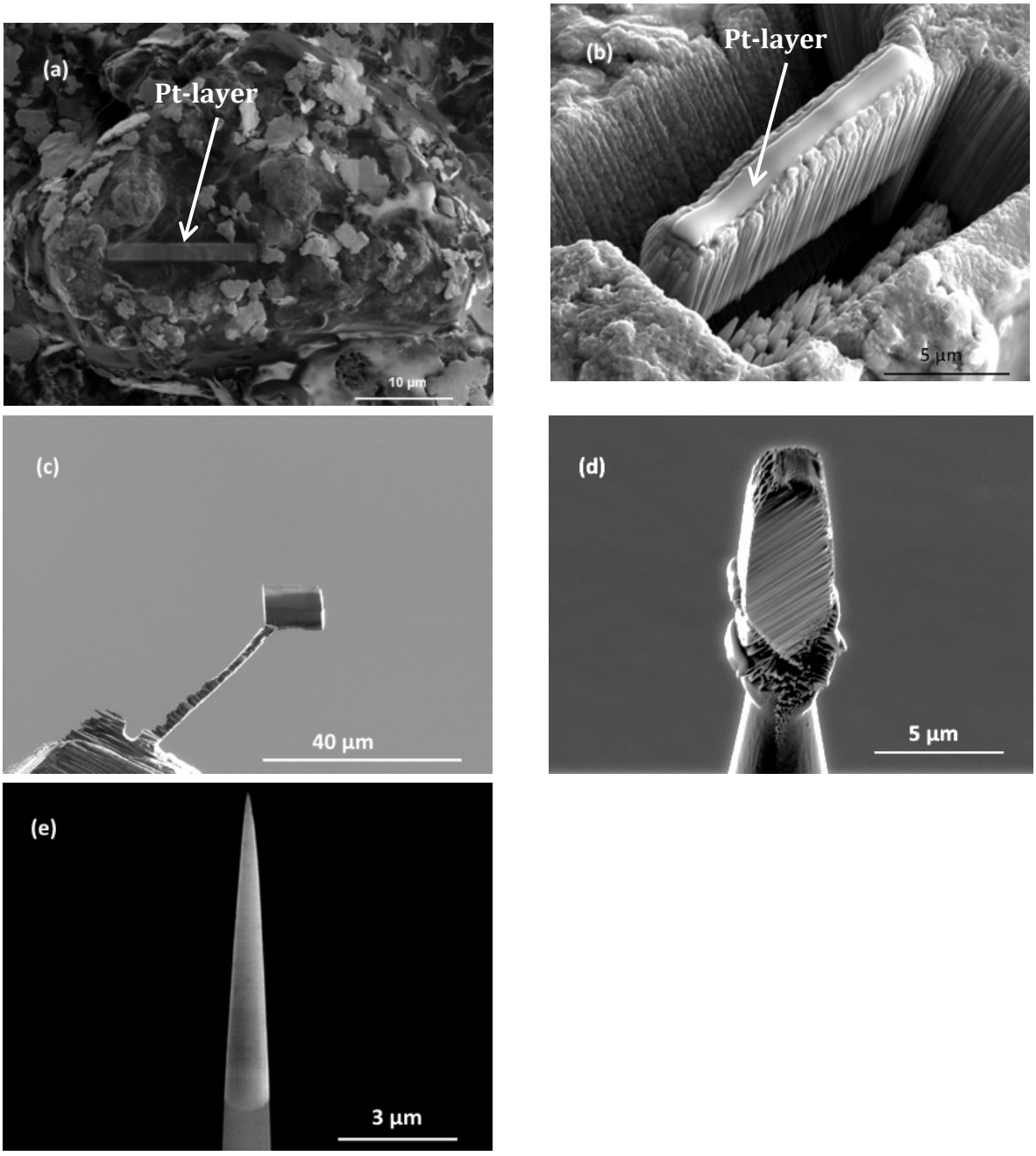

Figure 42: Sequence of the lift-out process stages using a FIB: platinum coating of the particle (a); cutting of a wedge (b); lift-out (c); fixation of a slice of the wedge on a pre-tip of a microtip coupon (d) and annular milling to prepare the tip (e).

3.5.1 Yttria distribution in soft-annealed, as-milled steel particles

In this chapter the microstructure of a soft-annealed, as-milled steel powder particle is analyzed. Results of the APT investigations are depicted in Figure 43. In Figure 43a a 3D reconstruction is shown which contains all ranged ions. In these atom maps irregularities can be seen. More detailed information, where the Y, O and Cu ions are

depicted separately, can be seen in Figure 43b-d. In these reconstructions two planes enriched in Y, O and also in Cu can be detected. Therefore, it can be concluded that a perfectly homogenous distribution cannot be obtained by milling a soft annealed high-alloyed steel powder with 0.5 m.% yttria for 48 h. In the same measurement carbides enriched in Mo and W can be found. Enrichments of C, Mo and W are illustrated in Figure 43e-g. It is assumed that carbides precipitated during soft-annealing interfere with the milling processes. The formation of defects during milling, which are assumed to cause the distribution of yttria in an extremely fine manner, can also be disturbed. Moreover, precipitates can act as obstacles for dislocation gliding and, thus, complicate an intermixing. As described in the previous chapters, it is also assumed that this can cause an intermixing of different phases. All in all, the higher amount of alloying elements as well as the presence of carbides enhances the strength of the powder material and, therefore, intermixing during mechanical alloying is more difficult. Hence, the milling duration must be increased.

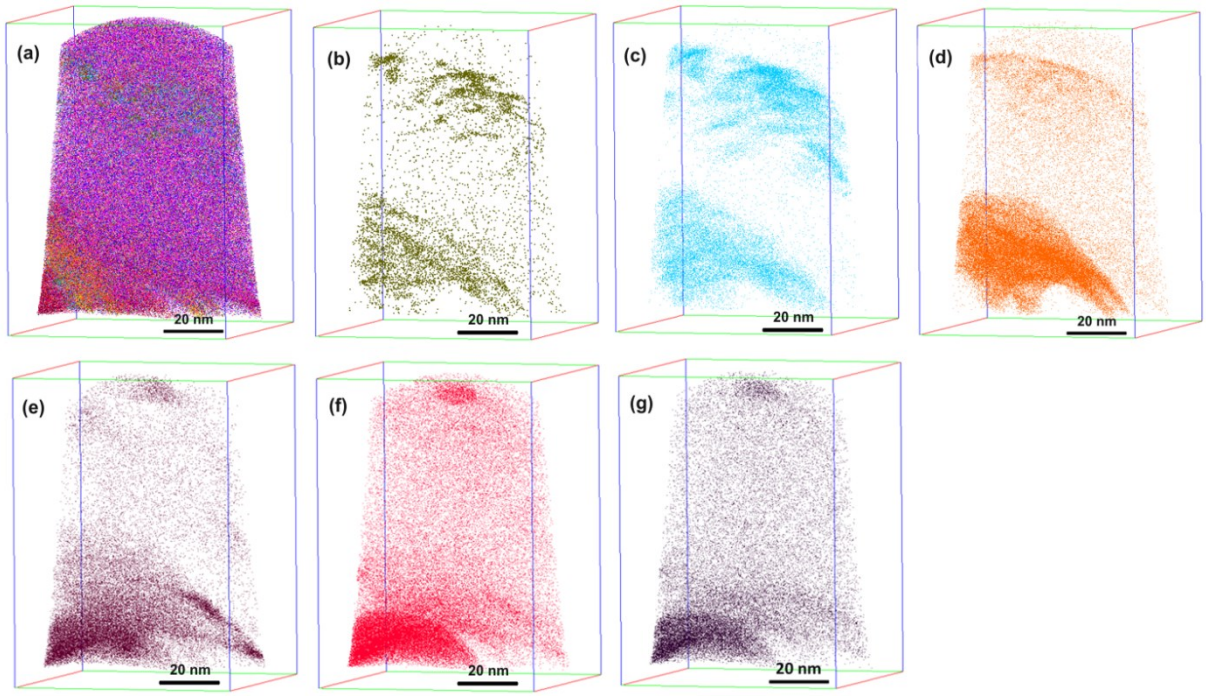

Figure 43: 3D tip reconstructions including all ranged ions (a) of a soft-annealed as-milled highly alloyed steel powder particle. In addition 3D atom maps of Y (b), O (c), Cu (d), C (e), Mo (f), and W (g).

3.5.2 Yttria distribution in as-milled high-alloyed steel particles without previous soft-annealing

In this chapter investigations on powder particles without soft-annealing are described. As already mentioned, these as-received N_2-gas-atomized powder particles have an almost martensitic microstructure with retained austenite. Despite the very hard and brittle microstructure, which contains high intrinsic stresses and therefore a lot of defects, Y and O are distributed in an extremely fine manner after a milling duration of 48 h. Illustrating 3D atom maps, Figure 44 gives detailed information about the atom distribution of different elements. It can also be assumed that in the center of the reconstructed tip Fe, Y and O is depleted.

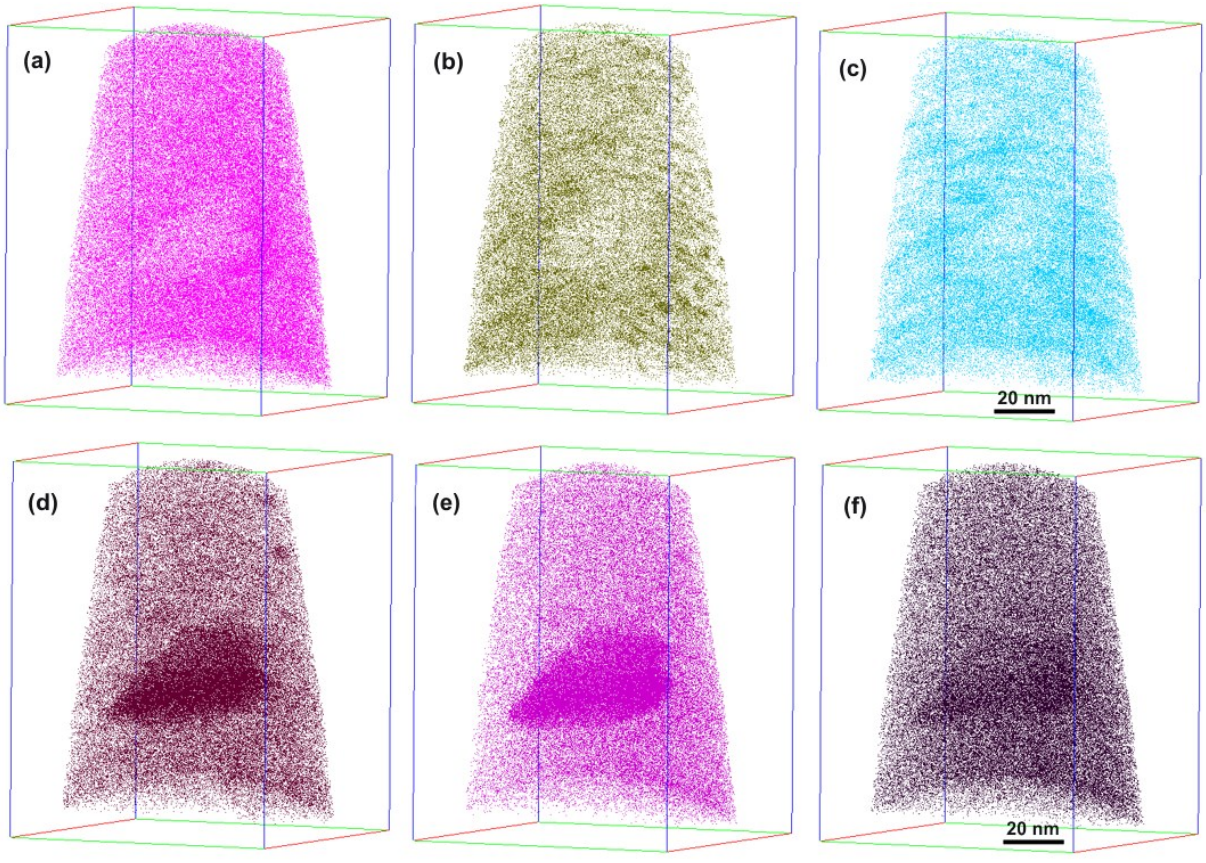

Figure 44: 3D-atom maps. The elements Fe (a), Y (b) and O (c), C (d), V (e), and W (f) are shown.

Since Fe, Y and O are depleted in the centre of the tip other elements were analyzed. Figure 44d-f shows the atom distribution of C, V and W, which are all enriched in the centre of the tip. By visual inspection of Figure 44 it can be assumed that this is a carbide with an approximate extent of 50 nm.

In Figure 45 this region is shown more in detail. Due to the fact that Fe is depleted and C as well as Cr is enriched it can be followed that a carbide has been detected. It is important to mention that in this particle no Y or O is dissolved and no Y-O clusters formed. Deformation is concentrated in the softer Fe matrix. Furthermore, it is also assumed that the deformed martensitic matrix exhibits a higher defect density, which is assumed to be a key factor for the mechanism of mechanical alloying Fe with Y_2O_3.

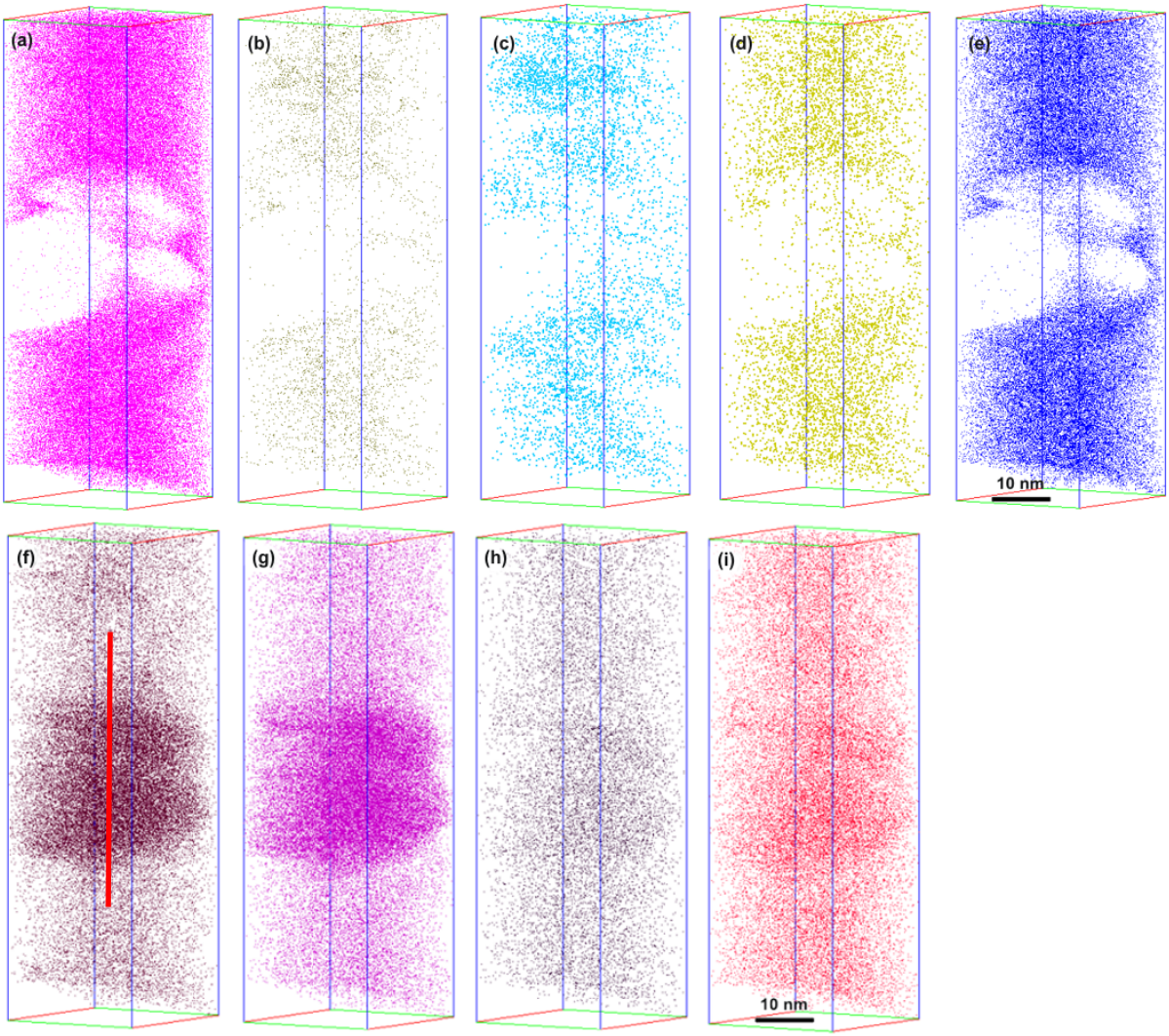

Figure 45: Region of interest of an as-milled pre-alloyed steel powder without soft-annealing where the carbide is shown. Examples of depleted elements as Fe (a), Y (b), O (c), Mn (d), and Co (e) are illustrated. In addition the elements C (f), V (g), W (h), and Mo (i) are illustrated which are enriched within the carbides. The red line in (f) indicates the line where the 1D concentration profile shown in Figure 46 is calculated.

Moreover, a 1D concentration profile along the red line drawn in Figure 45f was calculated. Results are shown in Figure 46. High amounts of C and V and also the elements Cr, Mo and W are enriched in the carbide. As can be seen in the previous figures (Figure 44 and Figure 45) Fe and Co as well as Y and O are depleted.

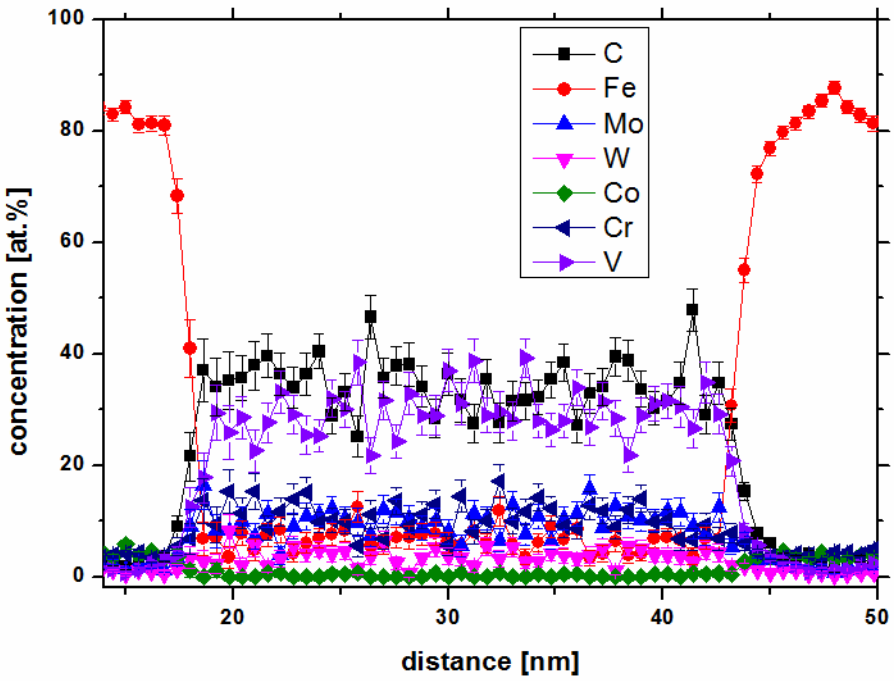

Figure 46: 1D concentration profile through a carbide measured in an as-milled pre-alloyed steel powder particle without soft-annealing.

From these results it follows that also without soft-annealing of the steel powder, yttria is distributed in the powder particles in a very fine manner. This agrees with the theory that defects such as dislocations or vacancies are the key for a successful mechanical alloying process. Consequently, it can be concluded that soft-annealing is not absolutely necessary for mechanical alloying. Furthermore, coarser carbides are formed during this process causing an inhomogeneous microstructure, where a successful milling process with homogenous distributed Y and O becomes more difficult.

3.6 Milled and soft-annealed high-alloyed steel in the HIPed stage

After mechanical alloying and HIPing the microstructure was investigated by means of APT. Rods were cut out of the bulk material with a length of 15 mm and a cross-section of $0.3 \times 0.3\ mm^2$. The rods were formed into tips by means of the standard electropolishing method [44]. The measurements revealed a very fine clustering of Y in this material. A distribution analysis of the different elements was done by using an X^2-test with a bin size of 100 ions. The difference between the experimental distribution of the element and the random distribution, also called null-hypothesis, is quantified with the X^2-value. By using a reduced X^2-value different experiments are comparable because

the size of the measurement is considered. Frequency distribution analyses were applied in several papers as in Moody et al. [80] or Leitner et al. [81]. Table 6 exhibits the μ-values, the reduced X^2-values and the degrees of freedom of the individual elements. The test shows that Y has a X^2-value of 872 with two degrees of freedom. At a significance level of 0.1 % and a degree of freedom of 2 the null hypothesis, which means homogenous distribution, is accepted when the X^2-value exceeds 13.816. This is the case for Y. Therefore, it can be concluded that Y is strongly inhomogeneous distributed. Also in Figure 47a Y particles can be seen and visual inspection agrees with the X^2-test, where the Y particles appear distributed in a very fine manner. O and Cu are enriched in most of these particles (Figure 47b and e), where also the X^2-test reveals an inhomogeneous distribution. In contrast to Y and O, C seems to cluster in a slightly different way. Figure 47a-d shows a cluster enriched in Y and O marked with a blue arrow. Conversely, C does not enrich in this cluster at all. Consequently, it can be concluded that there are two different types of particles coexisting in the as-HIPed material. On one hand there are Y-O-particles and on the other hand there are C particles, which are mainly enriched in V (Figure 47c and d) and Y. For V and also for all other elements except W the null hypothesis is not accepted and, therefore, inhomogeneous distribution is detected, which is listed in Table 6. Moreover, C is also enriched at grain boundaries. As an example a grain boundary is marked with two red arrows in Figure 47f. A chemical indicator of grain boundaries is phosphorus, which enriches at grain boundaries preferentially. The elements Mn, Mo (shown in Figure 47i and j), Cr and Si (not shown here) are mainly dissolved in the matrix, but show somewhat higher concentrations at the grain boundaries and also in the particles. Hence, the X^2-test reveals inhomogeneous distributions of these elements. In contrast, Co and W seem to be indifferent, because by visual inspection of Figure 47g and h it can be seen that these elements are enriched neither in particles nor at grain boundaries. In case of W the null hypothesis is accepted, which indicates homogenous distribution. Also for Co the null hypothesis is not accepted, although the visual inspection gives a hint for homogenous distribution. This might be explained by a slight Co depletion of the particles. Consequently, it can be assumed that Co and W did not influence the formation of these particles.

Concerning the particle distribution in the HIPed sample, Y and O particles can be found in different grains in this measurement but also in others which are not shown here.

Thus, it can be concluded that these particles are distributed over several grains in this investigated specimen.

Table 6: Results of the X^2-test of various elements in the HIPed specimen.

	Reduced X^2	Degrees of freedom	X^2-Test: Acceptance for random distribution at a level of 0.1 % significance
Y	872	2	No
O	3654	3	No
V	7574	3	No
C	4674	3	No
Mo	464	4	No
Cr	188	10	No
Mn	241	5	No
Si	23	5	No
W	7	3	Yes
Co	41	13	No

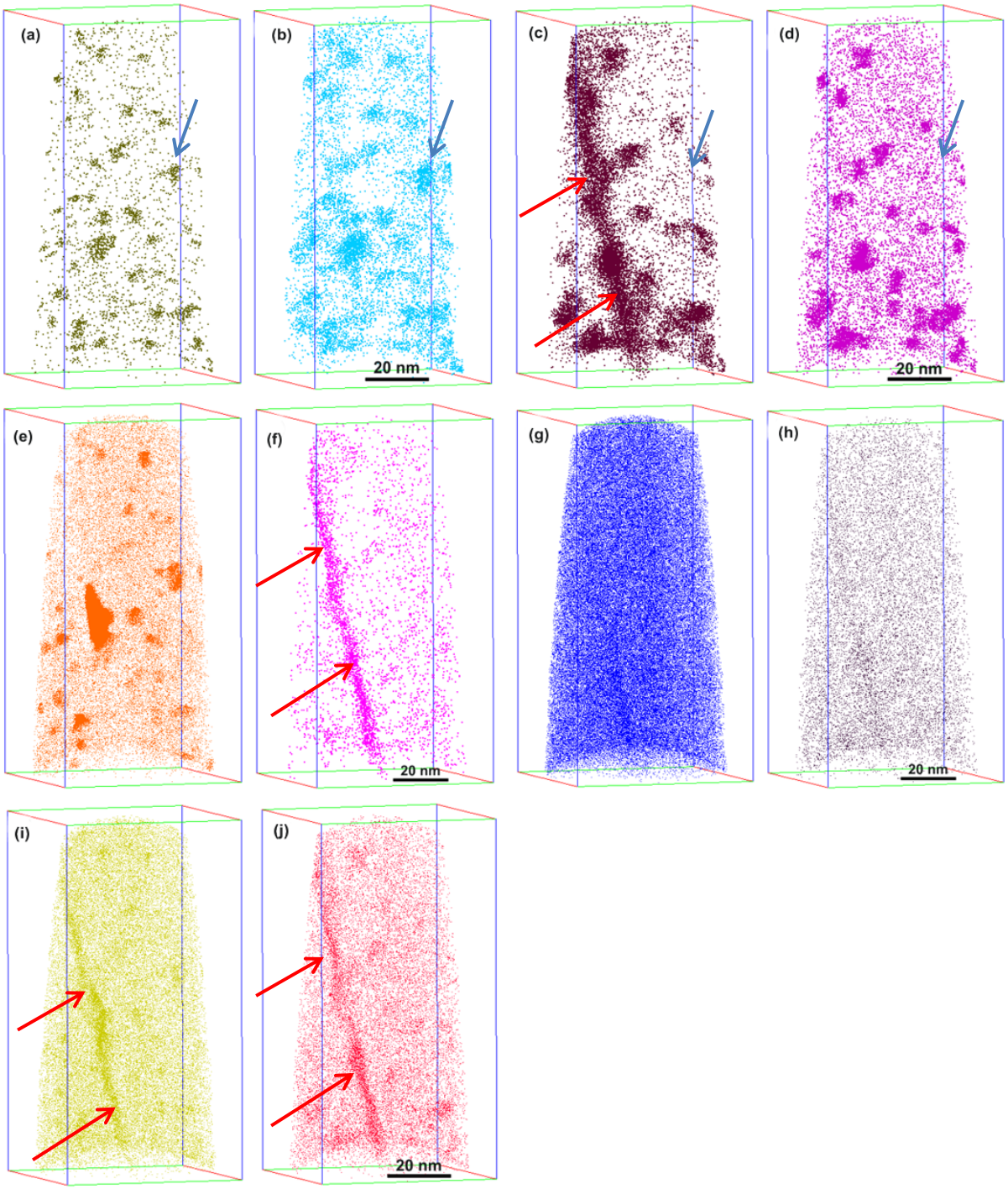

Figure 47: 3D-atom maps of Y atoms (a) and O atoms (b) of the HIPed state of the high-alloyed steel with soft-annealing. In addition, the 3D-atom maps of C atoms (c) and V atoms (d) as well as Cu atoms (e), P atoms (f), Co atoms (g), W atoms (h), Mn atoms (i) and Mo atoms (j) are shown. A grain boundary is marked with two red arrows and the blue arrows indicate Y-O particles which are not enriched in C or V.

To get an impression of the shape and size of the two different types of particles, they are displayed as isoconcentration surfaces [82]. In Figure 48 reconstructions of the milled high-alloyed steel containing isoconcentration surfaces of 1.5 at-% of Y and O (Figure 48a) depicted in yellow and of 1.5 at.% of V (Figure 48b) illustrated in pink as

well as the combination of both (Figure 48c) are shown. The shape of both particle types appears spherical.

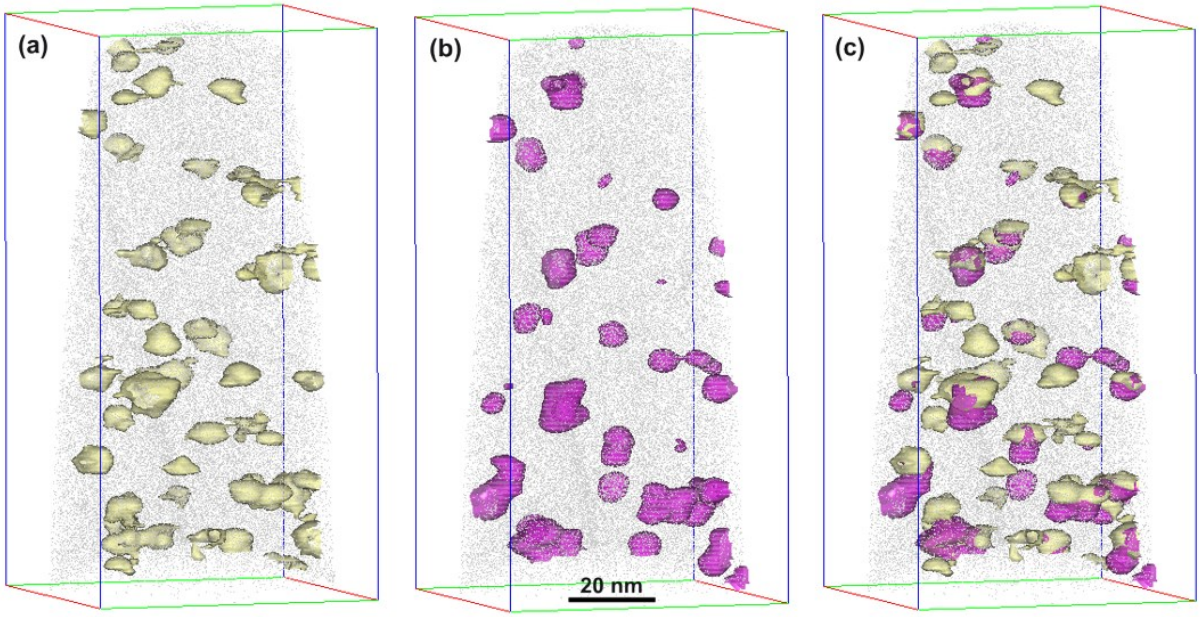

Figure 48: 3D atom maps including isoconcentration surfaces of Y-O (a), Y-V-C (b) particles as well as both types of particles (c).

By using such isoconcentration surfaces as interfaces a proximity histogram [83] can be calculated. A proximity histogram gives the average concentration profile normal to the isoconcentration surface. This profile is calculated to determine whether the particles are enriched or depleted in different elements. In Figure 49 the concentration profile of Y-O-particles is depicted. Negative distance values stand for the concentration amount outside the particles, whereas positive distance values are inside the particles. The large deviation at the end of the concentration profile can be explained by the fact that the particles are not perfectly spherical and the their size is not the same. Therefore, less data is available with the increasing distance. Besides Y and O these clusters are enriched in Cr, Mo, Si and also in V and C. In contrast to that Fe and Co are depleted. Cu seems to be enriched at the interface between the particles and the matrix, suggesting that Cu forms a shell around the particles. Consequently, it can be assumed that Cu is piled out of the Y-O particles. In the second type of particles, the V-C-Y-particles, also Mo, Mn, Si and W are enriched and again Fe and Co are depleted. Figure 50 shows the proximity histogram of these particles. At the surface of these clusters a slight depletion of Cu can be identified.

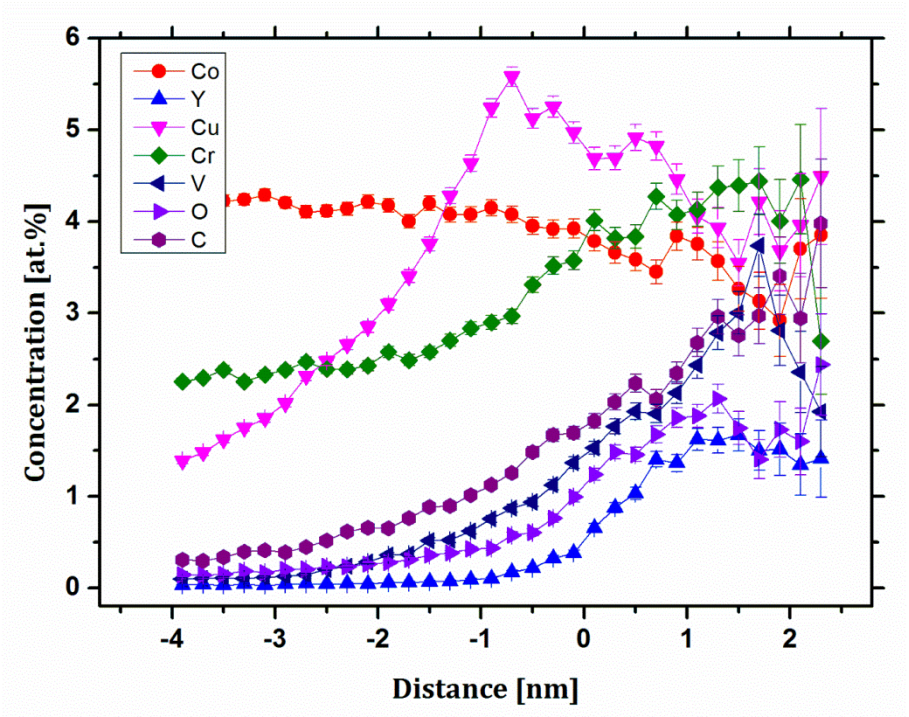

Figure 49: Isoconcentration profile of Y-Cu-Cr-O-particles in the highly alloyed sample, after soft-annealing, milling and HIPing.

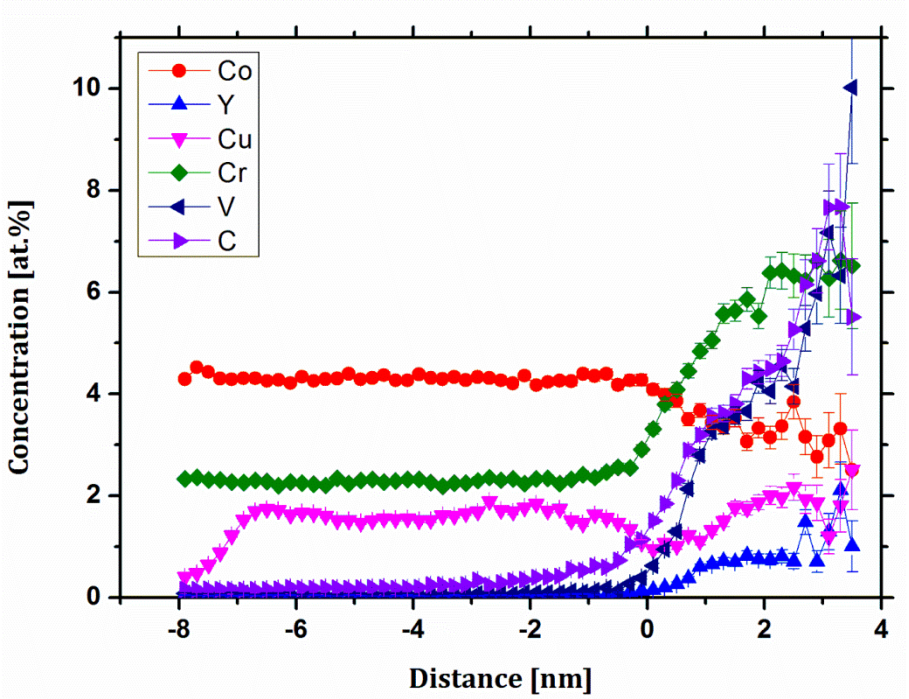

Figure 50: Isoconcentration profile of V-Cr-C-Y particles in the highly alloyed sample, after soft-annealing, milling and HIPing.

Several other methods have been developed to identify clusters of a dilute alloy systems [84,85]. For more detailed investigation a cluster search algorithm based on the maximum separation method was applied on both types of particles [86–88]. This method allows a determination of an approximate chemical composition of each particle

type. For the cluster search algorithm the orders of ions were set to 1. The parameter d_{max}, which is the distance that separates the solute atoms lying within the cluster from that lying outside, has been set to 0.8 nm for the Y-O clusters and 0.6 nm for the Y-V-C clusters. The distance parameter L, which takes all other atoms within the cluster into account, has been set to 0.8 nm and 0.6 nm for the clusters, respectively. The shell surrounding the cluster, which is generated because of the step before, is eroded with an erosion distance, that has been set to 0.6 nm and 0.5 nm for both cluster types. All particles which consisted of less than 7 atoms have been neglected in order to exclude randomly distributed atoms. In Table 7 the average composition and standard deviation of the Y-O particles is listed. In Table 8 and Table 9 the calculated composition of the Y-V-C particles and of the matrix are shown. Since the results indicate a depletion of Fe and Co and an enrichment of all other alloying elements in the particles it can be reported that the maximum separation method confirms the results of the previous proximity histograms. It should be mentioned that in case of the particle compositions the Y and O content is underestimated and the Fe and Co content is overestimated because of trajectory aberrations and tip irregularities, as the Y-O particles exhibit a preferred evaporation according to Marquis [45]. If the two different particles are compared it can be realized that an higher amount of Y is enriched at the Y-O particles whereas Fe and Co is stronger depleted at the Y-V-C particles. However, the Cu and Mn content is somewhat increased in the Y-O-particles in comparison to the Y-V-C particles. On the contrary, the Y-V-C particles are enriched in V and C up to 3.5 at.% and 4.6 at.%, respectively. Moreover, all the other elements show only a slight enrichment in the particles.

Table 7: Composition of the Y-O particles obtained by means of the maximum separation method.

Y-O-particles	Fe	Co	Y	O	Cu	V	C	Mn	Cr	Si
Concentration [at-%]	67.2	3.3	5.6	6.12	4.5	2.0	1.0	1.4	3.4	1.2
Standard-deviation	12.9	1.9	3.9	5.9	4.5	2.0	1.0	1.4	2.4	1.2

Table 8: Composition of the Y-V-C particles obtained by means of the maximum separation method.

Y-V-C-particles	Fe	Co	Y	V	C	O	Cu	Mn	Cr	Si
Concentration [at-%]	50.6	2.3	2.7	18.9	14.9	1.5	1.86	0.81	4.2	1.0
Standard-deviation	17.5	2.6	2.7	13.9	11.2	1.1	1.86	0.81	4.0	1.0

It must be mentioned that concentrations of Mo, Cr and W are lower in the analyzed volumes of the APT measurements compared to the overall composition of the steel. Thus, it can be assumed that these elements are enriched in coarser carbides which were not included in these atom probe measurements.

Table 9: Composition of the matrix obtained by means of the maximum separation method.

Matrix	Fe	Co	Y	O	V	C	Cu	Mn	Cr	Si
Concentration [at-%]	89.9	4.3	0.03	0.09	0.13	0.17	1.1	0.53	2.4	0.62

Generally, the extent of particles is given as radius of gyration (R_g). The use of R_g enables the comparison of the size of particles with different shapes. In this specimen the R_g has been calculated to 0.87 ± 0.3 nm, and 1.08 ± 0.3 nm for the Y-O-particles and the Y-V-C-particles, respectively.

Table 10: Comparison of the radii of gyration (R_g) of Y-O and Y-V-C particles.

	R_g
Y-O-particles	0.87 ± 0.3
Y-V-C-particles	1.08 ± 0.3

3.7 Milled high-alloyed steel in the HIPed stage without soft-annealing

To analyze the effect of soft-annealing, the material must be compared to the HIPed steel, which was not soft-annealed. Therefore, in order to reveal whether there are also nanometer-sized particles distributed in the material after HIPing, APT investigations were performed on this bulk material. Figure 51a presents the APT reconstruction including all ranged ions. In this type of material also very fine particles enriched in Y and O can be detected. Figure 51b and c show these particles. Furthermore, these particles are also enriched in V and Mn, which is illustrated in the 3D atom map in Figure 51d and e. The element Co is, as in the other materials, homogenously distributed and not enriched in the particles. The shape of the particles can be seen in Figure 52 where they are presented as isoconcentration surfaces with a Y concentration of 0.3 at.%. Isoconcentration surfaces give a hint that these particles have also a spherical shape as in the soft-annealed steel. The proximity histogram (Figure 53) of the isoconcentration profile shows elements enriched or depleted in the particles. Its results agree with the visual inspection of the atom maps showing enrichments of Y, O, V, Mn and a slight depletion of Co as well as Fe (not shown here). It should also be mentioned that Zr is enriched in the particles. It has been incorporated into the material due to previous milling experiments. As already mentioned, Zr is a key element for the formation of the particles and it is assumed that Zr enhances the nucleation rate.

Compared to the soft-annealed material, in this condition only a single type of particles can be detected. Again, a cluster search algorithm has been employed to calculate the approximate mean composition of the particles. In this evaluation all parameter have been set to 0.5 nm and the minimum cluster size has been set to 11 atoms. The detailed mean content of the nano-particles can be seen in Table 11. The investigated particles are strongly enriched in V (15.8 at.%). The Y content is approximately equal to the content of the Y-V-C particles in the soft-annealed condition. Conversely, atom probe investigations detected a higher O content of about 15.3 at.% in the particles. Furthermore, exhibiting a concentration of 3.9 at.% in these particles also C is enriched in the investigated condition.

All in all, this result shows that soft-annealing is not absolutely necessary for mechanical alloying the high-alloyed steel powder. Thus, it can be concluded that milling

mechanisms work also in the brittle martensitic powder particles. This fact suggests that diffusion-assisted intermixing with the help of defects, which are very frequent in martensite, is the most likely mechanism and not only fracturing and cold welding. For example Ashkenazy et al. [52] described the intermixing of various phases caused by shearing of dislocations. Furthermore, Schwarz [57] described a model after which diffusion along dislocation lines is responsible for the dissolution of different phases. The results of *publications A-C* in this thesis revealed that vacancy-type defects are responsible for effective milling a Fe-Y_2O_3 model alloy.

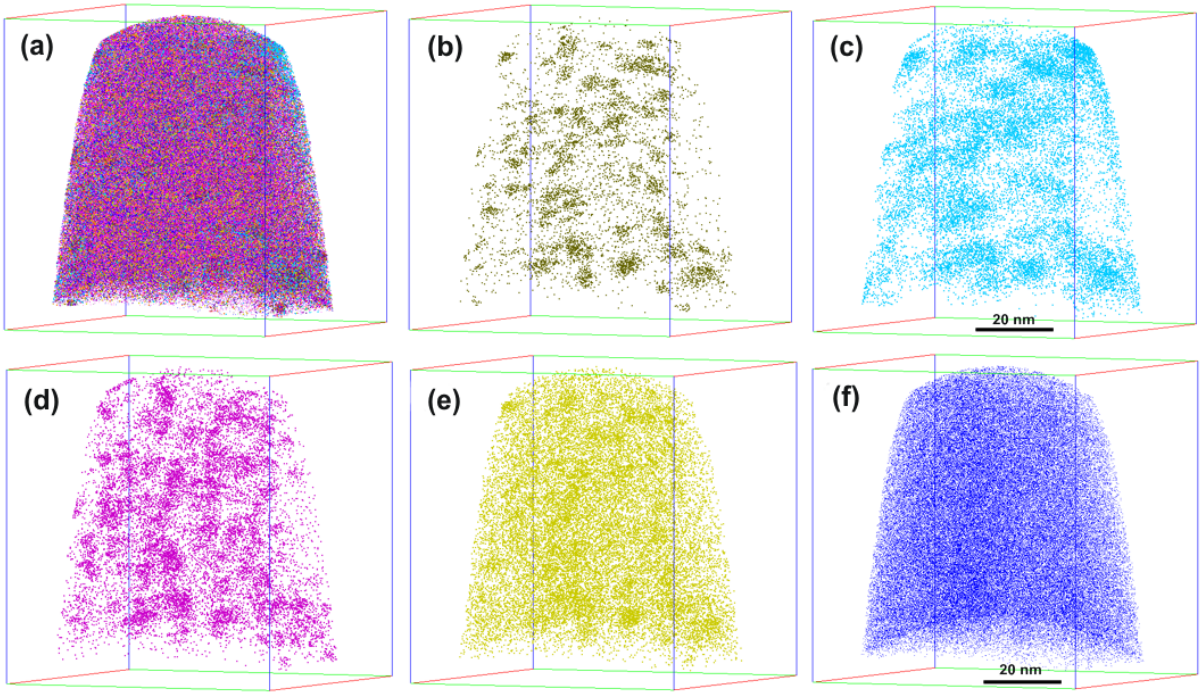

Figure 51: Atom probe tip reconstructions of the HIPed highly alloyed steel without the soft-annealing step. In this figure all ions are shown in (a) as well as the atoms of the elements Y (b), O (c), V (d), Mn (e), and Co (f).

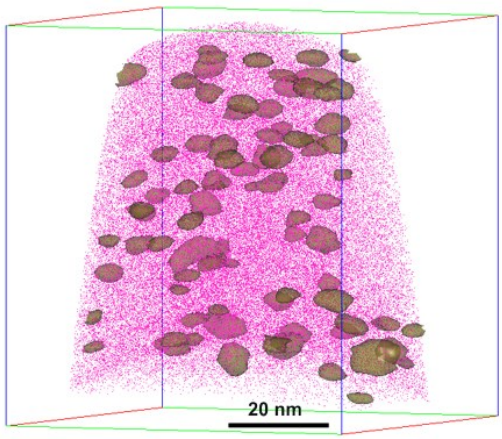

Figure 52: Illustration of the Y, O, V, Mn enriched particles with a isoconcentration profile for 0.3 at.% Y.

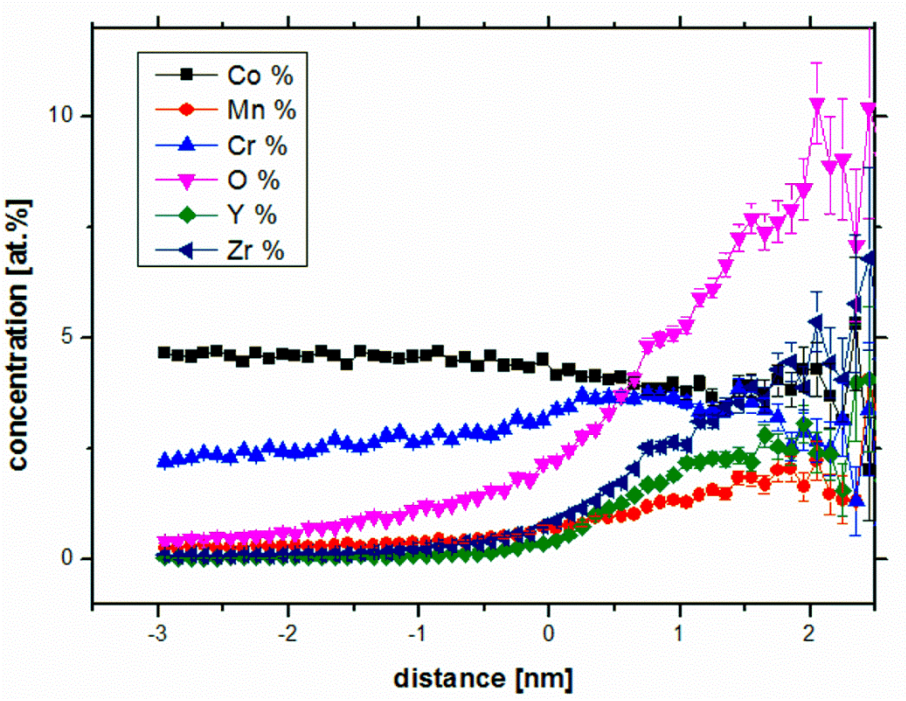

Figure 53: Proximity histogram, presenting the elements enriched or depleted in the particles of the HIPed high-alloyed steel without the soft-annealing step.

Table 11: Mean content of detected nanoparticles by means of atom probe tomography.

Particle composition	Fe	Co	Cu	Mn	Cr	V	O	Y	Zr	C
Concentration [at.%]	Bal.	2.3	5.9	4.7	2.5	15.8	15.3	2.9	2.7	3.9
Standard deviation [at.%]	20.9	2.2	5.6	4.7	2.3	8.8	6.2	2.9	2.7	3.4

3.8 Microstructure after tempering

In the common processing route of a high-alloyed steel a heat treatment follows after the HIPing process. This heat treatment is schematically depicted in Figure 33. After stress relieving the high-alloyed steel is hardened. Hardening has the effect that an almost martensitic matrix is formed in tool steels. Subsequently, the steels are tempered two or three times between 450 °C and 650 °C in order to transform the entire retained austenite to martensite. During this processing step so-called secondary hardening carbides are formed and also a higher amount of martensite is achieved, which both further increase the hardness of the material.

3.8.1 Microstructure of a milled, heat treated, high-alloyed steel

HIPed samples are subsequently heated in 5 min up to a temperature of 1070 °C, held isothermally for 20 min and then quenched, with a $t_{8/5}$ of 40 s, which is defined as the time of cooling from 800 °C to 500 °C. After that the samples were tempered three times for 2 h at temperatures between 480 °C and 700 °C. In this chapter the microstructure of the ODS high-alloyed steel at different tempering temperatures is analyzed. The question if also Y-O particles exist besides carbides is clarified in the following paragraphs.

Microstructure after tempering at 540 °C

In order to analyze the microstructure evolution during tempering atom probe measurements have been performed on the tempered ODS high-alloyed steel. APT measurements on the material tempered at 540 °C three times for 2 h revealed the existence of 3 different types of particles in the microstructure. A 3D reconstruction of the APT data is illustrated in Figure 54, showing different elements. First of all, Y-O-particles can be found where also V, Mo and C are enriched. It should be noticed, that these particles are not homogenously distributed over the entire volume. Secondly, a region of small carbides consisting mainly of Cr, V, and Mo is detected. For an improved illustration the carbides are depicted as isoconcentration surfaces in Figure 55 [82]. These carbides have a plate-like shape and seem to have an angle of 45° to each other. To evaluate the mean concentrations within these carbides, a proximity histogram was calculated [89]. This shows that the carbides are depleted in Fe (not shown here) and Co, but are mainly enriched in Cr, V and Mo. After secondary hardening these elements form typically M_2C carbides, which have also a plate-like shape [90]. This suggests that these particles are probably M_2C-type carbides.

The third kind of particles are Fe-Cu intermetallic particles, which are distributed in a very fine and homogenous manner. Cu has also been incorporated in the steel powder by mechanical alloying. The Fe-Cu particles can be seen in Figure 55a. All three particle types enhance the hardness of this condition, which is shown in Figure 64 and Figure 65.

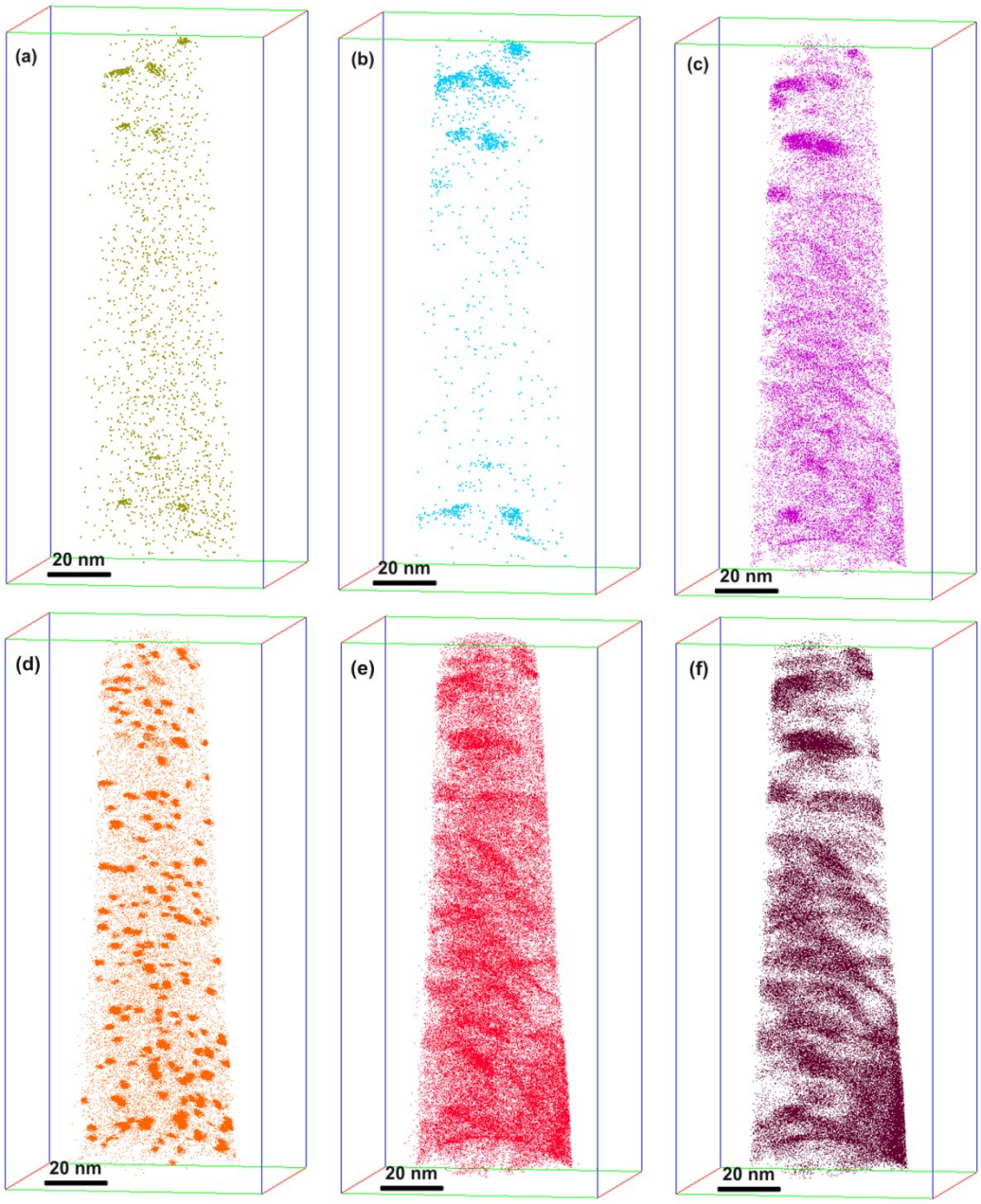

Figure 54: 3D reconstruction of Y (a), O (b), V (c), Cu (d), Mo (e), and C (f) atoms of the milled, soft-annealed and HIPed high-alloyed steel after 3 times tempering at 540 °C for 2 h, respectively.

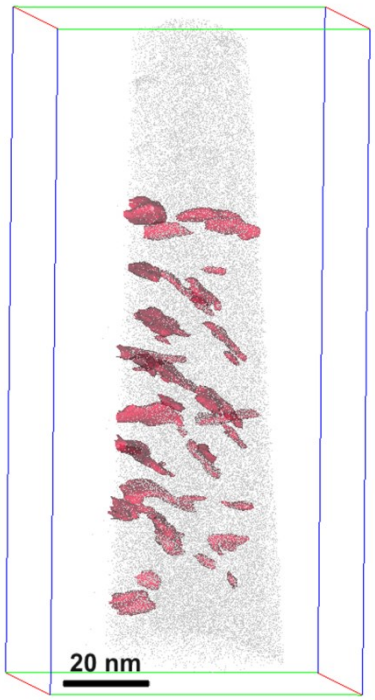

Figure 55: 3D reconstruction showing a 3 at.% Mo isoconcetration surface for a better illustration of the carbides present.

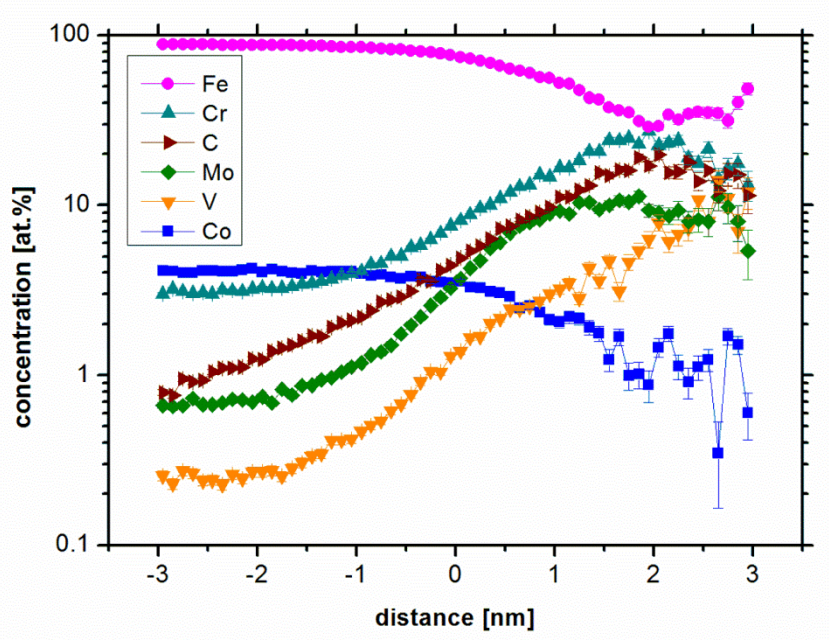

Figure 56: Proximity histogram of the isoconcentration surfaces of the secondary hardening carbides detected by APT presented in Figure 55. Enrichments and depletion of various elements can be determined.

Microstructure after tempering at 580 °C

To investigate the effect of the tempering temperature on the microstructure of the mechanically alloyed steel, a specimen tempered at 580 °C has been analyzed by means of APT. 3D reconstructions of the APT measurement are shown in Figure 57. In this state

the same types of particles can be detected. In this state the Y-O-particles (Y atoms are depicted in Figure 57a) are randomly distributed over the volume. Visual inspection gives a hint that in case of the Y-O particles shape, size and distribution seem to be similar to the ones after tempering at 540 °C. In Figure 57b the atom map of C is shown, which represents the size and distribution of secondary hardening carbides. For a better visibility, these carbides are presented in Figure 58 as isoconcentration surfaces with 12 at.% C and Cr. Most of these carbides have the same plate-like shape but they appear coarser in size. The proximity histogram (Figure 59) reveals enrichments in Cr, Mo, V, W, and C and a depletion of Fe and Co. The mean concentration of C in the carbides is about 30 at.%. The C concentration and the elements enriched in these carbides indicate that they are also M_2C type carbides. Considering the Cu atoms presented in Figure 57c these particles seem to coarsen at this annealing stage compared to the previous stage at lower annealing temperatures. Additionally, more Cu is dissolved in the matrix, suggesting that at 580 °C Cu has a higher solubility in the Fe matrix.

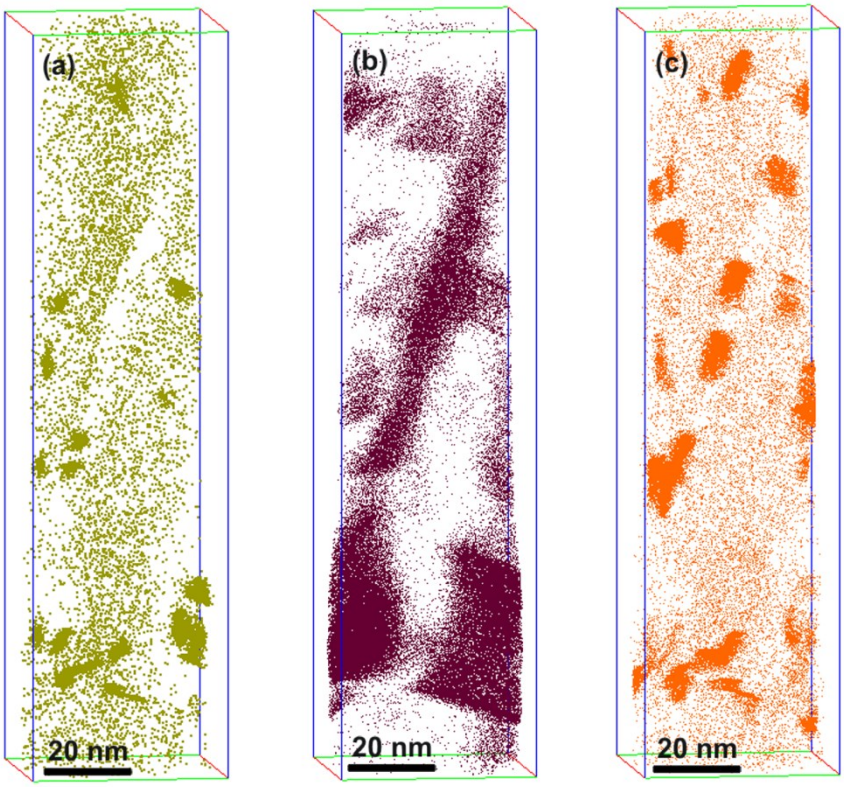

Figure 57: 3D atom maps of the elements Y (a), C (b) and Cu (c) of the milled, soft-annealed and HIPed high-alloyed steel after 3 times tempering at 580 °C for 2 h, respectively.

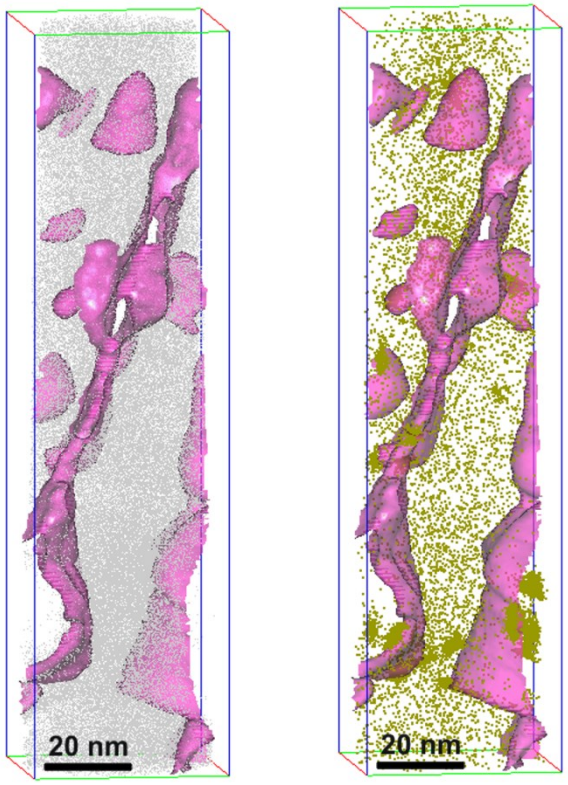

Figure 58: 3D atom map, presenting the isoconcentration profiles of the detected carbides.

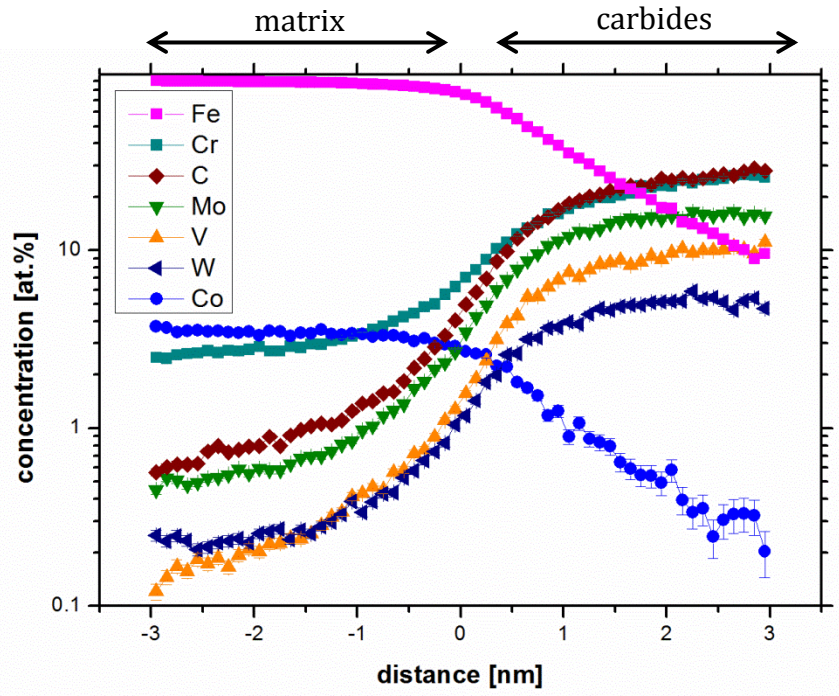

Figure 59: Proximity histogram calculated using the isoconcentration profiles in Figure 58.

Microstructure after tempering at 650 °C

In this condition one type of particle cannot be detected anymore. Therefore, two different types of particles are detected by APT. The first type of particles is the Y-O-

particle type and the second type is the carbide type. Atom maps of several elements are shown in Figure 60. The investigation of this condition gives a good impression of the thermal stability of the Y-O particles and, therefore, their influence on high-temperature hardness. Although the tempering temperature has been very high for secondary hardening, the size of the Y-O particles seems to be similar to the size of the annealing states with temperatures of 540 °C and 580 °C. Therefore, despite the elevated annealing temperatures, the Y-O particles will still contribute to the hardness, which suggests that these particles enhance the mechanical properties at elevated temperatures.

Furthermore, the plate-like shaped M_2C carbides identified at tempering at 540 °C and 580 °C vanished at 650 °C. Instead of these plate-like shaped carbides much coarser carbides can be detected in this state. These large carbides presented in Figure 61 as 5 at.% Mo and C isoconcentration surfaces consist of about 14 at.% C, which gives a hint that these carbides are of the M_6C type. Moreover, also the enrichment of Mo and W, which is illustrated in proximity histogram in Figure 62, underlines this assumption.

It must be mentioned that the Cu particles are homogenously distributed at the condition at 540 °C. However, they almost vanished after 3 times tempering at 650 °C (depicted in Figure 60a), indicating that the Cu particles coarsened during annealing and are not detected by APT anymore. Furthermore, Cu dissolved in the Fe-matrix, exhibiting an increased solubility of Cu in Fe at a temperature of 650 °C.

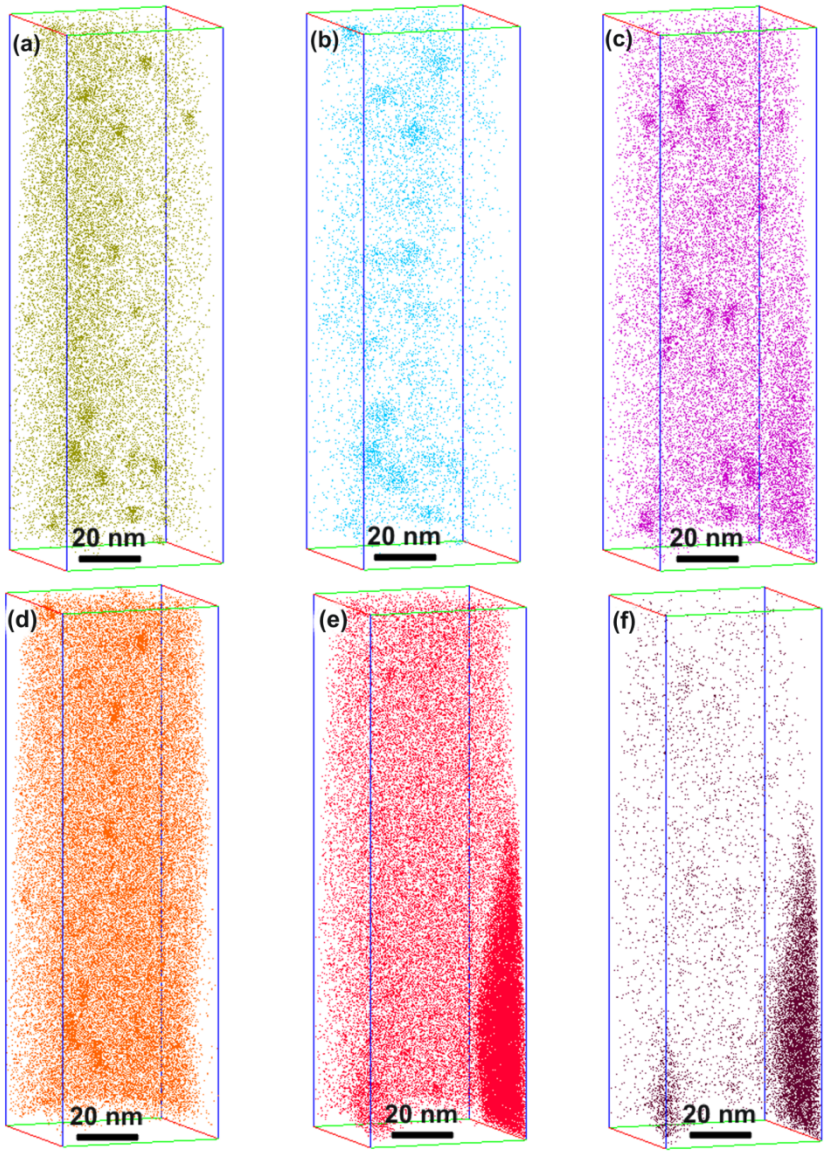

Figure 60: 3D atom maps of the milled, soft-annealed and HIPed high-alloyed steel after 3 times tempering at 650 °C for 2 h, respectively. It presents the elemental distribution of Y (a), O (b) and V (c). All these elements tend to enrich in the smaller particles. However, Cu (d) is almost dissolved in the matrix and slightly enriched in the small particles. Mo (e) as well as C (f) are enriched in the coarser carbides.

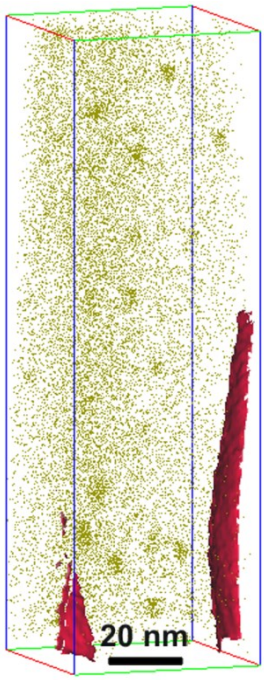

Figure 61: 3D atom map showing the Y atoms (yellow points) as well as the carbides, where the surface is illustrated as a red isoconcentration surface with a concentration of 5 at.% Mo and C.

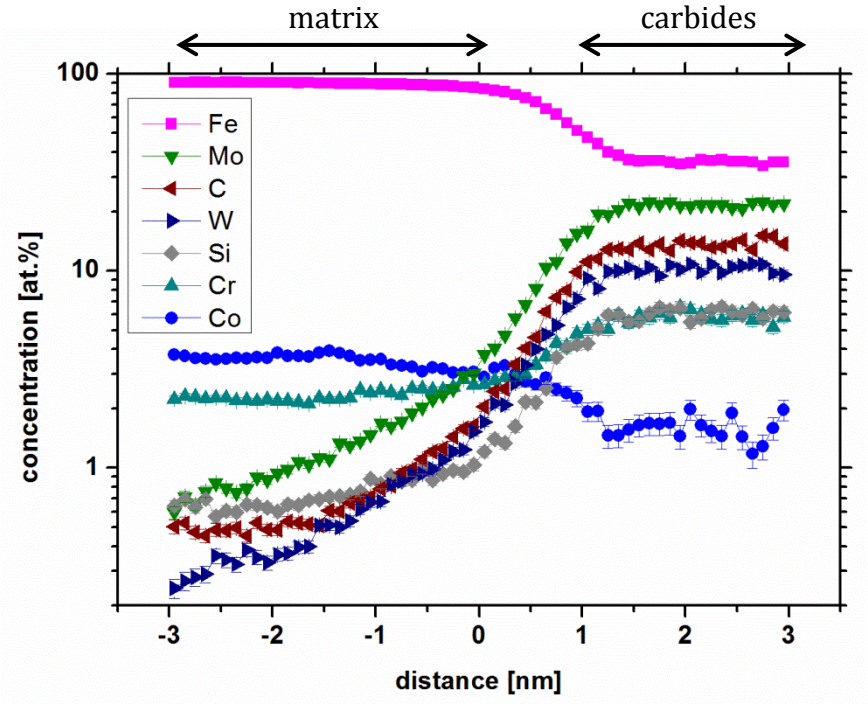

Figure 62: Proximity histogram of the carbide, calculated using the isoconcentration surface in Figure 61.

Comparison of the particles in the different tempered conditions

Table 12 shows the most important results concerning the particle size dependence on the tempering temperature. The particle size of the Y-O particles as well as the Fe-Cu

particles is given as radii of gyration (R_g). The particles have been defined using the maximum separation method which is described in [86–88]. As algorithm parameters for the Y-O particles, the ion order and Nmin were set to 2 and 8, respectively. Nmin defines the minimum cluster size, which is taken into account by the present algorithm. All other distance parameters were set to 1 nm. For the other states, the parameters were adapted, but did not differ drastically. For the Fe-Cu particles again an ion order and Nmin of 2 and 8 were chosen, respectively. All distance parameters were set to 0.35 nm. The comparison of R_g of the Y-O-particles in the different states shows that there is no drastic difference, as all mean radii were within the standard deviations. Therefore, it can be concluded that the Y-O-particles stay stable until 650 °C. This agrees with the results of previous works, which employed similar investigations on ferritic steels alloyed with Ti [69,91–93]. However, this result has not been evidenced in case of martensitic high-alloyed steels, which have a comparatively high C content. Thus, from these results it can be concluded that it is possible to introduce very stable Y-O-particles besides common carbides into a martensitic high-alloyed steel.

Considering the Cu-Fe precipitates the mean R_g in the condition tempered at 540 °C is 0.4 nm and, therefore, lower than the R_g of the Y-O-particles. However, also in case of these particles no increase in size can be evidenced by the APT data evaluation. Nevertheless, the ratio between the Cu concentration in the matrix and the Cu concentration in the overall specimen in Table 12 shows very well if Cu is dissolved in the matrix or still present in the particles. It must be mentioned that at the 650 °C state no Fe-Cu particles are detected, only some Y-O particles which were slightly enriched in Cu. Therefore, for the calculation of the matrix composition of the 650 °C annealed state a region of interest (ROI) has been placed in the measured volume without including any particles. In this region the Cu content was calculated. A matrix-overall ratio of 0 indicates that no Cu is dissolved in the matrix and all Cu atoms are in the particles. Conversely, a ratio of 1 shows that Cu forms no particles and all Cu atoms are dissolved. The calculated ratios of the 540 °C and the 580 °C condition are 0.3 and 0.45, respectively. From these low amounts it can be concluded that Cu is mostly enriched in the precipitates at lower temperatures and becomes dissolved in the matrix at higher annealing temperatures. Hence, the ratio of the 650 °C tempered state exhibits a ratio of 0.97 indicating that most of the Cu is dissolved in the matrix. This agrees with the visual inspection of the corresponding atom map (Figure 60d) showing that most of the Cu

particles have vanished and that Cu atoms are dissolved in the matrix. All in all, it can be concluded that a tempering temperature between 540 and 650 °C influences the Cu precipitation or dissolution effectively. Moreover, this fact suggests that a particle hardening contribution exists after 540 °C of tempering, whereas a solid solution hardening contribution is present in the 650 °C condition. In the 580 °C state a mixture of both hardening mechanisms of Cu is present.

Table 12: Comparison of the results of the maximum seperation method applied on the 540 °C, 580 °C and 650 °C tempered states. The matrix-overall Cu concentration ratio indicates the amount of Cu dissolution or in the precipitates, respectively.

Tempering temperature [°C]	R_g [nm] (Y-O-clusters)	R_g [nm] (Cu-Fe-precipitates)	Matrix/overall Cu concentration ratio
540	1.09 ± 0.4	0.4±0.18	0.30
580	0.92 ± 0.7	0.31±0.31	0.45
650	0.84 ± 0.5	-	0.97

Content of retained austenite

As proposed in the previous work of Cayron et al. [94] Y-O particles can affect the quenchability of an EUROFER steel (consisting of 8.9 m.% Cr, 1.1 m.% W and 0.1 m.% C). These authors supposed that the grain size of austenite during austenitization is smaller due to pinning effects of the Y-O particles and these small grains are less prone to a martensitic transformation than coarser grains. Consequently, also in this high-alloyed steel the quenchability is investigated by measuring the content of retained austenite by means of X-ray diffraction (XRD). Evaluation of the amount of retained austenite as well as the calculation of the R-value and the peak area have been carried out according to [95,96]. In Figure 63 the content of austenite in the different conditions is presented. First of all, the highest austenite content of about 5 % has been detected in the hardened condition. Further tempering at 500 °C and above reduced the retained austenite content clearly. All tempered conditions showed a content of retained austenite between 0 and 1.5 %, which is below the resolution limit of~2 % as mentioned in [95].

All in all it can be concluded that the addition of 0.5 m.% yttria by mechnanical alloying and about 1 m.% Cu have an insignificant effect on the martensite transformation.

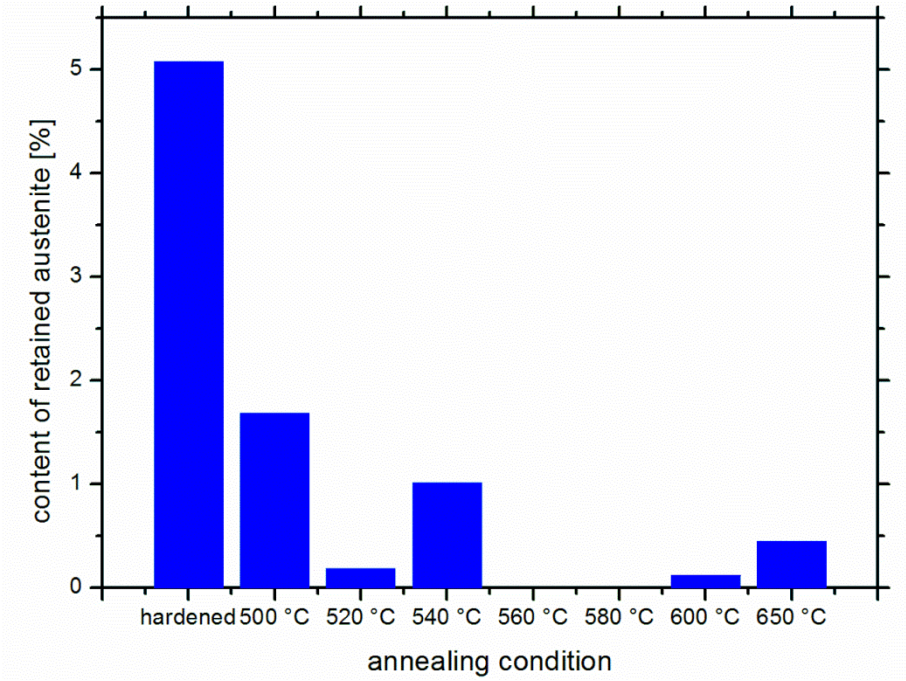

Figure 63: Comparison of the content of retained austenite in different heat treatment conditions of the high-alloyed steel.

3.8.2 Comparison of tempering curves

Particle hardening with three different particle types has been investigated for a high-alloyed steel. In order to evaluate the effect on hardness after tempering, the hardness evolution against the tempering temperature has been examined (Figure 64). The reference material is the high-alloyed steel without mechanical alloying, a common high-alloyed steel containing secondary hardening carbides after tempering. As shown in the previous chapters the 48 h mechanically alloyed steel with and without previous soft-annealing, also contains finest Y-O particles. Three Rockwell hardness indentations were done in each condition. Comparing the hardness after tempering at lower temperatures, Figure 64 shows that the hardness of the different specimens is approximately equal, suggesting that introducing Y-O particles into the steel has no significant influence on the peak hardness. The higher the tempering temperature applied the higher the detected drop in hardness. Especially, the reference material exhibits a dramatic decrease in hardness due to coarsening of secondary hardening carbides. After three times tempering at 700 °C for 2 h, respectively, the specimen exhibits a hardness of 31 HRC. If this hardness evolution is compared to the soft-annealed and mechanically alloyed specimen, it can be seen that this drop in hardness stops at about 45 HRC. At higher temperatures this hardness decrease is lower than in case of the reference

material. Furthermore, the hardness of the mechanically alloyed but not soft-annealed specimen shows the highest hardness values at elevated tempering temperatures. Thus, this alloy exhibits the lowest hardness decrease of all specimens. Hence, the measured mean hardness was 52.2 HRC after three times tempering at 675 °C for 2 h, respectively. This is an increase in hardness of about 21 HRC compared to the common reference steel. From previous microstructure investigations it is known that the higher the tempering temperature the coarser the secondary hardening carbides. Consequently, their contribution to the hardness is lower. However, it is also known that in the mechanically alloyed specimens these carbides coarsen but the fine Y-O particles stay stable at elevated tempering temperatures and can still contribute to the hardness, which causes higher hardness values in these specimens. It is also assumed that these Y-O particles can act as obstacles for the coarsening of the carbides.

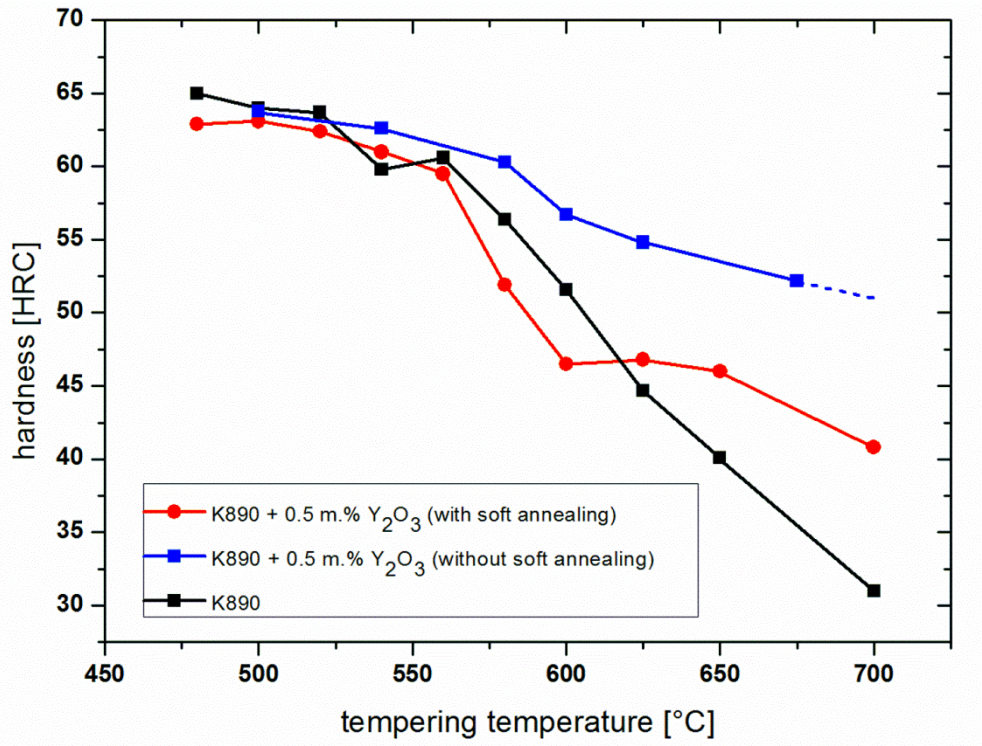

Figure 64: Tempering curves of the common high-alloyed steel (black), the 48 h milled steel with 0.5 m.% yttria with soft-annealing (red) and without soft-annealing (blue).

3.8.3 The effect of using ZrO_2 balls as milling media on the mechanical properties at elevated temperatures

As already mentioned in the previous chapters experiments were carried out by using Fe-Y_2O_3 model alloys to cause an intended incorporation of yttrium stabilized zirconia

(YSZ) during milling by ball abrasion to produce Y-Zr-O particles which exhibit an improved thermal stability. Such experiments were also performed using the high-alloyed steel powders. In Table 13 the intended incorporation contents of Zr and Y during milling for 12 h and 24 h are listed. The contents were measured by means of X-ray fluorescence spectroscopy (XRF). Again, a rather constant incorporation rate can be assumed. Milling the soft-annealed powders with YSZ balls an incorporation rate of 0.04 m.%/h Zr and 0.002 m.%/h Y can be derived from these results, which is approximately in the range of milling the ferritic powder in the Fe-Y_2O_3 model alloy. Milling of 48 h caused a too high amount of Zr incorporation and it was assumed that this caused an embrittlement which is too high for technical application. Therefore, this state was not investigated in more detail.

Table 13: Concentrations of incorporated Zr and Y during milling with YSZ balls in two batches determined by XRF.

Milling duration	Incorporated Zr [m.%]	Incorporated Y [m.%]
12 h	0.52	0.04
24 h	0.98	0.05

Comparison of tempering curves

In order to analyze the effect of an additional Zr incorporation on the hardness of the mechanically alloyed steel at different tempering temperatures, tempering curves were compared in Figure 65. First of all, both Zr incorporated specimens mechanically alloyed with YSZ balls show akin hardness values at elevated tempering temperatures. For the 24 h and 12 h condition 47.1 HRC and 46.6 HRC were measured, respectively. Thus, it can be concluded that longer milling durations, and therefore higher Zr amount, do not influence the hardness drastically after tempering at high temperatures. Moreover, analyzing these specimens shows that the YSZ ball milled specimens exhibit a higher hardness after tempering at elevated temperatures than the common reference sample (31 HRC) and the soft-annealed and 48 h steel ball milled specimen (40.8 HRC). However, the sample milled for 48 h with steel balls and without soft-annealing showed the highest hardness, suggesting that soft-annealing has a detrimental effect on the hardness after tempering at high temperatures of the milled high-alloyed steel.

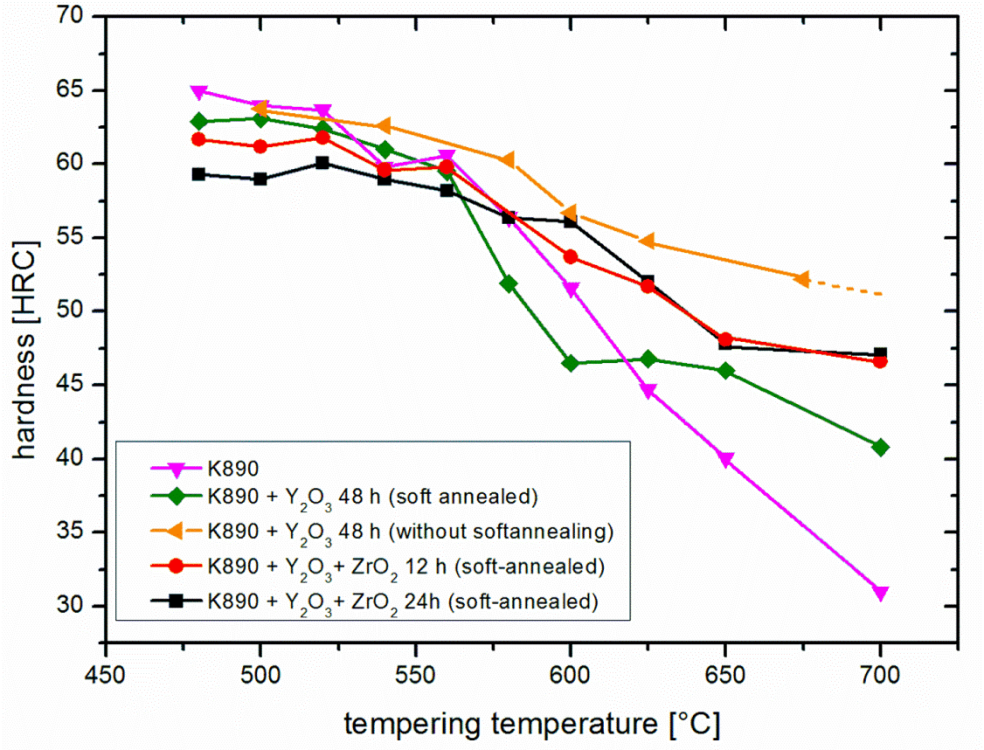

Figure 65: Tempering curves of the common high-alloyed steel (pink); of the 48 h milled high-alloyed steel with 0.5 m.% yttria with soft-annealing (green) and without soft-annealing (orange). Milling was conducted with steel balls. They are compared to soft-annealed specimens milled with YSZ balls for 12 h (black), 24 h (red).

3.9 Discussion

In the second part of this thesis the mechanical alloying process has been applied on a high-alloyed steel powder. Furthermore, it has been investigated if soft-annealing on powder particles has a positive effect on the milling process. The nanostructure of several milled powder particles, with and without soft-annealing, as well as the HIPed and tempered conditions of the ODS high-alloyed steel has been investigated by means of APT.

If the nanostructure of the milled high-alloyed steel particle is compared to the milled ferritic particles of *publications A-C* in part one, it can be followed that there is no dramatic difference of the Y distribution. From APT investigations it can be recognized that the Y atoms also tend to form clusters and these clusters are distributed homogenously. Also Williams et al. [50] found an akin Y distribution in ferritic powder particles. However, only at the soft-annealed, high-alloyed steel particles an inhomogeneous Y distribution can be detected, suggesting a detrimental effect of soft-annealing on milling a high-alloyed steel powder. It is supposed that the increased

carbide content in the high-alloyed steel powder causes an inhomogeneous structure, therefore an inhomogeneous deformation and defect generation in the powder during milling. Hence, it is assumed that carbides precipitated during soft-annealing with different mechanical properties interfere with the milling processes. As already mentioned, the formation of defects during milling, which are assumed to cause the distribution of yttria in an extremely fine manner, can also be disturbed. Moreover, precipitates can act as obstacles for dislocation gliding and, thus, complicate intermixing. As described in the previous chapters, it is also assumed that this can cause an intermixing of different phases. All in all, the lower defect density as well as the presence of larger carbides makes an intermixing during mechanical alloying more difficult. Hence, to get a better distribution of Y and O in the soft-annealed specimens an increased milling duration must be applied.

Concerning the nanostructure after HIPing the ODS high-alloyed steel exhibits also extremely small particles enriched in Y. Their size agrees with the results of the HIPed Fe-Y_2O_3 model alloy published in *publications A-C*. However, in the HIPed stage of the ODS steel without soft-annealing the nanoparticles show additional V, Mn and Zr enrichments. Furthermore, the soft-annealed steel exhibits two different types of nanoparticles. Some nanoparticles are mainly enriched in Y, V, Cr, and C, and other particles are enriched in Y, O, Cu, and Cr. These facts distinguish the HIPed ODS high-alloyed steel powder from the ODS model alloy.

Also in the high-alloyed ODS steels the extremely high stability of the Y enriched nanoparticles can be observed after hardening and tempering at various temperatures. APT nanostructure has evidenced that the Y enriched nanoparticles are formed in the steel and exist besides the typical secondary hardening carbides of these steels, which are comparatively high alloyed. Tempering at elevated temperatures showed that the carbides coarsen during annealing and the Y enriched nanoparticles remain at the same size.

A comparison of the tempering curves suggests that the small nanoparticles in ODS steels enhance the hardness after tempering at comparatively high temperatures. After tempering for 3 times at 700 °C for 2 h the ODS high-alloyed steels exhibit a hardness increase of up to 21 HRC compared to the commonly produced steel.

4 Summary and Outlook

In this thesis a comprehensive set of investigations were employed to elucidate the mechanisms during milling by the example of a simple Fe – yttria model alloy. The mechanisms during mechanical alloying differ, dependent on the individual powder constituents. For the mechanical alloying of this ductile-brittle system the following conclusions can be drawn:

- As shown in p*ublication A and B* Y and also O exhibit an extended solubility in the Fe matrix after mechanical alloying.
- Y and O are arranged in clusters which are distributed in the Fe matrix in a very fine manner.
- Additionally, these clusters are enriched in Al and Mn which have been incorporated during milling and which were not part of the original yttria powder. These enrichments indicate that diffusion processes, e.g. dissolution and reordering, are active during milling.
- During the first stages of milling open volumes such as grain boundaries, dislocations and vacancies are assumed to assist the intermixing of Fe and yttria.
- Investigations of the last stage directly after mechanical alloying reported in *publication C* that especially vacancies are enriched in Y and O, which are the cluster forming elements.
- Therefore, diffusion-assisted intermixing accelerated with the help of vacancies is the most likely mechanism during the last stage of milling.
- All in all, it is assumed that a combination of following effects can cause a dissolution of yttria in Fe during mechanical alloying, resulting in a metastable matrix. First of all, diffusion with the help of vacancies as well as the extremely high surface of the powder fractions have a positive effect on the dissolution. Moreover, the mechanical energy introduced by the ball impacts promotes the diffusion to overcome the diffusion barriers of Y in Fe. Finally, also shearing by dislocation gliding can also contribute to the distribution of Y and O in the Fe matrix.

- Due to subsequent HIPing, which is a compaction process, diffusion of dissolved Y, O and also other enriched atoms such as Al or Mn form distinct particles and deplete in the matrix.
- Moreover, it is also assumed that due to HIPing these defects annihilate and cannot act as diffusion accelerators anymore.
- Further annealing at 600 °C for 8 h has only a minor effect on the particle growth, which evidences the great thermal stability of these very small particles.
- Additionally, investigations were performed in order to achieve an intended Zr incorporation caused by abrasion of yttrium stabilized zirconia (YSZ) balls, which is reported in *publication D*. With the use of YSZ balls instead of steel balls, which is a new, cheaper as well as easier way of producing, it is possible to obtain minor additions of Zr in the Fe powder particles.
- This incorporation caused a distribution of Y-Zr-O particles in a much finer manner than the Y-O particles in the common milled specimens. Therefore, hardness measurements revealed increased hardness values with Zr than without after HIPing.
- Also mechanical alloying of steel powders with YSZ balls caused an improvement of mechanical properties at elevated temperatures.
- Various experiments were carried out in order to check if milling high-alloyed steel powders with yttria powders can further improve its mechanical properties at elevated temperatures. Demonstrated by using the example of a high-alloyed steel, this thesis combined the process routes of a high-alloyed steel with an common ODS steel and elucidated its possibilities.
- From the results of the microstructural investigations it can be concluded that it is possible to insert finest Y-O particles into the high-alloyed steel.
- During secondary hardening heat treatments also typical carbides are formed, suggesting that these Y-O particles do not suppress the formation of these so-called secondary hardening carbides.
- Comparison of specimens with and without soft-annealing revealed that previous soft-annealing of the gas-atomized steel powder has no positive effect on the mechanical alloying and, therefore, on a more homogenous distribution of Y and O in the high-alloyed steel.

- This fact supports the theory that defects, such as vacancies, are beneficial for mechanical alloying yttria with Fe. Gas-atomized steel powders without soft-annealing exhibit an almost martensitic matrix, where much higher intrinsic stresses and, consequently, also a higher defect density is present.
- Furthermore, hardness measurements after different tempering temperatures revealed that soft-annealing causes a loss in hardness after tempering at elevated temperatures in a range of 650 °C to 700 °C as well as peak hardness at lower tempering temperatures of 500 °C.

Topics for further investigations could be the optimization of the milling parameters such as milling duration, ball to powder mass ratio or atmosphere. In this work parameters have been chosen relating to different previous publications.

Furthermore, a comparison of mechanical alloying of a standard ferritic powder and a pre-milled ferritic powder would be an interesting subject for further investigations. In the pre-milled powder defects are already inserted prior to milling with yttria, because of its high deformation. Another idea to improve ODS steels is to add small amounts of yttrium continuously or stepwise to the milling system. This might cause a more homogenous distribution of Y and O atoms as well as finer Y-O particles. Experiments with a continuous milling process may be useful for industrial applications because of their lower costs.

Moreover, the amount of yttria added to the alloy (either ferritic or high-alloyed steel) can be optimized. Especially, in the high-alloyed steel it would be interesting if finest Y and O particles influence the coarsening of the secondary hardening carbides and, if this is the case, to know how much yttria is necessary to reduce carbide coarsening.

Additionally, an optimization of the intended Zr incorporation would be useful. The amount of intended incorporation of Zr due to YSZ ball abrasion can be controlled by adjusting the right steel/YSZ ball mixture as milling media.

For steel production also an optimization of the HIPing process would be very interesting for further investigations. It is well known that lowering the HIPing temperatures causes an increase of hardness at ODS steels [65]. However, the

density of the compacted material, which needs higher HIPing temperatures, should not decrease.

Finally, the influence on additional mechanical properties, such as toughness or high temperature hardness or strength, of the additional Y-O particles should be investigated. For some of these experiments a larger specimen size and, therefore, a larger milling volume are required.

The topic “Mechanical Alloying”, especially concerning the production of ODS-alloys, offers a large field of research for the next few years and is a promising candidate for advanced materials in the future. This is because materials with different properties can be combined, which is not possible by using the common process route.

5 Publications

5.1 List of appended publications

Publication A

G. Ressel, S. Primig, H. Leitner

The evolution of Y distribution during the processing route of mechanically alloyed iron studied by means of atom probe tomography

International Journal of Materials Research 104 (2013) 1088-1095.

Publication B

G. Ressel, D. Holec, A. Fian, F. Mendez-Martin, H. Leitner

Atomistic insights into milling mechanisms in an Fe - Y2O3 model alloy

accepted in Applied Physics A: Materials Science and Processing (2013).

Publication C

G. Ressel, P. Parz, S. Primig, H. Leitner, H. Clemens, W. Puff

New findings on the atomistic mechanisms active during mechanical milling of a Fe-Y2O3 model alloy

submitted to Journal of Applied Physics (2013).

Publication D

G. Ressel, S. Primig, H. Leitner

The effect of Zr incorporation caused by ball abrasion in a milled Fe – Y2O3 model alloy

accepted in Metallurgical and Materials Transactions A (2013).

Publication E

G. Ressel, P. Parz, A. Fian, D. Holec, S. Primig, W. Puff, H. Leitner and H. Clemens

On the behavior of yttria/yttrium during mechanical alloying of a Fe – Y2O3 model alloy system

Accepted in Materials Science Forum/Advanced Materials Research proceedings Thermec 2013 (2013).

Publication F

F. Mendez-Martin, G. Ressel, H. Leitner

Focused ion beam sample preparation of mechanically alloyed iron powders for atom probe tomography

MC 2013 Proceedings, (2013) 509-510.

6 References

[1] C. Suryanarayana, Mechanical Alloying and Milling, Marcel-Dekker, New York, 2004.

[2] E. Arzt, Acta Mater. 46 (1998) 5611.

[3] E. Arzt, J. Roesler, Acta Met. 36 (1988) 1053.

[4] E. Arzt, D. Wilkinson, Acta Met. 34 (1986) 1893.

[5] J. Roesler, E. Arzt, Acta Met. 36 (1988) 1043.

[6] S. Ukai, T. Nishida, T. Okuda, T. Yoshitake, J. Mater. Sci. Technol. 35 (1998) 294.

[7] R.C. Benn, P.K. Mirchandani, in:, E. Arzt, L. Schultz (Eds.), New Mater. by Mech. Alloy. Tech., DGM - Informationsgesellschaft, 1988, pp. 19–38.

[8] R. Klueh, J. Shingledecker, R. Swindeman, D. Hoelzer, J. Nucl.Mater. 341 (2005) 103.

[9] D.K. Mukhopadhyay, F.H. Froes, D.S. Gelles, J. Nucl. Mater. 258-263 (1998) 1209.

[10] S. Ukai, T. Kaito, S. Ohtsuka, T. Narita, M. Fujiwara, T. Kobayashi, ISIJ Int. 43 (2003) 2038.

[11] W. Haufe, Schnellarbeitsstähle, Carl Hanser Verlag München, 1972.

[12] A. Czyrska-Filemonowicz, B. Dubiel, J. Mater. Process. Technol. 64 (1997) 53.

[13] J.S. Benjamin, Met. Trans. 1 (1970) 2943.

[14] J.S. Benjamin, T.E. Volin, Met. Trans. 5 (1974) 1929.

[15] J. Roesler, E. Arzt, Acta Met. Mater. 38 (1990) 671.

[16] D.J. Srolovitz, M.J. Luton, R. Petkovic-Luton, D.M. Barnett, W.D. Nix, Acta Metall. 32 (1984) 1079.

[17] J.H. Schröder, E. Arzt, Scr. Metall. 19 (1985) 1129.

[18] M.K. Miller, D. Hoelzer, E. Kenik, K. Russell, Intermet. 13 (2005) 387.

[19] M.K. Miller, D.T. Hoelzer, E.A. Kenik, K.F. Russell, J. Nucl. Mater. 329-333 (2004) 338.

[20] M.K. Miller, E. Kenik, K. Russell, L. Heatherly, D. Hoelzer, P. Maziasz, Mater. Sci. Eng. A 353 (2003) 140.

[21] A. Hirata, T. Fujita, Y.R. Wen, J.H. Schneibel, C.T. Liu, M.W. Chen, Nat. Mater. 10 (2011) 922.

[22] M. Klimiankou, R. Lindau, A. Möslang, J. Cryst. Growth 249 (2003) 381.

[23] M. Klimiankou, R. Lindau, A. Möslang, J. Schröder, Powder Metall. 48 (2005) 277.

[24] M. Klimiankou, J. Nucl. Mater. 329-333 (2004) 347.

[25] S.V. Meschel, O.J. Kleppa, J. Alloys Compd. 257 (1997) 227.

[26] E.J. Huber, E.L. Head, C.E. Holley, J. Phys. Chem. 61 (1957) 497.

[27] R.F. Domagala, J.J. Rausch, D.W. Levinson, Trans. ASM 53 (1961) 137.

[28] K.A. Gschneider, Rare Earth Alloys, D. Van Nostrand company, Inc., Pinceton, 1961.

[29] O. Kubaschewski, Iron - Binary Phase Diagrams, 1982.

[30] W. Zhang, G. Liu, K. Han, Phase Diagrams of Binary Iron Alloys, ASM International, 1993.

[31] J.D. Whittenberger, in:, E. Arzt, L. Schultz (Eds.), New Mater. by Mech. Alloy., DGM Informationsgesellschaft, 1988, pp. 201–215.

[32] P.S. Gilman, J.S. Benjamin, Annu. Rev. Mater. Sci. 13 (1983) 279.

[33] M. Bodart, R. Baccino, F. Moret, J. Phys. IV 3 (1993) 709.

[34] T. Okuda, M. Fujiwara, J. Mater. Sci. Lett. 14 (1995) 1600.

[35] Y. Kimura, S. Suejima, H. Goto, S. Takaki, ISIJ Int. 40 (2000) 174.

[36] Y. Kimura, S. Takaki, S. Suejima, R. Uemor, H. Tamehiro, ISIJ Int. 39 (1999) 176.

[37] C. Suryanarayana, Prog. Mater. Sci. 46 (2001) 1.

[38] R.. Schwarz, C.C. Koch, Appl. Phys. Lett. 49 (1986) 164.

[39] L.Y. Pustov, S.D. Kaloshkin, V.V. Tcherdyntsev, I.A. Tomilin, E.V. Shelekhov, A.I. Salimon, Mater. Sci. Forum 360-362 (2001) 373.

[40] D. Turnball, Metall. Mater. Trans. A 12 (1981) 695.

[41] F.H. Froes, C. Suryanarayana, K. Russell, C. Li, Mater. Sci. Eng. A 192-193 (1995) 612.

[42] R.C. Benn, P.K. Mirchandani, in:, E. Arzt, L. Schultz (Eds.), Dispers. Strength. by Mech. Alloy., DGM Informationsgesellschaft, 1988, pp. 19–38.

[43] M.K. Miller, K.F. Russell, D.T. Hoelzer, J. Nucl. Mater. 351 (2006) 261.

[44] M.K. Miller, A. Cerezo, M.G. Hetherington, G.D.W. Smith, Atom Probe Field Ion Microscopy, 1996.

[45] E.A. Marquis, Appl. Phys. Lett. 93 (2008) 181904.

[46] F. Vurpillot, Appl. Phys. Lett. 76 (2000) 3127.

[47] H.R.Z. Sandim, R.A. Renzetti, A.F. Padilha, D. Raabe, M. Klimenkov, R. Lindau, A. Möslang, Mater. Sci. Eng. A 527 (2010) 3602.

[48] C.C. Eiselt, M. Klimenkov, R. Lindau, A. Möslang, J. Nucl. Mater. 386-388 (2009) 525.

[49] L. Barnard, G.R. Odette, I. Szlufarska, D. Morgan, Acta Mater. 60 (2012) 935.

[50] C.A. Williams, P. Unifantowicz, N. Baluc, G.D.W. Smith, E.A. Marquis, Acta Mater. 61 (2013) 2219.

[51] C.A. Williams, E.A. Marquis, A. Cerezo, G.D.W. Smith, J. Nucl. Mater. 400 (2010) 37.

[52] Y. Ashkenazy, N.Q. Vo, D. Schwen, R.S. Averback, P. Bellon, Acta Mater. 60 (2012) 984.

[53] S. Odunuga, Y. Li, P. Krasnochtchekov, P. Bellon, R. Averback, Phys. Rev. Lett. 95 (2005) 045901.

[54] N.Q. Vo, S. Odunuga, P. Bellon, R.S. Averback, Acta Mater. 57 (2009) 3012.

[55] S.N. Arshad, T.G. Lach, M. Pouryazdan, H. Hahn, P. Bellon, S.J. Dillon, R.S. Averback, Scr. Mater. 68 (2013) 215.

[56] T. Klassen, U. Herr, R.S. Averback, Acta Mater. 45 (1997) 2921.

[57] R.B. Schwarz, Mater. Sci. Forum 269-272 (1998) 665.

[58] R.W. Cahn, P. Haasen, eds., Physical Metallurgy, North-holland, 1996.

[59] D. Holec, G. Ressel, Unpublished Research, 2012.

[60] E. Teatum, K.A. Gschneidner, J. Waber, Compilation of Calculated Data Useful in Predicting Metallurgical Behavior of the Elements in Binary Alloy Systems, Los Alamos, N.M.: Los Alamos Scientific Laboratory of the University of California, 1960.

[61] R. Tucker, A. Laskar, R. Thomson, J. Appl. Phys. 34 (1963) 445.

[62] J.G. Lee, Computational Materials Science, CRC Press Taylor & Francis Group, 2012.

[63] A. Kelly, R.B. Nicholson, Prog. Mater. Sci. 10 (1963) 151.

[64] M.J. Alinger, S.C. Glade, B.D. Wirth, G.R. Odette, T. Toyama, Y. Nagai, M. Hasegawa, Mater. Sci. Eng. A 518 (2009) 150.

[65] M.J. Alinger, G.R. Odette, D.T. Hoelzer, Acta Mater. 57 (2009) 392.

[66] E.V. Pereloma, I.B. Timokhina, J.J. Jonas, M.K. Miller, Acta Mater. 54 (2006) 4539.

[67] S. Ukai, T. Nishida, H. Okada, T. Okuda, M. Fujiwara, K. Asabe, J. Nucl. Sci. Technol. 34 (1997) 256.

[68] S. Nomura, T. Okuda, S. Shikakura, M. Fujiwara, K. Asabe, in:, A.H. Clauer, J.J. DeBarbadillo (Eds.), Solid State Powder Process., Warrendale, Pa: Minerals, Metals & Materials Society, Indianapolis, 1989, pp. 203–211.

[69] C. A. Williams, G.D.W. Smith, E. A. Marquis, Scr. Mater. 67 (2012) 108.

[70] D. Murali, B.K. Panigrahi, M.C. Valsakumar, S. Chandra, C.S. Sundar, B. Raj, J. Nucl. Mater. 403 (2010) 113.

[71] D. Murali, B.K. Panigrahi, M.C. Valsakumar, C.S. Sundar, J. Nucl. Mater. 419 (2011) 208.

[72] I.M. Lifshitz, V.V. Slyozov, J. Phys. Chem. Solids 19 (1961) 35.

[73] C. Wagner, Zeitschrift Für Elektrochemie 65 (1961) 581.

[74] D.. Larson, P.. Maziasz, I.-S. Kim, K. Miyahara, Scr. Mater. 44 (2001) 359.

[75] Y. Uchida, N. Ohnuki, N. Hashimoto, T. Suda, T. Nagai, T. Shibayama, K. Hamada, S. Akasaka, S. Yamashita, S. Ohstuka, T. Yoshitake, Mater.Res.Soc.Symp.Proc. 981 (2007) 107.

[76] G. Roberts, G. Kraus, R. Kennedy, Tool Steels, 5th ed., ASM International, 1998.

[77] Datenblatt - Kaltarbeitsstahl K890, Böhler Edelstahl GmbH & Co KG, 2010.

[78] Datenblatt - Schnellarbeitsstahl S790, Böhler Edelstahl GmbH & Co KG, 2005.

[79] H. Danninger, C. Harold, F. Rouzbahani, H. Ponemayr, M. Daxelmüller, F. Simancik, K. Izdinsky, Int. J. Powder Metall. 45 (2009) 27.

[80] M.P. Moody, L.T. Stephenson, A. V Ceguerra, S.P. Ringer, Microsc. Res. Tech. 71 (2008) 542.

[81] H. Leitner, H. Clemens, J. Akre, F. Danoix, P. Staron, Int. J. Mater. Res. 98 (2007) 11.

[82] O.C. Hellman, J.B. du Rivage, D.N. Seidman, Ultramicroscopy 95 (2003) 199.

[83] O.C. Hellman, J.A. Vandenbroucke, D. Isheim, D.N. Seidman, Microsc. Microanal. 6 (2000) 437.

[84] R.P. Kolli, D.N. Seidman, Microsc Microanal 13 (2007) 272.

[85] W. Lefebvre, F. Danoix, G. Da Costa, F. De Geuser, H. Hallem, A. Deschamps, M. Dumont, Surf Interface Anal 39 (2007) 206.

[86] D. Vaumousse, A. Cerezo, P.J. Warren, Ultramicroscopy 95 (2003) 215.

[87] L.T. Stephenson, M.P. Moody, P. V. Liddicoat, S.P. Ringer, Microsc. Microanal. 13 (2007) 448.

[88] C. A Williams, D. Haley, E. A Marquis, G.D.W. Smith, M.P. Moody, Ultramicroscopy (2012) 1.

[89] O.C. Hellman, J.A. Vandenbroucke, D. Isheim, D.N. Seidman, Microsc. Microanal. (2000) 437.

[90] J. Akré, F. Danoix, H. Leitner, P. Auger, Ultramicroscopy 109 (2009) 518.

[91] M. Alinger, G.R. Odette, D.T. Hoelzer, J. Nucl. Mater. 329-333 (2004) 382.

[92] H. Sakasegawa, F. Legendre, L. Boulanger, M. Brocq, L. Chaffron, T. Cozzika, J. Malaplate, J. Henry, Y. de Carlan, J. Nucl. Mater. 417 (2011) 229.

[93] H. Sakasegawa, M. Tamura, S. Ohtsuka, S. Ukai, H. Tanigawa, a Kohyama, M. Fujiwara, J. Alloys Compd. 452 (2008) 2.

[94] C. Cayron, E. Rath, I. Chu, S. Launois, J. Nucl. Mater. 335 (2004) 83.

[95] G. Faninger, U. Hartmann, Physikalische Grundlagen Der Quantitativen Röntgenographischen Phasenanalyse (RPA), 1972.

[96] M. Nöhrer, Rückumgewandelter Austenit in Maraging Stählen, Montanuniversität Leoben, 2009.

Publication A:

The evolution of Y distribution during the processing route of mechanically alloyed iron studied by means of atom probe tomography

G. Ressel, S. Primig, H. Leitner

International Journal of Materials Research 104 (2013) 1088-1095.

G. Ressel[a], S. Primig[a,b], H. Leitner[a]
[a] Department of Physical Metallurgy and Materials Testing, Montanuniversität Leoben, Leoben, Austria
[b] Christian Doppler Laboratory for Early Stages of Precipitation, Montanuniversität Leoben, Leoben, Austria

The evolution of Y distribution during the processing route of mechanically alloyed iron studied by means of atom probe tomography

Oxide dispersion strengthening of steels has become quite popular during the last few years. Especially because of their thermal stability, Y–O clusters can improve high temperature properties such as strength, hardness and creep strength. Oxide dispersion strengthened steel is a promising candidate for applications mainly in fast breeder reactors. In order to establish a better understanding of the strengthening mechanism, this study focuses on an evolution of the Y distribution in mechanically alloyed iron during the process route, employing atom probe tomography. After mechanical alloying, Y seems to be distributed in extremely fine clusters and partly dissolved in the matrix. Enrichment of alloying elements in the Y–O clusters in the mechanically alloyed state is evidence for diffusion processes taking place during mechanical alloying. During hot isostatic pressing at elevated temperatures, dissolved Y atoms accumulate and build distinct clusters. These clusters stay stable even after annealing at 600 °C for 8 hours.

Keywords: Mechanical alloying; Iron; Yttria; Particle evolution; Atom probe tomography

1. Introduction

Mechanical alloying is a well-established technique for the synthesis of a variety of equilibrium and non-equilibrium alloy phases, also for nanostructered materials and especially for oxide dispersion strengthed (ODS) steels [1]. In the past, a lot of investigations have focused on ODS-iron based alloys such as PM-2000 or MA 957 [2–4]. These materials were mechanically alloyed with yttria and 5 nm Y–O clusters were found finely distributed in the material after hot isostatic pressing (hipping). These steels show much better thermal properties than steels without the Y–O clusters. Yttria is preferred because of its high thermal stability [4, 5]. This can be related to its extremely low formation energy (about $-1\,905.6 \pm 2.3$ kJ mol^{-1} [6]). Such chromium and titanium alloyed ferritic steels are dedicated for use as fuel claddings in fast breeder reactors because of their high creep resistance and their excellent microstructural stability in irradiated environments [7]. In contrast, common steels are strengthened by carbides or nitrides. These steels lose their hardness and strength at about 600 °C because of coarsening and dissolution of these particles. The free standard enthalpy of formation of, for example, $Cr_{23}C_6$ is -11.6 kJ mol^{-1} and for Cr_7C_3 it is -15.898 kJ mol^{-1} [8]. Also other carbides have similar free standard enthalpies of formation, which are 2 orders of magnitude less negative than that of yttria. Furthermore, Ukai et al. [9] found out that a simple addition of titanium to ODS steels leads to a further improvement of the high temperature properties. Ti enhances stability of the clusters and ensures that the clusters remain extremely fine [10]. By formation of $Y_xM_yO_z$ oxides with the minor alloying element M (e. g. Ti), the enthalpy of formation should decrease compared to common yttria. The lower the diffusivity of the alloying element, the higher is the stability of the oxide. The microstructure after hipping has been investigated in detail using transmission electron microscopy (TEM) [2, 11, 12] and atom probe tomography (APT) [13–15]. Recently, Williams et al. [16, 17] studied the Y–Ti–O particle evolution during processing of a 14-YWT (Fe-14 Cr-2 W-0.3 Ti) steel. Nevertheless, there is still a lack of information on the Y distribution directly after mechanically alloying and the evolution of these clusters through the processing route. In order to get a complete overview of cluster formation in ODS steels, this paper focuses on Y–Mn–Al–O particels in an Fe–Y model alloy. This could also give a better view of what happens with the clusters during processing. In order to understand the mechanism of finely distributed Y, this paper elucidates the evolution of the microstructure in pure iron during the processing route and compares the clustering behavior after mechanical alloying, hipping and further annealing by means of APT. One important tool for analyzing the clustering behavior is the radial distribution function (RDF), which has already been applied in several previous publications [18, 19].

2. Experimental procedure

Prior to hot isostatic pressing, the powder was mechanically alloyed for 48 h using a certony^{TM} attritor. For mechanical alloying, iron powder was produced by water atomization and was mixed with 0.5 wt.% yttria submicron powder with a d_{90} of 1.16 µm and a purity of 99.9 %. The chemical composition of the powder before mechanical alloying was measured using X-ray fluorescence spectroscopy (XRF). The O content was determined by means of the inert gas fusion method. The results for the mixed original powders are listed in Table 1. For milling, a speed of 600 rpm was applied and steel balls with a ball to powder ratio of 10:1 were

Table 1. Chemical composition of the powders prior to milling in wt.% and at.%.

	Iron powder						yttria
	Fe	Cr	Cu	Mn	Ni	O	Y_2O_3
wt.%	bal.	0.043	0.030	0.115	0.028	0.025	0.502
at.%	bal.	0.049	0.028	0.124	0.028	0.091	0.132

Table 2. APT overall composition of the different states in at.%.

state	Fe	Cr	W	Mn	Ni	Al	Si	V	Co	Cu	C	Y	O
MA	bal	0.32	0.09	0.16	0.23	0.05	0.04	0.006	0.01	0.04	0.17	0.14	0.69
H	bal	0.03	0.04	0.03	0.09	0.02	0.03	0.003	0.02	0.02	0.03	0.06	0.31
HA	bal	0.02	0.04	0.03	0.13	0.03	0.03	0.002	0.01	0.03	0.06	0.08	0.24

used. The entire mechanical alloying process was performed under Ar gas atmosphere to reduce oxidation and avoid incorporation of oxygen into the steel powder.

After mechanical alloying, the milled powder was hipped at 1 100 °C and a pressure of 100 MPa for 3 h. The following heat treatment was conducted in a Bähr™ DIL805 A dilatometer. The cylindrical specimen, which was 5 mm in diameter and 10 mm in length, was annealed at 600 °C for 8 hours with a heating and cooling rate of 2 K s^{-1}. The heat treatment was carried out in vacuum.

Atom probe investigations were performed on the as-milled powder, on the as hipped specimen and in the annealed state. For preparation of atom probe tips, small rods with a cross-section of 0.3×0.3 mm^2 and a length of 10 mm were cut out of the hipped and annealed bulk material. Then, the tips were prepared using the standard electrochemical polishing method [20]. The investigations were performed using a LEAP™ 3000X HR from Cameca™ (formerly Imago™) in voltage mode, and a 3DAP from Oxford nanoScience™ in voltage mode. Measurements were carried out under ultra-high vacuum conditions and at a temperature of 60 K. A pulse fraction of 15 % and 20 % to the standing voltage was used. It was verified that there was no influence on the overall condition of the specimens. The atom probe measurements were evaluated with the Cameca ™ software IVAS 3.4.3.

For the tip preparation from the mechanical alloyed powder particles, an FEI™ Versa3D™ Dual Beam focused ion beam (FIB) was used. Several publications deal with the method of how to prepare atom probe tips from a powder particle [21, 22]. The tips analyzed in the present investigation were prepared according to the literature, with the difference that the powder particles were mounted on an SEM stub with silver adhesive. At a convenient position of the powder particle a wedge was lifted out and its slices were placed onto several positions of a microtip coupon.

3. Results

3.1. APT measurements

Mechanical alloying was conducted in order to produce a very fine distribution of the yttria particles in the Fe matrix. To reveal the Y distribution, APT measurements were performed on samples prepared from mechanical alloyed powder particles (MA condition), on hipped specimens (H state) and on hiped and annealed (HA) samples. The overall compositions revealed by the APT measurements of the different states are listed in Table 2.

Compared with the as-received powders, minor concentrations of elements such as Al, Si, V, Co, Cu, C were incorporated during mechanical alloying. It should also be mentioned that the O content increased in the very fine iron powder during mechanical alloying. Due to its large surface area, Fe powder is chemically extremely active.

Figure 1 shows 3D atom map projections of the elements Y, O, Al and Mn in a powder particle after mechanical alloying for 48 h. These elements have been chosen for this

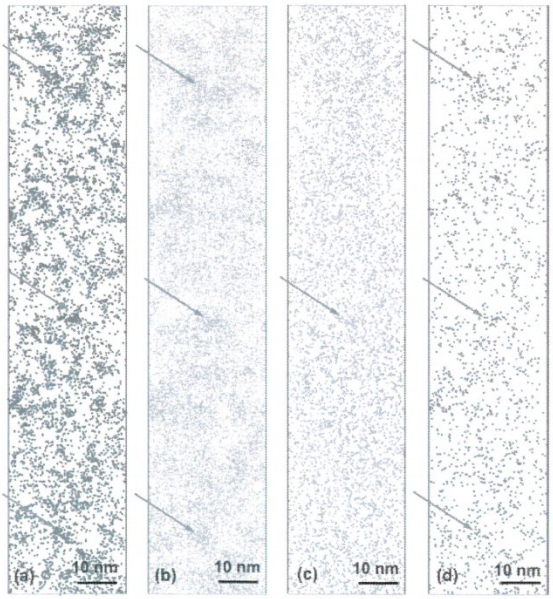

Fig. 1. 3D atom map projections of the mechanically alloyed powder. (a) Y; (b) O; (c) Al; (d) Mn. The arrows mark clusters of Y and O as well as minor enrichments of Al.

analysis because they are expected to show clustering in all material conditions studied. Indeed, the visual inspection of the 3D atom maps reveals that Y seems to have a tendency for clustering (Fig. 1a). Some of these clusters are marked with arrows in the atom maps. Nevertheless, Y seems also to be partly dissolved in the matrix. Additionally, O appears to be partly dissolved in the Fe matrix, moreover to a higher extent than Y. Figure 1b shows that O is also accumulating at the positions of the Y clusters.

The atom distribution of Al and Mn is depicted in Fig. 1c and d. The Al incorporated during mechanical alloying seems to be enriched in the Y clusters, marked with arrows in Fig. 1c. On the other hand Mn shows a mostly homogeneous distribution in the Fe matrix (Fig. 1d), except for one minor enrichment.

Hipping consolidates the powder into a completely dense bulk material. Because of the relatively high temperature and pressure, the distribution of the investigated elements might begin to change. Hipping is performed at temperatures where an austenitic matrix is present. APT measurements were performed to check the cluster evolution in an austenitic matrix. Figure 2 shows the 3D atom maps of Y, O, Al and Mn in the as-hipped state. Again, local enrichments of Y and O are obvious. Compared to Fig. 1, it seems that the atoms have already formed more distinct clusters under this condition. Figure 2c and d shows the atomic distributions of Al and Mn. In case of Al, the 3D atom map gives the impression that its clustering is slightly more pronounced than after mechanical alloying. Considering the Mn distribution, the 3D atom map in Fig. 2d suggests also that Mn is no longer homogeneously distributed. This means the Mn atoms accumulate during hipping at elevated temperature and pressure. Again some clusters enriched in Y, O, Al and Mn are marked with arrows in Fig. 2.

To check the thermal stability of the clusters at a typical application temperature where a ferritic matrix is present, the hipped material was annealed at 600 °C for 8 h. The corresponding distributions of the Y, O, Al and Mn are shown in Fig. 3. There are again clusters containing Y, O, Al and Mn, but visually no difference can be seen between the material in the conditions H and HA.

3.2. Comparison of radial distribution functions (*RDF*s) of Y, O and Mn atoms

To describe the clustering more precisely, *RDF*s were calculated. Compared with X^2-tests, *RDF*s offer spatial information which is more suitable for describing the evolution of the clusters. The *RDF* is defined as the mean concentration distribution of a component around a selected solute species. The surrounding of each solute center atom is divided into shells with a distance r, where the concentration of the component is calculated. Furthermore, these concentrations are normalized to the average bulk composition of the component. A detailed description of the theoretical background of *RDF*s can be found in [19]. For the calculations Y, O, Mn and Al are selected as solute center atom elements. The normalized bulk concentration is illustrated in Figs. 4–6 as a dashed line, which describes the perfect random distribution. A concentration value above or below the dashed line represents clustering or depletion, respectively. Each state is normalized to its bulk concentration. Figure 4 shows the *RDF*s of Y for all conditions investigated. In all three states, a rise in the *RDF* value with decreasing r is visible. Consequently, in all three conditions

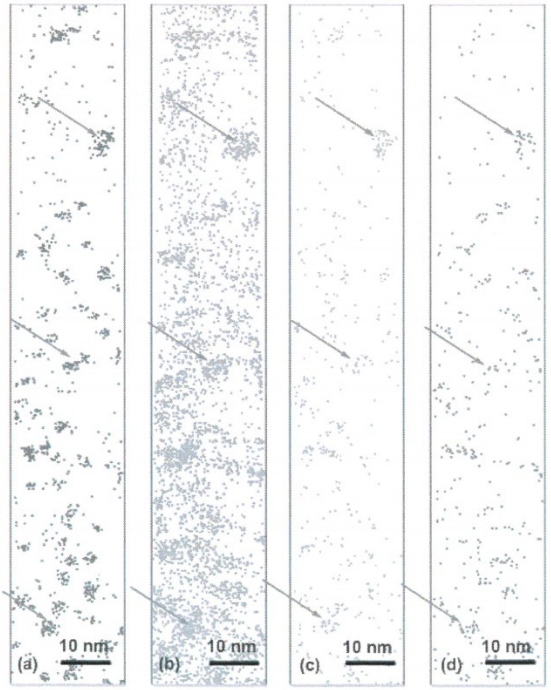

Fig. 2. 3D atom map projections after hipping. (a) Y; (b) O; (c) Al; (d) Mn. The arrows mark clusters of Y, O, Al and Mn.

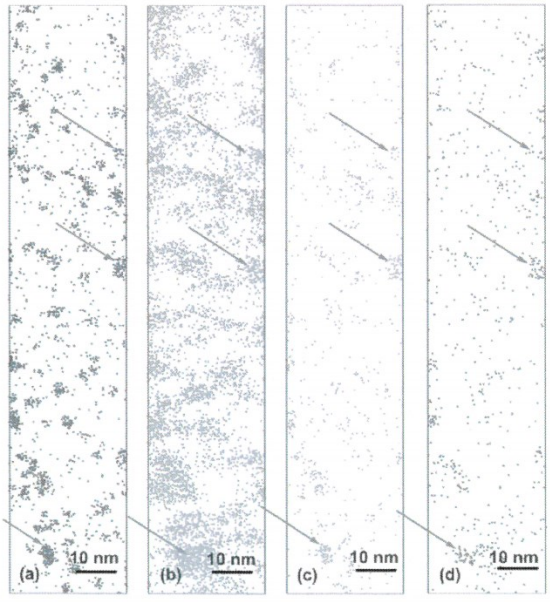

Fig. 3. 3D atom map projections after hiping and annealing at 600 °C for 8 h. (a) Y; (b) O; (c) Al; (d) Mn. The arrows mark clusters of Y, O, Al and Mn.

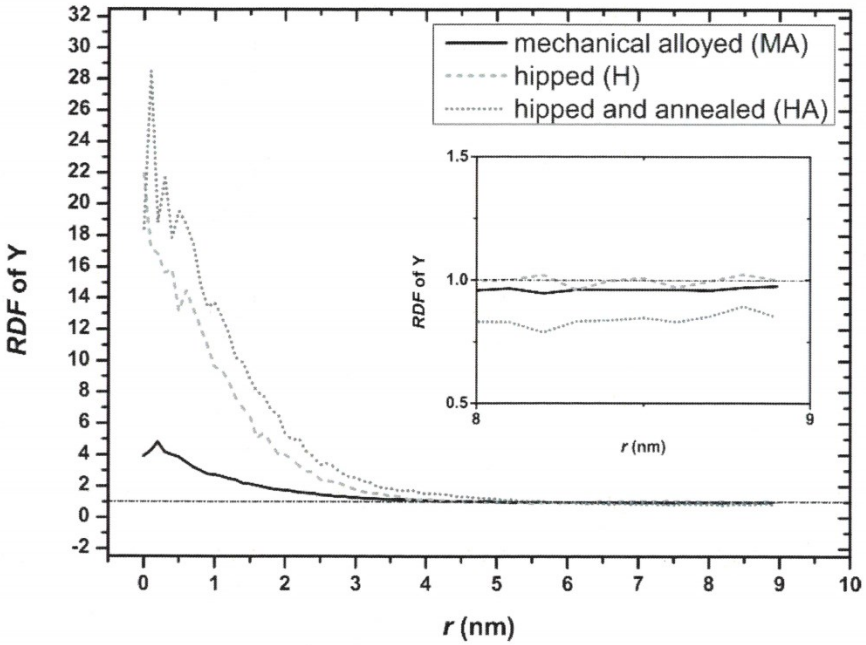

Fig. 4. Comparison of the RDFs of the MA, H and HA conditions for Y, showing the evolution of Y distribution through the processing route. The inset diagram illustrates the RDF values between 8 and 9 nm in detail.

a clustering of Y is verified. Furthermore, the curves reveal that in the mechanically alloyed state the *RDF* value at smaller *r* is significantly lower than under the other conditions. Accordingly, the *RDF* value in the mechanically alloyed specimen decreases less with increasing distance than in the other two. These two facts indicate a lower degree of clustering and a higher degree of distribution of Y in the MA condition than in the H and HA states. Therefore, a formation of more distinct Y clusters during the processing route is evidenced. Examination of the inset in Fig. 4 shows that the HA condition especially has a lower *RDF* value than the MA condition at high *r* values, indicating a higher value of dissolved Y in the Fe matrix after mechanical alloying and a depletion of Y after annealing. At a distance between 8 and 9 nm, the *RDF* value of the H state is higher than the *RDF* value of the MA condition, but is supposed to decrease to values below the MA value at higher *r* values. A comparison of the H state with the HA condition shows that the HA curve reaches higher *RDF* values than the H curve, i.e., further annealing after hiping has the effect of a somewhat stronger demixing of Y.

Figure 5 compares the radial distribution functions of O under the different conditions. Again, clustering in all three states can be seen due to the increasing *RDF* value at lower *r* values. The *RDF* value and its decrease with *r* of the mechanical alloyed condition is lowest at small *r* values. This indicates that the mechanically alloyed condition is closer to the perfect random distribution and that it has also the lowest degree of clustering. The *RDF* values increase from the MA state to the H and HA condition. Therefore, hipping and further annealing causes a stronger clustering of the O atoms and consequently a more pronounced depletion of O in the matrix. In principle, the characteristics of the *RDF* curves are akin to those in Fig. 4, but the values of all curves are significantly smaller, indicating a lower degree of clustering of O compared to Y. Considering the O content in the matrix of all three conditions (see inset in Fig. 5), the highest value of dissolved O is detected for the mechanically alloyed condition. The *RDF* values, especially the ones of the H and HA conditions, are expected to decrease further at higher distances.

Figure 6 shows the Mn distribution as *RDF*s at different conditions. According to the atom maps in Fig. 1d Mn is supposedly dissolved in the matrix after mechanical alloying. However, the *RDF* of this condition shows a slightly different picture here. In this condition, a faint clustering is present, because of a small increase in the *RDF* value at small *r* values. Therefore, besides Al (Fig. 1c), Mn is accumulating at the Y and O cluster sites directly after mechanical alloying. An analysis of the different *RDF* curves through the process route show that Mn diffuses, similarly to Y, into the clusters during hipping and supports the cluster formation. The curves of the H and HA condition are akin, but a somewhat stronger clustering of Mn after annealing is detected.

3.2.1. Evolution of the cluster size and matrix composition

In order to determine the cluster size, a cluster search algorithm based on the double maximum separation method was used [23, 24]. This algorithm allows identification of each Y-cluster and provides information about the chemical composition as well as the extent of the clusters. Evaluation

of all three samples indicated that the same cluster search parameters can be used. They were selected according to the procedure from Stephenson et al. [23] and Williams et al. [25]. The separation, the surrounding and the erosion distances were set to 0.75 nm, 0.7 nm and 0.7 nm, respectively. To prevent randomly distributed atoms being identified as clusters, a minimum cluster size of 12 atoms was used. Table 3 shows the calculated results of the cluster

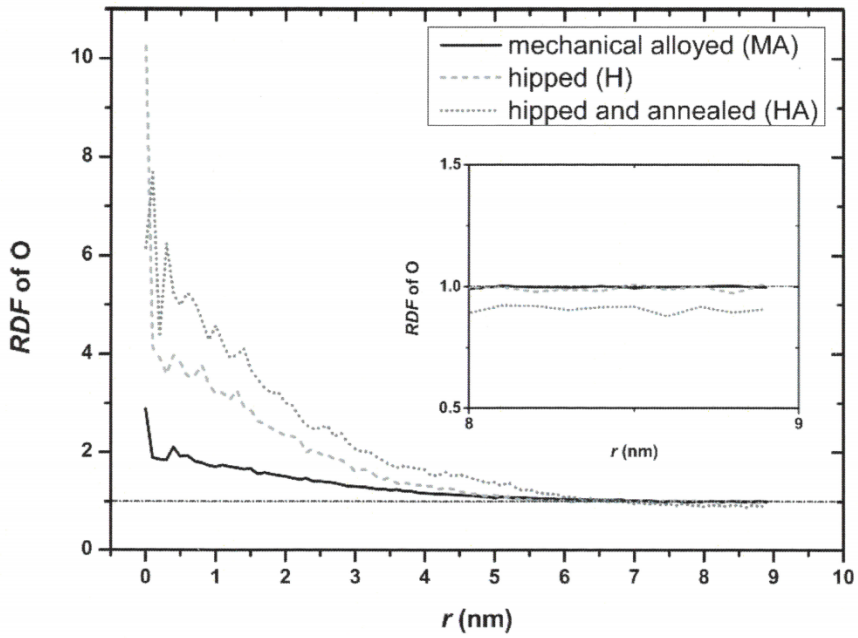

Fig. 5. Comparison of the RDFs of the MA, H and HA conditions for O, showing the evolution of O distribution through the processing route. The inset diagram illustrates the RDF values between 8 and 9 nm in detail.

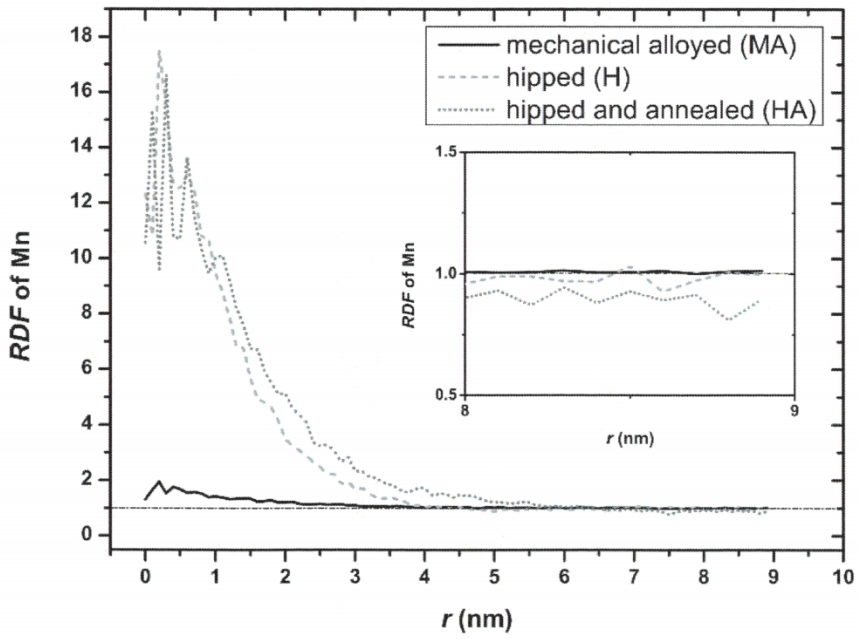

Fig. 6. Comparison of the RDFs of the MA, H and HA conditions for Mn, showing the evolution of Mn distribution through the processing route. The inset diagram illustrates the RDF values between 8 and 9 nm in detail.

Table 3. Comparison of the mean cluster size of the hipped condition and the hipped and annealed condition, describing the stability of the Y–O clusters as well as the evolution of the matrix and cluster composition of Y, O, Al and Mn.

		matrix composition (at.%)				cluster composition (at.%)				
	R_g (nm)	Y	O	Al	Mn	Y	O	Al	Mn	Y:O
mechanically alloyed (MA)	0.65 ± 0.25	0.13	0.48	0.05	0.15	14.68	23.18	0.17	0.19	0.63
hipped (H)	0.58 ± 0.18	0.03	0.15	0.017	0.02	17.23	11.36	0.36	0.32	1.52
hipped and annealed (HA)	0.67 ± 0.32	0.03	0.13	0.024	0.03	14.71	11.33	0.30	0.29	1.30

search algorithm and compares the mean radius of gyration (R_g) of the different conditions. The radius of gyration enables a comparison of the size of differently shaped clusters. In the MA state, the particle analysis reveals an R_g of 0.65 nm, in the H state of 0.58 nm and in the HA of 0.67 nm. Hence, through the processing route, the difference between the clusters is negligibly low and within the standard deviation of the particle size.

The matrix composition is determined by excluding the atoms which belong to the clusters by the cluster search algorithm of the overall dataset. The concentrations of the individual elements are listed in Table 3, where Fe is the balance. The cluster search algorithm reveals a Y content of 0.13 at.% dissolved in the matrix after mechanical alloying, whereas the hipped and annealed specimens exhibit a much lower dissolved Y concentration of 0.03 at.%. Considering the O content dissolved in the Fe matrix, particle analysis calculated a much higher amount of O dissolved in the iron matrix of about 0.48 at.%, while the hipped and annealed specimens have an O concentration of 0.15 at.% and 0.13 at.%, respectively. The alloying elements Al and Mn show the same tendency. The matrix after mechanical alloying exhibits the highest content of Al and Mn with 0.05 at.% and 0.15 at.%, respectively. Again, a depletion of Al and Mn during hipping and annealing in the matrix could be detected. Considering the cluster composition it can be stated that the O content is also decreasing during hipping and subsequent annealing. In contrast to that, Al and Mn enrich at the clusters during the process. Again this analysis suggests that Al and Mn are already enriched in the MA state. The Y : O ratio differs from the MA state to the H and HA conditions. After mechanical alloying, the Y : O ratio is about 0.63 in contrast to the Y : O ratio after hipping and annealing, which are ~1.52 and ~1.3, respectively.

4. Discussion

Atom probe measurements at three different stages during the processing route of mechanically alloyed iron, i. e., after mechanical alloying, after hipping and after annealing, were performed. As mentioned in the introduction, Williams et al. [16, 17] studied the cluster evolution of a 14-YWT (Fe-14 Cr-2 W-0.3 Ti) steel. However, the present investigation focuses on Y–Mn–Al–O particels in an Fe–Y model alloy. The clustering behavior of the individual elements was analyzed in all three conditions. Additionally, the clustering was supported by calculating *RDF*s. The evolution of the cluster size as well as the matrix composition was determined. These investigations should clarify the evolution of the particles during standard processing of ODS-steels, as well as explain what is happening during mechanical alloying. Until now, there has still been a lack of information in literature concerning atom probe investigations of pure iron particles mechanically alloyed with yttria. Miller et al. detected a different Y/O ratio (~1.2) in the Y–O nanoclusters of ferritic steels from atom probe measurements of hipped specimens. He concluded that these clusters could not be remnants of the original yttria powder [15]. In the model alloy of the present investigation a Y/O ratio between 1.5 and 1.3 after hipping and annealing was detected. In contrast to that in the MA state a Y/O ratio of 0.63 was detected, indicating an earlier stage of precipitation. This ratio matches the ratio of the original yttria (0.67) powder well. Other publications claimed that a decomposition of yttria during mechanical alloying took place [26–28]. However, owing to the relatively small yttria content in these studies, X-ray diffraction peaks were difficult to measure. Furthermore, they could disappear because of amorphization. Consequently, no clear evidence of what is happening during mechanical alloying was given until now.

Atom probe measurements of the as-mechanically alloyed specimen conducted in this study reveal a clustered arrangement of the Y atoms. Furthermore, partial dissolution can be assumed from the visual inspection. Due to their high affinity for each other, Y and O are accumulating at the same positions. The fact that Al enrichments, incorporated during milling, are detected at the Y and O clusters after mechanical alloying and before hipping suggests that these atoms are dissolved in the Fe matrix and rearranged in clusters during mechanical alloying. It is assumed that Al enriches due to its high affinity to O. Mn is mainly dissolved in the matrix, but a minor Mn enrichment is also detected by *RDF* and cluster search algorithm before hipping. Consequently, these Y and O clusters are not just remnants of the as-received Y_2O_3 powder in nanometer scale, which is evidence of the dissolution of Y and O and the reordering of Y, O, Al and Mn at favorable sites such as vacancies or dislocations. The reason that Al shows a stronger clustering tendency than Mn might be due to the higher diffusivity of Al compared to Mn. According to [29, 30] the diffusivity of Al ($D = 2.84204 \times 10^{-16}$ m^2 s^{-1}) in ferromagnetic ferritic Fe is about twice the diffusivity of Mn ($D = 1.23673 \times 10^{-16}$ m^2 s^{-1}) at a temperature of 737 °C. At lower temperatures, this difference could even increase because of the lower activation energy of diffusion of Al. Referring to *RDF* calculations, a tendency to clustering can be indicated for Y, O and Mn in the mechanically alloyed state. However, the gradient of the decreasing *RDF* value of the mechanically alloyed condition is the lowest in all cases. This fact indicates a more homogeneous distribution of Y, O and Mn in the MA condition and gives a hint that they have a higher content dissolved in the matrix. Calculation of the

cluster size in the MA state reveals a radius smaller than 1 nm, which agrees with the results of the study of Williams et al. [16]. However, evaluation of the matrix composition reveals a high Y content of about 0.13 at.% dissolved in the Fe matrix. Kubaschewski [31] calculated the solubility at thermodynamic eqilibrium to be much smaller than 0.6 wt.% at 1350 °C. This is also fulfilled in the present investigation, but at room temperature the equilibrium solubility is even smaller. Additionally, the dissolved O content of the MA state in the Fe matrix is about 0.48 at.%, although the O solubility in bcc Fe which was calculated from Swisher and Turkdogan [32] lies between 2 and 3 ppm at 881 °C at thermodynamic equilibrium. However, the amount of dissolved Y and O in the mechanical alloyed condition is high compared to literature. Due to this fact, it can be assumed that the Y and O atoms are partly dissolved after mechanical alloying and that this dissolved content is unusually high, metastable and far from the thermodynamic equilibrium. We propose that Y and O dissolve in the iron matrix during mechanical alloying, but are also arranging at convenient sites, e. g. lattice defects such as dislocations or vacancies. It has been shown, that vacancies play an important role at the early stages of precipitation in Al–Cu-based alloys [33]. The extremely high defect density could be a further reason for dissolution of Y and O, acting as an accelerator for diffusivity.

At the high temperatures and pressures which prevail during hipping, the dissolved Y, O and Mn atoms can diffuse over short distances in order to enrich at the clusters. Visual inspection of the atom maps is evidence of this. However, most of the defects annihilate during hipping. Consequently, the diffusion accelerator is missing, hence, coarsening of the clusters is not so pronounced and the thermal stability of the Y–O nanoclusters is extremely high. The difference in the Y cluster size at the H state compared to the MA condition is negligibly low and within the standard deviation. This is contrary to Williams et al. [16], who found a sharp increase in the cluster size during consolidation. The matrix composition of the H condition, which is definitely closer to the vicinity of the thermodynamic equilibrium, exhibits a content of about 0.03 at.% Y dissolved in the matrix. This is much lower compared to the MA condition. The dissolved content of O after hipping is calculated as 0.15 at.%, also much lower as in the MA condition. The inset diagrams of the *RDF*s in Figs. 4–6 showed in detail that these elements are depleted during the process route. Consequently, it can be stated that the mechanically alloyed Fe matrix exhibits, besides Y, an extended metastable solubility of O. In addition, the alloying elements Al and Mn have a lower concentration in the matrix of the H state than in the MA condition. Like Y and O, Al and Mn diffuse into the clusters, causing depletion in the matrix after hipping. Again, a comparison of the *RDF*s confirms this fact. After hipping a much stronger degree of clustering is detected. The cluster search algorithm also supports this conclusion showing an enrichment of Al and Mn. This agrees with Williams et al. [16, 34], who also found Mn enrichments in clusters in a hipped ODS-Eurofer steel and a decrease in the cluster-forming elements O, Y and Ti in the matrix during processing of a 14-YWT steel. A decrease in the concentration at the overall APT datasets of elements such as Cr, W, Ni, Mn, Al, C and O can be explained by the formation of larger oxides and carbides outside the range of the APT measurements. Hipping, which is for consolidation of the powder to zero porosity bulk material at high temperatures and pressures, accelerates the driving force of Y–O–Al–Mn clustering. These dissolved atoms diffuse to form more distinct clusters, which increases the concentration at lower r value in the *RDF* diagrams.

By visual inspection, no difference can be found between the HA and the H condition. Also in the matrix composition no distinct change can be detected, except a minor depletion of all alloying elements. If the *RDF*s of the H and HA conditions are compared they are all alike, but annealing also has the effect that a somewhat stronger clustering of all elements can be detected. In this state the difference in cluster size compared with the other conditions is very low and within the standard deviation. A minor coarsening, if any, can be assumed. This indicates that annealing at 600 °C affects the particle growth only negligibly. Consequently, this provides evidence for the exceptionally high stability of the clusters at this temperature in ferritic phase. The fact that these clusters were exposed to higher temperature during previous consolidation could be a reason for their high stability. Several papers deal with the enhanced stability of the Y–O clusters [5, 14], which is also shown in this study by the comparison of the mean cluster size of the different conditions. As already mentioned, vacancies and other crystal defects annihilate during hipping. Consequently, the diffusion of Y, O, Al and Mn in the matrix is much lower, which also might explain the high stability of the clusters.

5. Conclusions

The evolution of the Y distribution during the processing route of mechanically alloyed iron was analyzed by means of atom probe tomography. The results lead to following conclusions:

1. Directly after mechanical alloying Y, O are in a clustered arrangement.
2. An extended solubility of Y and O in the iron matrix was measured after mechanical alloying.
3. Al and Mn enrichments in the clusters indicate diffusion processes during mechanical alloying, e. g. dissolution and reordering of Y,O, Al and Mn.
4. It is assumed that Y, O, Al and Mn are dissolving during mechanical alloying, but are arranging at convenient positions, e. g. lattice defects such as dislocations or vancancies.
5. It is supposed that defects act as a diffusion accelerator, which enhances the solubility of Y and O.
6. Hipping causes diffusion of dissolved Y, O, Al and Mn atoms to form distinct particles and depletion of these atoms in the matrix.
7. Due to annihilation of the defects during hipping, it is expected that these diffusion accelerators are missing afterwards, which enhances the stability of the particles.
8. Further annealing at 600 °C for 8 h has minor effects on the particle growth, which proves the exceptionally high stability of these particles.

The authors want to thank Dr. J. Zbiral for supporting at mechanical alloying experiments and Dr. F. Mendez-Martin for supporting with the FIB preparation.

References

[1] C. Suryanarayana: Prog. Mater. Sci. 46 (2001) 1. DOI:10.1016/S0079-6425(99)00010-9
[2] M. Klimiankou, R. Lindau, A. Möslang, J. Schröder: Powder Metall. 48 (2005) 277. DOI:10.1179/174329005X64171
[3] A. Czyrska-Filemonowicz, B. Dubiel: J. Mater. Process. Technol. 64 (1997) 53. DOI:10.1016/S0924-0136(96)02553-8
[4] P. Krautwasser, A. Czyrska-Filemonowicz, M. Widera, F. Carsughi: Mater. Sci. Eng. A 177 (1993) 199. DOI:10.1016/0921-5093(94)90491-X
[5] S.Y. Zhong, J. Ribis, V. Klosek, Y. de Carlan, N. Lochet, V. Ji, M.H. Mathon: J. Nucl. Mater. 428 (2012) 154–59. DOI:10.1016/j.jnucmat.2011.12.028
[6] E.J. Huber, L. Head, C.E. Holley: J. Phys. Chem. 61 (1957) 497. DOI:10.1021/j150550a027
[7] S. Ukai, T. Nishida, H. Okada, T. Okuda, M. Fujiwara, K. Asabe: J. Nucl. Sci. Technol. 34 (1997) 256. DOI:10.1080/18811248.1997.9733658
[8] J.O. Anderson: Calphad 11 (1986) 271. DOI:10.1016/0364-5916(87)90045-9
[9] S. Ukai, T. Nishida, T. Okuda, T. Yoshitake: J. Mater. Sci. Technol. 35 (1998) 294.
[10] Y. Uchida, N. Ohnuki, N. Hashimoto, T. Suda, T. Nagai, T. Shibayama, K. Hamada, S. Akasaka, S. Yamashita, S. Ohstuka, T. Yoshitake: Mater. Res. Soc. Symp. Proc. 981 (2007) 107.
[11] A. Hirata, T. Fujita, Y.R. Wen, J.H. Schneibel, C.T. Liu, M.W. Chen: Nat. Mater. 10 (2011) 922. DOI:10.1038/nmat2897
[12] M. Klimiankou, R. Lindau, A. Möslang: J. Cryst. Growth 249 (2003) 381. DOI:10.1016/S0022-0248(02)02134-6
[13] M.K. Miller, D.T. Hoelzer, E.A. Kenik, K.F. Russell: J. Nucl. Mater. 329–333 (2004) 338. DOI:10.1016/j.jnucmat.2004.04.085
[14] M.K. Miller, D. Hoelzer, E. Kenik, K. Russell: Intermetallics 13 (2005) 387. DOI:10.1016/j.intermet.2004.07.036
[15] M.K. Miller, E. Kenik, K. Russell, L. Heatherly, D. Hoelzer, P. Maziasz: Mater. Sci. Eng. A 353 (2003) 140. DOI:10.1016/S0921-5093(02)00680-9
[16] C.A. Williams, P. Unifantowicz, N. Baluc, G.D.W. Smith, E.A. Marquis: Acta Mater. 61 (2013) 2219. DOI:10.1016/j.actamat.2012.12.042
[17] C.A. Williams, P. Unifantowicz, Z. Oksiuta, N. Baluc, G.D.W. Smith, E.A. Marquis, in: Advanced Materials for Applications in Extreme Environments, P. Hosemann, E. Stergar, A.T. Nelson, C. Vieh, and S.A. Maloy (Eds.), Mater. Res. Soc. Symp. Proc. (2011) 15.
[18] A. Shariq, T. Al-Kassab, R. Kirchheim, R.B. Schwarz: Ultramicroscopy 107 (2007) 773. PMid:17433547; DOI:10.1016/j.ultramic.2007.02.030
[19] C. Sudbrack, R. Noebe, D. Seidman: Phys. Rev. B 73 (2006) 212101. DOI:10.1103/PhysRevB.73.212101
[20] M.K. Miller, A. Cerezo, M.G. Hetherington, G.D.W. Smith: Atom Probe Field Ion Microscopy. Oxford University Press, (1996).
[21] M.K. Miller, K.F. Russell: Ultramicroscopy 107 (2007) 761. DOI:10.1016/j.ultramic.2007.02.023
[22] M.K. Miller, K.F. Russell, G.B. Thompson: Ultramicroscopy 102 (2005) 287. DOI:10.1016/j.ultramic.2004.10.011
[23] L.T. Stephenson, M.P. Moody, P.V. Liddicoat, S.P. Ringer: Microsc. Microanal. 13 (2007) 448. PMid:18001511; DOI:10.1017/S1431927607070900
[24] A. Cerezo, L. Davin: Interface (2007) 184.
[25] C.A. Williams, D. Haley, E.A. Marquis, G.D.W. Smith, M.P. Moody: Ultramicroscopy (2013) article in press. DOI:10.1016/j.ultramic.2012.10.003
[26] T. Okuda, M. Fujiwara: J. Mater. Sci. Lett. 14 (1995) 1600. DOI:10.1007/BF00455428
[27] Y. Kimura, S. Suejima, H. Goto, S. Takaki: ISIJ Int. 40 (2000) 174. DOI:10.2355/isijinternational.40.Suppl_S174
[28] Y. Kimura, S. Takaki, S. Suejima, R. Uemor, H. Tamehiro: ISIJ Int. 39 (1999) 176. DOI:10.2355/isijinternational.39.176
[29] I.A. Akimova, V.M. Mironov, A.V. Pokyev: Fiz. Met. Metall. 56 (1983) 1225.
[30] K. Nohara, K.I. Hirano: Proc. Int. Conf. Sci. Tech. Iron&Steel 7 (1970) 11.
[31] K.A. Gschneider: Rare Earth Alloys, D. Van Nostrand company, Inc., Pinceton (1961).
[32] J.H. Swisher, E.T. Turkdogan: Trans. Metall Soc. Aime 239 (1967) 426.
[33] A. Somoza, M. Petkov, K. Lynn, A. Dupasquier: Phys. Rev. B 65 (2002) 094107. DOI:10.1103/PhysRevB.65.094107
[34] C. A Williams, E.A. Marquis, A. Cerezo, G.D.W. Smith: J. Nucl. Mater. 400 (2010) 37. DOI:10.1016/j.jnucmat.2010.02.007

(Received January 23, 2013; accepted June 4, 2013; online since July 25, 2013)

Bibliography

DOI 10.3139/146.110964
Int. J. Mater. Res. (formerly Z. Metallkd.)
104 (2013) 11; page 1088–1095

ISSN 1862-5282

Correspondence address

Dipl. Ing. Gerald Ressel
Department of Physical Metallurgy and Materials Testing
Montanuniversität Leoben
Roseggerstraße 12
8700 Leoben
Austria
Tel.: +43 (0)3842/402-4266
Fax: +43 (0)3842/402-4202
E-mail: gerald.ressel@unileoben.ac.at

Publication B:

Atomistic insights into milling mechanisms in an Fe-Y_2O_3 model alloy

G. Ressel, D. Holec, A. Fian, F. Mendez-Martin and H. Leitner

accepted in Applied Physics A: Materials Science and Processing (2013).

Appl Phys A
DOI 10.1007/s00339-013-7877-y

Applied Physics A
Materials Science & Processing

Atomistic insights into milling mechanisms in an Fe–Y_2O_3 model alloy

G. Ressel · D. Holec · A. Fian · F. Mendez-Martin · H. Leitner

Received: 10 May 2013 / Accepted: 18 July 2013

Abstract This experimental study combined with first principles modeling focuses on the distribution and behavior of yttria in pure iron powder particles prepared by mechanical alloying. A profound verification of the mechanism during milling is still missing in literature. Atom probe tomography and X-ray photoelectron spectroscopy measurements directly after mechanical alloying revealed yttria dissolved in the iron matrix, which later rearranged in clusters. These findings are corroborated by ab initio calculations demonstrating that the formation energy for Y substitutional defect in bcc-Fe is significantly lower in the close neighborhood of vacancies. X-ray diffraction measurements revealed that mechanical alloying for at least 12 hours caused a dramatic decrease in domain size and an extraordinary increase of defect density.

1 Introduction

In order to improve the high temperature strength of steels, a fine Y_2O_3 powder is incorporated into the iron-based alloys [1, 2]. Such so-called oxide dispersion strengthened (ODS) alloys are commonly produced by mechanical alloying with an attritor or a ball mill [3]. It is known that Y–O clusters at nanometer scale are formed in ODS steels [4]. Thermodynamical calculations revealed that yttrium has a negligibly small solubility in Fe [5, 6]. Therefore, mechanical alloying is applied for producing such steels strengthened with very small and fine distributed yttrium oxide clusters [7]. While some studies reported that just a dispersion of Y–O based particles with a diameter of 5–20 nm occurred in the iron matrix during mechanical alloying [2, 3, 8–10]; others, especially in the last few years, reported of a refinement of these particles with support of Ti [11–17]. Nevertheless, regarding the mechanisms active during milling, only hints exist. Therefore, the mechanism is not clear until now. For instance, Miller et al. [15] investigated hot isostatic pressed (hiped) ferritic ODS steels and found Y clusters with an M:O ratio of about 1.2. This differs significantly from Y_2O_3 itself (0.67), leading to a conclusion that these particles could not be crushed remnants of the initial yttria powder. Based on transmission electron microscopy (TEM) and X-ray diffraction (XRD) investigations on hot extruded specimens, Okuda and Fujiwara [18] proposed that a decomposition of yttria occurs during mechanical alloying, since relevant XRD peaks were missing after milling but reappeared after annealing the powder. However, the missing XRD peaks could also be a consequence of amorphization of yttria as proposed by Kimura et al. [19, 20]. They proposed a decomposition of yttria based on differential scanning calorimetry (DSC) measurements, and suggested that yttria gets amorphous around crystalline iron areas. The assigned DSC peak was interpreted as a re-precipitation process, but alternatively it could be associated also with crystallization of the amorphous phase. In contrast, Klimiankou et al. [21] studied the yttrium oxide particles in already hiped ODS steels using high resolution TEM. They identified an orientation relationship between the yttrium oxide particles and the matrix, which is a strong evidence for a predissolution of yttria in the iron matrix, and a re-precipitation of yttrium oxide particles. Ab initio calculations revealed

G. Ressel (✉) · D. Holec · F. Mendez-Martin · H. Leitner
Department of Physical Metallurgy and Materials Testing, Montanuniversität Leoben, 8700 Leoben, Austria
e-mail: gerald.ressel@unileoben.ac.at
Fax: +43-3842-4024202

A. Fian
Institute for Surface Technologies and Photonics, Joanneum Research Forschungsgesellschaft GmbH, 8160 Weiz, Austria

Published online: 20 August 2013

that vacancies, created during mechanical alloying, play an important role in clustering of interstitial oxygen [22]. Finally, Williams et al. [17] analyzed the evolution of Y–Ti–O based particles in 14-YWT (Fe-14 Cr-2 W-0.3 Ti) steel during processing by TEM and APT. The generation of a large surface of the powder particles during mechanical alloying together with the extremely high mechanical deformations, which lead to high density of dislocations and vacancies, could be the key for the dissolution and extremely fine clustering of yttrium and oxygen. To resolve this longstanding question of whether there is dissolution of yttria in the iron matrix, atom probe tomography (APT) combined with X-ray photoelectron spectroscopy (XPS) measurements of the as-mechanically alloyed powder are employed. APT is used to resolve the distribution of yttrium in the powder particles after mechanical alloying. The chemical bonding of yttrium and oxygen before and after mechanical alloying is studied by XPS. Additionally, the domain size of the mechanically alloyed particles, as an indicator of defect density, was calculated from XRD patterns by diffraction line broadening analysis [23, 24]. Finally, ab initio calculations were carried out in order to reveal whether crystal defects, such as vacancies, could promote dissolution of Y in Fe.

2 Methods

Before mechanical alloying, a ferritic iron powder and 0.5 wt.% yttria powder with a $d_{90} = 1.16$ µm and purity of 99.9 % were blended in a tumbling mixer for 30 minutes. Afterwards, the mixture was mechanically alloyed in a Certony™ attritor under Ar-gas atmosphere for 12 and for 48 h. Steel balls with a ball-to-powder ratio (BPR) of 10:1 were used for milling. The chemical composition of the different states before and after milling is listed in Table 1. The elements Al, Mn, Ni, Cr, Mo and W are incorporated during milling. It should be noted that all compositions presented in this paper are given in at.% and that the 12-hour sample and the 48-hour specimen are different batches, leading to slight differing incorporation amounts. The powder mechanically alloyed for 48 h was subsequently hipped at a temperature of 1100 °C and a pressure of 100 MPa for 3 h.

Atom probe tomography (APT) investigations were performed on powder particles milled for 12 and 48 h using a Cameca™ Local Electrode Atom Probe (LEAP™) 3000X HR. For the tip preparation from the mechanically alloyed powder particles, an FEI™ Dual Beam focused ion beam (FIB) was used. A wedge was cut out of the powder particle at a convenient position, and the slices were placed on several tips of a microtip coupon. The measurements were run in a voltage mode applying a pulse fraction of 20 % at base temperature of 60 K. The reconstruction procedure was carried out with the Cameca™ software IVAS 3.4.3.

The XPS measurements were conducted by a Multiprobe-UHV-surface-analysis system from Omicron Nanotechnology equipped with a DAR 400 X-ray source (Al K_α1-line, 1486.70 eV), an XM 500 quartz crystal monochromator and an EA 125 hemispherical electron analyzer. The powder was fixed on a carbon adhesive tape and the whole investigation was carried out in an ultra-high vacuum at pressure of 9×10^{-11} mbar. The element peaks of the mechanically alloyed powder were recorded with a pass energy of 40 eV, the Y3d-peak was summed up with 120 sweeps to distinguish the signal from the background. The overall energy resolution of the spectrometer for these measurements was 0.7 eV.

A Bruker-AXS D8 Advance diffractometer equipped with a sol-x detector was used to get locked-couple XRD scans with a step size of 0.02° and a time per step of 1.2 s. The obtained XRD-patterns were analyzed by the single line method for the analysis of X-ray diffraction line broadening referring to the work of de Keijser et al. [23].

For first principles calculations the Vienna Ab initio Simulation Package (VASP) [25, 26] was used together with generalized gradient approximation of the exchange-correlation effects [27]. A $3 \times 3 \times 3$ cubic supercell with 54 atoms enabled point defect concentrations which are small enough and, at the same time, computationally affordable. The plane-wave cut-off energy set to 500 eV and the $6 \times 6 \times 6$ k-point mesh yielded a total energy accuracy of about 10^{-3} eV/at. The spin-polarization was allowed to account for the ferromagnetic state of Fe. Several configurations of vacancies and Y atoms substitutionally replacing Fe were considered and are described in detail in the results section.

3 Results

3.1 APT measurements

To compare the evolution of Y and O distributions during mechanical alloying, the respective 3D atom maps of the

Table 1 Chemical composition of the of the analyzed powders before and after milling (at.%)

	Fe	Al	Mn	Cr	Ni	Mo	W	Y_2O_3
Before milling	Bal.	–	0.124	0.049	0.028	–	–	0.132
12 h mechanically alloyed state	Bal.	0.34	0.14	0.09	0.05	0.01	0.8	0.12
48 h mechanically alloyed state	Bal.	0.1	0.16	0.24	0.1	0.01	0.05	0.13

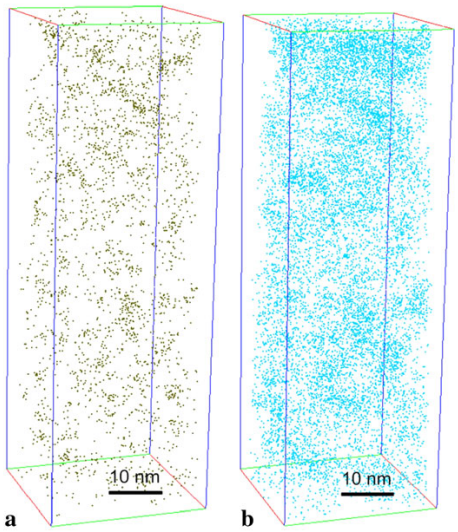

Fig. 1 3D atom maps of the 12-hour mechanically alloyed condition. (**a**) Y; (**b**) O

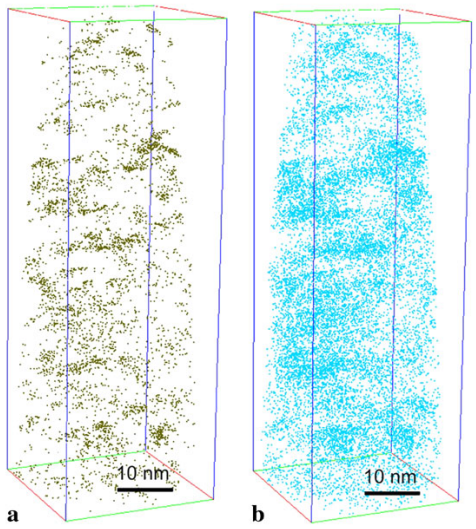

Fig. 2 3D atom maps of the 48-hour mechanically alloyed condition. (**a**) Y; (**b**) O

12-hour and the 48-hour samples are shown in Figs. 1 and 2. Y- and O-clusters can be detected in both states, nonetheless, the visual inspection reveals less distinctive clusters after 12 h than after 48 h of milling. Furthermore, other measurements (not presented here) showed cluster depleted zones in the 12-hour milled state, which suggests an inhomogeneous distribution of Y atoms after 12 h of mechanical alloying. In the 48-hour condition all measurements yield a homogeneous distribution of Y and O clusters, as demonstrated in Fig. 2. All elements exhibiting a clustering behavior after milling are analyzed. To identify the clusters and to analyze their size and chemical composition, the cluster search algorithm based on the double maximum separation method [28, 29] was used. The cluster search parameters in both states were defined by the method of Vaumousse et al. [30] and Stephenson et al. [29]. The separation distance, the surrounding distance and the erosion distance in the 12-hour state were all set to 0.65 nm, respectively. At the 48-hour state the separation distance was set to 0.75 nm, the surrounding- and the erosion-distance were both set to 0.7 nm. To prevent randomly distributed atoms from being identified as clusters, a minimum cluster size of 10 atoms at the 12-hour condition and 12 atoms at the 48-hour state were used. Results, such as the matrix and the cluster composition as well as the radius of gyration (R_g) are listed in Table 2. The radius of gyration enables for a comparison of the size of differently shaped clusters. It follows that R_g has a slightly lower value at the 12-hour state than in the 48-hour sample. Calculations reveal a mean R_g of 0.50 nm and 0.65 nm for the 12- and 48-hour conditions, respectively. Consequently, mechanical alloying for longer than 12 h causes a slight increase of the cluster size, which remains, nonetheless, within the standard deviation. Calculations of a matrix composition, excluding the Y and O enriched clusters, reveal a content of 0.08 ± 0.04 at.% Y and 0.35 ± 0.14 at.% O in the 12-hour condition, and 0.13 ± 0.01 at.% Y as well as 0.48 ± 0.06 at.% O in the 48-hour condition. Comparison of both conditions leads to a conclusion that Y and O are more dissolved in the matrix after 48 h than after 12 h of milling. The average Y content of the clusters is roughly the same in both cases, the O content is slightly increased at the 12-hour state, but also within the standard deviation. The standard deviations of all cluster compositions are very high compared to the mean content values, indicating that these enrichments are clusters without a defined composition. Additionally, the Y/O ratios differ slightly at both conditions (0.5 for the 12-hour state and 0.63 for the 48-hour condition), and they are slightly lower than the Y:O ratio of Y_2O_3 (Y/O = 0.67). Additional calculations reveal an enrichment of Mn and Al and a Fe concentration in the clusters between 50 and 60 at.% in both states. Comparison of the compositions of the different states in Table 2 shows that Al and Mn as well as other elements are incorporated during milling. Mn and Al concentration of 0.24 at.% and 0.53 at.%, respectively, was measured in the clusters formed after 12 h of milling. This is a clear increase compared with the matrix content of 0.09 at.% and 0.22 at.% for Mn and Al, respectively. An akin trend can be seen at the 48-hour state.

3.2 XPS-measurements

XPS provides information about the quantitative composition of chemical elements but, also about the chemical state

Table 2 Comparison of the mean cluster size (R_g), as well as the Y and O content in the matrix and the clusters of the 12 and 48 h mechanically alloyed conditions, describing the evolution of the Y–O clusters during mechanical alloying

	Matrix composition [at.%]				
	Fe	Y	O	Mn	Al
12 h of mechanical alloying	98.68 ± 0.91	0.08 ± 0.04	0.35 ± 0.14	0.09 ± 0.07	0.22 ± 0.2
48 h of mechanical alloying	98.34 ± 0.08	0.13 ± 0.01	0.48 ± 0.06	0.15 ± 0.01	0.05 ± 0.01

	Cluster composition [at.%]						
	R_g [nm]	Fe	Y	O	Mn	Al	Y/O
12 h of mechanical alloying	0.50 ± 0.23	49.11 ± 20.37	15.65 ± 11.93	31.08 ± 18.87	0.24 ± 0.24	0.53 ± 0.53	0.5
48 h of mechanical alloying	0.65 ± 0.25	59.38 ± 19.2	14.68 ± 9.6	23.18 ± 15.03	0.17 ± 0.17	0.19 ± 0.19	0.63

of a specific element. A shift of the binding energy of core level electrons indicates a change of chemical environment of this element. In case of yttrium a chemical shift from 155.6 eV (metal) to 157 eV [31] of the $Y3d_{5/2}$-peak is expected in the original powder corresponding to an Y_2O_3 oxide state. During the mechanical alloying the Y–O bond might be partially released as the Y_2O_3 is milled and dissolved in the iron matrix. The chemical environment is more electropositive within the ferritic matrix compared to the original powder, and the binding energy of $Y3d_{5/2}$ decreases in that case. An enrichment of other alloying elements such as Al or Mn can also slightly decrease the binding energy to lower values. In Fig. 3 the $Y3d_{5/2}$ peaks of the mechanically alloyed powders and the hiped sample are compared with those of pure yttria powder. All measurements are charge-corrected and the binding energy is referred to the carbon–carbon bond at 284.6 eV as an internal calibration standard, which is detected as a surface contamination layer generated by sample transfer under ambient conditions in all measurements. The XPS spectra were fitted by using a Lorentzian/Gaussian peak deconvolution (Voigt function) which is described in detail in [32]. The Lorentzian contribution of the peak profile can be attributed to the core-hole lifetime broadening and is 0.1 eV in the case of Y3d according to [33]. To allow for a comparison of the two different samples with various contents of yttria, the photoelectron intensity is normalized to the intensity maximum and presented in arbitrary units (a.u.). The lower signal to noise ratio in the mechanically alloyed and hipped conditions, even after 120 sweeps, can be explained by the very low Y-content of only 0.1 at.%. A slight shift of the binding energy to lower values can be seen, which indicates a more electropositive environment of yttrium atoms in the mechanically alloyed specimens. The binding energies of the $Y3d_{5/2}$ electrons of the reference material and of the different specimens are marked in Fig. 3 with vertical dashed lines. A Lorentzian/Gaussian peak deconvolution of the reference yttria powder yields a binding energy of 157.66 eV for the $Y3d_{5/2}$ electrons and 159.69 eV for $Y3d_{3/2}$. In contrast to that, the binding energies in the specimen mechanically alloyed for 48 hours are 157.23 eV for $Y3d_{5/2}$ and 159.27 eV for $Y3d_{3/2}$. The $Y3d_{5/2}$ and $Y3d_{3/2}$ binding energies in the 12-hour specimen are fitted to be 157.20 and 159.24 eV, respectively. The peak fits of the hiped specimen spectrum revealed 156.92 eV for the $Y3d_{5/2}$ electrons and 158.96 eV for the $Y3d_{3/2}$ electrons, respectively.

3.3 First principles calculations

To get an insight in the energy changes of differently modified crystal structures at the atomic scale, ab initio calculations were employed. The energy of formation of a single vacancy in the iron bcc lattice is calculated as

$$\begin{aligned} E_f(1\text{vac}) &= E(3\times3\times3+1\text{vac}) - \left[E(3\times3\times3)\right. \\ &\quad \left. - E(1\text{Fe})\right] \\ &= E(3\times3\times3+1\text{vac}) - 53E(1\text{Fe}) \end{aligned} \tag{1}$$

where $E(3\times3\times3+1\text{vac})$ is the total energy of a $3\times3\times3$ lattice with 53 Fe atoms and 1 vacancy. $E(3\times3\times3)$ and $E(1\text{Fe})$ are the total energies of bcc iron corresponding to 54 and 1 Fe atom, respectively, ($E(3\times3\times3) = 54E(1\text{Fe})$). The energy of formation of one vacancy is 2.193 eV/vacancy. This value is in a good agreement with previously published result [34], where even a larger supercell was used. The positive value means that work has to be applied to form a vacancy.

The energy of solution of Y in a perfect bcc crystal, which expresses the energy needed to substitutionally replace one Fe atom with one Y atom, reads:

$$\begin{aligned} E_{\text{sol}}(1\text{Y}) &= E(3\times3\times3+1\text{Y}) \\ &\quad - \left[E(3\times3\times3) - E(1\text{Fe}) + E(1\text{Y})\right] \end{aligned} \tag{2}$$

where $E(1\text{Y})$ is the total energy per atom of Y in the hcp structure. Equation (2) yields $E_{\text{sol}}(1\text{Y}) = 2.115$ eV/Y. That

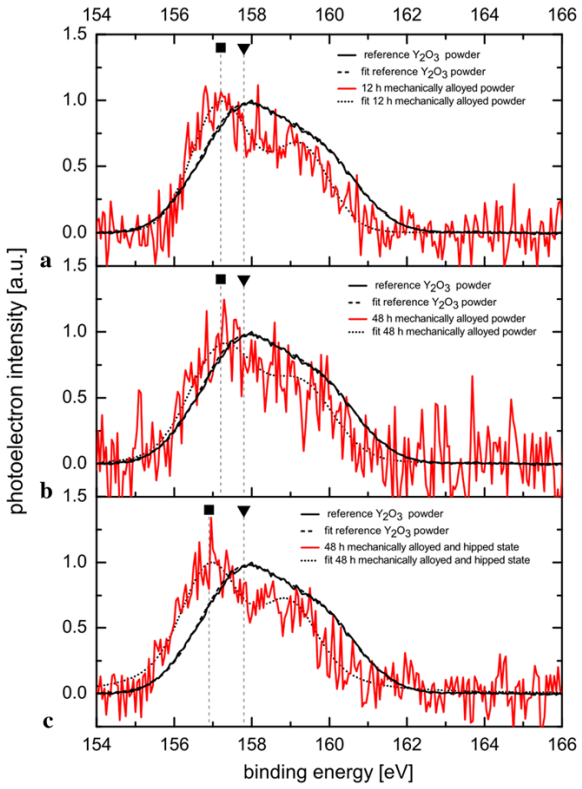

Fig. 3 Comparison of the Y3d peaks of the mechanically alloyed samples, for 12 h (**a**) and for 48 h (**b**), as well as of the hiped state (**c**) and the reference Y_2O_3 powder. The $Y3d_{5/2}$ peak maxima positions of mechanical alloyed samples (*squares*) and reference Y_2O_3 powder (*triangles*) are marked with *dashed vertical lines*. A slight chemical change of yttria during mechanical alloying is clearly indicated

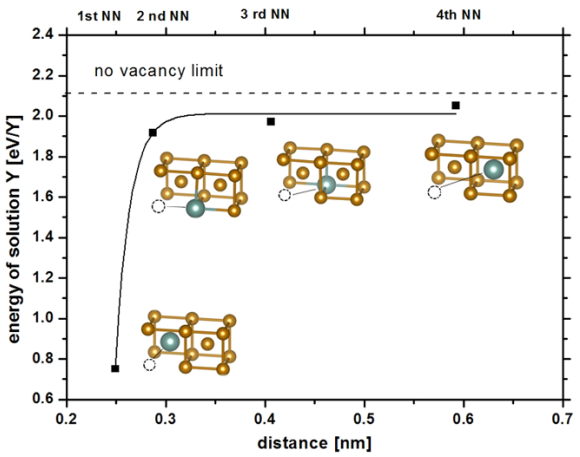

Fig. 4 Energy of solution of 1Y atom in Fe matrix (*smaller orange balls*) as a function of the distance between the Y atom (*larger blue ball*) and the vacancy (*gray circle*). The *dashed line marks* the limit for energy of solution in a perfect Fe crystal

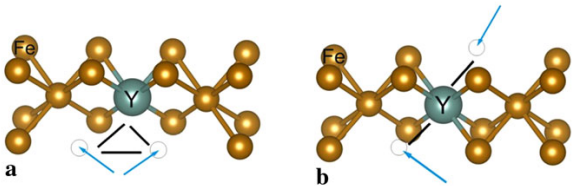

Fig. 5 (**a**) Y–vacancy–vacancy triangle configuration, (**b**) Y–vacancy–vacancy line configuration

means that an extremely high energy input is needed to dissolve Y in a perfect Fe structure, i.e. thermodynamically Y has no driving force for dissolution in the Fe lattice. The corresponding mixing enthalpy of the hypothetical Fe–Y alloy is 0.039 eV/atom. The positive value represents a thermodynamical force for de-mixing of this alloy.

Next, the effect of lattice defects, such as vacancies, on the energy of solution of Y in the Fe lattice is investigated. It is assumed that a vacancy exists in the Fe matrix before Y is dissolved. Results shown in Fig. 4 were calculated according to

$$E_{\mathrm{sol}}(1\mathrm{Y}) = E(3\times3\times3+1\mathrm{vac}+1\mathrm{Y}) - \left[E(3\times3\times3+1\mathrm{vac}) - E(1\mathrm{Fe}) + E(1\mathrm{Y})\right] \quad (3)$$

The energy of solution decreases dramatically by about 1.364 to 0.751 eV/Y when the Y atom and the vacancy are in the first nearest neighbor (NN) distance. Vacancies lower the energy of solution also for more distant neighbors, but not so strongly. This is likely due to the fact that a vacancy allows for a relaxation of internal stresses caused by replacing Fe with a much larger Y atom, and obviously such mechanism is most effective when the Y atom and the vacancy are as close as possible to each other. In any case, the decrease of the $E_{\mathrm{sol}}(1\mathrm{Y})$ with decreasing Y–vacancy distance suggests a tendency for Y–vacancy clustering.

Furthermore, the effect of increasing defect density is addressed. Again, the energy of solution of one yttrium atom in the iron lattice with two vacancies is calculated with respect to a state with two pre-existing vacancies. Two extreme configurations with Y and a vacancy being nearest neighbors in a triangle configuration (Fig. 5a) and a line configuration (Fig. 5b) are calculated.

An addition of the second vacancy causes a further decrease of the energy of solution of Y in bcc Fe. Figure 6 illustrates the energy of solution of Y as a function of the number of vacancies. For the line configuration, the ab initio calculations reveal energy of solution of 0.739 eV/Y, which is slightly lower as compared with the one vacancy configuration. However, in the triangle configuration the energy of solution of Y is −0.514 eV/Y. Because of the lowest value of E_{sol}, the triangle configuration is the most favorable ar-

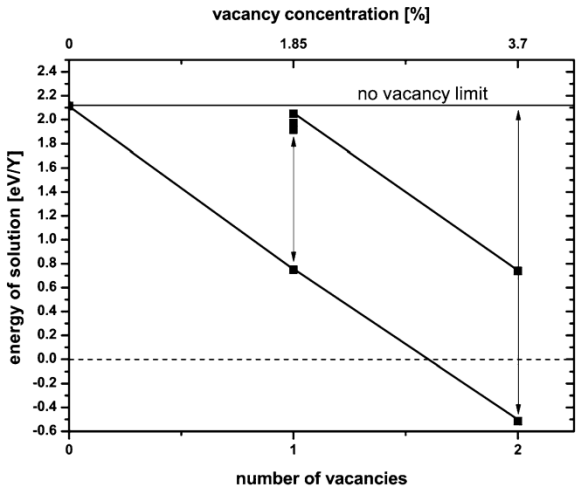

Fig. 6 Drop of the energy of solution as a function of the vacancy density. The presented data suggest an increased solubility of Y in a bcc Fe lattice with increasing vacancy density

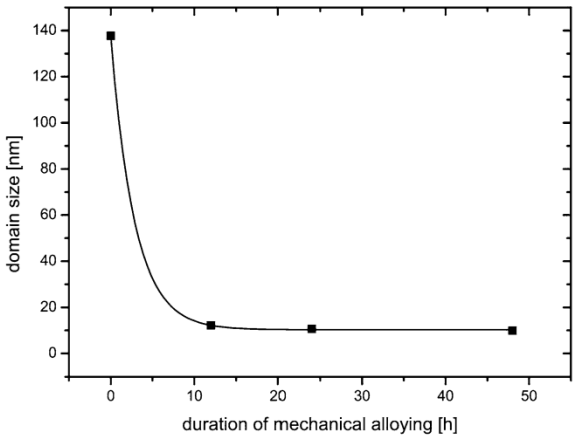

Fig. 7 Domain size, calculated by diffraction line broadening analysis, against the duration of mechanical alloying

rangement. Moreover, it stays stable even at 0 K due to its negative value. Consequently, increasing defect density, in this case vacancy density, promotes the solubility of Y in Fe.

3.4 Domain size

Concerning formation of very fine clusters in the size of a few nanometers, it is assumed that an extremely high deformation, which is provided by mechanical alloying in an attritor, supports the dissolution and very fine cluster formation of yttrium oxide. Especially, vacancies and dislocations act as an accelerator in diffusion of Y in Fe. The domain size is a measure of defect density, such as grain boundaries, dislocations or vacancies, and could be estimated by the line broadening method applied on XRD patterns [23, 24]. The smaller the domain size is the smaller is the lattice space without defects and the higher is the defect density. In this case Y impurities do not influence the domain size. In Fig. 7 the domain sizes obtained for the unmilled ferritic iron powder and the powders milled for different durations are compared. Milling for 12, 24 and 48 hours causes a dramatic decrease in domain size from about 137.7 nm, for the unmilled condition, to about 12 to 10 nm, for the milled conditions. There is no significant change of the domain size from 12 to 48 h. At a domain size of about 10 nm after milling for 48 h an extremely high defect density can be assumed. Its extent is nearly the same as the distance of each Y-cluster detected by APT.

4 Discussion and summary

APT, XPS, XRD as well as ab initio calculations have been employed to clarify the mechanism during mechanical alloying Fe with Y_2O_3. Results of atom probe investigations on powder particles are listed in Table 2. Our analysis revealed a roughly similar cluster size after 12 and 48 hours of milling. Furthermore, in both specimens an extended solubility of Y and O in the Fe matrix caused by mechanical alloying is proven. Additionally, an enrichment of Al and Mn concentration, as well as Fe content of 50–60 at.% is detected. The Y/O ratio in the clusters in the milled states differs from original stoichiometric yttria powder. In contrast to the investigations by Miller et al. [15], where even after hiping the Y/O ratio of the Y–O clusters is proposed to be 1.2 and beyond the stoichiometric Y_2O_3, the Y/O ratio before hiping lies slightly under this value. However, the results presented in Table 2 indicate a roughly similar cluster size of the 12- and 48-hour conditions. The fact that there is a saturation in cluster size during milling, which agrees with the findings of Suryanarayana [7], we interpret as a hint that these particles are not crushed remnants of original brittle Y_2O_3 powder particles. Moreover, we assume that the same cluster size indicates dissolution with following formation of these clusters. Additionally, the dissolved amounts of Y and O in the Fe matrix, which are listed in Table 2, support this theory. Domagala et al. [5] and Swisher and Turkdogan [35] reported a solubility at elevated temperatures much smaller than 0.6 at.% Y and about 2 ppm O in Fe, respectively. At room temperature, the solubility limit in thermodynamical equilibrium of Y and O in Fe is even lower. Compared with these thermodynamical calculations, the amounts of Y and O as listed in Table 2, are even enhanced. According to the composition of the clusters, the Fe concentration should be treated with care, because of reconstruction uncertainties of APT measurements, but it is assumed that the Fe concentration is not zero. Also the fact that an enrichment of Al, Mn and Fe can be detected in the clusters directly after milling, gives a hint that these clusters

are a result of dissolution of Y and O in the Fe matrix and a following rearrangement of Y, O as well as Mn and Al. This is supported by the XPS results, revealing a shift of about 0.46 eV to lower values of the $Y3d_{5/2}$ binding energies during mechanical alloying. This means that the binding energy changes due to a more electropositive chemical environment at the Y clusters. However, based on the previous APT results it can be concluded that the Mn and Al enrichments and also Fe decreases the $Y3d_{5/2}$ binding energy to lower values. Further hiping decreases the $Y3d_{5/2}$ binding energy again to about 0.28 eV, which is an overall decrease of 0.74 eV. These results confirm atom probe findings recently submitted to IJMR, where an increased Al and Mn concentration in the clusters is detected after hiping. Other papers reported an enrichment of Ti at these Y–O clusters at already hiped titanium alloyed ferritic steels [11, 36, 37]. During hiping, these alloying elements further enrich at the clusters, and the binding energy as measured by XPS drops slightly again.

The line broadening of XRD patterns (Fig. 7) reveals high defect density present after mechanical alloying. Based on the ab initio calculations presented in Fig. 4 , the strong energy decrease as the first nearest neighbor indicates a strong affinity of Y and vacancy in building of Y–vacancy pairs. This is due to the elastic relaxation of the larger Y atom at the "free space" offered by a vacancy. These pairs have a much higher diffusivity in the Fe lattice than Y alone, and make a dissolution of Y in Fe easier. This is similar to e.g. Al–Cu-based alloys, where vacancies also play an important role at the early stages of precipitation [38]. The effect of a vacancy can also be related to dislocations. Edge dislocations, for example, offer also "free space" in their cores where these large Y atoms can relax their stress field. Therefore, also dislocations can enhance Y dissolution in Fe. Schwarz [39] assumed that larger atoms diffuse at dislocations much faster and that during mechanical alloying the solute is diffusing into solvent by dislocations. Further milling forces dislocations to move, they detach from these diffused atoms and can act as diffusion pipe. This hypothesis agrees with results of different APT measurements of the 12-hour condition (Fig. 1). They reveal a less homogeneous distribution of these clusters than of the 48-hour state (Fig. 2), which leads to the conclusion that at latter condition more time for diffusion is available, which causes a better distribution of the Y and O clusters.

In order to analyze the mechanism of the mechanical alloying process and its dependence on defect density, also ab initio calculations have been performed in this paper. Fu et al. [22], for example, worked on the behavior of interstitial O in the Fe matrix in dependence of the vacancy mechanism. Also Gopejenko [40] calculated the interaction of oxygen and yttrium in fcc iron. Calculations in this paper concentrated on the influence of vacancies on the Y solubility in bcc Fe lattice. Results presented in Fig. 6 reveal that an increasing vacancy density decreases the energy of solution of Y in bcc Fe. At a configuration, which is defined as the vacancy–Y–vacancy triangle configuration, the energy of solution is −0.514 eV/Y. This negative value means that there is a thermodynamical driving force to get Y substituted in the lattice, when two vacancies are arranged side by side and stays stable at 0 K. Consequently, we propose that lattice defects, such as vacancies promote the dissolution of Y in the Fe lattice. Energy needed to produce these vacancies is supplied by the impact of the balls. Although vacancies are not stable at 0 K the whole mechanical alloying process is conducted at room temperature (298 K), and moreover the maximum temperature reached by powder particles that become trapped between colliding balls was estimated to 423 K [41]. At these temperatures the stability of the vacancies is enhanced compared to 0 K. Further calculations proved that if Y is dissolved in the Fe matrix, the creation of additional vacancies becomes easier. Also in the vicinity of vacancies, the creation of the next vacancy costs less energy. Consequently we propose that Y gets step by step implanted in the Fe matrix assisted by defects such as vacancies or dislocations. Nevertheless, the corresponding mixing enthalpy of the hypothetical Fe–Y alloy is 0.039 eV/atom. This positive value represents a thermodynamical force for decomposition of this alloy. It follows that temporarily dissolved Y has a driving force to form clusters, which also agrees with the atom probe measurements indicating partly dissolved Y with already formed clusters. Consequently, because of all of these facts we propose that during mechanical alloying Y and O as well as Al and Mn are able to dissolve and diffuse by the support of defects into the Fe lattice, and rearrange in clusters at convenient lattice positions, such as dislocations or vacancies.

5 Conclusions

Mechanically alloyed powder as well as mechanically alloyed and hiped samples were analyzed by APT, XPS and XRD. Additionally, ab initio calculations were performed in order to elucidate the mechanism of mechanical alloying. Evaluation of the measurements and calculations lead to following conclusions:

1. Y and O dissolves during mechanical alloying in the bcc Fe matrix, which is proved by APT and XPS measurements.
2. Y and O are mainly arranged in clusters after mechanical alloying and before hiping, and are not crushed remnants of the original yttria powder. A mixing enthalpy of a hypothetical Fe–Y alloy is positive, which is an evidence that temporarily dissolved Y has a driving force to form clusters.

3. After 12-hour milling these clusters are not as homogeneously distributed as after 48 h. Also the dissolved amount of Y and O in Fe is lower. This is because of missing time for diffusion compared to longer milling durations.
4. The defect density of the mechanically alloyed Fe powder particles is exceptionally high, but there is only a negligible difference between the defect density of the 12-hour sample and the 48-hour specimen.
5. Defects such as vacancies promote dissolution of Y in Fe. At a vacancy–Y–vacancy triangle configuration, the solution energy of Y in bcc Fe becomes negative. This suggests that at this special configuration a substitution of Y at a Fe site is energetically favorable.
6. Because of the fact that vacancies have a positive effect in dissolution of Y due to "free space" and stress relaxation it is assumed that this can be transformed also to dislocations.
7. The creation of vacancies in the vicinity of dissolved Y or of already created vacancies is easier as in the perfect bulk ferrite.

Acknowledgements The authors gratefully thank Dr. Johannes Zbiral for supporting at the milling process and TU Wien using its facilities.

References

1. S. Ukai, T. Nishida, T. Okuda, T. Yoshitake, J. Mater. Sci. Technol. **35**, 294 (1998)
2. A. Czyrska-Filemonowicz, B. Dubiel, J. Mater. Process. Technol. **64**, 53 (1997)
3. J.S. Benjamin, T.E. Volin, Metall. Trans. **5**, 1929 (1974)
4. G. Odette, M. Alinger, B. Wirth, Annu. Rev. Mater. Res. **38**, 471 (2008). doi:10.1146/annurev.matsci.38.060407.130315
5. R.F. Domagala, J.J. Rausch, D. Levinson, Trans. Am. Soc. Met. **53**, 137 (1961)
6. W. Zhang, G. Liu, K. Han, *Phase Diagrams of Binary Iron Alloys* (ASM International, Materials Park, 1993)
7. C. Suryanarayana, Prog. Mater. Sci. **46**, 1 (2001). doi:10.1016/S0079-6425(99)00010-9
8. J. Benjamin, Metall. Trans. **1**, 2943 (1970)
9. R. Benn, P. Mirchandani, in *Dispersion Strengthening by Mechanical Alloying*, ed. by E. Arzt, L. Schultz (DGM Informationsgesellschaft, Oberursel, 1988), pp. 19–38
10. J.D. Whittenberger, in *New Materials by Mechanical Alloying Techniques*, ed. by E. Arzt, L. Schultz (DGM Informationsgesellschaft, Oberursel, 1988), pp. 201–215
11. M.K. Miller, K.F. Russell, D.T. Hoelzer, J. Nucl. Mater. **351**, 261 (2006). doi:10.1016/j.jnucmat.2006.02.004
12. I.S. Kim, J.D. Hunn, N. Hashimoto, D.L. Larson, P.J. Maziasz, K. Miyahara, E.H. Lee, J. Nucl. Mater. **280**, 264 (2000). doi:10.1016/S0022-3115(00)00066-0
13. D. Larson, Scr. Mater. **44**, 359 (2001). doi:10.1016/S1359-6462(00)00593-5
14. M. Miller, D. Hoelzer, E. Kenik, K. Russell, J. Nucl. Mater. **329–333**, 338 (2004). doi:10.1016/j.jnucmat.2004.04.085
15. M. Miller, E. Kenik, K. Russell, L. Heatherly, D. Hoelzer, P. Maziasz, Mater. Sci. Eng. A **353**, 140 (2003). doi:10.1016/S0921-5093(02)00680-9
16. M. Miller, D. Hoelzer, E. Kenik, K. Russell, Intermetallics **13**, 387 (2005). doi:10.1016/j.intermet.2004.07.036
17. C.A. Williams, P. Unifantowicz, N. Baluc, G.D. Smith, E.A. Marquis, Acta Mater. **61**, 2219 (2013). doi:10.1016/j.actamat.2012.12.042
18. T. Okuda, M. Fujiwara, J. Mater. Sci. Lett. **14**, 1600 (1995). doi:10.1007/BF00455428
19. Y. Kimura, S. Suejima, H. Goto, S. Takaki, ISIJ Int. **40**, 174 (2000). doi:10.2355/isijinternational.40.Suppl_S174
20. Y. Kimura, S. Takaki, S. Suejima, R. Uemor, H. Tamehiro, ISIJ Int. **39**, 176 (1999)
21. M. Klimiankou, R. Lindau, A. Möslang, J. Cryst. Growth **249**, 381 (2003). doi:10.1016/S0022-0248(02)02134-6
22. C. Fu, M. Krčmar, G. Painter, X.Q. Chen, Phys. Rev. Lett. **99**, 1 (2007). doi:10.1103/PhysRevLett.99.225502
23. T.H. de Keijser, J.I. Langford, E.J. Mittemeijer, A.B.P. Vogels, J. Appl. Crystallogr. **15**, 308 (1982). doi:10.1107/S0021889882012035
24. P. Dasgupta, Fizika A **9**, 61 (2000). doi:10.1177/097152150401100101
25. G. Kresse, J. Furthmüller, Phys. Rev. B **54**, 11169 (1996)
26. G. Kresse, D. Joubert, Phys. Rev. B **59**, 1758 (1999)
27. J.P. Perdew, K. Burke, M. Ernzerhof, Phys. Rev. Lett. **77**, 3865 (1996)
28. A. Cerezo, L. Davin, Surf. Interface Anal. **39**, 184 (2007). doi:10.1002/sia.2486
29. L.T. Stephenson, M.P. Moody, P.V. Liddicoat, S.P. Ringer, Microsc. Microanal. **13**(6), 448 (2007). doi:10.1017/S1431927607070900
30. D. Vaumousse, A. Cerezo, P.J. Warren, Ultramicroscopy **95**, 215 (2003)
31. D. Briggs, M. Seah, *Practical Surface Analysis*, 2nd edn. (Willey, New York, 1993)
32. R. Hesse, P. Streubel, R. Szargan, Surf. Interface Anal. **39**, 381 (2007). doi:10.1002/sia.2527
33. J.C. Fuggle, J.E. Inglesfield (eds.), *Unoccupied Electronic States—Fundamentals for XANES, EELS, IPS and BIS—Introduction* (Springer, Berlin, 1992)
34. Y. Jiang, J. Smith, G. Odette, Phys. Rev. B **79**, 064103 (2009). doi:10.1103/PhysRevB.79.064103
35. J.H. Swisher, E.T. Turkdogan, Trans. Metall. Soc. AIME **239**, 426 (1967)
36. M. Klimiankou, J. Nucl. Mater. **329–333**, 347 (2004). doi:10.1016/j.jnucmat.2004.04.083
37. S. Yamashita, S. Ohtsuka, N. Akasaka, S. Ukai, S. Ohnuki, Philos. Mag. Lett. **84**, 525 (2004). doi:10.1080/09500830412331303609
38. A. Somoza, M. Petkov, K. Lynn, A. Dupasquier, Phys. Rev. B **65**, 094107 (2002). doi:10.1103/PhysRevB.65.094107
39. R. Schwarz, Mater. Sci. Forum **269–272**, 665 (1998)
40. A. Gopejenko, *Nanodevices and Nanomaterials for Ecological Security* (Springer, Berlin, 2012)
41. R. Schwarz, C. Koch, Appl. Phys. Lett. **49**, 164 (1986)

Publication C:

New findings on the atomistic mechanisms active during mechanical milling of a Fe-Y_2O_3 model alloy

G. Ressel, P. Parz, S. Primig, H. Leitner, H. Clemens, W. Puff

Submitted to Journal of Applied Physics.

New findings on the atomistic mechanisms active during mechanical milling of a Fe-Y_2O_3 model alloy

G. Ressel [a,b,1], P. Parz [c,2], S. Primig [a,b,3], H. Leitner [a,d,4], H. Clemens [a,5], W. Puff [c,6]

[a] Department of Physical Metallurgy and Materials Testing, Montanuniversität Leoben, A-8700 Leoben, Austria

[b] Christian Doppler Laboratory for Early Stages of Precipitation, Montanuniversität Leoben, A-8700 Leoben, Austria

[c] Institute of Materials Physics, Graz University of Technology, A-8010 Graz, Austria

[d] now at: Böhler Edelstahl GmbH & Co KG, 8605 Kapfenberg, Austria

Abstract

In order to improve the mechanical properties at elevated temperatures, several types of steels are mechanically alloyed with yttria. The processes active during milling differ dependent on the individual powder constituents. Nevertheless, some theories exist which try to describe the mechanism of producing a metastable phase during milling. However, even in the system iron – yttria the mechanisms taking place during milling are still not well understood. Demonstrated by the example of a simple iron – yttria model alloy, this paper attempts to elucidate the structure of mechanically milled powder particles and, consequently, to clarify the functionality of mechanical alloying in the last stage of milling. Positron annihilation experiments employed on milled materials revealed “open” volumes which are enriched in yttria. Electron backscatter diffraction and atom probe tomography as complimentary techniques allowed an identification of these “open” volumes as mainly vacancies, where enrichment of Y and O occurs. From these results it can be concluded that especially vacancies are responsible for producing a metastable phase, where yttria is dissolved in pure iron.

Keywords

Mechanical alloying; yttria; positron annihilation spectroscopy; electron backscatter diffraction (EBSD); Atom probe tomography

1. Introduction

Mechanical alloying or mechanical milling is a common method to produce metastable phases. For example, yttria exhibits an extended solubility in Fe during mechanical alloying[1–3]. After hot isostatic pressing (HIPing) the corresponding metastable phase forms very fine particles in the range of 1 to about 50 nm [2,4–8]. It is well known that these thermodynamically extremely stable particles can enhance the mechanical properties of a material at elevated temperatures [9–12]. However, even in case of the system Fe-Y_2O_3 the longstanding question what are the mechanisms which take place during milling is not fully clear until now. The paper of Ashkenazy et al. [13] describes the shear-induced intermixing of two initially separate phases during heavy deformation. These authors calculated the intermixing introduced by gliding dislocations using molecular dynamics (MD) and investigated the system combinations Cu with Ag or Ni, which are all of a fcc crystal type, as well as Cu with Fe, Nb and V, which are fcc-bcc systems. These systems were compared to the Cu-Cu system, which was chosen as the reference material in these calculations. These different systems include wide ranges of heat of mixing, which strongly influences shear mixing [14,15], and also differences in elastic properties, atomic size and crystalline structure. Ashkenazy et al. [13] revealed that an intermixing of different phases can take place especially when dislocations can transfer between the different phases. This is the case in fcc-fcc systems. Conversely, in fcc-bcc systems gliding dislocations form an amorphous shell around the particles instead of intermixing. Furthermore, according to Odunuga [14] in a system with hard particles in a soft matrix, shear-induced mixing is suppressed by localized deformation. Consequently, for the system Fe-Y_2O_3 the theory of intermixing by dislocation shearing might fail. A second microscopic model trying to explain the extended solubility of one phase in another was published by Schwarz [16]. In this theory diffusion is accelerated along dislocations. Therefore, due to ball impacts as well as increased temperatures of the particles trapped between the balls, as, for example, estimated in [17,18], it is assumed that atoms of one phase can diffuse into the other phase along dislocations, making use of so called ‘diffusion pipes’. Especially between ball impacts atoms have time for diffusion and decorate the dislocations. The deformation due to the next ball impact forces dislocations to move and causes a detachment of the dislocations from the second phase atoms. These dislocations are again free for decoration of the second phase. During mechanical milling this process

should occur continuously. In a recent study [3] the interaction of Y with defects, especially with vacancies, has been shown by means of ab-initio calculations.

However, until now these theories are not completely consistent and, consequently, the occurring mechanisms not well understood. This paper tries to elucidate the structure of milled powder particles of a Fe-Y_2O_3 model alloy. Furthermore, the findings of this paper clarify the distribution of Y and O in Fe and help to understand the mechanism during mechanical alloying. Atom probe tomography (APT) combined with positron annihilation spectroscopy (PAS) of as-milled powder particles was applied to analyze the distribution of Y and to investigate the interaction of Y with the "open" volume in Fe particles, such as mono- or divacancies or grain boundaries. For a more detailed analysis, the crystallite size within the powder particles was determined by electron backscatter diffraction (EBSD) measurements.

2. Experimental

Mechanical alloying was applied on a mixture of ferritic Fe powder and 0.5 m.% (which corresponds to 0.132 at.% or 0.78 vol.%) Y_2O_3 powder. The yttria powder had a d_{90} of 1.16 µm and a purity of 99.9 %. Different batches with milling durations of 12, 24 and 48 h were produced using a Certony™ attritor. As milling parameter a ball-to-powder ratio (BPR) of 10:1 was chosen. In the present experiments steel balls as grinding media were used. The process was carried out under Ar-gas atmosphere to avoid the oxidation of the extremely reactive Fe powders. It must be mentioned that a side effect during the milling of powders is an incorporation of different elements due to abrasion of the grinding media and the container. The chemical composition of the powders prior and after milling was determined by means of X-ray fluorescence spectroscopy (XRF) and is listed in Table 1.

Table 1: Chemical composition of the of the analyzed powders before and after milling (in at.%).

	Fe	Al	Mn	Cr	Ni	Mo	W	Cu	Y_2O_3
before milling	bal.	-	0.12	0.05	0.03	-	-	-	0.13
12 h mechanically alloyed state	bal.	0.34	0.14	0.09	0.05	0.01	0.8	-	0.12
24 h mechanically alloyed state	bal.	-	0.18	0.08	0.1	0.08	-	0.23	0.13
48 h mechanically alloyed state	bal.	0.1	0.16	0.24	0.1	0.01	0.05	-	0.13

Atom probe tips of powder particles were prepared using a FEI™ Versa™ Dual beam focused ion beam (FIB). At convenient positions of the particles wedges were lifted out. Various slices of these wedges were welded on pre-tips provided by a micro-tip coupon. This procedure is similar to the procedures described in [19,20]. Subsequently, APT measurements were conducted on a Cameca™ Local Electrode Atom Probe (LEAP™) 3000X HR. The measurements were done in voltage mode employing a pulse fraction of 20 %, an evaporation rate of 1 % and a base temperature of 60 K. The data evaluation was carried out with the Cameca™ software IVAS 3.6.6.

Positron lifetime measurements were performed using a fast-fast spectrometer with a time resolution of 221 ps (full width at half maximum, FWHM, for details see [21]). The spectra, containing at least 5×10^6 coincidence counts, were analyzed by using the program pfposfit [22] taking a single component source correction of 318 ps with an intensity of 14.5 % into account. Studies of 2d-Doppler broadening (DB) of positron annihilation radiation were employed according to [21]. For 2d-DB measurements two high purity Ge detectors (typical energy resolution of about 1.3 keV at 511 keV) were installed in a coincidence setup. The two detector system exhibited an effective resolution of 0.88 keV (FWHM – value) related to the 511 keV γ-line. The experimental setup achieved a peak-to-background ratio of approximately 8×10^5, which enabled a high sensitivity to annihilation events with high momentum core-electrons. The nearly background free 2d-DB spectra were obtained with an energy width of about 1 keV per channel and $6 – 8 \times 10^7$ counts were collected. All measurements were performed at

room temperature. For the numerical evaluation, the measured 2d-DB spectra were fitted by a weighted linear combination of the spectra measured on pure deformed elements as reported by Somoza et al. [23]:

$$S = w_{Fe} \times S_{Fe} + w_{Y2O3*} \times S_{Y2O3*}, \quad (1)$$

where S_{Fe} and S_{Y2O3*} correspond to the spectra measured on the ferrite powder and the Y_2O_3 powder, respectively. The weighting factors (w) characterize the contribution of the pure elements to the fitted spectrum and, therefore, give information on the chemical environment of the positron annihilation site. The fitting was performed at a momentum range of $5 - 35 \times 10^{-3} \times m_0c$ to reduce the dominating influence of the valence electrons to the spectra (cf. Fig. 2 and chapter 3.1.2.). The product m_0c means the electron momentum, where m_0 is the electron mass and c the speed of light.

For EBSD measurements powder particles were also prepared by FIB (FEI™ Versa™). The surface was prepared stepwise with a voltage of 30 kV and currents of 15, 5, 3, and 1 nA, respectively. In Fig.1 a scanning electron microscope (SEM) image of the 12 h milled powder is shown where the square marks the scanning position of the EBSD map presented in section 3. The EBSD scan was carried out with 15 kV and a step size of 10 nm. For the grain size evaluation it must be mentioned that the minimum boundary misorientation angle was set to 8° and the minimum grain size was set to 30 nm. For the grain size calculation the number of points, the hexagonal shape of the points and the step size were considered. The diameter was derived from the area by assuming that the grains are circular. The low quality data points close to the grain boundaries were removed by setting the minimum confidence index to 0.1. Due to these removed points it must be mentioned that the calculated grain size is underestimated.

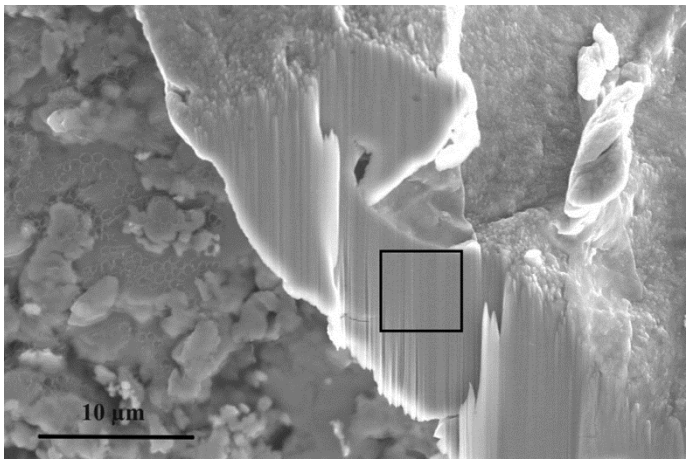

Fig. 1: SEM image present the FIB prepared surface of a powder particle after 12 h milling time. The area where an EBSD scan was conducted is marked with a square.

3. Results

To elucidate the mechanisms taking place during mechanical alloying of a Fe-Y_2O_3 model system various experiments such as PAS, EBSD and APT were employed to find out how Y and O atoms are arranged in the Fe matrix and how they interact with defects.

3.1. Positron annihilation spectroscopy (PAS)

In order to analyze the behavior of Y in the as-milled Fe powder particles they were investigated by PAS. First of all, lifetime measurements on 12 h milled particles were conducted to find out the type of defects where annihilation occurs. Moreover, Doppler broadening (DB) experiments should give information about the elemental surroundings of these defects.

3.1.1. Lifetime measurements

Positron lifetime measurements were performed on two sets of samples, namely an unmilled reference sample, consisting of Fe with 0.5 m.% Y_2O_3 powder and a Fe with 0.5 m.% Y_2O_3 powder sample after 12 h of milling. The results of a two component analysis of the positron lifetime spectra are shown in Table 2.

Table 2: Results of the PAS lifetime measurements conducted on an unmilled Fe – 0.5 m.% Y_2O_3 mixture (reference) and on a 12 h milled Fe – 0.5 m.% Y_2O_3 powder.

	τ_1 [ps]	τ_2 [ps]
Reference powder	160	453
12 h milled	186	355

The reference sample exhibits a short positron lifetime τ_1 of 160 ps and a longer second lifetime τ_2 of 453 ps, while the sample after milling shows a short positron lifetime τ_1 of 186 ps and a longer second lifetime τ_2 of 355 ps. These results give a hint that annihilation sites are dislocations, monovacancies, divacancies or grain boundaries of grains smaller than about 100 nm in diameter. Because the positron diffusion behavior is limited to ~100 nm, it can be assumed that positrons are annihilating within the grains and will not reach the grain boundaries in case of grains larger than 100 nm [24,25].

3.1.2. Doppler broadening (DB)

The 2d-DB spectra are presented and analyzed in the following two ways in order to cross-check the reliability of the obtained results. Each normalized 2d-DB spectrum F is presented as ratio curve $F/F_{Fe\text{-}Y2O3}$ with respect to the normalized 2d-DB spectrum of mixed pure Fe – Y_2O_3 powder. The region ranging from electron momenta of 0 to approximately
$2.5 \times 10^{-3} \times m_0c$ indicate annihilation with valence electrons, while the region from approximately $15 \times 10^{-3} \times m_0c$ onwards can be attributed to the annihilation with high momentum core electrons. The momenta of the core electrons give chemical information and, therefore, show the elemental surrounding at annihilation sites.

In Fig. 2 the 2d-Doppler broadening spectra of the pure Fe and Y_2O_3 powders as well as Fe with 0.5 m.% Y_2O_3 after 12, 24 and 48 hours of milling are shown with respect to the unmilled Fe powder mixed with 0.5 wt.% Y_2O_3 (reference mixture). The spectra of Fe with 0.5 m.% Y_2O_3 show a similar behaviour after 12, 24 and 48 h. All three milled samples show an enhanced similarity to the pure Y_2O_3 powder sample. This reveals that the defects introduced by milling are decorated with yttria or, in atomistic scale, atomic

Y and O. As positron lifetime measurements reveal the existence of vacancies, besides others, these "open" volumes are decorated with Y.

A numerical analysis of the spectra according to equation (1) reveals a strong contribution of Y_2O_3 (w_{Y2O3} ~8.8%) compared to the amount of 0.13 at.% Y_2O_3 within the powder sample. This high Y signature may be attributed to the much higher positron affinity of Y compared to Fe [26]. After milling the contribution of the Y signature to the analysis increases even more to w_Y ~48 %. This increase to approximately 48 % Y may in no way be attributed to the higher positron affinity, but has to be attributed to a decoration of the "open" volumes by Y.

However, it is necessary to know the mean grain size of the powder particles, as from PAS lifetime measurements a distinction of whether the positrons annihilate at grain boundaries or within monovacancies cannot be made. Therefore, the grain size was measured by EBSD and, furthermore, the distribution of Y and O as well as other elements was investigated by APT.

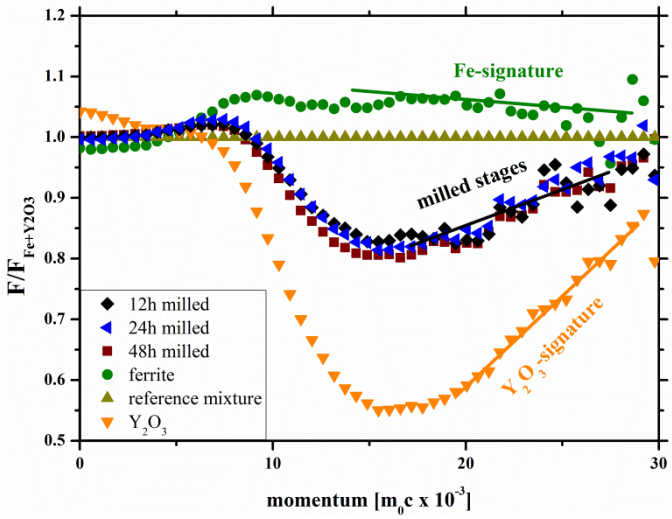

Fig. 2: Comparison of 2d-DB spectra of milled powders (see inset) normalized to an unmilled Fe-Y_2O_3 mixture, which appears as a horizontal line at a ratio of 1. It shows that at the 2d-DB spectra milling causes a shift towards the Y_2O_3 reference powder. The duration of milling does not influence the signature at higher momenta.

3.2. Electron backscatter diffraction (EBSD)

Fig. 3 shows the overlay of an inverse pole figure (IPF) map on an image quality map. Especially on the left side of the image, grains with a typical deformed appearance after

mechanical alloying can be observed. It suggests that after 12 h milling a very high degree of deformation is introduced into the powder particles.

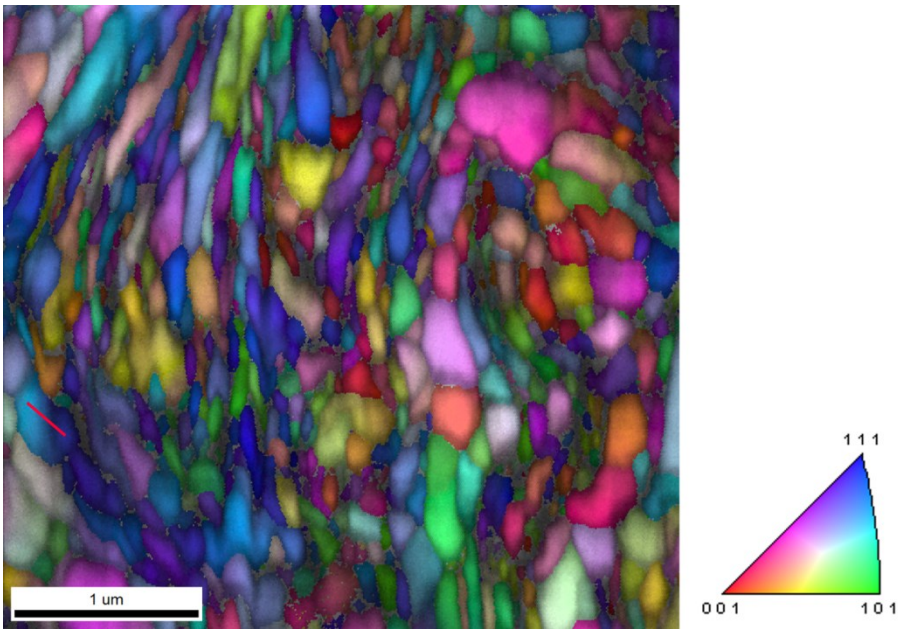

Fig. 3: Overlay of an inverse pole figure (IPF) map on an image quality map derived from an EBSD scan conducted on a powder particle which experienced a milling of 12 h. Along the red line on the left side of the figure the misorientation plot (Fig. 4) was calculated.

In Fig. 4 the misorientation along the red line drawn on the left hand side in Fig. 3 inside one single grain is ploted against the distance. In the grain a misorientation of about 12° from the origin to the end is detected. The fact that the point-to-point misorientation is rather constant at ~1° allows the assumption that there is no low-angle boundary inside the grain. However, the so-called point-to-origin misorientation indicates that the deformation of this grain is extremely high.

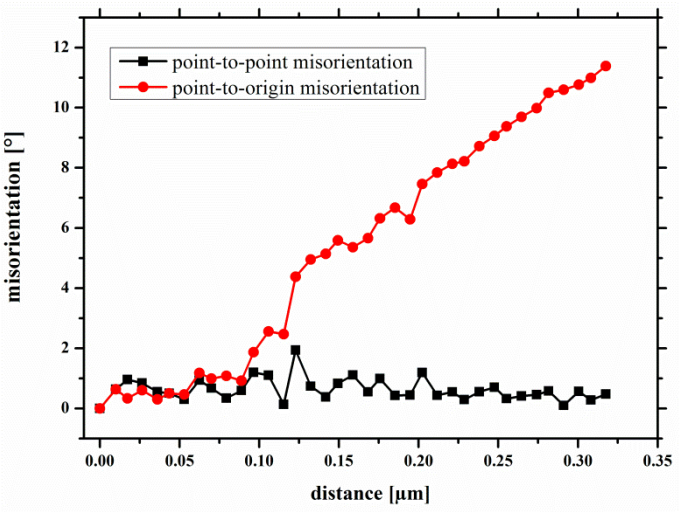

Fig. 4: Point-to-origin and point-to-point misorientation plots along the red line marked in Fig. 3. The rather constant point-to-point misorientation suggests that no low-angle boundary is detected within the grain. However, the high origin-to-end misorientation indicate a high defect density inside the grain.

Furthermore, a grain size distribution was calculated using the map shown in Fig. 3. The result is illustrated in Fig. 5. It indicates that the majority of grains is larger than 100 nm in diameter. The maximum of the area fraction is approximately at 300 nm. Additionally, the average grain diameter was calculated to be about 138 ± 92 nm. Thus, according to PAS and the studies of Oberdorfer and Würschum [24] or Puff et al. [25] this fact allows to exclude the possibility that grain boundaries are enriched in Y.

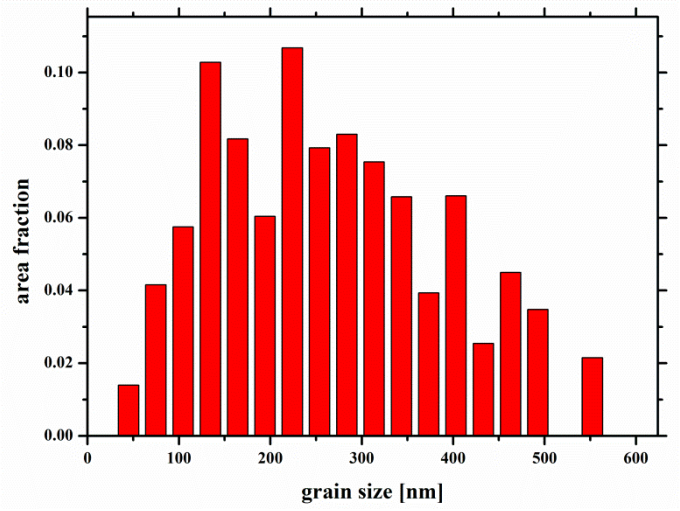

Fig. 5: Grain size distribution as determined by EBSD. It demonstrates that the majority of the scanned area (see Fig. 3) is occupied with grains exhibiting diameters above 100 nm.

3.3. Atom probe tomography (APT)

APT measurements can elucidate the remaining unknown questions concerning the type of "open" volume where Y atoms preferably arrange. Therefore, the distribution of Y and O atoms and other elements in as-milled powder particles were investigated. As shown in Figs. 6a and b Y and O atoms exhibit a distribution in a very fine manner already after 12 h of milling. Nevertheless, APT measurements reveal that Y and O enrich in clusters. Moreover, in previous works it has been proven that the solubility of Y and O, and also of other elements, seems to be extended in the Fe matrix [2,3].

Furthermore, Fig. 6c shows the Mn atom distribution in the same atom probe tip. Visual inspection gives a hint that Mn is enriched at some positions in the specimen. As the shape of these enriched positions is two-dimensional it is assumed that Mn is enriched at grainboundaries and/or interfaces between "cold-welded" powder particles. To get a better impression of the shape and size of this interface it is displayed in an isoconcentration surface [27]. In Fig. 6d a reconstruction of the particle tip containing isoconcentration surfaces at 0.6 at.% of Mn is depicted in yellow.

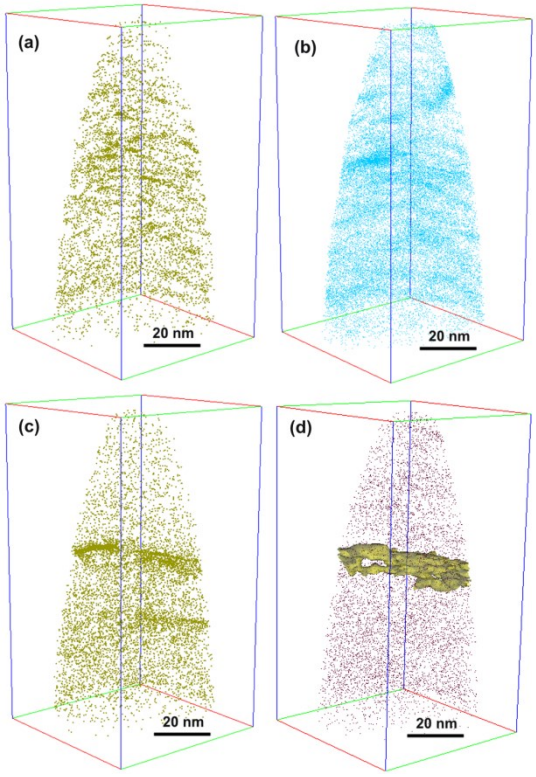

Fig. 6: 3D atom map of a 12 h milled state, presenting Y atoms (a), O atoms (b) and Mn atoms (c) as well as showing a reconstruction with a 0.6 at.% Mn isoconcentration surface in (d).

An enrichment of Mn can be found at an interface marked by an isoconcentration surface. Using these isoconcentration surfaces, so-called proximity histograms [28] can be calculated as depicted in Fig. 7. A proximity histogram gives the average concentration profile normal to the isoconcentration surface. This profile was calculated to determine whether the clusters are enriched or depleted in different elements. From Fig. 7 it is obvious that the interface is enriched in Mn and O, whereas for Y, Al and W no enrichment is found.

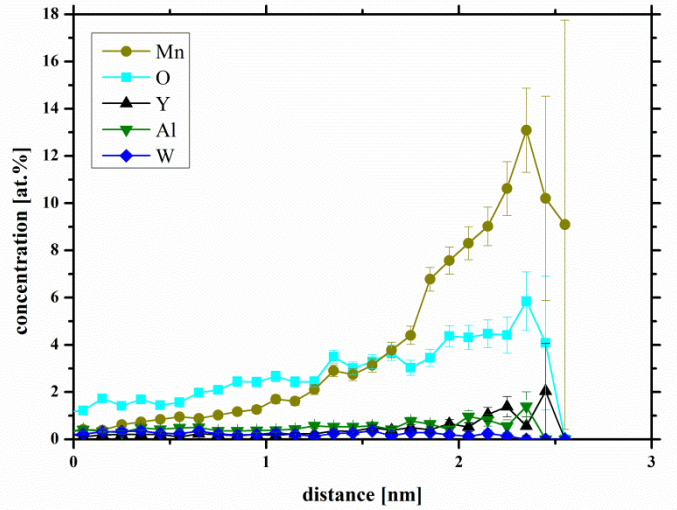

Fig. 7: Proximity histogram of the 0.6 at.% Mn isoconcentration surface shown in Fig. 6d. For an improved visibility the illustration of Fe is omitted. Enrichments of Mn and O can be detected at these interfaces, whereas Y, Al and W do not show such effects.

Additionally, measurements of the 48 h milled specimens presented in Fig. 8 show Cr enriched interfaces with a distance of about 100 nm or larger. The Cr and Mn enriched interfaces are marked with arrows in Figs. 8a and b. Moreover, Figs. 8c and d present the reconstructed APT measurements of the elements Y and O. However, an enrichment of Y atoms is not proven. Furthermore, in this stage Y and O atoms are arranged in clusters and these clusters are distributed homogenously, suggesting that no enrichment at one- or two-dimensional defects is present. All in all, in both milling states these enriched interfaces were detected in distances of 100 nm or larger (as shown in Fig. 6 and Fig. 8), which agrees with the EBSD results.

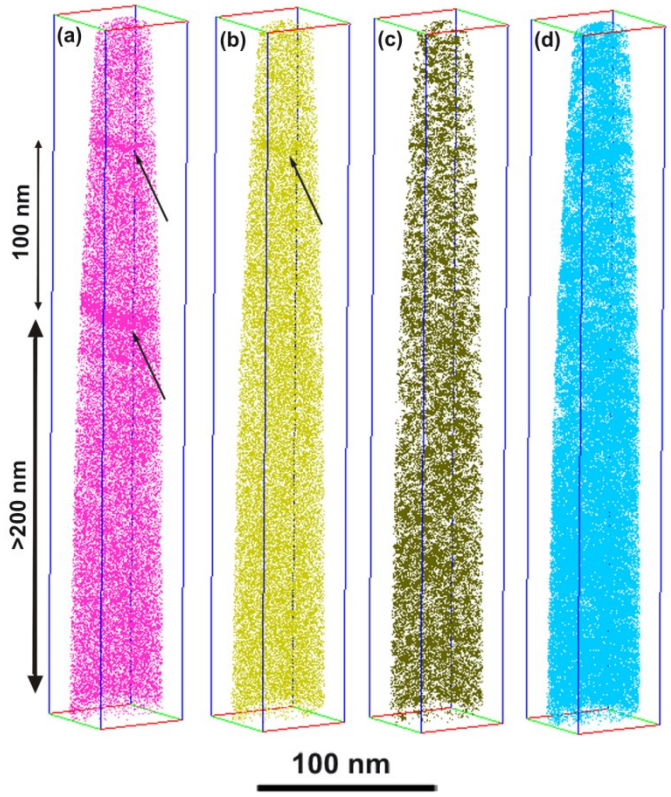

Fig. 8: 3D atom maps of the powder which was mechanically alloyed for 48 h. Cr (a), Mn (b), Y (c), and O (d). Interfacial enrichments of Cr and also slightly of Mn can be observed. The distance of the interfaces (marked by arrows) is 100 nm or larger. Y and O are not enriched at the interface, but form homogenously distributed clusters.

4. Discussion

In order to get a better understanding of the mechanisms occurring during the last stages of mechanical alloying in the framework of this study a comprehensive set of experimental techniques were combined. Positron annihilation experiments give detailed information about the "open" volume defects introduced by mechanical alloying as well as their chemical environment. The results of the Doppler broadening spectroscopy are presented in Fig. 2. They clearly reveal an increase of the Y atoms at the "open" volume, created during milling, where positrons annihilate. A numerical analysis gives an approximate content of about 52 % Fe and 48 % Y around the positron annihilation sites. These results suggest that Y is enriched at the "open" volume of the material, because only an overall content of about 0.048 at.% Y (derived from 0.132 at.% Y_2O_3) was added to the system prior to the milling process, which is much lower than the estimated content at the annihilation sites. Further milling does not change the high momentum signature of the 2d-Doppler broadening spectra significantly. Thus, it can be

concluded that the Y arrangement is akin in all milling states and further milling has only a slight influence on the arrangement of Y atoms. Additionally, positron lifetime measurements listed in Table 2 can give a hint at which defects positron annihilation occurs. Mechanically alloyed powder particles show a short lifetime (τ_1) of 186 ps and a longer second lifetime (τ_2) of 355 ps, whereas the unmilled reference powder showed an even shorter τ_1 and an even longer τ_2. The second positron lifetime τ_2 can usually be attributed to positron annihilation at particle surfaces and is a typical feature found in compressed powder samples as reported in [29,30]. The positron lifetime τ_1 of 160 ps in the reference sample, which is larger than the positron lifetime in defect-free iron of 110 ps [30,31], indicates the existence of a large amount of "open" volume defects, such as dislocations ($\tau_d \sim$ 150-167 ps [32–34]), grain boundaries ($\tau_{GB} \sim$126-174 ps [35,36]), impurity stabilized vacancies ($\tau_{v\text{-}imp} \sim$165 ps [31,37]) or monovacancies ($\tau_{vac} \sim$ 175 ps [31,32,37]). After milling for 12 h, the positron lifetime τ_1 increases to 186 ps. Because of limited resolution (positron lifetimes within 50 ps cannot be numerically separated) this positron lifetime cannot be attributed to a single type of "open" volume defect, but derives from a mixture of defect lifetimes in the range of 160 ps to 210 ps. However, this increase of the lifetime suggests the creation of larger "open" volumes in the material, such as divacancies ($\tau_{2vac} \sim$ 210 ps [31,34,38]). Furthermore, the decrease of τ_2 to 355ps after milling is attributed to positron trapping at vacancy-clusters with a cluster size of about 10-15 vacancies [34,38]. These PAS results almost agree with those of Lee [39], although lifetime measurements differ slightly. Lee investigated Fe powders containing 1 m.% yttria were 12 h milled, which differs from the experimental setup of this work. Additionally, Alinger et al. [40] studied only HIPed U14YWT material with 0.25 m.% Y_2O_3, which is a ferritic Fe–14Cr–3W–0.4Ti–0.25Y_2O_3 steel. Although assumptions about the milling mechanisms cannot be made with HIPed specimens, the authors also derived that about 50 % of annihilations occur at Y-Ti-O features, which almost agrees with results of investigations on milled powder particles performed in this work.

However, as already mentioned, due to limited resolution, annihilation at nano-crystalline grain boundaries or dislocations cannot be excluded definitely by PAS. The information of the crystallite grain size can help to obtain a more precise result. In Lee's work [39] experimental evidence is missing to exclude enrichment at grain boundaries or dislocations. Thus, in the present work the grain size was determined in order to exclude Y enrichments at grain boundaries. According to the studies described in [24,25]

it can be assumed that for grain sizes well beyond 100 nm dominant positron trapping at grain boundaries, and consequently Y enrichment, can be excluded because the positron diffusion length is limited to about 100 nm.

Therefore, EBSD measurements were employed to reveal the grain size of mechanically alloyed particles. After 12 h of milling the grain size distribution showed an average grain size of about 130 nm as well as a great majority of area fraction far beyond 100 nm in grain diameter (Fig. 5). Therefore, the results of EBSD, and τ_1 from positron lifetime experiments reveal that a simple Y enrichment at grain boundaries after 12 h of milling can be excluded. This result can also be related to the 24 h and 48 h milled states, because in these states an even more homogenous distribution is expected. Considering the results of up to 12° misorientation inside one single grain, which is plotted in Fig. 4, EBSD investigations also indicate a high concentration of defects inside crystallite grains of milled powder particles. This hypothesis agrees with the one derived from PAS. To get more detailed information about the distribution of Y in milled Fe powders, additional APT measurements were conducted.

APT allows a reconstruction of materials with atomic resolution. Investigations of the 12 h milled as well as of the 48 h milled state revealed Y and O atoms distributed in a very fine manner. The Y and O atoms form extremely small clusters, which are distributed homogenously in the Fe matrix. The spherical shape of these detected clusters, their distribution and how they are formed give a hint that they are enriched at randomly distributed vacancies. In the work of Pogatscher et al.[41] also Mg and Si enriched so-called co-clusters bound to quenched-in vacancies were detected in an Al-Mg-Si alloy by means of APT. Furthermore, Kelly and Nicholson described in their work the correlation between clusters and vacancies by using the example of aluminium alloys [42]. For our materials both EBSD and PAS suggest an extremely high defect density inside the grains. Enrichments at dislocation lines, so-called Cottrell clouds, are expected to be one-dimensional with a linear shape, which was shown for C in the work of Pereloma et al. [43]. However, Y is not enriched in linear shapes and, consequently, dislocation enrichments and pipe diffusion can be excluded during the last stage of milling. Additionally, APT measurements revealed interfaces enriched in Cr or Mn, but they were not enriched in Y (Fig. 8). Cr and Mn are incorporated due to abrasion of the grinding media during milling. These Cr or Mn enriched interfaces are supposed to be grain boundaries or fine lamellae caused by the severe plastic deformations during

particle-ball impacts. Other studies also evidenced grain boundary enrichment with Cr or Mn [43–46]. All in all grain boundary diffusion and dislocation diffusion cannot be excluded during the first stages of milling, however, APT combined with PAS and EBSD show that diffusion by support of deformation-induced vacancy-type defects is the most likely mechanism in the last stage of mechanical alloying. It is well known that single atom vacancies in Fe become mobile at temperatures of about -50°C [31,37]. This is significantly lower than the deformation temperature during milling, which is estimated to be far above the room temperature [17,18]. However, vacancies may be stabilized by impurity atoms even at higher temperatures [31], but can also be mobilized by plastic deformation to act again as diffusion accelerator, as reported by Kelly and Nicholson [42]. Ab-inito calculations in [3] agree with these findings suggesting that an attractive force exists between vacancies and substitutional Y atoms in the Fe matrix, because it is energetically most favorable if a Y atom and a vacancy are next nearest neighbors. Furthermore, it is assumed that not heat energy but mainly mechanical energy, which is introduced into the particles by continual ball impacts, is the driving force for Y-motion in Fe. This energy promotes these diffusional effects, e.g. site exchange of a vacancy and a Y atom, and helps to overcome the diffusion energy barrier.

5. Conclusion

The results of the PAS, EBSD and APT experiments employed in this work lead to the following conclusions:

- The mechanism occurring during milling is most likely diffusion-assisted intermixing with the aid of defects.
- During the first stages “open” volumes, such as grain boundaries, dislocations and vacancies are assumed to assist intermixing of both constituents.
- Investigations of the last stage, directly after mechanical alloying, revealed vacancies to be enriched in Y and O by forming clusters.
- Therefore, it can be concluded that especially during the last stage of mechanical alloying, these vacancies are responsible for the metastable distribution of Y and O in an extremely fine manner.

- All in all, it is assumed that a combination of following effects can cause dissolution of Y in ferrite, resulting in a metastable matrix. First of all, the diffusion with the help of vacancies as well as the extremely high surface area due to the small size of the powder particles have a positive effect on dissolution. Furthermore, not heat energy but mainly mechanical energy, introduced into the particles by ball impacts, promotes these diffusional effects and helps to overcome the diffusion energy barrier. In addition, shearing by dislocation glide can also contribute to the dissolution of Y in Fe during the last stage of milling.

Acknowledgements

The authors want to thank Dr. J. Zbiral and the TU Wien for using their instruments and for their help during processing.

References

[1] Suryanarayana C. Prog Mater Sci 2001;46:1.

[2] Ressel G, Primig S, Leitner H. Int J Mater Res in press.

[3] Ressel G, Holec D, Fian A, Mendez-Martin F, Leitner H. Appl Phys A in press.

[4] Ressel G, Primig S, Leitner H. Metall Mater Trans A in press.

[5] Miller MK, Hoelzer DT, Kenik EA, Russell KF. J Nucl Mater 2004;329-333:338.

[6] Miller MK, Russell KF, Hoelzer DT. J Nucl Mater 2006;351:261.

[7] Hirata A, Fujita T, Wen YR, Schneibel JH, Liu CT, Chen MW. Nat Mater 2011;10:922.

[8] Klimiankou M. J Nucl Mater 2004;329-333:347.

[9] Roesler J, Arzt E. Acta Met 1988;36:1043.

[10] Arzt E, Roesler J. Acta Met 1988;36:1053.

[11] Arzt E, Wilkinson D. Acta Met 1986;34:1893.

[12] Roesler J, Arzt E. Acta Met Mater 1990;38:671.

[13] Ashkenazy Y, Vo NQ, Schwen D, Averback RS, Bellon P. Acta Mater 2012;60:984.

[14] Odunuga S, Li Y, Krasnochtchekov P, Bellon P, Averback R. Phys Rev Lett 2005;95:045901.

[15] Vo NQ, Odunuga S, Bellon P, Averback RS. Acta Mater 2009;57:3012.

[16] Schwarz RB. Mater Sci Forum 1998;269-272:665.

[17] Schwarz R., Koch CC. Appl Phys Lett 1986;49:164.

[18] Pustov LY, Kaloshkin SD, Tcherdyntsev VV, Tomilin IA, Shelekhov EV, Salimon AI. Mater Sci Forum 2001;360-362:373.

[19] Miller MK, Russell KF. Ultramicroscopy 2007;107:761.

[20] Miller MK, Russell KF, Thompson GB. Ultramicroscopy 2005;102:287.

[21] Puff W, Rabitsch H, Wilde G, Dinda GP, Würschum R. J Appl Phys 2007;101:123512.

[22] Puff W. Comput Phys Commun 1983;30:359.

[23] Somoza A, Petkov M, Lynn K, Dupasquier A. Phys Rev B 2002;65:094107.

[24] Oberdorfer B, Würschum R. Phys Rev B 2009;79:184103.

[25] Puff W, Zhou X, Oberdorfer B, Scherwitzl B, Parz P, Sprengel W, Würschum R. J Phys Conf Ser 2013;443:012033.

[26] Puska MJ, Lanki P, Nieminen RM. J Phys Condens Mater 1989;1:6081.

[27] Hellman OC, du Rivage JB, Seidman DN. Ultramicroscopy 2003;95:199.

[28] Hellman OC, Vandenbroucke JA, Isheim D, Seidman DN. Microsc Microanal 2000;6:437.

[29] Staab TEM, Krause-Rehberg R, Kieback B. J Mater Sci 1999;34:3833.

[30] Schaefer H, Würschum R, Birringer R, Gleiter H. Phys Rev B 1988;38:9545.

[31] Vehanen A, Hautojärvi P, Johansson J, Yli-Kauppila J, Moser P. Phys Rev B 1982;25:762.

[32] Hidalgo C, González-Doncel G, Linderoth S, San Juan J Phys Rev B 1992;45:7017.

[33] Schaefer HE, Würschum R. Phys Lett A 1987;119:370.

[34] Mohamed HFM, Kwon J, Kim Y-M, Kim W. Nucl Inst Meth Phys Res B 2007;258:429.

[35] Kuriplach J, Melikhova O, Hou M, Van Petegem S, Zhurkin E, Šob M. Phys Stat Sol 2007;4:3461.

[36] Kuriplach J, Melikhova O, Hou M, Van Petegem S, Zhurkin E, Šob M. Appl Surf Sci 2008;255:128.

[37] Hautojärvi P, Johansson J, Vehanen A, Yli-Kauppila J, Moser P. Phys Rev Lett 1980;44:1326.

[38] Puska MJ, Nieminen RM. J Phys F 1983;13:333.

[39] Lee JH. J Nanosci Nanotechnol 2012;12:1670.

[40] Alinger MJ, Glade SC, Wirth BD, Odette GR, Toyama T, Nagai Y, Hasegawa M. Mater Sci Eng A 2009;518:150.

[41] Pogatscher S, Antrekowitsch H, Leitner H, Ebner T, Uggowitzer PJ. Acta Mater 2011;59:3352.

[42] Kelly A, Nicholson RB. Prog Mater Sci 1963;10:151.

[43] Pereloma EV, Timokhina IB, Jonas JJ, Miller MK. Acta Mater 2006;54:4539.

[44] Chen Y, Schuh CA. Scr Mater 2007;57:253.

[45] Stender P, Balogh Z, Schmitz G. Ultramicroscopy 2011;111:524.

[46] Raabe D, Sandlöbes S, Millán J, Ponge D, Assadi H, Herbig M, Choi P-P. Acta Mater in press.

Publication D:

The effect of Zr incorporation caused by ball abrasion in a milled Fe-Y2O3 model alloy

G. Ressel, S. Primig and H. Leitner

accepted in Metallurgical and Materials Transactions A (2013).

The Effect of Zr Incorporation Caused by Ball Abrasion in a Milled Fe-Y_2O_3 Model Alloy

GERALD RESSEL, SOPHIE PRIMIG, and HARALD LEITNER

Y-O nanoparticles which are homogeneously distributed in the matrix can improve the thermal properties of steels. Several studies of mechanically alloyed steels showed that especially Y-Ti-O particles can cause a further improvement of the mechanical properties at elevated temperatures. It is also assumed that an addition of Zr instead of Ti may have a similar or even stronger effect. This study presents a new way of producing nanostructured ferritic alloys as Zr is incorporated by attrition of yttrium-stabilized zirconia balls during milling. Additionally, the effect of Zr incorporation is demonstrated as well as the particle size distribution of the Y-Zr-O nanoparticles analyzed by transmission electron microscopy. This is compared to a specimen milled with common steel balls. Atom probe tomography and transmission electron microscopy show that the incorporated zirconia lowers the minimum particle size and causes a finer particle distribution. This particle refinement causes a higher hardness after hipping.

DOI: 10.1007/s11661-013-2052-9

I. INTRODUCTION

IN the last few years, mechanical alloying became quite popular as it is a method to distribute fine yttria powders in steel powders in order to improve the thermal properties of steels.[1–5] Especially for fuel claddings in fast breeding reactors mechanically alloyed steel is a promising candidate. It is known that milling causes a metastable dissolution of yttria in Fe and, subsequently, a formation of Y-O particles in nanometer scale.[6] However, besides yttria also other alloying elements have a very strong effect on the thermal properties of ODS steels. Ukai *et al.*[7,8] found out that the addition of a small amount of Ti can enhance the effect of the Y-O clusters and further improve the mechanical properties at elevated temperatures. Transmission electron microscopy (TEM) investigations on such alloys were employed for example by Klimiankou[9] and Hirata *et al.*[10] Klimiankou found an orientation correlation of a nanometer-sized particle with a 9Cr ferritic alloy lattice. Using energy-filtered (EF)-TEM, he verified Y-Ti-O particles with a stoichiometry of $Y_2Ti_2O_7$. Hirata made 3D structure modeling of a (Ti, Y, Fe, Cr)O nanocluster by C_s corrected TEM. He concluded that these clusters have a defective NaCl structure and a high degree of lattice coherency with the bcc steel matrix. Furthermore, Nomura *et al.*[11] investigated the effect of other alloying elements such as Zr besides Ti. In the case of Ti as alloying element, they detected fine complex oxides as Y_2TiO_5 and $Y_2Ti_2O_7$ besides the original Y_2O_3. They suggested that Ti can decompose Y_2O_3 to produce such fine complex oxides. They concluded that also Zr, Nb, and V are effective in strengthening the ODS 12Cr ferritic steel. This strength improvement is mainly attributed to the refinement of the particles. Uchida *et al.*[12] investigated the effect of minor alloying elements on dispersed nanoparticles in ODS steels. They reported that Ti, Zr as well as Hf have a strong effect of cluster refinement. By the formation of an oxide with the stoichiometry $Y_xM_yO_z$ with the minor alloying element M (*e.g.*, Ti), the enthalpy of formation should decrease compared to common yttria. They assumed that the lower the diffusivity of the alloying element M is the higher is the stability of its oxide and the smaller are the resulting particles. Recently, Unifantowicz *et al.*[13] published a statistical analysis of oxide particles in an ODS ferritic steel alloyed with Ti using TEM. Several atom probe tomography (APT) measurements especially on as-consolidated Cr- and Ti-alloyed ferritic steels were conducted in order to reveal the cluster composition and size.[2,14,15] These publications also showed that Ti is enriched at the Y-O particles and their mean radius is ~2 nm.

Up to now Ti or Zr were added as simple alloying elements prior to milling. In this paper, a new way of producing a nanostructured ferritic alloy (NFA) for improved thermal properties is proposed. Alloying of Ti or Zr to the powders prior to milling can be economized using yttrium stabilized zirconia (YSZ) balls as grinding media resulting in Zr incorporation by the attrition of the balls during milling. To get insights into the basic mechanisms and to exclude effects of other alloying elements, these investigations concentrate on a Fe-Y2O3-Zr model alloy. The amount of Zr attrition during milling Y_2O_3 with pure iron powder is analyzed by X-ray fluorescence spectroscopy (XRF). Additionally, APT resolves the

GERALD RESSEL, Doctoral Student, is with the Department of Physical Metallurgy and Materials Testing, Montanuniversität Leoben, 8700 Leoben, Austria. Contact e-mail: gerald.ressel@unileoben.ac.at SOPHIE PRIMIG, Head of the Steel Group, is with the Department of Physical Metallurgy and Materials Testing, Montanuniversität Leoben, and also Scientist, with the Christian Doppler Laboratory for Early Stages of Precipitation, Montanuniversität Leoben. HARALD LEITNER, formerly Head of the Steel Group with the Department of Physical Metallurgy and Materials Testing, Montanuniversität Leoben, is now Employee with the Böhler Edelstahl GmbH and Co KG Company, Mariazellerstraße 25, Kapfenberg, Austria.
Manuscript submitted July 12, 2013.

Published online: 22 October 2013

Table I. Powder Compositions Before and After 12 h Milling with Steel and YSZ Balls (at. pct) Determined by XRF

	Fe	Mn	Cr	Ni	Mo	Zr	Y2O3
As-recieved	bal.	0.124	0.049	0.028	—	—	0.132
After Milling with Steel Balls	bal.	0.159	0.083	0.333	0.202	—	0.123
After Milling with YSZ Balls	bal.	0.113	0.082	0.041	—	0.564	0.133

distribution of zirconia and investigates whether there is a difference in minimum particle size or composition compared to a common steel ball milled iron model alloy. Particle size distributions are obtained by TEM investigations in order to analyze the effect of Zr attrition also on larger particles. Finally, the comparison of hardness measurements clarifies if Zr attrition has a beneficial effect on mechanical properties.

A. *Experimental*

A ferritic iron powder and 0.5 wt pct yttria powder with a d_{90} = 1.16 μm and a purity of 99.9 pct were blended in a tumbling mixer for 30 minutes prior to mechanical alloying. Afterward, the mixture was milled in a Certony™ attritor under Ar-gas atmosphere for 12, 24, and 48 hours. Common steel balls and YSZ balls with a composition of 95 wt pct ZrO_2 and 5 wt pct Y and a density of 6.05 g cm^{-3} were used for milling. In both cases, the ball-to-powder ratio (BPR) was 10:1 and the milling speed 600 rpm. The chemical composition of the individual powders before and after milling is listed in Table I. It should be noted that all compositions presented in this paper are given in at. pct. Chemical compositions and especially the Y and Zr contents were measured by a wavelength-dispersive Axios PANalytical™ X-ray fluorescence spectrometer. A fundamental parameter calibration applying the program UniQuant™ was used.

After mechanical alloying, the milled powders were hot isostatically pressed (hipped) at a temperature of 1373 K (1100 °C) and a pressure of 100 MPa for a duration of 3 hours.

APT investigations were performed on the as-hipped specimens using a Cameca™ Local Electrode Atom Probe (LEAP™) 3000X HR. For the preparation of atom probe tips of the consolidated materials, small rods with a cross-section of 0.3 × 0.3 mm^2 and a length of 10 mm were cut out of the bulk materials. Furthermore, the tips were prepared by the standard electrochemical polishing method.[16] Several measurements on both specimens were carried out in voltage or laser mode, applying a pulse fraction of 20 pct and a laser energy of 0.5 nJ at a base temperature of 60 K (−213 °C). The data reconstruction procedure was carried out with the Cameca™ software IVAS 3.4.3.

TEM experiments were conducted on a Philips™ TEM CM12 with a camera constant of 680 Å cm at a length of 680 mm and an operation voltage of 120 kV. Specimens were prepared by the electrochemical standard method.[17]

Hardness measurements (HV5) were carried out on an Emco™ Vickers hardness measuring instrument. Five indents were made on each specimen.

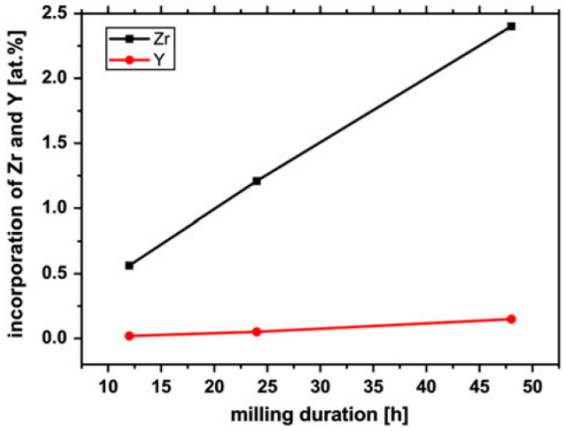

Fig. 1—Incorporation of zirconia and Y against the milling duration. The diagram shows a constant incorporation during milling.

II. RESULTS

In order to reveal the effect of Zr attrition on the thermal properties of mechanically alloyed iron, two alloys were produced. The first alloy was milled with YSZ balls while for the second alloy common steel balls were used. In the following section, the results of these alloys studied by XRF, APT, TEM, and HV5 are compared.

A. *Incorporation of Zr*

In order to reveal the amount of Zr incorporated in Fe, XRF measurements were conducted. For the processing of mechanically alloyed Fe, it is important to study the incorporated amount as a function of the milling time. Parameters such as ball-to-powder ratio (BPR) as well as milling speed and milling duration are the main influences and should be considered. In the present investigation only YSZ balls were used as grinding media. The incorporation of Zr and Y in at. pct *vs* the milling duration is shown in Figure 1. Abrasion of the YSZ balls caused the intended incorporation of Y and Zr. The graph reveals that the attrition process is constant, which means that Zr is continuously incorporated during milling. Consequently, the process is also predictable. According to the XRF measurements of the individual milled states a constant incorporation rate of about 0.05 and 0.003 at. pct/h is determined for Zr and Y, respectively. This means that after 48 hours mechanical alloying a content of 2.4 at. pct Zr is incorporated. XRF analysis of the 12 hours state reveals a Zr incorporation of 0.563 at. pct, which is similar to the range of Zr additions in the work of Nomura *et al.*[11] and is supposed to be an

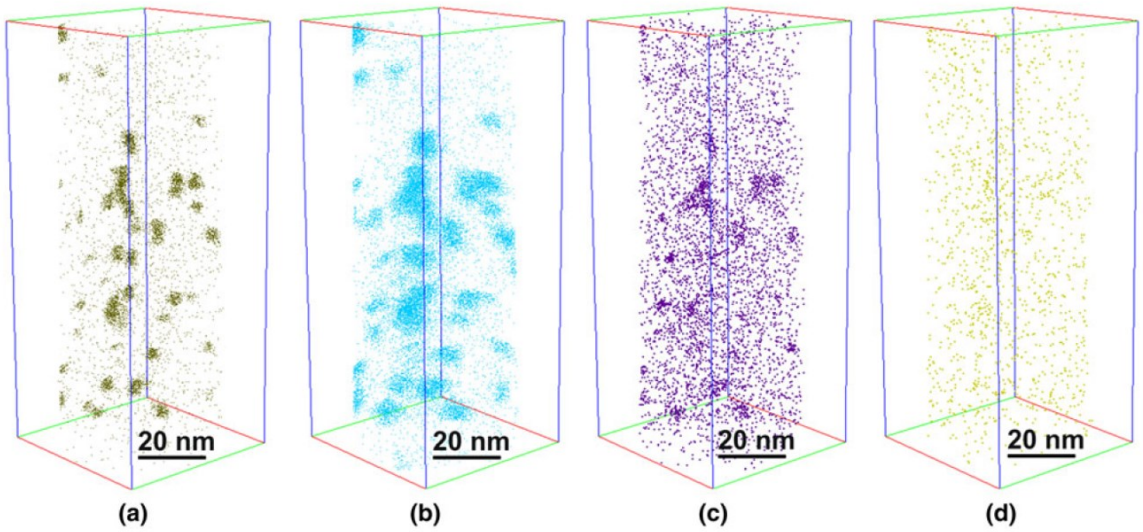

Fig. 2—3D atom maps of the specimen which was produced by Zr attrition showing clusters enriched in Y (*a*), O (*b*), ZrO (*c*), and Mn (*d*).

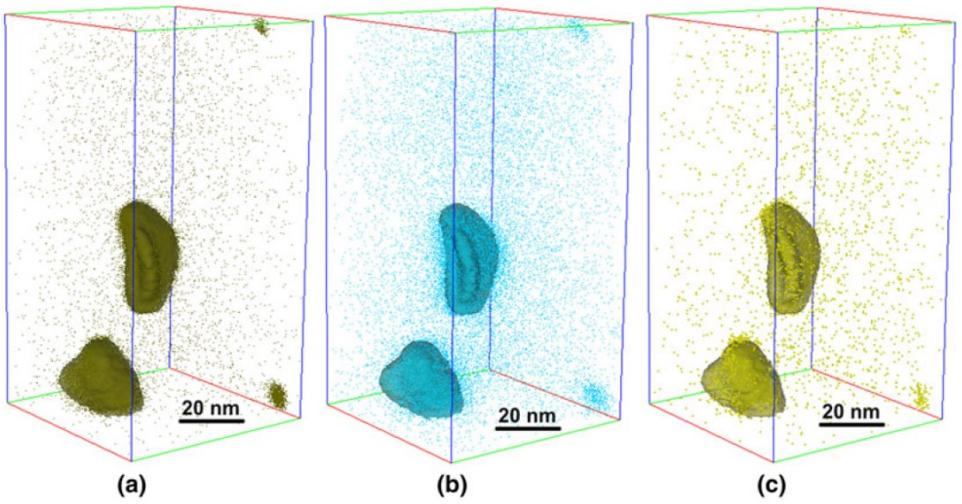

Fig. 3—3D atom maps illustrating particles of the specimen milled with steel balls. Y (*a*), O (*b*), and Mn (*c*) are enriched at these clusters. For a better visibility, the larger particles are shown with Y 7 at. pct isosurfaces.

effective amount of Zr. Therefore, the 12 hours conditions are further analyzed in this work.

B. *Atom Probe Investigations of the Nanoparticles*

In order to investigate the distribution of Zr in the YSZ ball sample and to compare the Y-O nanoparticles of the conditions milled for 12 hours with steel and YSZ balls, APT measurements were employed. An example of 3D reconstructions of the sample milled with YSZ balls is shown in Figure 2. In this specimen, a high amount of small clusters are present which are enriched in Y, O, Mn as well as Zr. Abrasion of the YSZ balls results in a very fine distribution of ZrO ions in the Fe matrix and enrichments of these elements even in the smallest particles. The APT reconstruction of the sample milled with steel balls is depicted in Figure 3. Y-O particles, which are also enriched in Mn can be seen. Here, a bimodal particle distribution with a low amount of small particles but also coarser particles can be detected. The larger particles are shown with 7 at. pct Y isosurfaces for improved visibility. In this measurement, their shape is not perfectly spherical as shown in Figure 3. Visual inspection of several atom probe measurements of both samples reveals a much higher amount of only small particles in case of the YSZ ball specimen; whereas, at the steel ball sample, a higher amount of coarser particles compared to the YSZ ball sample is detected.

The clusters in both samples were analyzed by a standard cluster search algorithm.[18,19] Parameter studies

Table II. Comparison of the Average Radius of Gyration (R_g) and the Mean Particle Composition of the Specimen Milled with Steel Balls and YSZ Balls Determined by a Standard Cluster Search Algorithm

	R_g (nm)	Fe (at. pct)	Y (at. pct)	O (at. pct)	Zr (at. pct)	Mn (at. pct)	Y/O	Zr/Y
12 h Milling with Steel Balls								
mean value	1.76 ± 1.22	bal.	5.06	7.78	—	0.32	0.65	—
coarser particles	6.18 ± 1.17	bal.	12.86	24.62	—	0.45	0.52	—
smaller particles	1.448 ± 0.413	bal.	6.36	10.10	—	0.27	0.63	—
12 h Milling with YSZ Balls	1.26 ± 0.12	bal.	5.34	7.74	0.54	0.12	0.68	0.263

revealed that in both specimens, the same parameters can be chosen. The separation distance, the surrounding distance, and the erosion distance have all been set to 0.7 nm, respectively. To exclude randomly distributed atoms identified as clusters and to analyze the composition of the particles by the cluster search algorithm, the minimum cluster size has been set to 31 atoms.

In Table II, the results of both samples are compared. The mean radius of gyration, which enables a size comparison of clusters with different shape, is in case of the steel ball specimen more than 0.5 nm larger than in case of the YSZ ball sample. The standard deviation of the mean value of the steel ball specimen is 1.22 nm and, therefore, higher than the standard deviation in case of YSZ ball specimen. This can be related to the bimodal particle distribution in the steel ball specimen, where also larger particles are present besides the smaller particles. Hence, in Table II, the particles of the steel ball sample were divided in coarser and smaller particles. At a R_g beyond 3 nm, each particle was counted to the coarser particles. It should be mentioned that the Fe concentration in the particles is overestimated due to atom probe uncertainties during measurements. Field ion microscopy investigations revealed that these Y-O nanoparticles show a preferential evaporation compared to the Fe matrix.[20] Therefore, tip irregularities occur during APT measurement resulting in lower local magnification and increased amount of matrix atoms inside detected nanoparticles. Also the shape of the particles can differ from the real appearance.[21,22] As a consequence, the Y, O, Zr, Mn concentrations are underestimated by the cluster search algorithm. This effect is less pronounced at the larger particles. Therefore, the underestimation is lower in case of these particles. The analysis of the composition of the particles shows that in the YSZ specimen a content of 0.54 at. pct Zr is measured, whereas Mn is enriched in the particles milled with the steel balls. Furthermore, the Y and O content is approximately the same in both specimens. Hence, the Y/O ratio of both samples is approximately equal, suggesting that these particles have a similar stoichiometric composition. Also the Y/O ratio of the larger and smaller particles is nearly similar. The Y/O ratio for the YSZ ball and the steel ball sample is 0.68 and 0.65 (0.52 for the coarser particle and 0.63 for the smaller), respectively.

C. *TEM Investigations*

In order to gain information about the particle size distribution of particles larger than 5 nm in diameter, TEM investigations were employed. Figure 4 shows a comparison of TEM images illustrating the microstructures of the hipped specimens milled with steel and YSZ balls. Most of the particles, which appear as dark regions in Figure 4, are in the range between 2 and 10 nm in diameter in both specimen and, therefore, the distribution is extremely fine. However, a higher amount of these extremely small particles can be detected in the YSZ ball-milled sample than in the steel ball-milled specimen.

Figure 5 compares the particle size distributions of both samples, which were determined by several TEM images. This evidences that a finer particle distribution can be measured in the YSZ specimen. This agrees with the results of APT, suggesting that after hipping a finer distribution of particles is available. The highest amount of particles can be found between 4 and 6 nm in diameter in the YSZ sample. Hence, the average particle diameter is 10.49 nm. On the contrary, the steel ball specimen shows a maximum between 8 and 10 nm and a higher amount of coarser particles leading to a mean particle diameter of 15.88 nm. Consequently, also the particle size distributions of the TEM investigations evidence that milling with YSZ balls causes a finer distribution of the analyzed particles.

In order to determine the composition of the coarse particles in TEM, energy dispersive X-ray (EDS) measurements were conducted. The analyzed particles of both specimens are shown in Figure 6. The quantitative EDS analysis of a particle in each specimen is shown in Table III. It suggests that these spherical particles consist of Y, O, Cr, Mn, and Fe in the case of the steel ball specimen. In case of the YSZ ball specimen particles exhibiting a size of about 50 nm in diameter are additionally enriched in Zr. The Zr content in the particles is with 13.2 at. pct much higher than detected in APT. Fe is probably overestimated due to iron matrix influence. The particle composition differs from the nanoparticles analyzed by atom probe. Therefore, it is suggested that the coarser particles are a different sort of particles than the smaller clusters or that the matrix influence is too strong for proper analysis.

D. *Hardness Measurements*

To reveal the effect of a finer distribution of particles in the YSZ ball specimen on the mechanical properties, HV5 at room temperature were conducted. The reference specimen milled with steel balls showed a hardness of 169 ± 2.6 HV5, whereas the YSZ ball sample exhibited a hardness of 190 ± 4.5 HV5. Thus, a Zr attrition of 0.563 at. pct after 12 hours milling leads to the finer distribution of the oxide particles after hipping and this

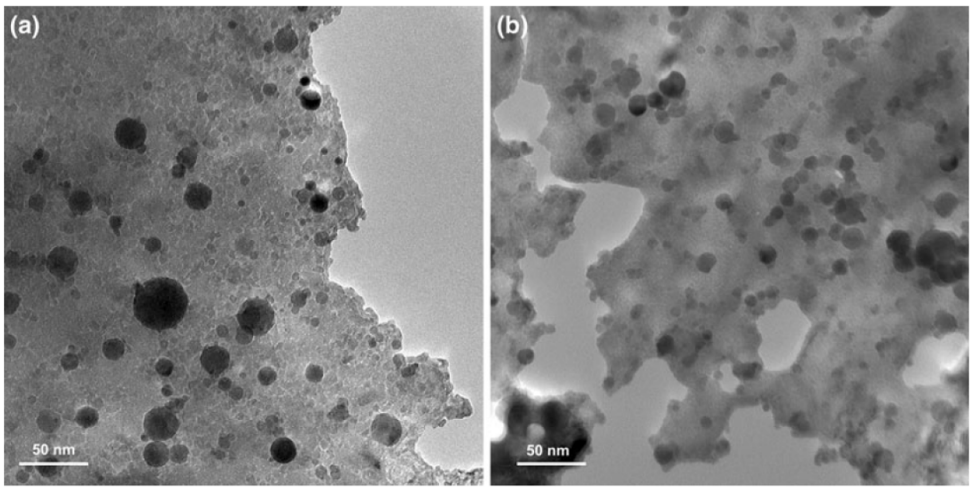

Fig. 4—TEM image of the hipped condition milled for 12 h: with YSZ balls (*a*) and steel balls (*b*). The dark appearing regions are particles.

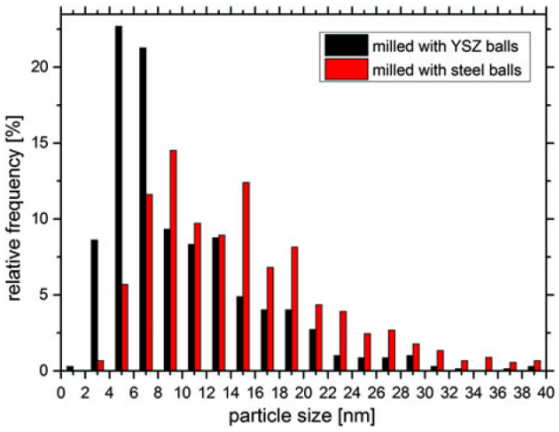

Fig. 5—Particle size distributions of YSZ and steel ball-milled specimens.

causes an increase in hardness even at room temperature. Due to results of previous works, it is assumed that these particles improve the mechanical properties also at elevated temperatures.[7,11]

III. DISCUSSION

In 1989 Nomura *et al.*[11] and also in 2007 Uchida *et al.*[12] added Zr as alloying element to the mechanical alloying system and proposed a positive effect in mechanical properties at elevated temperatures. A new and improved way of producing a nanostructured yttria-iron-model-alloy is proposed in this paper, where no Zr addition is necessary. During this new milling procedure, YSZ balls are used instead of common steel balls. As the YSZ has a density of 6.05 g cm^{-3}, which is near to the density of steel, the milling behavior of these balls is rather similar to steel balls. Abrasion of the YSZ balls causes an intended incorporation of Zr and Y in the Fe powder. Therefore, an advantage of this new way of production is an easier and cheaper way of preparing advanced Zr-doped ODS steels, as the alloying addition of Zr is economized compared to the common way of production. However, due to the limited toughness of YSZ, lower milling speed can be required compared to steel balls to impede a cracking of the balls. Nevertheless, in this work, 12 hours milling at a speed of 600 rpm caused no fracture of the YSZ balls. As proposed in Reference 6 milling causes a metastable dissolution of the yttria powder in Fe. The particles analyzed in the present work show in both specimens a Y/O ratio between 0.5 and 0.7. These ratios agree approximately with the typical ratio of Y_2O_3 (about 0.67). However, enrichments of Zr or Mn show that these particles are not original yttria powder particles. This indicates the dissolution of the yttria powder, but also the dissolution of Y and zirconia originating from the balls. Hence, it can be proposed that it is possible to dissolve Zr and yttria in the material. A Zr incorporation of 0.5 to 0.6 at. pct is supposed to be the optimal amount. Therefore, the corresponding specimen milled with YSZ balls for 12 hours is analyzed in more detail. A high Zr incorporation is undesirable, because it is assumed that the toughness of the final alloy decreases dramatically with increasing Zr content. At lower Zr contents, no refinement of the clusters is expected. If higher milling durations with lower Zr incorporation amount are required, the use of balls with higher attrition resistance or a mixture of YSZ and steel balls as grinding media is suggested.

APT measurements on the YSZ ball milled specimen are compared to the common steel ball sample. Particles about 1 nm in radius are detected in both specimens. During the APT investigations of the YSZ ball sample, only these small particles are detected. In contrast, also larger particles can be detected in case of the steel ball sample. This bimodal particle distribution and the higher amount of coarser particles shown by APT measurements is related to the absence of Zr in the particles. Also, the particle size distribution and the

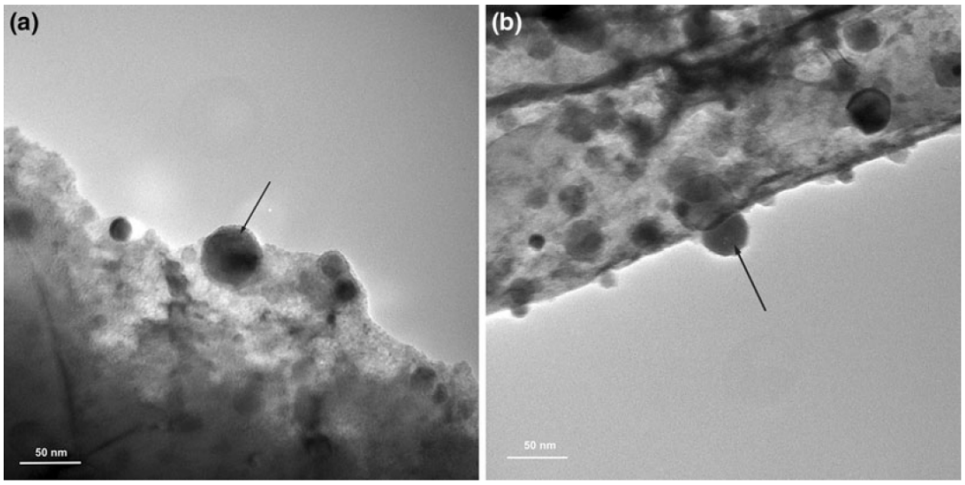

Fig. 6—TEM image of the particle (marked with an arrow), which was analyzed by EDS (Table III) in case of the YSZ ball specimen (*a*) and the steel ball specimen (*b*).

Table III. Quantitative EDS Analysis of Larger Particles in the Steel Ball and the YSZ Ball Specimen in at. pct

	Fe (at. pct)	Zr (at. pct)	Y (at. pct)	O (at. pct)	Cr (at. pct)	Mn (at. pct)	Y/O
12 h Milled with Steel Balls	39.4	—	4.3	52.7	2.2	1.4	0.08
12 h Milled with YSZ Balls	32.4	13.2	2.6	49.6	1.2	1.1	0.05

particle mean values of several TEM images agree with the APT results. Higher particle mean values from TEM images in contrast to APT results are explained by much larger particles taken into account. It can be concluded that Zr abrasion of the YSZ balls influences the formation of the smallest particles. As the amount of smaller particles in the YSZ ball sample after hipping at 1373 K (1100 °C) for 3 hours is higher, it can be concluded that the stability of these clusters and particle formation, *i.e.*, nucleation rate, is enhanced and particle growth during hipping is decreased in case of YSZ ball specimen. Murali *et al.*[23] employed first principles calculations of Y-Ti-O clusters suggesting that Ti improves the thermal stability of the Y-O clusters. He also proposed that the binding energies inside the clusters increase by replacing Ti by Zr. Therefore, he assumed that the improved stability by addition of Zr can contribute to an accelerated nucleation rate due to a lower diffusivity of the alloying element, which can lead to a finer distribution of the nanoparticles. He concluded that this may result in a further improved performance of the ferritc alloy. Also Uchida *et al.*[12] and Nomura *et al.*[11] reported a finer particle distribution because of Zr alloying addition. This is also the case in the present investigation. Due to the finer distribution and higher stability the use of YSZ balls has a positive effect on the hardness and strength, even at room temperature. Nevertheless, several works investigated the stability of these Y-O and Y-Zr-O particles against coarsening and evidenced that the mechanical properties also at elevated temperatures are, therefore, improved.[7,11]

Consequently, this study reveals that YSZ balls as grinding media have the same milling effect as steel balls, as the yttria powder dissolves in the iron powder. Additionally, the simple abrasion of the YSZ balls can improve mechanical properties of the final material as it can cause a finer distribution of Y-Zr-O particles. Therefore, an alloying addition of Ti or Zr can be economized.

IV. CONCLUSIONS

The microstructure as well as the hardness of a Fe-Y_2O_3 model alloys milled with YSZ balls and steel balls with similar milling parameters is compared. Moreover, the Zr incorporation during milling with YSZ balls as well as the composition of the particles is analyzed.

The new way of mechanical alloying causes a very fine Zr distribution and a refinement of the particle size in the hipped samples by simple attrition of YSZ balls. Also the minimum particle size is lower in case of the YSZ ball specimen, which has also a positive impact on the resulting hardness at room temperature. It is assumed that the addition of Zr improves the stability of the particles leading to smaller particle sizes.

ACKNOWLEDGMENTS

The authors want to thank the Institute of Chemical Technologies and Analytics at the University of

Technology in Vienna for the use of its facilities. The authors especially thank Dr. Johannes Zbiral helping at the mechanical alloying process.

REFERENCES

1. G.R. Odette, M.J. Alinger, and B.D. Wirth: *Annu. Rev. Mater. Res.*, 2008, vol. 38, pp. 471–503.
2. M.K. Miller, D.T. Hoelzer, E.A. Kenik, and K.F. Russell: *J. Nucl. Mater.*, 2004, vols. 329–333, pp. 338–41.
3. M.K. Miller, D. Hoelzer, E. Kenik, and K. Russell: *Internet*, 2005, vol. 13, pp. 387–92.
4. C.A. Williams, E.A. Marquis, A. Cerezo, and G.D.W. Smith: *J. Nucl. Mater.*, 2010, vol. 400, pp. 37–45.
5. C.A. Williams, P. Unifantowicz, N. Baluc, G.D.W. Smith, and E.A. Marquis: *Acta Mater.*, 2013, vol. 61, pp. 2219–35.
6. G. Ressel, S. Primig, and H. Leitner: *Int. J. Mater. Res.* DOI: 10.3139/146.110964.
7. S. Ukai, T. Nishida, T. Okuda, and T. Yoshitake: *J. Mater. Sci. Technol.*, 1998, vol. 35, pp. 294–300.
8. S. Ukai, T. Nishida, H. Okada, T. Okuda, M. Fujiwara, and K. Asabe: *J. Nucl. Sci. Technol.*, 1997, vol. 34, pp. 256–63.
9. M. Klimiankou: *J. Nucl. Mater.*, 2004, vols. 329–333, pp. 347–51.
10. A. Hirata, T. Fujita, Y.R. Wen, J.H. Schneibel, C.T. Liu, and M.W. Chen: *Nat. Mater.*, 2011, vol. 10 (12), pp. 922–26.
11. S. Nomura, T. Okuda, S. Shikakura, M. Fujiwara, and K. Asabe: *Solid State Powder Processing*, Metals & Materials Society, Indianapolis, 1989, pp. 203–11.
12. Y. Uchida, N. Ohnuki, N. Hashimoto, T. Suda, T. Nagai, T. Shibayama, K. Hamada, S. Akasaka, S. Yamashita, S. Ohstuka, and T. Yoshitake: *Mater. Res. Soc. Symp. Proc.*, 2007, vol. 981, pp. 107–12.
13. P. Unifantowicz, R. Schäublin, C. Hebert, T. Plocinski, G. Lucas, and N. Baluc: *J. Nucl. Mater.*, 2012, vol. 422, pp. 131–36.
14. D. Larson: *Scripta Mater.*, 2001, vol. 44, pp. 359–64.
15. M.K. Miller, E. Kenik, K. Russell, L. Heatherly, D. Hoelzer, and P. Maziasz: *Mater. Sci. Eng. A*, 2003, vol. 353, pp. 140–45.
16. M.K. Miller, A. Cerezo, M.G. Hetherington, and G.D.W. Smith: *Atom Probe Field Ion Microscopy*, Clarendon Press, Oxford, 1996, pp. 476–38.
17. H.J. Penkalla: *Proc. 1st Summer Sch. Adv. Electron Microsc.*, A. Czyrska-Filemonowicz and B. Dubiel, eds., 2003, pp. 4–23.
18. L.T. Stephenson, M.P. Moody, P.V. Liddicoat, and S.P. Ringer: *Microsc. Microanal.*, 2007, vol. 13, pp. 448–63.
19. D. Vaumousse, A. Cerezo, and P.J. Warren: *Ultramicroscopy*, 2003, vol. 95, pp. 215–21.
20. E.A. Marquis: *Appl. Phys. Lett.*, 2008, vol. 93 (18), p. 181904.
21. F. Vurpillot: *Appl. Phys. Lett.*, 2000, vol. 76, p. 3127.
22. M.K. Miller, A. Cerezo, M.G. Hetherington, and G.D.W. Smith: *Atom Probe Field Ion Microscopy*, Clarendon Press, Oxford, 1996, pp. 196–99.
23. D. Murali, B.K. Panigrahi, M.C. Valsakumar, S. Chandra, C.S. Sundar, and B. Raj: *J. Nucl. Mater.*, 2010, vol. 403 (1–3), pp. 113–16.

Publication E:

On the behavior of yttria/yttrium during mechanical alloying of a Fe – Y2O3 model alloy system

G. Ressel, P. Parz, A. Fian, D. Holec, S. Primig, W. Puff, H. Leitner and H. Clemens

Accepted in Materials Science Forum/Advanced Materials Research proceedings Thermec 2013 (2013).

On the behavior of yttria/yttrium during mechanical alloying of a Fe – Y_2O_3 model alloy system

Gerald Ressel[1,a], Peter Parz[2,b], Alexander Fian[3,c], David Holec[1,d], Sophie Primig[4,e], Werner Puff[2,f] Harald Leitner[1,g] and Helmut Clemens[1,h]

[1] Department of Physical Metallurgy and Materials Testing, Montanuniversität Leoben, A-8700 Leoben, Austria

[2] Institute of Materials Science, Graz University of Technology, A-8010 Graz, Austria

[3] Institute for Surface Technologies and Photonics, Joanneum Research Forschungsgesellschaft mbH, A-8160 Weiz, Austria

[4] Christian Doppler Laboratory for Early Stages of Precipitation, Montanuniversität Leoben, A-8700 Leoben, Austria

[a]gerald.ressel@unileoben.ac.at, [b]p.parz@tugraz.at, [c]alexander.fian@joanneum.at, [d]david.holec@unileoben.ac.at, [e]sophie.primig@unileoben.ac.at, [f]werner.puff@tugraz.at, [g]harald.leitner@unileoben.ac.at, [h]helmut.clemens@unileoben.ac.at

Keywords: mechanical alloying, yttria, iron, atom probe tomography (APT), positron annihilation spectroscopy (PAS), ab initio calculation, X-ray photoelectron spectroscopy (XPS)

Abstract. Mechanical alloying (MA) is an established way to prepare nanocrystalline materials and metastable solutions of materials, which normally have no mutual solubility. This is also the case for oxide dispersion strengthened (ODS) steels with improved mechanical properties at elevated temperatures. It is known that a small addition of yttria (Y_2O_3) has a beneficial effect on high temperature strength and reduces the creep rate in mechanically alloyed ferritic steels by about six orders of magnitude. In this work we present an experimental study using atom probe tomography, X-ray photoelectron spectroscopy, and positron annihilation spectroscopy combined with first principles modeling focusing on the distribution and behavior of yttria in pure iron prepared by mechanical alloying. Atom probe tomography and X-ray photoelectron spectroscopy measurements as well as positron annihilation spectroscopy conducted on powder particles directly after milling have revealed that a predominantly fraction of the yttria powder dissolves in the iron matrix and Y atoms occupy convenient positions, such as vacancies or dislocations. This is supported by *ab initio* calculations demonstrating that the formation energy for Y substitutional defects in bcc-Fe is significantly lower in the close neighborhood of vacancies.

Introduction

For the production of a variety of equilibrium or non-equilibrium alloy phases mechanical alloying is a well-established method. An important class of materials produced by mechanical alloying, also called milling, are nanostructured materials and especially oxide dispersion strengthened (ODS) steels [1]. Most of these materials are mechanically alloyed with yttria and subsequently Hot Isostatically Pressed (HIPed). These steels show much better mechanical properties at elevated temperatures than steels without the Y–O clusters. Therefore, ODS steels are promising candidates to be used as fuel claddings in nuclear power reactors [2]. Yttria is preferred because of its high thermal stability [3], caused by its extremely high enthalpy of formation of about -1905.6 ± 2.3 kJ mol^{-1}[4]. While some studies reported that a dispersion of Y-O based particles with a diameter of 5-20 nm occurred in the iron matrix during mechanical alloying [5,6], others, especially in the last few years, reported a refinement of these particles by adding small amounts of Ti [7,8].

Ashkenazy et al. [9] employed molecular dynamic (MD) calculations in order to obtain insight into the effect of mechanical shear-induced intermixing of two different phases during MA. They investigated various phase combinations, such as fcc-fcc systems (Cu with Ag or Ni) and fcc-bcc systems (Cu with Fe, V and Nb). They revealed that especially in the fcc-fcc systems intermixing can take place because of dislocation gliding. The intermixing is much weaker in the fcc-bcc systems, which has been explained by the fact that the dislocations can hardly transfer from one phase to the other. Consequently, it seems unlikely for the Fe-Y_2O_3 system investigated here that dislocations can pass the interface between the two phases. A competing theory has been proposed by Schwarz [10], according to which diffusion is accelerated along dislocations. Y_2O_3, i.e. Y and also O atoms, is expected to diffuse into Fe matrix along these "diffusion pipes", encouraged by ball impacts and high temperatures.

However, the exact mechanisms during milling in the Fe-Y_2O_3 system have not yet been clarified. In the present study investigations were conducted with the purpose to get the distribution of Y and O in the as-milled powder particles. In order to analyze whether there is an extended solubility of Y and O in Fe, atom probe tomography (APT) investigations and X-ray photoelectron spectroscopy (XPS) measurements were performed on as-milled powder particles and on as-HIPed specimens. Furthermore, positron annihilation spectroscopy (PAS) was used to investigate the occupation of the 'free volume' in milled powder particles in order to show if they are diffusion pathways or not. Finally, these results are corroborated with *ab inito* calculations.

Methods

The model system studied in the present investigation were produced by mechanical alloying. For milling, ferritic iron powder was produced by water atomization and was blended with 0.5 wt.% yttria submicron powder with a d_{90} of 1.16 µm and a purity of 99.9 %. This corresponds to a volume fraction of 0.78 vol.% Y_2O_3. The powders were mechanically alloyed for 48 h using a Certony^{TM} attritor. The chemical compositions of the powders before and after milling were measured using X-ray fluorescence spectroscopy (XRF) and are listed in Table 1. A milling speed of 600 rpm was applied and steel balls with a ball-to-powder ratio of 10:1 were used as grinding media. To reduce oxidation effects and avoid incorporation of oxygen into the steel powder, the entire milling process was conducted under Ar gas atmosphere.

Table1: Material composition before and after 48 h of mechanical alloying. All details are presented in at.%.

	Fe	Al	Mn	Cr	Ni	Mo	W	Y_2O_3
Before milling	bal.	-	0.12	0.05	0.03	-	-	0.13
48 h milled state	bal.	0.10	0.16	0.24	0.10	0.01	0.05	0.13

After milling, the powders were HIPed for 3 h. The applied parameters were 1100 °C, and 100 MPa.

Atom probe investigations were performed on the as-milled powder particles and on as-HIPed materials. The tip preparation of the mechanically alloyed powder particles was performed by an FEI^{TM} Versa3D^{TM} Dual Beam focused ion beam (FIB). Numerous works describe how to prepare atom probe tips from powder particles, e.g. see [11,12]. We adopted a similar procedure with the difference that the powder particles were mounted on an SEM stub with silver adhesive. Subsequently, a wedge was lifted out at a proper position of the powder

particle and its slices were welded onto various positions of a microtip coupon, which provided the pre-tips for the APT measurements.

The HIPed bulk material was cut into small rods 15 mm long and a cross-section area of 0.3 x 0.3 mm². Subsequently, the standard electrochemical polishing method was used to prepare the tips [13].

The APT investigations were performed using a LEAP™ 3000X HR from Cameca™ (formerly Imago™) and a 3DAP from Oxford nanoScience™ both operating in voltage mode. Measurements were carried out under ultra-high vacuum conditions at a temperature of 60 K. A pulse fraction of 15 % and 20 % to the standing voltage was used. The atom probe measurements were evaluated using a Cameca ™ software IVAS 3.4.3.

XPS measurements were conducted in order to detect chemical changes of materials, especially changes of the binding energy of core level electrons. Investigations were performed with a Multiprobe-UHV-surface-analysis system from Omicron Nanotechnology ™. The powder was put on a carbon adhesive tape and the measurement was employed under ultra-high-vacuum. 120 sweeps were summed up to distinguish the Y3d signal from the background.

Studies of 2d-Doppler broadening (DB) of positron annihilation radiation were performed in the same manner as described in [14]. The 2d-DB measurements were performed in a coincidence setup of two high purity Ge detectors (typical energy resolution of ~1.3 keV at 511 keV) which corresponds to an effective resolution of the two detector system of 0.88 keV (full width at half maximum (FWHM) – value) related to the 511 keV γ-line. A peak-to-background ratio of $\sim 8\times10^5$ was achieved, which ensured a sensitivity to annihilation events with high momentum (core) electrons. Two-dimensional spectra with an energy width of ~1 keV per channel and $6\text{-}8\times10^7$ counts were collected, from which the background-free Doppler spectra were obtained. All measurements were performed at room temperature.

Ab initio calculations were performed using the Vienna *ab initio* simulation package (VASP). For these calculations a 3x3x3 cubic supercell with 54 atoms was employed and the plane-wave cut-off energy was set to 500 eV. Additionally, the 6x6x6 k-point mesh showed a total energy accuracy of about 10^{-3} eV/at.

Results

Atom probe investigations. APT measurements were conducted on as-milled powder particles in order to investigate the distribution of Y and O atoms in the material [15]. As shown in the atom maps in Figs.1a and b, Y and O atoms are distributed in a very fine manner, however, these atoms tend to form clusters already. Moreover, a visual inspection of Figs.1c and d which relates to the Mn and Al atom distribution, also shows a mostly homogenous distribution. In addition, it can be assumed that these extremely fine clusters are also enriched in Mn and Al, which have been incorporated during milling and they are not a component of the original yttria powder.

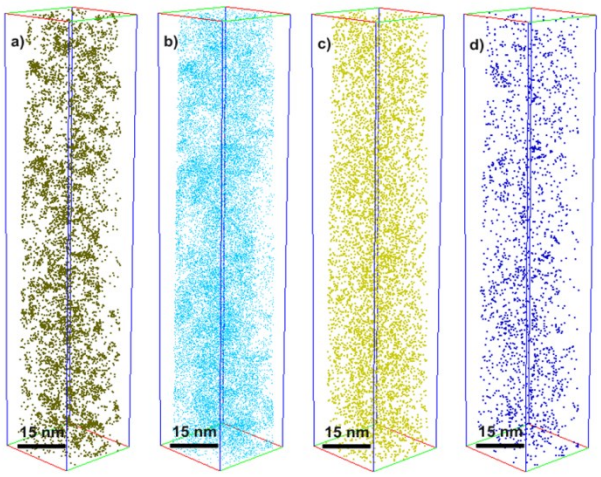

Fig. 1: Representative of an atom probe measurement of the as-milled powder particle. Atom distribution maps of Y(a), O(b), Mn(c), and Al(d) [15].

Comparing the materials before (Fig. 1) and after HIPing (Fig. 2) by means of APT it is evident that much more distinct particles are formed during HIPing. Additionally, the matrix which surrounds these distinct particles seems to be depleted in Y and also in O (Figs. 2a and b). The same trend can be found in case of the elements Mn and Al. High temperatures and pressures during HIPing seem to enhance the precipitation of particles from a supersaturated material produced by mechanical alloying.

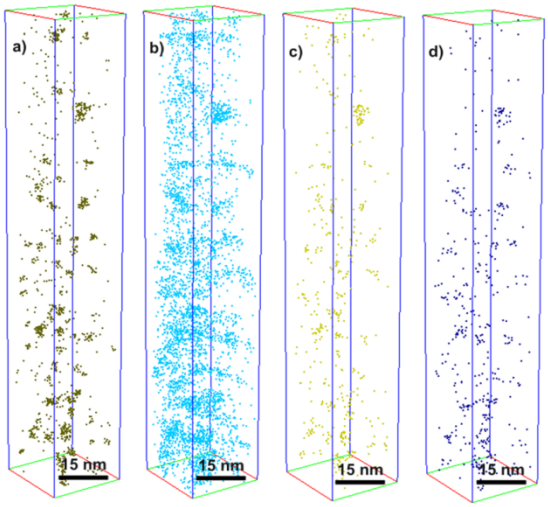

Fig. 2: Representative of an atom probe measurement of the as-hipped state. Atom distribution maps of Y(a), O(b), Mn(c), and Al(d) [15].

XPS investigations. To get more detailed information of the as-milled state, XPS measurements were employed. XPS allows to analyze a chemical change of Y_2O_3 caused by dissolution in the matrix or enrichment of other elements. The $Y3d_{5/2}$ signal of the milled powder is compared to the original Y_2O_3 powder in Fig. 3. The measurement is charge corrected, and the binding energy is calibrated to the carbon-carbon bond (284.6 eV), which is detected in all measurements as a surface contamination layer caused by sample transfer. According to [16], the Lorentzian/Gaussian peak fit of the 48 h milled powder yields a binding energy of 157.23 eV for the $Y3d_{5/2}$ electrons. Conversely, the peak fit of the reference Y_2O_3 curve reveals a binding energy of 157.66 eV for the same electrons. This means, that the chemical surrounding of the Y atoms in the milled stage is more electropositive, leading to weaker bonded core electrons. However, the shift is too low for a dissolution or a change of bonding partner. Therefore, we assume that Y is mainly bonded to O, but other enrichments of Mn or Al slightly weakens the binding energy of the electrons in Y, which agrees with APT findings, showing higher concentrations of Mn and Al at the clusters. Because of this, diffusion processes can be assumed during milling. To investigate if defects are responsible for these assumed diffusion processes, PAS and *ab initio* calculations have been conducted.

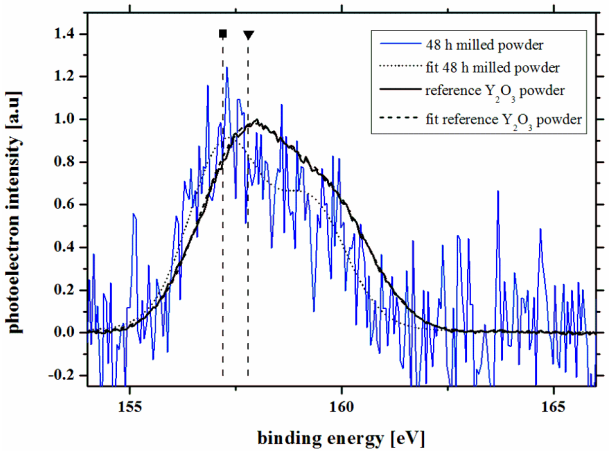

Fig. 3: Y3d signal of the as-milled powder particles compared to the original reference Y_2O_3 powder. The maxima of the $Y3d_{5/2}$ peaks are marked as vertical dashed lines. It shows a shift towards lower binding energy between the reference powder (triangle) and the milled powder (square) [16].

Positron annihilation spectroscopy. In Fig. 4 each normalized 2d-DB spectrum F (F represents the number of counts) is presented as a $F/F_{reference}$ ratio curve with respect to the normalized 2d-DB spectrum measured on a mixture of iron and Y_2O_3. The region ranging from electron momenta of 0 to approximately $2.5 \times 10^{-3} \times m_0c$ indicate annihilation with valence electrons, while the region from approximately $15 \times 10^{-3} \times m_0c$ onwards can be attributed to the annihilation with high momentum core electrons (the product m_0c stands for the electron momentum, where m_0 is the mass and c the speed of light). The momenta of the core electrons give information about the chemical sort of element and, therefore, this region provides an elemental fingerprint. Fig. 4 shows the 2d-DB spectra of ferrite, pure Y_2O_3 and the Fe-0.5 m.%Y_2O_3 sample milled for 48 h with respect to a Fe-0.5 m.% Y_2O_3 mixture specimen. The spectra measured on the 48 h ball milled sample reveals, compared to the reference ferrite-Y_2O_3 mixture sample, two main features. First of all, at low momenta (that means less than $2.5 \times 10^{-3} \times m_0c$) the ball milled sample shows enhanced F-ratios compared to the sample before milling, which suggests positron trapping at open volume defects. Furthermore, PAS yields a positive gradient at a momentum of $15 \times 10^{-3} \times m_0c$ onwards, which is similar to pure Y_2O_3. These two characteristic features indicate that annihilation of positrons occurs at vacancy-type defects in the ferrite matrix with a significant enrichment of Y in their vicinity. These defects with Y environment are created by mechanical alloying. Works on similar alloys with differing amount of yttria can be found in [17,18], which support results of this study and give a more complete overview of mechanical alloying of the Fe – Y_2O_3 system.

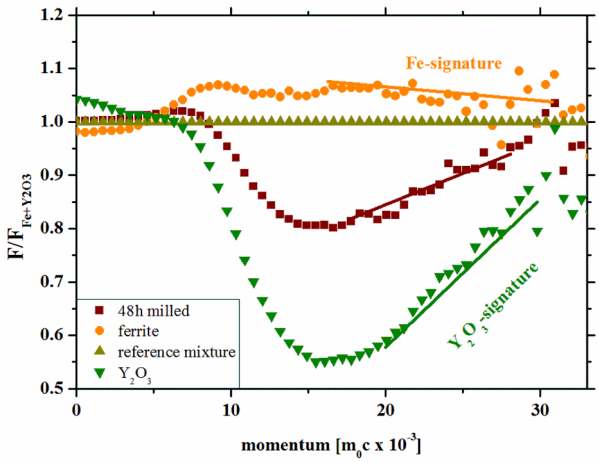

Fig. 4: Comparison of 2d-DB spectra of pure Y_2O_3 powder, pure ferrite powder and as-milled sample after 48 h of mechanical alloying. The ratio curves are normalized to the signal of a ferrite and 0.5 m% Y_2O_3 mixture without milling.

***Ab initio* calcualtions.** In this work the experimental results are corroborated with computational simulation. As shown in Ref. [16], the Gibbs energy of the system decreases with shorter distance between a substitutional Y atom and a single vacancy (vac) in a perfect bcc Fe lattice. The Gibbs energy against the Y-vacancy distance is depicted in Fig. 5. This is an evidence for attraction forces between substitutional Y atoms and vacancies, which

suggests a tendency for clustering of Y atoms and vacancies. This fact agrees with the results of the PAS showing that Y_2O_3 is enriched in the 'free volume'. The calculations also show that the energy of formation of the vacancies, which happens due to ball impacts during milling, changes if the system once has dissolved Y atoms. In the 54 atom Fe supercell in the vicinity of a substitutional Y atom the energy of formation of one vacancy decreases. Producing a vacancy as the first nearest neighbor of a Y atom, which is a distance of $\sqrt{3}\cdot a/2$, where a is the lattice parameter of bcc Fe, the energy of formation is 0.829 eV/vac. This is a reduction of 1.364 eV/vac of the energy of vacancy formation compared with a perfect bcc lattice. Additionally, the energy of formation is lowered also for the second, third and fourth neighbor distance between Y and a vacancy. All these results give a hint that defects are a key factor for mechanical alloying, as assumed in the theory of Schwarz [10]. If this is the case the reduction of vacancy formation energy can further enhance the efficiency of the milling process with the effect of producing a supersatured Fe material with Y.

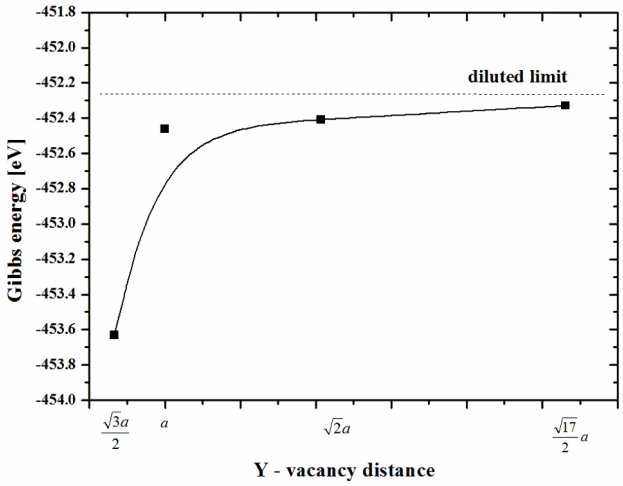

Fig. 5: Evolution of the Gibbs energy of the calculated system in dependence of the distance of a vacancy to a substitutional Y atom [16].

Conclusions

In this work APT, XPS, as well as PAS investigations were combined with *ab initio* calculations in order to reveal the Y_2O_3/Y distribution after 48 h milling in ferritic powder particles. APT and XPS measurements are in good agreement with PAS and first principle calculations. It can be concluded that Y is distributed in the Fe matrix in a very fine manner. Additionally, to form clusters Y is enriched in close vicinity of vacancies which were generated by the milling process. This fact gives a hint that these defects are a key factor for the distribution of Y in Fe.

References

[1] C. Suryanarayana, Prog. Mater. Sci. 46 (2001) 1.

[2] S. Ukai, T. Nishida, H. Okada, T. Okuda, M. Fujiwara, and K. Asabe, JNucl Sci Technol 34 (1997) 256.

[3] S. Y. Zhong, J. Ribis, V. Klosek, Y. de Carlan, N. Lochet, V. Ji, and M. H. Mathon, J Nucl Mater 428 (2012) 154.

[4] E. J. Huber, L. Head, and C. E. Holley, J Phys Chem 61 (1957) 497.

[5] A. Czyrska-Filemonowicz and B. Dubiel, J. Mater. Process. Technol. 64 (1997) 53.

[6] J. S. Benjamin, Metall. Trans. 1 (1970) 2943.

[7]. M. K. Miller, K. F. Russell, and D. T. Hoelzer, J. Nucl. Mater. 351 (2006)261.

[8] D. Larson, Scripta Mater. 44 (2001) 359.

[9] Y. Ashkenazy, N. Q. Vo, D. Schwen, R. S. Averback, and P. Bellon, Acta Mater 60 (2012) 984.

[10] R. B. Schwarz, Mater. Sci. Forum 269-272 (1998) 665.

[11] M. K. Miller and K. F. Russell, Ultramicroscopy 107 (2007) 761.

[12] M. K. Miller, K. F. Russell, and G. B. Thompson, Ultramicroscopy 102 (2005) 287.

[13] M. K. Miller, A. Cerezo, M. G. Hetherington, and G. D. W. Smith, Atom Probe Field Ion Microscopy (1996), pp. 1–483.

[14] W. Puff, H. Rabitsch, G. Wilde, G. P. Dinda, and R. Würschum, Journal of Applied Physics 101 (2007) 123512.

[15] G. Ressel, S. Primig, H. Leitner, The evolution of Y distribution during the processing route of mechanically alloyed iron studied by means of atom probe tomography, accepted for publication in Int. J. Mater. Res.

[16] G. Ressel, D. Holec, A. Fian, F. Mendez-Martin, H. Leitner, Atomistic insights into milling mechanisms in an Fe-Y2O3 model alloy, accepted for publication in Appl. Phys. A.

[17] M. J. Alinger, S. C. Glade, B. D. Wirth, G. R. Odette, T. Toyama, Y. Nagai and M. Hasegawa, Materials Science and Engineering: A 518 (2009) 150–157.

[18] J. H. Lee, J Nanosci Nanotechnol, 12 (2012) 1670–1674.

Publication F:

Focused ion beam sample preparation of mechanically alloyed iron powders for atom probe tomography

F. Mendez-Martin, G. Ressel, H. Leitner

MC 2013 Proceedings, (2013) 509-510.

Materials for Energy Technology

MS.4.P092
Focused ion beam sample preparation of mechanically alloyed iron powders for atom probe tomography

F. Mendez-Martin[1], G. Ressel[1], H. Leitner[1]

[1]MontanUniversität Leoben, Department Physical Metallurgy and Materials Testing, Leoben, Austria

francisca.mendez-martin@unileoben.ac.at
Keywords: focused ion beam, atom probe tomography, steel powders

Higher temperature strength in steels can be achieved with addition of finely distributed Yttrium oxides by mechanical alloying. Nevertheless, the strengthening mechanism during mechanical alloying is still not clearly understood. In order to clarify the effects of Y and O distribution during the alloying process, 4 different manufactured powders were analysed.

Two different iron-rich powders have been analysed, see figure 1. The powder was mechanically alloyed for 12h and 48h using a Certony^{TM} attritor. The iron powder was produced by water atomization and was mixed with 0.5 wt% yttria powder with a d_{90} of 1.16 µm. The chemical composition is presented in table 1.

For the characterization of the different powder conditions, atom probe tomography (APT) has been used [1]. For APT measurements needle-shaped specimens are needed, with radii between 30 to 100 nm on the tip and an angle near to or lower than 10°. Traditional methods as chemically or electrochemically polishing [2] are impossible to use in powder material. Therefore, the method for preparation of needle-shaped tips for powder samples via focused ion beam (FIB) was chosen [3, 4]. A single grain of each powder was selected for a thick lift out in a wedge form and a platinum layer was deposited on the interesting zone, first via electron deposition and afterwards with ion deposition, to minimize gallium implantation. Multiple specimens were cut from the thick lift out wedge and welded on a micotip coupon, which provides the pre-tips for the APT measurements. Afterwards, the following annular milling at 30 kV, 5 kV and 2 kV were the last process, for the preparation of the APT tips free of Gallium implantation. The atom probe investigations were completed in a LEAP^{TM} 3000X HR of Cameca^{TM} with a Local Electrode system. The analyses were performed in voltage mode at 60 K in ultra-high vacuum. A pulse fraction of 15 % and 20 % was used. The atom probe measurements were evaluated with IVAS 3.4.3 software. The analysed volume was about 25x25x150 nm^3 and the different material conditions were compared.

The atom probe investigations reveal a clustered arrangement of Y and O atoms during mechanical alloying; see figure 2 a) and b). Yttrium atoms together with oxygen, rearrange during mechanical alloying to form clusters. Aluminium and manganese enrichments (see figure 2 c) and d)) could be also detected, which suggests that diffusion processes are active during the mechanical alloying process. These clusters are not only remnants of the Y_2O_3 powder, yttrium and oxygen dissolve in the matrix to rearrange afterwards at favourable sites as lattice defects, vacancies or dislocations to form clusters.

By using focused ion beam, needles-shape specimens for atom probe tomography could be prepared for two different grain size powder samples after 12 and 48 h of mechanical alloying. The atom probe investigations reveal fine distributed yttrium oxide clusters as well as yttrium dissolved in the matrix. Moreover enrichments of alloying elements as aluminium and manganese reveal that diffusion processes are active during mechanical alloying clarifying the mechanism during this process.

1. W.R. McKenzie, E.A. Marquis and P.R. Munroe, "Microscopy: Science, Technology, Applications and Education", ed. A. Méndez-Vilas and J. Díaz (2010) p. 1800.
2. M.K. Miller, A. Cerezo, M. G, Hetherington and G.G.W. Smith, "Atom Probe Field Ion Microscopy", ed. R.J. Brook, A. Heuer, T.J. Marks, D.A. Smith, A. Cheetham, S.P. Hirsch, J. Silcox, M.V. Tirrell, V.Vitek (1996) p.476.
3. M.K. Miller, K.F. Russel, K. Thompson, R. Alvis and D. J. Larson, Microscopy and Microanalysis 13 (2007), p. 428.
3. M.K. Miller and K.F. Russel, Ultramicroscopy 107 (2007), p. 761.

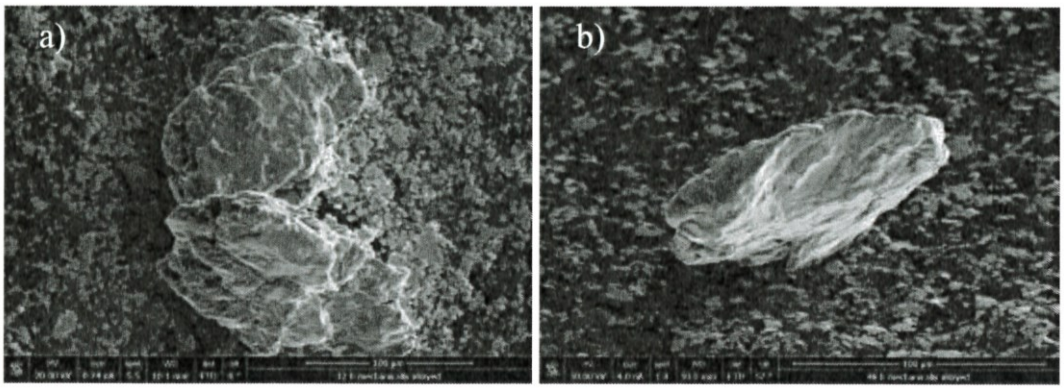

Figure 1. Powder after 12 h mechanically alloyed (a) and after 48 h mechanically alloyed (b).

	Fe	Al	Mn	Cr	Ni	Mo	W	Y_2O_3
12 h mechanically alloyed	bal.	0.34	0.14	0.09	0.05	0.01	0.8	0.12
48 h mechanically alloyed	bal.	0.1	0.16	0.24	0.1	0.01	0.05	0.13

Table 1. Chemical composition of the of the analyzed powders (at.%).

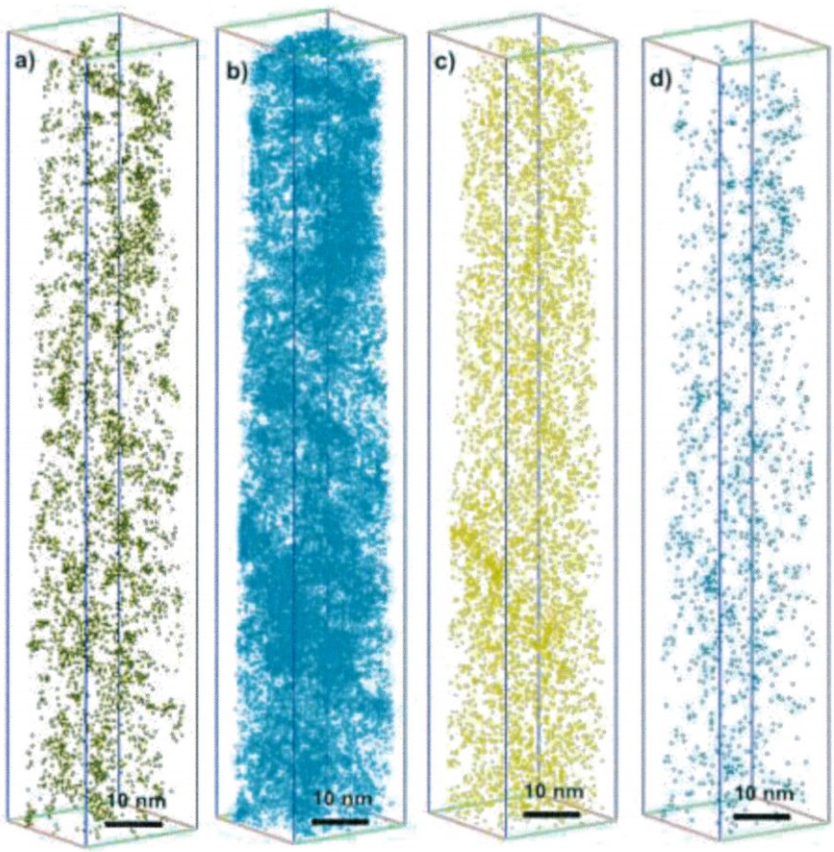

Figure 2. 3D atom maps of the 48 h mechanically alloyed condition. a) Y; b) O. 3D atom maps of the 48 h mechanically alloyed state, showing enrichments of Al and Mn at the Y-O clusters c) Mn and d) Al.